Flow and stability of a viscoelastic liquid curtain

Antoine Gaillard

Université Sorbonne
Paris Cité

université
PARIS
DIDEROT
PARIS 7

Thèse de doctorat
de l'Université Sorbonne Paris Cité
Préparée à l'**Université Paris Diderot**
Ecole doctorale **Physique en Île-de-France** (ED 564)
Laboratoire **Matière et Systèmes Complexes - UMR 7057**

Thèse de doctorat de Physique

Écoulement et stabilité d'un rideau liquide viscoélastique

Flow and stability of a viscoelastic liquid curtain

Présentée par **Antoine Gaillard**

Dirigée par Laurent Limat

Soutenue publiquement le 19 Décembre 2018 devant un jury composé de

Présidente du Jury :	Anke LINDNER, Professeur, Université Paris Diderot
Rapporteur :	John HINCH, Professeur, University of Cambridge
Rapporteur :	Guillaume OVARLEZ, Dir. de Recherche, Université de Bordeaux
Examinatrice :	Camille DUPRAT, Maître de Conférences, École Polytechnique
Directeur de thèse :	Laurent LIMAT, Dir. de Recherche, Université Paris Diderot

Résumé : Écoulement et stabilité d'un rideau liquide viscoélastique

L'écoulement et la stabilité des rideaux liquides viscoélastiques sont étudiés pour des solutions de polymères flexibles et semi rigides. Ces liquides viscoélastiques sont extrudés à partir d'une fente à débit constant et s'écoulent à l'air libre sous l'effet de la gravité. L'écoulement de ces liquides se caractérise par un équilibre initial entre la gravité et les forces élastiques causées par les déformations des chaînes de polymère, jusqu'à ce que l'inertie du liquide finisse par dominer et que l'on retrouve le comportement classique de chute libre. Nous montrons que l'écoulement est principalement influencé par la valeur du temps de relaxation extensionnel mesuré par une méthode de filamentation. Un nouvel éclairage sur l'écoulement des rideaux liquides Newtoniens nous permet de trouver une courbe maîtresse de l'écoulement dans le cas viscoélastique par analogie. En ce qui concerne la stabilité du rideau, nous observons que le débit critique de formation du rideau n'est pas affecté par la présence de polymères, tandis que le débit minimum en deçà duquel le rideau se rompt diminue après ajout de polymères, ce qui révèle une plus grande résistance de la nappe à l'initiation de trous. Par ailleurs, nous observons une instabilité de l'écoulement pour les solutions les plus rhéofluidifiantes, où des bandes épaisses (où la vitesse du liquide est supérieure à la moyenne) sont formées au sein du rideau. Une visualisation de l'écoulement à l'intérieur de la filière d'extrusion révèle que ce phénomène est lié à une instabilité de l'écoulement de contraction en amont de la fente, où l'écoulement est de nature instationnaire et tridimensionnelle.

Mots clefs : Mécanique des fluides, Écoulement à surface libre, Fluides complexes, Polymères, Instabilités élastiques

Abstract : Flow and stability of a viscoelastic liquid curtain

The flow and the stability of viscoelastic liquid curtains are investigated using solutions of flexible and semi-rigid polymer chains. These viscoelastic liquids are extruded from a slot at constant flow rate and fall in ambient air under gravity. We show that the curtain flow of polymer solutions is characterised by an initial balance between gravity and the elastic stresses arising from the stretching of polymer molecules, until inertia finally dominates and the classical free-fall behaviour is recovered. We show that the flow is mostly influenced by the value of the extensional relaxation time of the solution measured by a filament thinning technique. New insights on the theoretical description of Newtonian curtains allow us to find the master curve of the viscoelastic curtain flow by analogy. Concerning the curtain stability, we show that the critical flow rate for curtain formation is not affected by the presence of polymers whereas the minimum flow rate below which the curtain rapidly breaks is reduced by polymer addition, thus revealing a greater resistance of the sheet to hole initiations. Furthermore, we observe the onset of a flow instability for the most shear-thinning solutions, where thick bands (where the liquid velocity is larger than average) are formed within the curtain. Visualisations of the flow inside the die reveal that this phenomenon is linked to a flow instability at the contraction plane upstream of the slot where the flow is unsteady and three-dimensional in nature.

Keywords : Fluid mechanics, Free-surface flow, Complex fluids, Polymers, Elastic instabilities

Remerciements

Je tiens tout d'abord à remercier chaleureusement John Hinch, Guillaume Ovarlez, Anke Lindner et Camille Duprat pour avoir accepté de faire parti de mon jury de thèse et pour avoir fait le déplacement jusqu'à Paris pour assister à ma soutenance. J'ai été très touché par l'intérêt qu'ils ont manifesté pour mes travaux et j'ai beaucoup apprécié les discussions qui ont suivi la soutenance.

J'écris ces quelques lignes depuis Manchester (UK) où je viens de commencer mon premier post-doctorat. Ces quelques semaines passées loin du laboratoire MSC suffisent à me faire réaliser à quel point c'est un chouette labo. C'est évidemment un super lieu de travail, mais c'est également un lieu de vie très agréable. Avec ses grand "thésariums" et ses nombreux espaces de convivialité, le bâtiment est pensé de manière à maximiser les interactions sociales. Ainsi, au cours de ces quatre dernières années passées en son sein, j'ai rencontré des gens exceptionnels que je tiens maintenant à remercier.

Je remercie tout d'abord mes encadrants officiels, mon directeur de thèse Laurent Limat ainsi que Luc Lebon, pour m'avoir soutenu et encouragé dans mon travail tout au long de ma thèse. Je n'oublierai pas tous ces super moments passés ensemble, à Paris ou à l'étranger à l'occasion de conférences internationales, où nous avons eu l'occasion d'échanger en dehors du cadre professionnel. Je remercie également mes encadrants non officiels: Matthieu Roché, Sandra Lerouge et Cyprien Gay, à qui je dois beaucoup. Matthieu, tu as toujours été là pour m'aider à avancer, même au tout début en prenant de mes nouvelles régulièrement quand tu passais en salle 790. Tu es très vite devenu la personne avec qui je pouvais échanger au jour le jour pour discuter science (mais pas que), et ce jusqu'à cet article dont l'écriture a généré de nombreux débats (souvent houleux mais toujours pertinents) qui m'ont fait mûrir scientifiquement. Sandra et Cyprien, vous êtes arrivés un peu plus tard (à l'occasion d'un séminaire interne), mais suffisamment tôt pour avoir également largement contribué à la qualité des résultats présentés dans ma thèse. Sandra, je te suis très reconnaissant pour tes nombreux conseils qui ont permis de mettre de l'ordre dans mes résultats scientifiques, ainsi que pour m'avoir très justement orienté vers l'étude de l'écoulement de contraction, que tu as eu la gentillesse d'encadrer en mettant à ma disposition ta salle de manip, ton matériel, ainsi que ton énergie. Cyprien, merci pour m'avoir guidé dans mes travaux analytiques, notamment dans le monde sinueux des

modèles de liquides viscoélastiques. Tu étais toujours partant pour qu'on écrive des équations ensemble. Même si, à cause de mon manque de recul, je ne comprenais pas toujours du premier coup, je finissais toujours pas me dire "Ah mais oui, il a raison!".

Merci également à tous les gens du MSC qui étaient là pour m'aider dans mes travaux: Henri Lhuissier, Adrian Daerr, Chi-Tuong Pham, Alain Ponton, Laurent Royon, Mathieu Receveur, Laurent Réa, Yann Le Goas, Arnaud Grados, Olivier Cardoso, Sylvain Courrech du Pont, Julien Dervaux, et tous ceux que j'oublie sûrement. Je remercie également Arnol Cyrille Noah Adina que j'ai eu le plaisir d'encadrer pendant son stage de Master.

Mais parce que la science, c'est pas la seule chose qui compte dans la vie, le moment est venu de remercier les fines équipes des salles 777 et 911 (+ satellites) dont j'ai eu le plaisir de partager le quotidien pendant presque quatre ans. Merci Rémy H, Rémy O et Amir pour la super ambiance et tous ces bons moments passés ensemble, pour les bonhommes de neige sur le toit en hivers et les barbecues/apéros + musique en été (*Beep beep I'm a sheep*!). Thank you Menghua for being the ideal experiment-room-mate and for all your Chinese lessons! Merci Robin (Peepoodo) pour ton beau cadeau qui me tient chaud à Manchester! Merci Tanguy pour m'avoir aidé dans mon entreprise d'épuisement des nerfs de la 911 à coup de chants polyphoniques, et pour tes encouragements dans nos transitions respectives vers un régime alimentaire moins carné. Merci Solène pour organiser toutes les cagnottes de thèse à l'approche de nos soutenances, alors que tu es toi même sous la vague de la rédaction, merci pour m'avoir appris à dire des phrases qui claquent en chinois telles que " 你什么都不知道。", et pour ces repas frugaux partagés en tête à tête les dimanches pluvieux au labo. Merci Mathieu et Oliver pour avoir égayé nos repas au CROUS avec de nombreuses citations (*La pâte d'amande!!*) et références culturelles (obligeant ainsi les autres à se cultiver, sous peine de ne comprendre aucune vanne), et pour avoir assuré la bonne tenue des débats politiques. Merci Raph pour m'avoir fait découvrir les pépites cachées du YouTube underground et pour m'avoir enseigné l'art subtil de lancer des cartes à jouer en mode shuriken! Merci Romain pour avoir supporté ma présence en face de toi pendant de longs mois, ainsi que pour tes cours de swing et de sociologie. Merci Paul pour ces discussions enthousiastes sur les maths et la musique, et pour m'avoir accepté parmi vous malgré mon retard dans la livraison du gâteau escompté (pour reprendre l'expression de ta chanson). Merci Quentin pour nous avoir nourri régulièrement avec tes gâteaux, et n'oublie pas de ne surtout pas peindre la chambre de tes enfants en rose ou en bleu! Merci Mallory pour avoir été le seul à renvoyer mes avions en papier avec enthousiasme, et pour avoir renormalisé mon échelle de WTF en terme de diapositive et de présentation orale.

Je tiens enfin à remercier ma famille pour son soutien, et en particulier mes parents sans qui je n'en serais pas là aujourd'hui, ainsi que tous mes amis hors labo, à Toulouse et à Paris, sans qui la vie serait moins fun. Vous venez à Manchester quand vous voulez!

Contents

General introduction

Liquid curtains are sheets of liquid flowing freely in ambient air under gravity. Industrial curtains are usually produced by extruding a liquid through a vertical slot die at constant flow rate, or by producing a liquid film which turns into a curtain when falling off the edge of an inclined plane. Such physical objects are characterised by a large aspect ratio, meaning that the falling distance of the liquid is much larger than the sheet thickness. One of the best everyday examples are the "pool water curtains" found in some swimming pools: the inertia of the sheet hitting your body (neck, back, shoulders) produces a pleasant massage effect. Curtains can also be found in some overflow fountains if the flow rate is large enough to prevent early breaking of the sheet into independent jets. An original and aesthetic example can be found in the work of the Polish artist Małgorzata Chodakowska who designed bronze statues equipped with a hydraulic system producing liquid sheets. These sheets can represent, among other examples, the wings of an angel or the skirt of a ballerina.

In the case of water curtains falling vertically, the velocity of the liquid is very well approximated by a free-fall law, meaning that viscous dissipation is negligible and that all the gravitational potential energy is converted into kinetic energy. Hence, every fluid particle falls like an independent friction-free rigid body with constant acceleration $g = 9.81$ m^2/s. By continuity, the increase in velocity produces a progressive thinning of the sheet, as is commonly observed in jets of tap water which is the axisymmetric version of the problem. In the case of Newtonian liquids with high viscosity, intuition suggests a different behaviour: a jet of honey seems to fall with lower velocities. The first experimental measurements by Brown (1961) using viscous Newtonian liquids extruded through a slot indeed revealed a shift from the classical free-fall behaviour close to the slot. A simple one-dimensional force balance equation of the flow derived by Sir G. I. Taylor (in the appendix of Brown (1961)) was shown to fit experimental velocity fields $U(z)$, where U is the local mean velocity (averaged along the curtain thickness) and z is the distance from the slot exit. Analytical contributions by Clarke (1966, 1968), Aidun (1987) and Ramos

(1996) provided a deeper understanding of this equation and revealed that free-fall behaviour with constant acceleration g is asymptotically recovered at a distance $z_v^* = F_v \times z_v$ from the slot, where $z_v = ((4\eta/\rho)^2/g)^{1/3}$, ρ and η being the density and dynamic viscosity of the liquid, and where F_v is a dimensionless decreasing function of the initial velocity U_0 at the slot exit which is about 7 when $U_0/\sqrt{gz_v} \ll 1$.

An other interesting aspect of liquid curtains is their stability in terms of spontaneous hole opening events. Brown (1961) showed that the future of a hole initiated within the curtain (due to impurities) was principally determined by a balance between capillary forces, pulling up the rim of the hole towards the slot, and the inertia of the surrounding liquid which pulls the hole downward. This argument has later been refined by Sünderhauf et al. (2002) and Karim et al. (2018a) to take into account stabilising viscous effects.

One of the main industrial applications of liquid curtains is the well documented curtain coating technique described by Miyamoto & Katagiri (1997) which aims at depositing a material layer of uniform thickness on a solid surface. In its simplest version, a liquid is extruded from a thin slot and the resulting vertical liquid sheet impacts a solid substrate moving horizontally underneath at constant speed. Curtain coating is one of the main manufacturing steps in the production of functional films used in displays, solar panels and many other applications. Since most industrial coating liquids are non-Newtonian, recent experimental studies have been dedicated to the characterisation of non-Newtonian curtains (i.e. made of a complex fluid) such as viscoelastic curtain made of polymer solutions. Existing works have mostly focused on the impact of viscoelasticity on curtain stability (Becerra & Carvalho, 2011; Gugler et al., 2010; Karim et al., 2018b), revealing a stabilising effect of polymer additives. However, the structure of the liquid velocity field has only been discussed by Karim et al. (2018b) who measured free-falls for polymer solutions with millisecond-scale relaxation times. In comparison, the effect of fluid elasticity on the analogous film casting process, involving thick polymer melts stretched by a rotating drum to produce plastic sheets, is much more documented (Alaie & Papanastasiou, 1991; Satoh et al., 2001). However, since gravity and inertia are negligible in film casting, these results can not be generalised to the curtain coating technique which involves liquids of much lower viscosity.

In the present work, we investigate the role of viscoelasticity in the flow and stability of liquid curtains extruded from a die in the context of polymer solutions. This manuscript is organised in three main parts.

Part one We first introduce the main analytical concepts which will be useful when interpreting the experimental results. In chapter 1, we provide a detailed analytical analysis of the flow of Newtonian curtains. This analysis contains new contributions which revealed to be useful for the description of viscoelastic curtains. The main aspects of Newtonian curtain stability are also presented. Then, we introduce in chapter 2 the main concepts of viscoelasticity and viscoelastic flows. This includes the presentation of the basic constitutive equations derived from the microscopic description of polymer molecules and an overview of the unusual flow characteristics of viscoelastic fluids.

Part two We present in chapter 3 the experimental set-up used to produce liquid curtains, as well as the particle image velocimetry technique used to measure the curtain velocity field. We also introduce the different polymer solutions used in this study, as well as their rheological characterisation, both in shear and extensional flows. Then, in chapter 4, we present the experimental results concerning the curtain velocity field. We show that elasticity has a dramatic effect on the flow by reducing the liquid velocity, or, more precisely, the liquid acceleration which is less than g and decreases when increasing the polymer relaxation time. We show that the curtain flow of polymer solutions is characterised by an initial balance between gravity and the elastic stresses arising from the stretching of polymer molecules, until inertia finally dominates and the classical free-fall behaviour is recovered. A simple scaling is found and a master curve is identified. The effect of the history of polymer deformations inside the die is also investigated. We also provide an attempt of theoretical description using the Oldroyd-B model.

Part three The last part is dedicated to the study of the curtain stability. In chapter 5, we first discuss the stability in the familiar context of spontaneous breaking events. Then, we discuss the stability in the more classical meaning of the term which is the instability of the flow itself, and not the stability of the curtain seen as a physical object. We characterise a new spatial and temporal flow instability observed for the most shear-thinning solutions, which is characterised by a varicose horizontal modulation of the sheet thickness and by a modulation of the velocity field. In chapter 6, using a new experimental setup, we show that this modulation is linked to a strongly unsteady and 3-dimensional flow instability appearing at the slot inlet of the die where the liquid undergoes a planar contraction. These results are compared to analogous elastic instabilities reported in the literature.

Chapter 1

Liquid curtains

Contents

In this chapter, we first present an analysis of the flow of Newtonian liquid curtains. After a general overview, we derive a general force balance equation for the mean velocity field $U(z)$ averaged over the curtain thickness. We recover the equation derived by G. I. Taylor in the specific case of a Newtonian liquid. The analytical solution of this equation is investigated in order to identify a master curve which had not been clearly identified in the literature. This analysis will be a useful guide for the interpretation of the experimental results concerning viscoelastic liquid curtains. Then, we present the classical criterion for the stability of a Newtonian curtain. We conclude this chapter by a state of the art concerning viscoelastic liquid curtains.

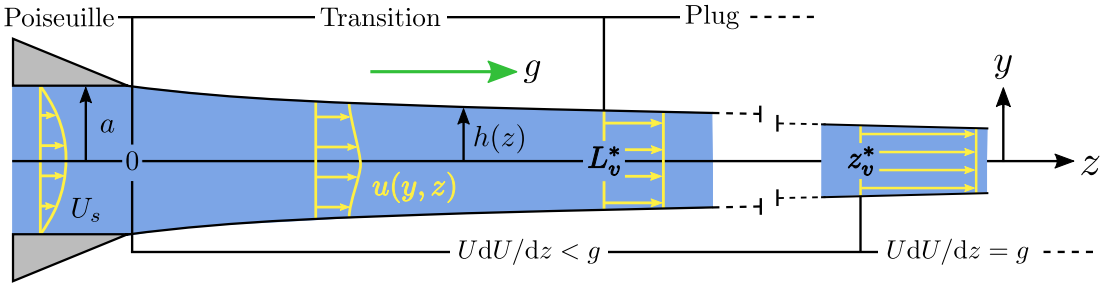

Figure 1.1 – Sketch of an infinitely long Newtonian curtain (cross-sectional view). The local vertical velocity field $u(y, z)$ switches from a Poiseuille flow inside the slot to a plug flow at a distance $z = L_v^*$ from the slot. In parallel, the mean velocity field $U(z)$ averaged over the curtain thickness is characterised by a transition from a sub-gravitational regime to an asymptotic free-fall regime at a distance $z = z_v^*$ from the slot.

1.1 Newtonian curtain flow

1.1.1 General overview

Before deriving any equation, we give a general overview of the different flow transition observed in Newtonian curtain. In this section, we consider that the flow rate is large enough to produce a continuous sheet of liquid.

We consider a Newtonian liquid of density ρ, dynamic viscosity η and surface tension Γ extruded from a vertical slot of thickness $2a$, as shown in figure 1.1. The part of the flow which is in contact with ambient air is called a liquid curtain. It is characterised by its linear flow rate q which is the volumetric flow rate per unit slot width. The mean liquid velocity in the slot is

$$U_s = \frac{q}{2a} \tag{1.1}$$

We note z the direction of the flow (axial direction) and y is the transverse direction. We assume a laminar and steady flow which is translation invariant along x, meaning that we can neglect any edge effect, as if the curtain had an infinite width. In curtain coating, the liquid is stopped by a flat solid surface moving horizontally at constant speed. The length L_c of the curtain (i.e. the distance between the slot exit and the substrate) is generally much larger than the slot thickness $2a$.

We assume that a fully developed Poiseuille flow is established in the slot. At the slot exit, the wall boundary condition switches to a free-surface boundary condition, i.e. zero shear stress at the liquid-air interface. Hence, due to viscous diffusion, the Poiseuille flow switches to a plug flow, as illustrated in figure 1.1. We note $u(y, z)$ the local vertical velocity and $U(z)$ the mean velocity averaged over the curtain

thickness. Since the liquid is accelerated by gravity, the curtain thickness $2h(z)$ decreases by continuity. Brown (1961) showed experimentally that this contraction gives rise to viscous stresses which impact the curtain velocity. Therefore, the local mean acceleration $U\mathrm{d}U/\mathrm{d}z$ may be initially less than g. Brown (1961) showed that an asymptotic free-fall regime where $U\mathrm{d}U/\mathrm{d}z = g$ is reached when inertia overcomes the resistance of the liquid. We now discuss these two flow transitions.

Poiseuille - plug transition For Newtonian liquids, a fully developed plug flow is expected to be established after a distance from the slot exit which scales as

$$L_v = \frac{\rho U_s a^2}{\eta} = Re\, a \qquad \text{where} \qquad Re = \frac{\rho U_s a}{\eta} \tag{1.2}$$

is the Reynolds number. A large viscosity results in a fast transitionan due to efficient momentum diffusion. The plug flow is fully established at a distance $L_v^* = P_v \times L_v$ from the slot, where P_v is a dimensionless prefactor. In the analogous case of an axisymmetric laminar capillary jet, Sevilla (2011) shows that P_v is a function of the Weber number $We = \rho U_s^2 a/\Gamma$ where a is the injector radius, and gives $P_v(We = 10) \approx 0.2$.

Sub-gravitational - free-fall According to Brown (1961), the mean acceleration effectively reaches the asymptotic free-fall value g at a distance $z_v^* = F_v \times z_v$ ("v" for "viscous") from the slot where

$$z_v = \left(\frac{(4\eta/\rho)^2}{g}\right)^{1/3} \tag{1.3}$$

and where the prefactor F_v is a decreasing function of the initial curtain velocity $U_0 = U(z = 0) = U_s$. In other words, $U\mathrm{d}U/\mathrm{d}z(z = z_v^*) \approx g$. As will be presented in the next sections, $F_v \approx 7$ for negligibly small initial velocities $U_0 \ll \sqrt{gz_v}$. Contrary to the previous transition, a large viscosity results in a slow transition.

Comparison Ignoring the prefactors, the ratio between the Poiseuille to plug and sub-gravitational to free-fall transition lengths is

$$\frac{L_v}{z_v} = Re\,\frac{a}{z_v} = \frac{U_s\, a^2 \rho^{5/3} g^{1/3}}{4^{2/3}\eta^{5/3}}, \tag{1.4}$$

We deduce that liquids of large viscosity ($L_v/z_v \ll 1$) exhibit a long sub-gravitational plug flow whereas liquids of low-viscosity ($L_v/z_v \gg 1$) fall with a mean acceleration g while exhibiting velocity gradients along the thickness direction y. In the first case, the curtain flow is purely extensional with no shear component. Of course,

this discussion if only valid if the curtain length L_c is much larger than both L_v^* and z_v^*. For example, if the liquid viscosity is such that $z_v^* > L_c$, the fluid particles may never reach the gravitational acceleration g.

1.1.2 General force balance equation

In the appendix of Brown (1961), Sir Geoffrey Taylor proposed the following force balance equation for Newtonian liquid curtains

$$U\frac{\mathrm{d}U}{\mathrm{d}z} = g + \frac{4\eta U}{\rho}\frac{\mathrm{d}}{\mathrm{d}z}\left(\frac{1}{U}\frac{\mathrm{d}U}{\mathrm{d}z}\right) \tag{1.5}$$

where ρ and η are respectively the liquid density and dynamic viscosity. The first term accounts for the liquid inertia, the second is the gravitational acceleration, and the last term represents visous dissipation. This equation was found to capture the experimental results by Brown (1961). As shown by Aidun (1987) and Ramos (1996), Taylor's equation 1.5 can be derived rigorously from a long-wave approximation of the Navier-Stokes equation using the aspect ratio $a/L_c \ll 1$ as a small parameter where $2a$ and L_c are respectively the slot thickness and the curtain length.

Following the simple derivation of G. I. Taylor, we now derive a more general force balance equation which does not rely upon a particular constitutive equation. This equation will be used in future descriptions for viscoelastic curtains.

A slice of curtain between altitudes z and $z + \mathrm{d}z$ travels a distance $\mathrm{d}z = U\mathrm{d}t$ between times t and $t + \mathrm{d}t$. Its momentum per unit curtain width is $2h\rho U\mathrm{d}z$. We consider the gravitational force $2h\rho g\mathrm{d}z$ and the contact forces $2h(z)\pi_{zz}(z)$ and $2h(z + \mathrm{d}z)\pi_{zz}(z + \mathrm{d}z)$ acting respectively on the upper and lower side, where $\boldsymbol{\pi}$ is the mean stress tensor. Using the flow rate conservation

$$2hU = q = 2aU_s \tag{1.6}$$

along with $\mathrm{d}z = U\mathrm{d}t$, we obtain

$$U\frac{\mathrm{d}U}{\mathrm{d}z} = g + \frac{U}{\rho q}\frac{\mathrm{d}(2h\pi_{zz})}{\mathrm{d}z} \tag{1.7}$$

Note that the mean quantities can be written as

$$U = \frac{1}{h}\int_0^h u\,\mathrm{d}y \qquad \text{and} \qquad \pi_{zz} = \frac{1}{h}\int_0^h \pi_{zz}^*\mathrm{d}y \tag{1.8}$$

where $u(y, z)$ and $\pi_{zz}^*(y, z)$ are respectively the vertical component of the local ve-

locity field and the z normal component of the local stress tensor $\boldsymbol{\pi}^*$. Let us write $\pi^*_{ij} = -P^*\delta_{ij} + \sigma^*_{ij}$ for the local stress tensor and

$$\pi_{ij} = -P\delta_{ij} + \sigma_{ij} \tag{1.9}$$

for the mean stress tensor where δ_{ij} is the Kronecker delta. Although the exact definition of P^* and P relies upon a particular definition of the extra stress tensors $\boldsymbol{\sigma}^*$ (local) and $\boldsymbol{\sigma}$ (mean), the derivation can continue without specifying them. Neglecting surface tension and using the slender curtain approximation $\mathrm{d}h/\mathrm{d}z \ll 1$ (equivalently $v \ll u$ where v is the y component of the velocity field), the key argument of Taylor was to assume that

$$\pi_{yy} = -P_a \tag{1.10}$$

where P_a is the atmospheric pressure. According to equation 1.9, this leads to

$$P(z) = P_a + \sigma_{yy} \tag{1.11}$$

which, according again to equation 1.9, gives

$$\pi_{zz} = -P_a + (\sigma_{zz} - \sigma_{yy}) \tag{1.12}$$

Normalising pressure such that $P_a = 0$, and defining the mean normal stress difference

$$\Delta \equiv \sigma_{zz} - \sigma_{yy} = \frac{1}{h}\int_0^h (\sigma^*_{zz} - \sigma^*_{yy})\,\mathrm{d}y \tag{1.13}$$

we can finally combine equations 1.6, 1.7, 1.12 and 1.13 to write the following force balance equation

$$\boxed{U\frac{\mathrm{d}U}{\mathrm{d}z} = g + \frac{U}{\rho}\frac{\mathrm{d}}{\mathrm{d}z}\left(\frac{\Delta}{U}\right)} \tag{1.14}$$

This equation is valid for any continuous material. If the last term is negligible, i.e. if inertia overcomes the resistance of the liquid, we obtain the classical free-fall law

$$U = \sqrt{U_0^2 + 2gz} \tag{1.15}$$

observed for water curtains for example, where $U_0 = U(z = 0)$.

In the following, in order to acknowledge the remarkable physical insight of Sir Geoffrey Taylor who first derived the Newtonian version of this force balance equation, equation 1.14 will be referred to as the (Eulerian) Taylor equation. The proper

derivation of this equation from the local Cauchy equation if not obvious. Therefore, following the analysis of Ramos (1996) for Newtonian liquids, we provide in appendix A a rigorous derivation of the Taylor equation.

In the case of a Newtonian liquid, we have $\sigma^*_{zz} = 2\eta\partial u/\partial z$ and $\sigma^*_{yy} = 2\eta\partial v/\partial y$ which gives $\sigma_{zz} = 2\eta \mathrm{d}U/\mathrm{d}z$ and $\sigma_{yy} = -2\eta \mathrm{d}U/\mathrm{d}z$ for an incompressible flow. Hence, the mean normal stress difference is simply

$$\Delta = 4\eta \frac{\mathrm{d}U}{\mathrm{d}z} \tag{1.16}$$

and we recover Taylor's force balance equation 1.5. Note that for laminar jets, the transverse surface curvature gives rise to additional capillary stresses, and a supplementary term has to be added (see the appendix of Clasen et al. (2009)).

1.1.3 Analysis of the Newtonian Taylor equation

As we will now show, the velocity field $U(z)$ of an infinitely long Newtonian curtain collapses on a master curve which, to the best of our knowledge, had not been clearly identified in the literature so far. This analytical description of Newtonian curtains will be a useful guide when describing the analogous case of viscoelastic curtains.

Equation 1.5 can be put into non-dimensional form when rescaling by

$$\begin{cases} \bar{z} = z/z_v \\ \bar{U} = U/U_v \end{cases}, \qquad z_v = \left(\frac{(4\eta/\rho)^2}{g}\right)^{1/3}, \qquad U_v = \sqrt{g\, z_v} = (4\eta g/\rho)^{1/3} \tag{1.17}$$

We obtain

$$\bar{U}\bar{U}' = 1 + \bar{U}'' - \bar{U}'^2/\bar{U} \tag{1.18}$$

where $'$ denotes spatial derivation $\mathrm{d}/\mathrm{d}\bar{z}$. The general solution of this equation was found by Clarke (1966, 1968) and is given by

$$\bar{U}(\bar{z}) = 2^{-1/3}\left[\left(\frac{\mathrm{Ai}'(Z) + C\,\mathrm{Bi}'(Z)}{\mathrm{Ai}(Z) + C\,\mathrm{Bi}(Z)}\right)^2 - Z\right]^{-1}, \qquad Z = 2^{-1/3}(\bar{z} + k) \tag{1.19}$$

where Ai and Bi are the Airy functions, i.e. the two solutions of the differential equation $y'' - xy = 0$ which can be expressed as (Abramowitz & Stegun, 1964)

$$\begin{cases} \mathrm{Ai}(x) = \dfrac{1}{\pi}\displaystyle\int_0^\infty \cos\left(\frac{t^3}{3} + xt\right)\mathrm{d}t \\ \mathrm{Bi}(x) = \dfrac{1}{\pi}\displaystyle\int_0^\infty \left[\exp\left(-\frac{t^3}{3} + xt\right) + \sin\left(\frac{t^3}{3} + xt\right)\right]\mathrm{d}t \end{cases} \tag{1.20}$$

and where C and k are integration constants which have to be determined from the upstream and downstream boundary conditions. Note that for a given value of C, varying k simply translates the curve along the $\bar{z}$-axis.

Boundary conditions

The upstream boundary condition is simply

$$\bar{U}(\bar{z} = 0) \equiv \bar{U}_0 = \frac{U_0}{U_v} = \frac{\rho U_0 z_v}{4\eta} \tag{1.21}$$

where the initial liquid velocity U_0 at the slot exit can be chosen experimentally by varying the flow rate. This dimensionless number can be seen as a Reynolds number based on the viscous length scale z_v.

Three types of downstream boundary conditions can be chosen depending on the particular experimental conditions (Ramos, 1996). As shown in figure 1.2.a, the type of downstream boundary condition depends on the value of C in Clarke's solution 1.19. Imposing an arbitrarily large velocity at a given distance L_c from the slot corresponds to a film casting experiment where the liquid is collected by a drum rotating at a constant arbitrary angular velocity. This case corresponds to $C > 0$ where Clarke's solution diverges in finite time. On the other hand, the boundary condition $U(L_c) = 0$ leads to the transition to a plane stagnation flow where the liquid spreads onto a motionless horizontal solid plate (or substrate) placed at $z = L_c$ from the slot. In the latter case, which corresponds to $C < 0$, the liquid velocity first increases due to gravitational forces and reaches a maximum value at a distance z_m from the slot before finally decreasing down to 0 when approaching the stagnation point at $z = L_c$. According to figure 1.2.a, the presence of the solid plate only affects the flow significantly within a distance from the plate which is of order $L_c - z_m$. In figure 1.2.b, we present $\bar{L}_c - \bar{z}_m = (L_c - z_m)/z_v$ against the dimensionless curtain length $\bar{L}_c = L_c/z_v$ for various initial velocities. These results suggest that $L_c - z_m$ is always less of equal to $2.3z_v$. However, as pointed out by Ramos (1996), the slender approximation is not justified near the stagnation point where the transverse velocity component becomes larger than the axial one. In this case, although solution 1.19 may be valid far enough from the impingement zone, a two-dimensional analysis is required when focusing on this zone. We can however

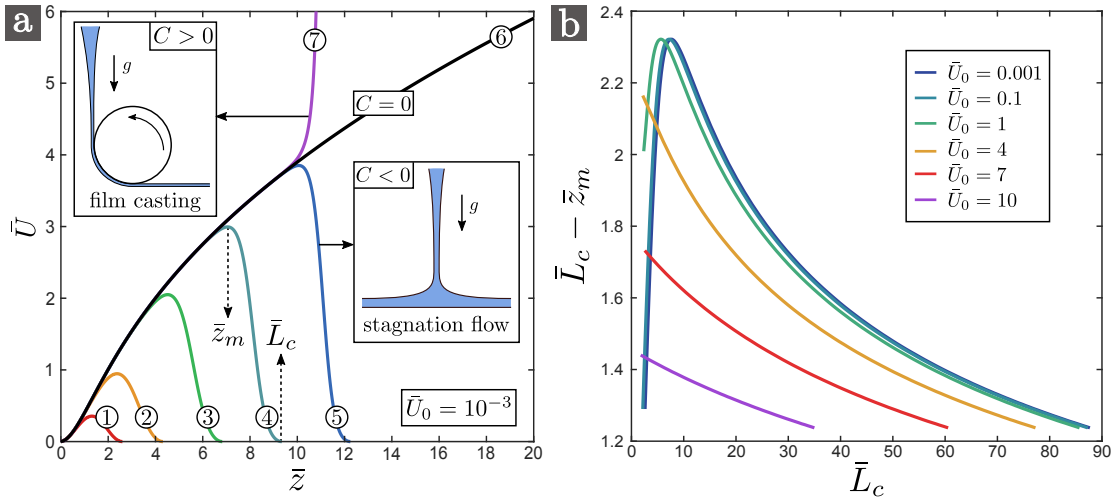

Figure 1.2 – (a): Clarke's solution (equation 1.19) for $C = -10^2$ (1), $C = -10^{-1}$ (2), $C = -10^{-3.5}$ (3), $C = -10^{-7}$ (4), $C = -10^{-12}$ (5), $C = 0$ (6) and $C = +10^{-12}$ (7), where k is chosen to ensure that the initial velocity is $\bar{U}_0 = 10^{-3}$ for each curve. Solutions with $C < 0$, $C = 0$ and $C > 0$ correspond to different types of downstream boundary condition, respectively a plane stagnation flow for $C < 0$ where $U(\bar{L}_c) = 0$ when impacting a flat solid plate at a distance $L_c = \bar{L}_c z_v$ from the slot, an infinite curtain which converges to a free-fall for $C = 0$, and a film casting experiment for $C > 0$ where the velocity imposed by the rotation speed of the drum can be arbitrarily large. When $C < 0$, the presence of the solid plate only affects the flow within a (dimensionless) distance from the plate which is of order $\bar{L}_c - \bar{z}_m$ where $\mathrm{d}U/\mathrm{d}\bar{z}(\bar{z} = \bar{z}_m) = 0$. (b): $\bar{L}_c - \bar{z}_m$ against $\bar{L}_c$ for different initial velocities $\bar{U}_0$. Since varying k for a given C only translates the curve along the $\bar{z}$-axis in equation 1.19, $\bar{L}_c - \bar{z}_m$ does not depend on k. Hence, all the curves in (b) corresponding to different values of $\bar{U}_0$ can be deduced from each other by simple translation along the $\bar{L}_c$-axis.

reasonably assume that the presence of the solid plate only affects the flow within a distance before impact which is of order z_v.

According to the previous results, if the curtain length L_c is much greater than z_v, the flow close to the slot is universal and is not influenced by the downstream boundary condition. Therefore, in order to characterise this universal flow far from the impingement zone, we can use the following boundary condition

$$\lim_{\bar{z}\to\infty} \bar{U}\bar{U}' = 1 \tag{1.22}$$

which ensures that the flow would converge asymptotically to a free-fall with constant acceleration g for a curtain of infinite length. This boundary condition corresponds to $C = 0$ in solution 1.19 (see figure 1.2.a). It is the case discussed by Clarke (1966, 1968). In curtain coating, note that the liquid falls onto a horizontal solid surface moving horizontally at constant speed, which breaks the symmetry of the problem. However, we can reasonably assume that the flow far from the impinge-

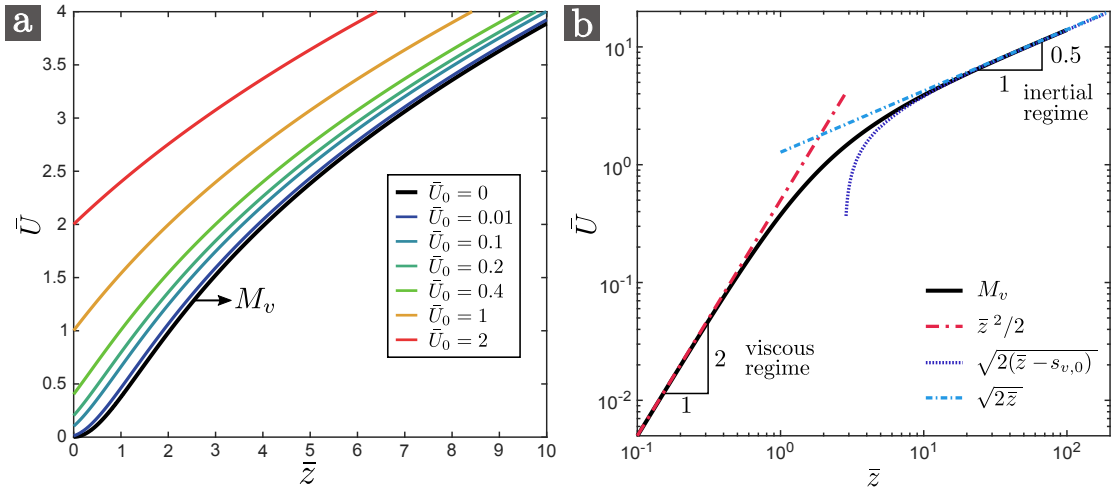

Figure 1.3 – (a): Dimensionless velocity field $\bar{U}(\bar{z})$ for an infinitely long curtain made of a Newtonian liquid (equation 1.19 for $C = 0$), starting from various initial velocities $\bar{U}_0$ ranging between 0 and 2. All the curves for $\bar{U}_0 > 0$ collapse on the master curve M_v corresponding to $\bar{U}_0 = 0$ after translation of each curve along the $\bar{z}$ axis by a distance $M_v^{-1}(\bar{U}_0)$ (equation 1.24). (b): Confirmation with the experimental velocity field of the pure glycerin curtain of figure 4.1 where $\bar{U}_0 = 0.14$. The master curve M_v is characterised by an initial sub-gravitational viscous regime and an asymptotic free-fall regime (equation 1.25).

ment zone is also not influenced by this boundary condition.

To summarise, the three types of downstream boundary condition are

- $C = 0$: Infinite curtain converging to a free-fall
- $C > 0$: Film casting experiment
- $C < 0$: The flow turns into a plane stagnation flow

Master curve

Analytical solutions $\bar{U}(\bar{z})$ are shown in figure 1.3.a for $C = 0$ and initial velocities $\bar{U}_0$ ranging between 0 and 2. The curves are similar. In fact, they all rescale on a unique master curve after translation along the $\bar{z}$ axis. Indeed, let M_v ("M" for "Master curve") be the particular solution corresponding to $\bar{U}_0 = 0$. We have

$$M_v(\bar{z}) = 2^{-1/3}\left[\left(\frac{\mathrm{Ai}'(Z)}{\mathrm{Ai}(Z)}\right)^2 - Z\right]^{-1}, \qquad Z = 2^{-1/3}(\bar{z} + k_0) \tag{1.23}$$

where $\mathrm{Ai}(2^{-1/3}\,k_0) = 0$ which gives $k_0 \approx -2.94583$. This curve is shown in figure 1.3.b in log-log scale. Of course, achieving a curtain of zero initial velocity with

infinite initial thickness is not physically possible. Yet, we can easily demonstrate that any physical solution with initial velocity $\bar{U}_0 > 0$ writes

$$\boxed{\bar{U}(\bar{z}) = M_v\left(\bar{z} + M_v^{-1}(\bar{U}_0)\right)} \tag{1.24}$$

where M_v^{-1} is the functional inverse of M_v. Indeed, since $\bar{z}$ does not appear explicitly in equation 1.18, if M_v is a particular solution, then $\bar{z} \mapsto M_v(\bar{z} + \text{cst})$ is also a solution. Since expression 1.24 is the only one satisfying both the upstream ($\bar{U}(\bar{z} = 0) = \bar{U}_0$) and downstream ($\bar{U}\bar{U}' \to 1$) boundary conditions, it is the only solution. Hence, any curve $\bar{U}(\bar{z})$ with initial velocity $\bar{U}_0 > 0$ will collapse on the master curve $M_v(\bar{z})$ after translation along the $\bar{z}$ axis by a distance $M_v^{-1}(\bar{U}_0)$ on the right. This will be shown in chapter 4 using a curtain made of glycerol.

The master curve is characterised by two regimes:

$$M_v(\bar{z}) = \begin{cases} \bar{z}^2/2 & \bar{z} \ll 1 : \text{ viscous regime} \\ \sqrt{2\left(\bar{z} - s_{v,0}\right)} & \bar{z} \gg 1 : \text{ inertial regime} \end{cases} \tag{1.25}$$

where $s_{v,0} \approx 2.8$. The initial viscous regime ($\bar{z} \ll 1$) corresponds to a balance between gravity and viscous forces where inertia is negligible in the force balance equation 1.5. As the liquid velocity increases, we enter into an intermediate inertio-viscous regime where none of the terms of equation 1.5 can be neglected. Finally, inertia dominates over viscous forces for $\bar{z} \gg 1$ and the local acceleration reaches the asymptotic free-fall value. More precisely, the full asymptotic inertial regime is given by $M_v^2 = 2\left(\bar{z} - s_{v,0}\right)$. Note that the viscous regime can be found directly by injecting $\bar{U}(\bar{z}) = K\bar{z}^\alpha$ in equation 1.18 where inertia $\bar{U}\bar{U}'$ is neglected. We find that the only solution is $K = 1/2$ and $\alpha = 2$.

For real curtains with non-zero initial velocity U_0, according to equations 1.24 and 1.25, the viscous regime only exists if U_0 is much smaller than U_v, i.e. $\bar{U}_0 \ll 1$. This is illustrated in figures 1.4.a and 1.4.b where we plot the local extension rate $\bar{U}'(\bar{z})$ and the local acceleration $\bar{U}\bar{U}'(\bar{z})$ for $C = 0$ and initial velocities $\bar{U}_0$ ranging between 0 and 10. For low values of $\bar{U}_0$, $\bar{U}'$ first increases (viscous regime) before finally decreasing (inertial regime). However, as $\bar{U}_0$ increases, $\bar{U}'$ becomes a monotonous decreasing function. Equivalently, the acceleration at the slot exit $\bar{U}\bar{U}'(0)$ goes from 0 for $\bar{U}_0 = 0$ to 1 for $\bar{U}_0 \gg 1$, in which case inertia dominates over viscous forces even close to the slot. In practice, we can assume that the flow of a Newtonian curtain is very well approximated by a free-fall $\bar{U}^2 = \bar{U}_0^2 + 2\bar{z}$ if $\bar{U}_0 \geq 10$. Physically, it can be explained by considering $\bar{U}_0$ as a Reynolds number based on the characteristic length z_v (equation 1.21). To summarise:

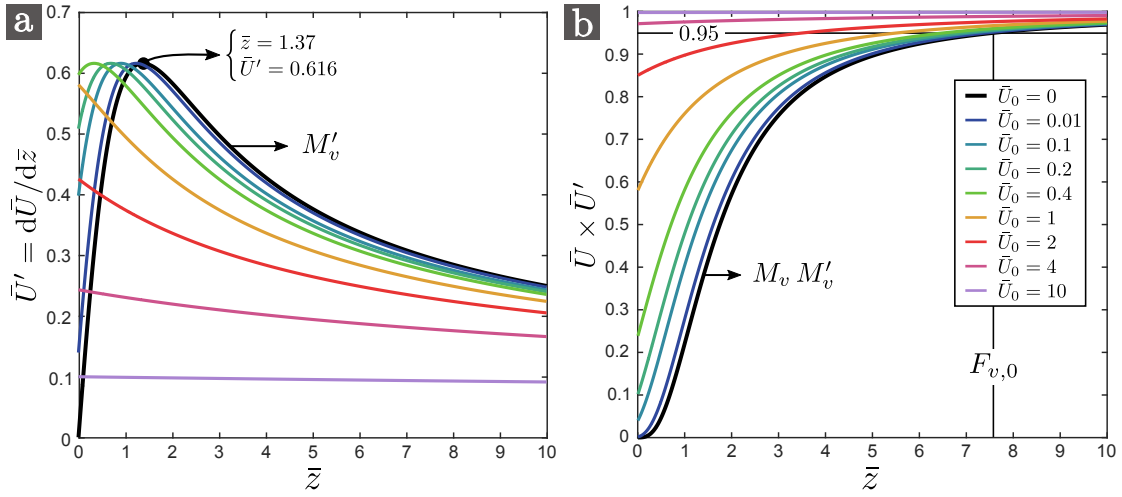

Figure 1.4 – Dimensionless extension rate $\bar{U}'(\bar{z})$ (a) and acceleration $\bar{U}\bar{U}'(\bar{z})$ (b) for an infinitely long curtain made of a Newtonian liquid (equation 1.19 for $C = 0$), starting from various initial velocities $\bar{U}_0$ ranging between 0 and 10. The master curve M_v has an inflection point at $\bar{z} \approx 1.37$, where the elongation rate reaches a maximum value $M'_v(1.37) \approx 0.616$, and reaches the asymptotic free-fall regime at $\bar{z} = F_{v,0} \approx 7.56$ since $M_v\, M'_v(F_{v,0}) = 0.95$, where 0.95 is an arbitrary value close to 1.

- $\bar{U}_0 \ll 1 \quad \Rightarrow \quad$ viscous regime for $\bar{z} \ll 1$ and inertial regime for $\bar{z} \gg 1$
- $\bar{U}_0 \gg 1 \quad \Rightarrow \quad$ inertial regime only

In the case of a negligible initial velocity $U_0 \ll U_v$ (equivalently $\bar{U}_0 \ll 1$), according to equations 1.24 and 1.25, the viscous regime of the flow ($z \ll z_v$) writes

$$\bar{U}(\bar{z}) = \frac{1}{2}\left(\bar{z} + \sqrt{2\bar{U}_0}\right)^2 \tag{1.26}$$

This regime has not received much attention in the literature since achieving such a flow experimentally is quite difficult. Indeed, z_v has to be of the order of a few centimetres, which implies using a liquid of dynamic viscosity $\eta \geq 10^1$ Pa.s. Besides, in addition to the difficulty of achieving a large enough flow rate to maintain a continuous curtain, one must use a very wide slot in order to avoid the edge effects (this point will be developed in §3.1.4). Finally, the curtain length L_c has to be larger than z_v to observe the universal behaviour which is not affected by the downstream boundary condition.

Regardless of the value of the initial velocity, in the inertial regime, again using equations 1.24 and 1.25, the dimensionless velocity field writes

$$\bar{U}(\bar{z}) = \sqrt{\bar{U}_0^2 + 2(\bar{z} - s_v)} \tag{1.27}$$

where $s_v = s_{v,0} + \bar{U}_0^2/2 - M_v^{-1}(\bar{U}_0)$. In his early experiments, Brown (1961) found

$s_v = 2$. For negligible initial velocities $U_0 \ll U_v$, this regime is observed for $z \gg z_v$. For large initial velocities $U_0 \gg U_v$, it is observed immediately after the slot exit. In fact, since s_v goes to 0 for $U_0 \gg U_v$, we recover the free-fall $U^2 = U_0^2 + 2gz$.

Length of the sub-gravitational regime

We can now derive an expression of the length z_v^* of the sub-gravitational part of the curtain introduced in §1.1.1. Let us define this length as $U\mathrm{d}U/\mathrm{d}z(z = z_v^*) = 0.95g$ where 0.95 is an arbitrary value close to 1. For $\bar{U}_0 = 0$, let $F_{v,0}$ be such that $M_v\, M_v'(\bar{z} = F_{v,0}) = 0.95$. We obtain the value $F_{v,0} \approx 7.56$ close to 7 mentioned in §1.1.1 (see figure 1.4.b). According to equation 1.24, we have

$$z_v^* = F_v \times z_v \qquad \text{with} \qquad F_v = F_{v,0} - M_v^{-1}(\bar{U}_0) \tag{1.28}$$

where the prefactor F_v is a decreasing function of the initial velocity. This result holds if $F_v \geq 0$, i.e. if $\bar{U}_0 \leq M_v(F_{v,0}) \approx 3.23$. For simple numerical estimations, note that $F_v \approx 2.34\,(3.23 - \bar{U}_0)$ with an error less than 0.65. This result had not been derived in the literature so far since the master curve had not been explicitly identified.

1.2 Newtonian curtain stability

1.2.1 Dynamics of hole opening

Industrial liquid curtains used in curtain coating may spontaneously break due to impurities in the liquid such as bubbles. In such cases, a large area of the substrate will remain "dry" (uncoated). An example of ruptured industrial curtain is shown in figure 1.5 to illustrate this major problem. The holes forming within the curtain are generally initiated far from the slot, where the sheet is thin. As the sheet retracts (i.e. as the hole grows), the liquid is collected into a rim forming the edge of the hole. Different scenarios can be observed depending on the position of hole initiation: the hole may be advected by the flow or propagate upwards, thus causing irreversible breaking of the curtain.

The question of curtain stability in terms of spontaneous hole opening events has first been raised by Brown (1961) who proposed a simple criterion for the two different hole propagation scenarios. This criterion is based on a balance between capillary forces, pulling up the rim of the hole towards the slot, and the inertia of the surrounding liquid which pulls the hole downwards. This can be reformulated as follows. According to Taylor (1959) and Culick (1960), if capillary forces are only

Figure 1.5 – Industrial curtain used in curtain coating (the liquid is a paint). Photo taken by Julien Beaumont from Saint Gobain Recherche in 2015 in Avilés.

balanced by inertia, the local retraction speed of the sheet in the reference frame of the moving liquid is

$$V = \sqrt{\frac{\Gamma}{\rho h}} \tag{1.29}$$

where ρ and Γ are the liquid density and surface tension and $2h(z)$ is the local thickness of the curtain. Hence, the part of the liquid rim corresponding to the upper edge of the hole propagates at velocity $V - U$ in the reference frame of the laboratory, where $V(z)$ is calculated based on the local curtain thickness $2h(z)$ and where $U(z)$ is the local velocity of the surrounding liquid. This local competition can be written in terms of a local Weber number

$$We = \left(\frac{U}{V}\right)^2 = \frac{\rho h U^2}{\Gamma} = \frac{\rho q U}{2\Gamma} \tag{1.30}$$

which can be less than one close to the slot and become larger than one downstream. Therefore, if a hole opens at an altitude where $We > 1$, i.e. where advection is faster than the hole opening process, it will be carried away by the flow. This process is often referred to as "self-healing". However, if a hole opens in the unstable part of the curtain where $We < 1$, the upper edge of the hole propagates upwards and stops when reaching the slot whereas the lower end propagates downwards, in which case the curtain is finally split into two parts delimited by a rim which takes the form of an arch. Hence, there is a separation between an unstable zone upstream of the curtain (where $We < 1$) and a stable zone downstream of the curtain (where $We > 1$).

1.2.2 Effect of viscosity

Viscous forces may also play a role. For Newtonian liquids, Savva & Bush (2009) showed that the velocity of the edge of a hole initiated in a motionless sheet of constant thickness goes from 0 to V in a time which increases as the Ohnesorge number Oh increases, where

$$Oh = \frac{\eta}{(\rho h \Gamma)^{1/2}} = \frac{\eta V}{\Gamma} \tag{1.31}$$

which can be seen as a capillary number based on the Taylor-Culick velocity in its last form. Capillary forces are initially balanced by viscous forces before inertia finally dominates. Based on similar results, Sünderhauf et al. (2002) concluded that increasing the liquid viscosity stabilises the curtain since the dynamics of hole opening is slowed down temporarily. Note that, since the curtain thickness $2h(z) = q/U(z)$ is a function of the distance z from the slot, the Taylor-Culick velocity V and the Ohnesorge number Oh are also function of z.

1.3 Viscoelastic curtains

1.3.1 Curtain flow

The influence of viscoelasticity has been investigated in industrial processes involving free-surface extensional flows such as fibre spinning (Papanastasiou et al., 1987) and film casting (Alaie & Papanastasiou, 1991; Satoh et al., 2001). These techniques aim at producing plastic tubes or sheets respectively. In film casting, a polymer melt is extruded through a slot die and the resulting liquid sheet is cooled before reaching a rotating drum where it is collected. Alaie & Papanastasiou (1991) reports that viscoelastic films thin more rapidly at the slot exit than Newtonian films with the same viscosity. The liquids involved in film casting are so viscous that gravity and inertia can generally be neglected. The force exerted by the rotating drum dominates the process and stretches the liquid in the flow direction. Indeed, as will be illustrated in figure 2.13.a, a fibre-spinning-like experiment can even be performed "upside down", the liquid being forced to flow in the direction opposite to gravity.

Curtain coating is a similar process which aims at depositing a material layer of uniform thickness on a solid substrate by forming a thin sheet of coating liquid (paint for example) extruded vertically through a slot and falling on the substrate. The major difference with film casting is that the liquids involved in curtain coating are generally much less viscous. Therefore, contrary to film casting, the process is

dominated by gravity which is now the driving force of the problem.

To date, although the structure of the flow is now well understood in film casting, i.e. in the absence of gravity and inertia, very few authors have addressed the issue of the possible influence of elasticity in the context of curtain coating. The only measurements reported in the literature are the very recent measurements performed by Karim et al. (2018b) who observed free-falls (constant acceleration g) for low-viscosity polymer solutions with millisecond-scale extensional relaxation times. No similar measurements were performed on other solutions with larger relaxation times. Consequently, the influence of elasticity on the curtain flow remains an open question.

To highlight the importance of this question, we recall that in most experimental and industrial applications involving Newtonian curtains, the length z_v^* of the sub-gravitational regime derived in §1.1 is very small compared to the length of the curtain. Indeed, typical orders of magnitude for z_v (equation 1.3) are 0.01 cm for water of viscosity $\eta = 10^{-3}$ Pa.s and 1 cm for pure glycerin of viscosity $\eta = 1$ Pa.s, while the curtain length is typically of order $L_c = 10$ cm. However, to date, the length of the sub-gravitational regime remains unknown in the case of a viscoelastic curtain. This gap in the literature might lead some authors to assume, incorrectly, that the flow of viscoelastic curtains or jets can be approximated by a free-fall based on the small value of the viscous length $z_v = ((4\eta_0/\rho)^2/g)^{1/3}$ where η_0 is the zero-shear viscosity of the liquid.

1.3.2 Curtain stability

In contrast, the stability of viscoelastic curtains has already received some attention in recent literature, mostly from the group of Marcio S. Carvalho (Becerra & Carvalho, 2011; Karim et al., 2018b). Two different aspects have been examined.

Karim et al. (2018b) recently measured the local retraction speed of the sheet when a hole is initiated in a curtain made of low-viscosity PEO solutions. They report that the ratio of the local retraction speed to the local Taylor-Culick velocity decreases when the local Ohnesorge number increases for Oh ranging between 0.22 and 0.43. This ratio was 0.95 (slightly less than one) for the solution with the highest extensional relaxation time τ (= 0.16 s, measured by a capillary breakup extensional rheometer) and the authors concluded that elastic stresses may slow down the hole opening process.

For a given coating liquid, there is a minimum flow rate Q_{min} below which it becomes impossible to form a continuous curtain. Below Q_{min}, the sheet breaks and equidistant jets are ultimately generated from the die instead of a continuous curtain. This is one of the most severe industrial limitations of the curtain coating technique. Therefore, recent studies have investigated the role of polymer additives in curtain stability by measuring Q_{min} for polymer solution. Becerra & Carvalho (2011) and Karim et al. (2018b) showed that Q_{min} could be decreased by adding a small amount of polymer molecules to a low-viscosity Newtonian solvent, thus allowing the formation of continuous curtains at lower flow rates. Karim et al. (2018b) proposed an interpretation based on measurements of the sheet response to a local disturbance produced by an air jet blown through a needle. The authors observed that Newtonian curtains break much more easily than viscoelastic curtains and concluded that the growth rate of any disturbance leading to the formation of a hole is delayed by polymer addition.

Chapter 2

Generalities on viscoelasticity

Contents

In a famous text published in 1964 in *Physics today*, Markus Reiner (Reiner, 1964) tells us about the birth of Rheology, a now active branch of Physics. This field concerns the study of the deformation of materials which are intermediate between Hookean elastic solids and Newtonian viscous liquids and which could not be captured by the two theories existing at the time, namely the theories of elasticity and of fluid mechanics. The story began in 1928 when Reiner was invited at Lafayette College by Eugene Cook Bingham who had heard of his recent collaboration with a chemist on solving an extrusion problem involving a plastic material. Convinced that this kind of collaboration were to become increasingly necessary, Reiner and Bingham agreed on the designation of "Rheology" from the Greek "rhéō" (flow) and "logia" (study of). The term was inspired by the aphorism of Heraclitus of Ephesus "πάντα ῥεῖ" (panta rhei), literally "everything flows".

Reiner pointed out a possible misunderstanding of this term which seems to exclude solids since most of them do not "flow" in the usual meaning of the word. He found the solution in the words of the prophetess Deborah "The mountains flowed before the Lord", meaning that mountains do flow, but only before the Lord whose time of observation is infinite, and not before men who can not perceive their motion in the course of their short lives. Reiner concluded that the difference between solids and fluids lies in the magnitude of the Deborah number

$$De = \text{relaxation time/observation time} \tag{2.1}$$

which measures the relaxation time of the material, which depends on its internal structure, relatively to the time of observation which depends only on the observer. Bringing solids and liquids under a common concept, the Deborah number has now become one of the fundamental numbers of rheology. Its value helps scientists choosing the appropriate mechanical description for a given problem. For example, rocks forming the mantle can be considered as solids at human time scales but have to

be modelled as liquids when considering the convective motion in the mantle which are responsible for continental drift which is hardly noticeable for us human beings since the continental plates move at a few centimetres per year.

In this chapter, we first present the basic models describing elastic solids ($De \gg 1$) and viscous fluids ($De \ll 1$). Then, we introduce some simple models and simple constitutive equations describing the behaviour of viscoelastic liquids ($De \approx 1$). Next, we present the fundamental concepts of the microscopic description of polymers solutions and melts, two classical examples of viscoelastic liquids. Since these two aspects of viscoelasticity are often presented separately, the link between them is not always obvious. Hence, we dedicate the next section to the connection between constitutive equations and the microscopic description of polymers. Finally, we present some of the many unusual flow characteristics observed with viscoelastic liquids which have historically motivated the development of the previously presented theories.

2.1 Elastic solid vs. viscous fluid

In this section, we present the classical descriptions of solids and liquids in their simplest (non tensorial) form. The general form will be given in §2.3.3 for Newtonian fluids.

2.1.1 Elastic solid

Hooke's law

Hooke's law describes the behaviour of an ideal elastic solid (called Hookean solid). It writes

$$\boxed{\sigma = G\,\gamma} \tag{2.2}$$

and indicates that the applied stress (force per unit surface) σ is proportional to the deformation γ with some proportionality coefficient G called elastic modulus. In the example of a shear deformation (see figure 2.1), σ is the shear stress, $\gamma = \delta/L$ is the shear deformation - or shear strain - and G is the shear modulus. For an extensional deformation, the strain (length increment divided by original length) is noted ϵ and stress to strain ratio is called Young's modulus and is generally noted E. Both G and E measure the stiffness of the solid and are related by $E = 2G(1 + \bar{\nu})$ where the Poisson ratio $\bar{\nu}$ is the ratio of transverse to axial strain in the direction of a

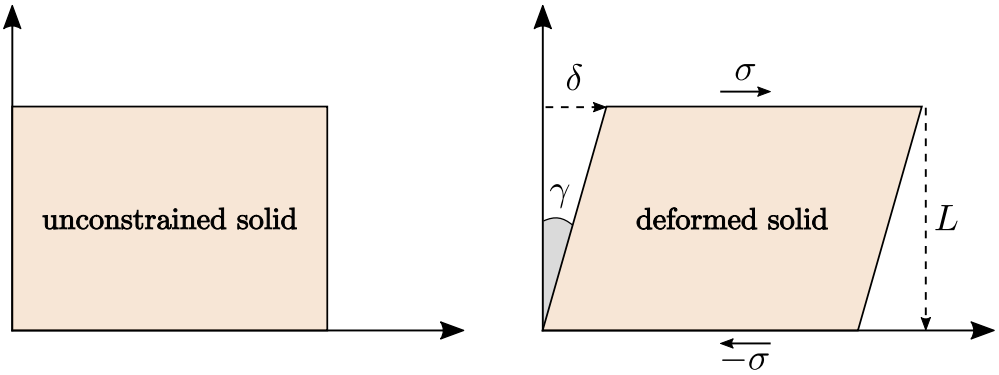

Figure 2.1 – Shear deformation of magnitude $\gamma = \delta/L$ of an elastic solid.

stretching force.

Hooke's law suggests that the material responds instantaneously to mechanical solicitations since it has no internal relaxation time, i.e. the stress instantaneously switches from 0 to $G\gamma$ after a sudden deformation γ. Besides, a material described rigorously by Hooke's law will always recovers its original shape once the source of stress is being removed. In other words, it does not "flow" since the internal structure of the material is not altered at all by the deformation, even when being applied for a long time. Elastic deformations are *reversible* and elasticity is in fact closely linked to the idea of memory. A Hookean elastic solid is the limiting case of a material with *infinite memory*.

For usual "hard" solids such as metals and minerals, the elastic modulus ranges typically from 10^{10} Pa for sodium and 10^{11} Pa for quartz and aluminium to 10^{12} Pa for diamond. Elasticity comes from the electrostatic restoring force arising from the stretching of bonds (covalent, ionic, metallic, intermolecular, ...) between atoms or molecules during deformation (enthalpic elasticity). On the other hand, for "soft" solids such as elastomers (rubber) or gels, the elastic modulus is much lower. It ranges between 10^8 Pa for hardest rubbers to 10^3 Pa for softest gels. For elastomers and polymeric gels, elasticity comes from the loss of configurational entropy of the polymer chains during deformation (entropic elasticity).

Hooke's law is generally valid in the regime of small deformation, i.e. a few 0.1% for hard solids and more than 100% for some elastomers. Above this critical deformation, we are in the plastic regime where the material starts creeping. This behaviour is in fact more related to the behaviour of fluids since permanent structural modifications observed in the plastic regime.

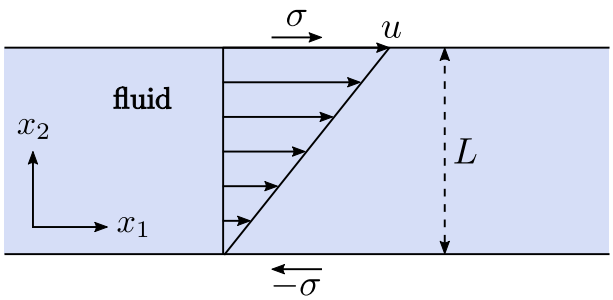

Figure 2.2 – Shear flow of a viscous fluid between two parallel plates separated by a distance d, one moving at velocity u and the other one stationary (Couette flow).

2.1.2 Viscous fluid

Newton law

Newton's law describes the behaviour of an ideal viscous fluid (called Newtonian fluid). It writes

$$\boxed{\sigma = \eta\,\dot{\gamma}} \tag{2.3}$$

and indicates that the applied stress σ is proportional to the the rate of deformation $\dot{\gamma}$ with some proportionality coefficient η called (dynamic) viscosity. In the example of a shear deformation (see figure 2.2), σ is the shear stress and $\dot{\gamma} = \mathrm{d}\gamma/\mathrm{d}t = u/L$ is the shear rate. η measures the resistance of the liquid to flow. Newton's law suggests that the material responds instantaneously to mechanical solicitations since it has no internal relaxation time, i.e. the shear stress instantaneously switches from 0 to $\eta\dot{\gamma}$ after initiating a sudden shear flow of shear rate $\dot{\gamma}$. Besides, any stress σ applied during a short time t causes a permanent and *irreversible* deformation $\gamma = \sigma t/\eta$, i.e. the fluid will never spontaneously recover its previous internal structure once stress is removed, contrary to Hookean elastic solids. In fact, a Newtonian viscous fluid is the limiting case of a material with *no memory*.

Newton's law can describe both liquids and gases. Viscosity is associated to energy dissipation within the fluid and is due to internal friction. At the macroscopic level, viscosity measures the conversion of the kinetic energy of the flow into heat energy. In the shear flow shown in figure 2.2, viscosity describes the transfer of momentum due molecular collisions between the different portions of liquids (along x_2) which have different average velocities.

The dynamic viscosity of air is 1.8×10^{-5} Pa.s at a temperature 20°C and is an increasing function of temperature. On the other hand, the dynamic viscosity of liquids is a decreasing function of the temperature. Some orders of magnitudes

at 20°C are $\eta = 10^{-3}$ Pa.s for water, 10^0 Pa.s for pure glycerin and 10^1 Pa.s for honey. Furthermore, as mentioned earlier, "solids" do also flow on long time scales. A famous example is the pitch drop experiment started in 1927 in the university of Queensland where a piece of pitch, which appears to be solid at human time scales, flows under its own weight and drips at a rate of one drop every eight years. Viscosity is of order 10^8 Pa.s. The description of the convective motions in the mantle requires a much larger viscosity of order 10^{21} Pa.s.

2.2 Linear viscoelasticity: Simple models

In many experiments, the Deborah number defined in equation 2.1 is either extremely low or extremely large depending on the material and on the time scale of the experiment. Hence, Newton's law 2.3 ($De \ll 1$) and Hooke's law 2.2 ($De \gg 1$) provide respectively appropriate mechanical descriptions. However, a new description must be adopted when considering a material deforming on a time scale which is of the order of its internal relaxation time, i.e. when the Deborah number is of order one. Materials which behave as elastic solids on short time scales and as viscous liquids on long time scales are called viscoelastic liquids. In the following, we introduce the classical models of viscoelastic liquids in their simplest (non tensorial) form. Their tensorial equivalents will be presented in §2.3.5.

A classical example is a silicone based material called Silly Putty. It bounces when hitting a flat surface (elastic behaviour) but forms a puddle after laying on a flat surface for a few minutes, i.e. it flows (viscous behaviour). Two families of viscoelastic liquids are of particular interest in industrial applications: polymer melts and polymer solutions. Polymer melts are purely polymeric materials with no solvent and correspond to the large temperature state of plastic materials such as polyethylene (PE) which is used to produce plastic bags. In polymer solutions, polymer molecules are dissolved in a liquid solvent. Many biological liquids fall in that category, such as saliva, egg white, semen, and the slime produced by hagfishes to choke predators when under attack.

2.2.1 Maxwell model

The simplest analytical descriptions of viscoelastic liquids is the model introduced in 1867 by James Clerk Maxwell. The behaviour of the material is assumed to be analogous to that of a purely viscous damper and a purely elastic spring connected in series, as illustrated in figure 2.3.a. We consider that the material is subjected to a pure shear deformation under shear stress σ, and the response is described by

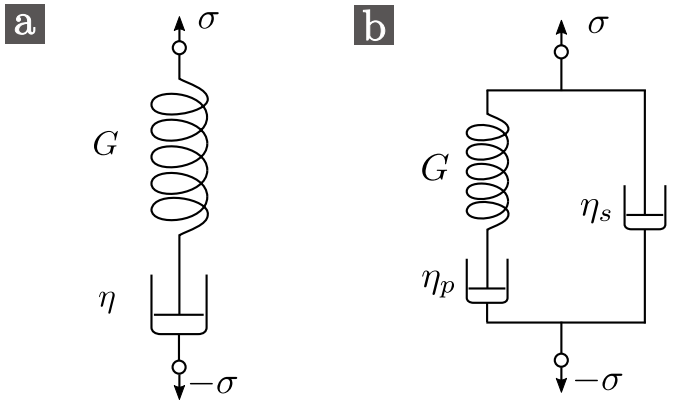

Figure 2.3 – (a) Maxwell model: purely viscous damper of viscosity η in serie with a purely elastic spring of elastic modulus G. (b) Jeffrey model: Maxwellian spring-damper element of elastic modulus G and viscosity η_p (polymers) in parallel with a purely viscous damper of viscosity η_s (solvent).

analogy with the spring-damper device. The total deformation γ of the device is $\gamma = \gamma_e + \gamma_v$ where γ_e is the deformation of the spring and γ_v is the deformation of the damper. Hence, the total deformation rate is $\dot{\gamma} = \dot{\gamma}_e + \dot{\gamma}_v$. Both spring and damper undergo the same stress σ. The spring follows Hooke's law $\sigma = G\gamma_e$ while the damper follows Newton's law $\sigma = \eta\dot{\gamma}_v$ where G and η are respectively the shear modulus and the shear viscosity of the material. This gives

$$\dot{\gamma} = \frac{\dot{\sigma}}{G} + \frac{\sigma}{\eta} \qquad \Leftrightarrow \qquad \boxed{\tau\dot{\sigma} + \sigma = \eta\dot{\gamma}} \tag{2.4}$$

where τ is the *Maxwell relaxation time* defined as

$$\boxed{\tau = \frac{\eta}{G}} \tag{2.5}$$

2.2.2 Jeffrey model

The Jeffrey model is a refined version of the Maxwell model to take into account the viscous response of the solvent in polymer solutions. In this model, the rheological response of the material consists of a superposition of the viscous response of the solvent and of the viscoelastic response of the particles. The analogous device is shown in figure 2.3.b and consists of a Maxwellian spring-damper element of elastic modulus G and viscosity η_p (particles) in parallel with a purely viscous damper of viscosity η_s (solvent). The total stress σ is the sum of the stresses σ_p and σ_s developed in each branch, i.e.

$$\sigma = \sigma_p + \sigma_s \tag{2.6}$$

and the rate of deformation $\dot{\gamma}$ is the same in each branch, which gives

$$\tau\dot{\sigma}_p + \sigma_p = \eta_p\dot{\gamma} \qquad \text{and} \qquad \sigma_s = \eta_s\dot{\gamma} \tag{2.7}$$

where the relaxation time is now

$$\boxed{\tau = \frac{\eta_p}{G}} \tag{2.8}$$

2.2.3 Generalised Maxwell model

Most viscoelastic liquids such as polymer melts and polymer solutions are better described by considering a distribution of relaxation times. The analogous device is a succession of n Maxwell elements are assembled in parallel, each element following

$$\dot{\gamma} = \frac{\dot{\sigma}_i}{G_i} + \frac{\sigma_i}{\eta_i} \qquad i = 1, 2, 3 \dots n \tag{2.9}$$

with its own relaxation time $\tau_i = \eta_i/G_i$. Note that the Jeffrey model is a special case of generalised Maxwell model where $n = 2$ with $G_1 = G$, $\eta_1 = \eta_p$, $G_2 = +\infty$ and $\eta_2 = \eta_s$.

For polymer melts and polymer solutions, this distribution of relaxation times accounts for the different segments lengths along the polymer molecule relaxing on different characteristic times. Said differently, a polymer chain has various modes of vibration. We can often define a *terminal relaxation time* τ_1 corresponding to the slowest mode, i.e. $\tau_i < \tau_1$ for $i = 2, 3, \dots n$. This slowest relaxation mode is often considered as the relevant time scale of the polymer chain and is sometimes enough to capture some experimental results, such as in the capillary filament breakup problem which will be discussed in chapter 3 (Anna & McKinley, 2001; Entov & Hinch, 1997).

2.3 Constitutive equations

In this section, we introduce the general tensorial formalism in which the different models presented in the previous section have to be expressed.

2.3.1 Cauchy equation and stress tensor

Cauchy equation

The branch of physics dealing with the motion of continuous materials such as fluids and solids is called continuum mechanics. It has been developed in the 19th cen-

tury by mathematicians, engineers and physicists including Augustin-Louis Cauchy, Claude-Louis Navier and Sir George Gabriel Stokes who derived the fundamental equations continuum mechanics. These equations include the conservation of mass which, in the case of an incompressible flow, is simply

$$\nabla \cdot \boldsymbol{u} = 0 \tag{2.10}$$

and the conservation of momentum

$$\rho \left(\frac{\partial \boldsymbol{u}}{\partial t} + (\boldsymbol{u} \cdot \nabla)\boldsymbol{u} \right) = \rho \boldsymbol{g} + \nabla \cdot \boldsymbol{\pi} \tag{2.11}$$

also known as Cauchy equation. In these equations, $\boldsymbol{u}(\boldsymbol{r}, t)$ is the local velocity field, $\boldsymbol{r}$ and t are position and time, ρ is the material density (which is constant for an incompressible flow), $\boldsymbol{g}$ accounts for any external body force (for example gravity) and $\boldsymbol{\pi}(\boldsymbol{r}, t)$ is the local *stress tensor* describing the internal forces (counted per unit surface) arising at any position in the material during deformations (it was noted $\boldsymbol{\pi}^*$ in chapter 1). We now provide a formal definition of $\boldsymbol{\pi}$.

Stress tensor

The force exerted on a surface $\mathrm{d}S$ of normal unit vector $\boldsymbol{n}$ can be written as

$$\mathrm{d}\boldsymbol{f} = \boldsymbol{\pi}(\boldsymbol{n})\, \mathrm{d}S \tag{2.12}$$

By convention, it is the contact force exerted by the external part of the material (pointed by $\boldsymbol{n}$) on the internal part (from which $\boldsymbol{n}$ points). For any surface, we can show that (Petit et al., 2012)

$$\boldsymbol{\pi}(\boldsymbol{n}) = \boldsymbol{\pi} \cdot \boldsymbol{n} \tag{2.13}$$

which then defines the stress tensor $\boldsymbol{\pi}$. Hence, once knowing the expression of the components π_{ij} in a given coordinate system of unit vectors $\boldsymbol{l}_1$, $\boldsymbol{l}_2$ and $\boldsymbol{l}_3$, we can express the force exerted on any surface using

$$\boldsymbol{\pi} \cdot \boldsymbol{n} = \sum_i \left(\sum_j \pi_{ij}\, n_j \right) \boldsymbol{l}_i \tag{2.14}$$

This tensor is symmetric for classical materials (without long-range order in molecular orientation), i.e. $\pi_{ji} = \pi_{ij}$. In the following, we only consider incompressible flows and symmetric stress tensors. It is often convenient to decompose $\boldsymbol{\pi}$ as

$$\boldsymbol{\pi} = -P\boldsymbol{\delta} + \boldsymbol{\sigma} \tag{2.15}$$

where $\boldsymbol{\delta}$ is the unit tensor and where P and $\boldsymbol{\sigma}$ are called pressure and *extra stress tensor*. Of course, the exact definition of P depends on the exact definition of $\boldsymbol{\sigma}$. Examples of extra stress tensors, describing both elastic and dissipative viscous effects, will be given later. We use this decomposition in §2.3.2 since only normal stress differences are considered, i.e. $\pi_{ii} - \pi_{jj} = \sigma_{ii} - \sigma_{jj}$ regardless of the exact definition of $\boldsymbol{\sigma}$.

Constitutive equation

While the momentum equation 2.11 describes the dependence of the velocity field on the stress field, one needs a second equation describing the dependence of the stress field on the velocity field to close the system. Such an equation is called *constitutive equation* and depends on the particular physical constitution of the fluid. This equation often involves the *strain rate tensor* $\boldsymbol{D}$ defined as

$$\boldsymbol{D} = \frac{1}{2}\left(\nabla \boldsymbol{u} + (\nabla \boldsymbol{u})^T\right) \qquad \Leftrightarrow \qquad D_{ij} = \frac{1}{2}\left(\frac{\partial u_i}{\partial x_j} + \frac{\partial u_j}{\partial x_i}\right) \tag{2.16}$$

which describes the local rate of change of the material deformation, where ^{T} is transposition and $\nabla \boldsymbol{u}$ is the *velocity gradient tensor* defined as (we choose the usual convention)

$$(\nabla \boldsymbol{u})_{ij} = \frac{\partial u_i}{\partial x_j} \tag{2.17}$$

2.3.2 Shear and extensional flows

Two types of flow have been of particular interest for investigating the mathematical structure of constitutive equations: pure shear flows and pure extensional flows. We now discuss these two flows.

Shear flow

The velocity field and the associated strain rate tensor for a pure shear flow are

$$\boldsymbol{u} = \begin{cases} u_1 = \dot{\gamma}\, x_2 \\ u_2 = 0 \\ u_3 = 0 \end{cases} \qquad \text{and} \qquad \boldsymbol{D} = \dot{\gamma} \begin{bmatrix} 0 & 1/2 & 0 \\ 1/2 & 0 & 0 \\ 0 & 0 & 0 \end{bmatrix} \tag{2.18}$$

where 1 and 2 are respectively the direction of the flow and the direction of the velocity gradient (see figure 2.2), and $\dot{\gamma}$ is the shear rate. By symmetry, we can show that some components of the stress tensor are 0. The most general form of the stress tensor is

$$\boldsymbol{\pi} = \begin{bmatrix} -P + \sigma_{11} & \sigma_{12} & 0 \\ \sigma_{12} & -P + \sigma_{22} & 0 \\ 0 & 0 & -P + \sigma_{33} \end{bmatrix} \tag{2.19}$$

The three experimentally accessible physical quantities are

- the shear stress σ_{12}
- the first normal stress difference $N_1 = \sigma_{11} - \sigma_{22}$
- the second normal stress difference $N_2 = \sigma_{22} - \sigma_{33}$

The shear viscosity, also called *apparent shear viscosity*, is defined as

$$\eta \equiv \frac{\sigma_{12}}{\dot{\gamma}} \tag{2.20}$$

Extensional flow

The velocity field and the associated strain rate tensor for a pure extensional flow are

$$\boldsymbol{u} = \begin{cases} u_1 = e_1 \, \dot{\epsilon} \, x_1 \\ u_2 = e_2 \, \dot{\epsilon} \, x_2 \\ u_3 = e_3 \, \dot{\epsilon} \, x_3 \end{cases} \qquad \text{and} \qquad \boldsymbol{D} = \dot{\epsilon} \begin{bmatrix} e_1 & 0 & 0 \\ 0 & e_2 & 0 \\ 0 & 0 & e_3 \end{bmatrix} \tag{2.21}$$

where incompressibility requires that $e_1 + e_2 + e_3 = 0$. We consider two types of extensional flows:

- $e_1 = 1$ and $e_2 = e_3 = -1/2$: three-dimensional extensional flow along x_1,
- $e_1 = -e_2 = 1$ and $e_3 = 0$: planar extensional flow along x_1.

$\dot{\epsilon}$ is called extension rate in both cases. By symmetry, we can show that the most general form of the stress tensor is

$$\boldsymbol{\pi} = \begin{bmatrix} -P + \sigma_{11} & 0 & 0 \\ 0 & -P + \sigma_{22} & 0 \\ 0 & 0 & -P + \sigma_{33} \end{bmatrix} \tag{2.22}$$

In the case of a three-dimensional extensional flow, since directions x_2 and x_3 are equivalent, there is only one normal stress difference $\sigma_{11} - \sigma_{22}$ and the *extensional viscosity* is defined as

$$\eta_e \equiv \frac{\sigma_{11} - \sigma_{22}}{\dot{\epsilon}} \tag{2.23}$$

Although the definition of the extensional viscosity found in textbooks is based on the three-dimensional case, the same definition applies in the planar case.

2.3.3 Newtonian fluids

The simplest constitutive equation relating the stress field to the velocity field is

$$\boxed{\boldsymbol{\sigma} = 2\eta \boldsymbol{D}} \qquad \Leftrightarrow \qquad \sigma_{ij} = \eta \left(\frac{\partial u_i}{\partial x_j} + \frac{\partial u_j}{\partial x_i} \right) \tag{2.24}$$

where η is the shear viscosity defined by equation 2.20. It is a constant parameter of the fluid, independent of the shear rate. Equation 2.24 is the tensorial form of Newton's law 2.3. The normal components of the extra stress tensor $\boldsymbol{\sigma}$ are 0 in a pure shear flow, i.e. $N_1 = N_2 = 0$, and the extensional viscosity is $\eta_e = 3\eta$ for a three-dimensional pure extensional flow. Combining equations 2.10, 2.11, 2.15 and 2.24 gives the Navier-Stokes equation

$$\rho \left(\frac{\partial \boldsymbol{u}}{\partial t} + (\boldsymbol{u} \cdot \nabla)\boldsymbol{u} \right) = \rho \boldsymbol{g} - \nabla P + \eta \Delta \boldsymbol{u} \tag{2.25}$$

where $\Delta \boldsymbol{u}$ is the Laplacian of the velocity field. This equation contains a nonlinear inertial term $(\boldsymbol{u} \cdot \nabla)\boldsymbol{u}$ which is responsible of inertial turbulence. It can be neglected when viscous dissipation overcomes inertia, i.e. when the Reynolds number

$$\boxed{Re = \frac{\rho U L}{\eta}} \tag{2.26}$$

is much lower than one, where U and L are typical velocity and length scales of the problem.

Fluids which follow equation 2.24 are called Newtonian fluids. These include water, air, alcohol, glycerin and some oils. These liquids are considered Newtonian since they follow equation 2.24 over a wide range of shear rates and frequencies. Although the list is short, large quantities of these fluids are found on earth, especially water and air. This explains why the branch of fluid mechanics has historically mostly focused on Newtonian flows (i.e. flows of Newtonian fluids).

2.3.4 Non-Newtonian fluids

Any fluid which do not follow equation 2.24 is called a non-Newtonian fluid. Most fluids containing microstructures such as deformable particles are non-Newtonian.

They can be found in nature (biological fluids, mud, magma, ...), food industry (sauces, soups, yogurts, jams, mayonnaise, ...), cosmetics (cremes, gels, foams, ...) and civil engineering (concretes, paints, ...) for example. Different adjectives are used to describe particular non-Newtonian properties of a material, and "viscoelastic" is one of them. Polymer melts and polymer solutions are generally also shear-thinning, meaning that their apparent shear viscosity is a decreasing function of the shear rate. They are also strain-hardening, meaning that the extensional viscosity is an increasing function of the extension rate.

One of the goals of rheology is to propose constitutive equations accounting for non-Newtonian properties. These equations can be derived from microstructure theories or proposed empirically to match experimental data. A valid constitutive relation must follow some general principles first set out by James Gardner Oldroyd in 1950 (Oldroyd, 1950) and developed by Clifford Ambrose Truesdell and Walter Noll in 1953 and 1958 (Truesdell & Noll, 2004). These principles (or axioms) are (Bertram, 2005; Bertram & Glüge, 2015)

1. *Principle of determinism*: The stresses in a material point at a certain instant of time are determined by the current and the past (but not the future) motion of the body.

2. *Principle of local action*: The stresses at a material point depend on the motion of only its infinitesimal neighbourhood.

3. *Principle of material frame-indifference* or *Principle of material objectivity*: Constitutive equations must be invariant under changes of frame of reference.

4. *Principle of invariance under superimposed rigid body motions*: Stresses in a body are not directly caused by translations or rotations of the body.

In the following, we present some of the most popular constitutive equations of viscoelastic liquids, in particular polymer solutions. It is customary to separate the solvent and polymer contributions to the extra stress tensor by writing

$$\boxed{\boldsymbol{\sigma} = \boldsymbol{\sigma}_s + \boldsymbol{\sigma}_p} \qquad \text{where} \qquad \boxed{\boldsymbol{\sigma}_s = 2\eta_s \boldsymbol{D}} \tag{2.27}$$

is the Newtonian contribution of the solvent of viscosity η_s and $\boldsymbol{\sigma}_p$ is the polymer contribution. Note that the equations we present now are used for different types of viscoelastic liquids, not only polymer solutions.

2.3.5 The Oldroyd-B model

The first attempt to generalise the Maxwell model to a tensorial form consists of writing equation 2.4 as $\tau\left(\partial_t \boldsymbol{\sigma}_p + (\boldsymbol{u}\cdot\nabla)\boldsymbol{\sigma}_p\right) + \boldsymbol{\sigma}_p = 2\eta_p \boldsymbol{D}$. However, this constitutive equation violates the fourth principle (invariance under superimposed rigid body motions) and needs some refinements. A valid constitutive equation is

$$\boxed{\tau \overset{\triangledown}{\boldsymbol{\sigma}}_p + \boldsymbol{\sigma}_p = 2\eta_p \boldsymbol{D}} \tag{2.28}$$

where τ is the polymer (terminal) relaxation time, $\eta_p = G\tau$ where G is the elastic modulus and $\triangledown$ is a notation for the *upper-convected time derivative* defined for any vector $\boldsymbol{X}$ as

$$\overset{\triangledown}{\boldsymbol{X}} = \frac{\partial \boldsymbol{X}}{\partial t} + (\boldsymbol{u}\cdot\nabla)\boldsymbol{X} - (\nabla \boldsymbol{u})\boldsymbol{X} - \boldsymbol{X}(\nabla \boldsymbol{u})^T \tag{2.29}$$

Equations 2.27, 2.28 and 2.29 form the *Oldroyd-B* or *upper-convected Jeffrey* model (Oswald & Saint-Jean, 2005) which is the tensorial version of the Jeffrey model presented in 2.2.2. In the case of a negligible solvent viscosity, i.e. when the solvent to total viscosity ratio

$$\boxed{S = \frac{\eta_s}{\eta_s + \eta_p}} \tag{2.30}$$

is $S = 0$, we obtain the *upper-convected Maxwell (UCM)* model ($\boldsymbol{\sigma} = \boldsymbol{\sigma}_p$) which is the tensorial version of the Maxwell model presented in 2.2.1. The term $\boldsymbol{\sigma}_p + \partial_t \boldsymbol{\sigma}_p$ makes any change in stress relax on the time scale τ, the term $(\boldsymbol{u}\cdot\nabla)\boldsymbol{\sigma}_p$ describes the advection of the stress along the flow streamlines and the two nonlinear terms $(\nabla \boldsymbol{u})\boldsymbol{\sigma}_p - \boldsymbol{\sigma}_p(\nabla \boldsymbol{u})^T$ are added to satisfy the fourth principle. Since this constitutive equations is nonlinear, flow instabilities can be observed even at low Reynolds numbers (Groisman & Steinberg, 2000; Morozov & van Saarloos, 2007). These phenomena are referred to as *elastic instability*. The dimensionless number governing elastic instabilities is the Weissenberg number

$$\boxed{Wi = \frac{\tau U}{L}} \tag{2.31}$$

where U and L are typical velocity and length scales of the problem.

We now derive the predictions of the Oldroyd-B model for the pure shear and extensional flows. We assume that the stress components $\sigma_{p,ij}(t)$ are homogeneous in space and we note $\dot{\sigma}_{p,ij} \equiv \partial_t \sigma_{p,ij}$.

Shear flow

For a shear flow, we obtain the following equations

$$\begin{cases} \tau(\dot{\sigma}_{p,12} - \dot{\gamma}\sigma_{p,22}) + \sigma_{p,12} = \eta_p\dot{\gamma} \\ \tau(\dot{\sigma}_{p,11} - 2\dot{\gamma}\sigma_{p,12}) + \sigma_{p,11} = 0 \end{cases} \qquad \begin{cases} \tau\dot{\sigma}_{p,22} + \sigma_{p,22} = 0 \\ \tau\dot{\sigma}_{p,33} + \sigma_{p,33} = 0 \end{cases} \tag{2.32}$$

Therefore, assuming that the liquid is initially at rest at $t = 0$, i.e. $\sigma_{p,ij}(0) = 0$ we obtain $\sigma_{p,22} = \sigma_{p,33} = 0$ and

$$\begin{cases} \sigma_{p,12}(t) = \eta_p\dot{\gamma}\,[1 - \exp(-t/\tau)] \\ \sigma_{p,11}(t) = 2\eta_p\tau\dot{\gamma}^2\,[1 - (1 + t/\tau)\exp(-t/\tau)] \end{cases} \tag{2.33}$$

After transient growth, the shear and normal stress components reach the asymptotic values

$$\sigma_{p,12} = \eta_p\dot{\gamma} \qquad \text{and} \qquad \sigma_{p,11} = 2\eta_p\tau\dot{\gamma}^2 \tag{2.34}$$

and the measurable quantities defined in §2.3.2 become

$$\sigma_{12} = (\eta_s + \eta_p)\dot{\gamma}, \qquad N_1 = 2\eta_p\tau\dot{\gamma}^2 \qquad \text{and} \qquad N_2 = 0 \tag{2.35}$$

The shear viscosity $\eta \equiv \sigma_{12}/\dot{\gamma}$ is $\eta_0 = \eta_s + \eta_p$ and does not depend on the shear rate. The first normal stress difference scales as $N_1 \propto \dot{\gamma}^2$ which is in agreement with most experimental data, including dilute and semidilute polymer solutions at low shear rates (see for example Zell et al. (2010)). This is due to the deformation of polymer chains and to their tendency to align in the direction of the flow, both effects being proportional to $\dot{\gamma}$. Experimentally, the second normal stress difference is much smaller, typically $N_2 \approx -N_1/10$, but not 0.

Extensional flow

For an extensional flow, we obtain the following equations

$$\tau(\dot{\sigma}_{p,ii} - 2e_i\dot{\epsilon}\,\sigma_{p,ii}) + \sigma_{p,ii} = 2\eta_p e_i\,\dot{\epsilon} \qquad i = 1, 2, 3 \tag{2.36}$$

Therefore, assuming a three-dimensional extensional flow starting at $t = 0$, we obtain

$$\begin{cases} \sigma_{p,11} = \dfrac{2\eta_p\dot{\epsilon}}{1 - 2\tau\dot{\epsilon}} + \left(\sigma_{p,11}(0) - \dfrac{2\eta_p\dot{\epsilon}}{1 - 2\tau\dot{\epsilon}}\right)\exp\left[2\dot{\epsilon}t\left(1 - \dfrac{1}{2\tau\dot{\epsilon}}\right)\right] \\ \sigma_{p,ii} = \dfrac{-\eta_p\dot{\epsilon}}{1 + \tau\dot{\epsilon}} + \left(\sigma_{p,ii}(0) - \dfrac{-\eta_p\dot{\epsilon}}{1 + \tau\dot{\epsilon}}\right)\exp\left[-\dot{\epsilon}t\left(1 + \dfrac{1}{\tau\dot{\epsilon}}\right)\right] \qquad i = 2, 3 \end{cases} \tag{2.37}$$

which are function of both the strain $\epsilon = \dot{\epsilon}t$ and the strain rate $\dot{\epsilon}$. While the transverse components $\sigma_{p,22}$ and $\sigma_{p,33}$ always reach a finite asymptotic value at long times, the axial component $\sigma_{p,11}$ only reaches a finite value if $\tau\dot{\epsilon} < 1/2$. In the case where $\tau\dot{\epsilon} > 1/2$, the Oldroyd-B model predicts unbounded stress growth in time. This non physical behaviour is known to be the major deficiency of this model. Note that the effect of the initial axial stress $\sigma_{p,11}(0)$ only vanishes with time if $\tau\dot{\epsilon} < 1/2$. Otherwise, the initial stress does not decay and affects the flow at all further times, i.e. the fluid does not exhibit a fading memory. McKinley (2005) pointed out the possible relevance of this effect in the context of jet breakup where the effect of an upstream shear flow (pre-shear in a pipe) can significantly modify the dynamics of breakup. For $\tau\dot{\epsilon} < 1/2$, the stress components reach the asymptotic values

$$\sigma_{p,11} = \frac{2\eta_p\dot{\epsilon}}{1-2\tau\dot{\epsilon}} \qquad \text{and} \qquad \sigma_{p,ii} = \frac{-\eta_p\dot{\epsilon}}{1+\tau\dot{\epsilon}} \qquad i = 2,3 \tag{2.38}$$

and the extensional viscosity defined in equation 2.23 becomes

$$\eta_e = 3\eta_s + \frac{3\eta_p}{(1-2\tau\dot{\epsilon})(1+\tau\dot{\epsilon})} \tag{2.39}$$

Note that experiments reveal a strong increase of the extensional viscosity at $\tau\dot{\epsilon} = 1/2$. This phenomenon, called *coil-stretch transition*, arises when the stretching exerted by the flow overcomes the relaxation of polymer molecules. At the microscopic level, it means that polymer molecules unravel to a nearly fully extended state (De Gennes, 1974; Petrie, 2006).

The Oldroyd-B model captures some of the main features of viscoelastic liquids: the stress at time t is influenced by the past history of the flow, the fluid exhibits a non-zero first normal stress difference N_1 and the extensional viscosity η_e is an increasing function of the extension rate. For these reasons, it has become the working horse of theoretical studies of viscoelastic liquids (Larson, 1999; Morozov & van Saarloos, 2007). This simple model has been successfully used to describe, at least qualitatively, many physical phenomena such as elastic instabilities (Shaqfeh, 1996; Alves & Poole, 2007) or turbulent drag reduction (T. Min & Joseph, 2003).

The limitations of this model are a constant shear viscosity, the absence of a second normal stress difference N_2, and more importantly a diverging extensional viscosity at the coil-stretch transition. Although many industrial polymer solutions are shear-thinning, note that laboratory experiments are often performed with dilute polymer solutions in a highly viscous solvent ($S \approx 1$, equation 2.30) in order to "screen" the natural tendency of polymers to produce a shear-thinning behaviour.

For such liquids, the viscous response is dominated by the solvent while the elastic response is determined by the polymer chains. These liquids with constant shear viscosity, called *Boger fluids*, are therefore more suitable for analytical descriptions using the Oldroyd-B model.

2.3.6 Linear vs nonlinear viscoelasticity

In order to give a better insight on the validity domain of the Oldroyd-B model, it is important to define the linear and nonlinear flow regimes of viscoelasticity. In simple words, the intrinsic deformation of the particles (polymers, micelles, ...) under flow is proportional to the imposed stress in the linear regime. When the imposed stress increases, the deformation saturates in the nonlinear regime and nonlinear terms appear in the intrinsic stress-strain relationship of the material. Since the Oldroyd-B model predicts a constant apparent shear viscosity, i.e. a linear stress-strain relationship, it is reasonable to say that this constitutive equation should be valid in the linear flow regime. A more complete constitutive equation should include nonlinear terms reflecting the nonlinearities of the intrinsic stress-strain relationship of the particles.

In the general case, we can define a critical intrinsic deformation γ_c beyond which we are no longer in the linear regime. Under a shear flow of shear rate $\dot{\gamma}$, since the particle deformation is $\dot{\gamma}\tau$, we are in the linear regime if $\dot{\gamma} < \dot{\gamma}_c$ where

$$\boxed{\dot{\gamma}_c = \frac{\gamma_c}{\tau}} \tag{2.40}$$

The value of γ_c depends on the material and is of order one in molten polymers far from the glass transition, i.e. we are in the linear regime when $\tau\dot{\gamma} \ll 1$ (Oswald & Saint-Jean, 2005). The condition becomes $\tau\dot{\epsilon} \ll 1$ in an extensional flow, well below the coil-stretch transition.

For a shear flow, the apparent viscosity $\eta \equiv \sigma_{12}/\dot{\gamma}$ is constant in the linear regime since shear stress must be proportional to shear rate. We introduce $\sigma_{12} = \eta_0\dot{\gamma}$ for $\dot{\gamma} < \dot{\gamma}_c$ where η_0 is the constant *zero-shear viscosity* of the material. For polymer solutions, the apparent viscosity usually decreases in the non linear regime before reaching a second plateau value η_∞ which is larger or equal to the solvent viscosity η_s. Several empirical laws have been proposed to fit experimental data. One of them is the five-parameters Carreau law

$$\frac{\eta - \eta_\infty}{\eta_0 - \eta_\infty} = \left[1 + \left(\frac{\dot{\gamma}}{\dot{\gamma}_c}\right)^{a_1}\right]^{\frac{n-1}{a_1}} \tag{2.41}$$

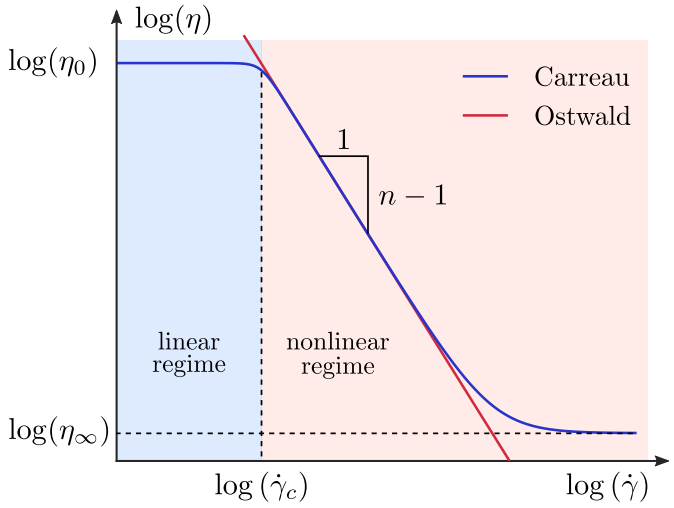

Figure 2.4 – Apparent viscosity η against shear rate $\dot{\gamma}$ according to Carreau 2.41 and Oswald 2.42 laws. The boundary between the linear and nonlinear regime is $\dot{\gamma} = \dot{\gamma}_c$.

where a_1 encodes the sharpness of the transition from linear to nonlinear regime and n is the degree of shear thinning. If $\eta_\infty \ll \eta_0$, in the range of shear rates such that $\eta_\infty \ll \eta \ll \eta_0$, this law reduces to an Ostwald power law

$$\eta = K_0 \dot{\gamma}^{n-1} \tag{2.42}$$

with $K_0 = \eta_0/\dot{\gamma}_c^{n-1}$. This gives $\sigma_{12} = K_0\dot{\gamma}^n$. Both laws are shown in figure 2.4. However, it is possible to obtain $n = 1$ (or equivalently $\eta_\infty = \eta_0$) artificially by raising the solvent viscosity. For such Boger fluids, the intrinsic shear-thinning nature of the fluid is "screened" and it becomes impossible to directly measure $\dot{\gamma}_c$ on the apparent shear viscosity curve. In the following of this thesis, the quantity η_p is defined as the polymer contribution to the zero-shear viscosity, i.e.

$$\boxed{\eta_p \equiv \eta_0 - \eta_s} \tag{2.43}$$

We saw in equation 2.35 that $\eta_p = \tau G$ for the Oldroyd-B model where τ and G are the fundamental material parameters.

2.3.7 The FENE-P model

The FENE-P model is one of the most commonly used constitutive equation taking into account intrinsic nonlinearities. As will be presented in §2.5, it has been derived by R.B. Bird, C.F. Curtiss, R.C. Armstrong and O. Hassager from the kinetic theory of dilute polymer solution where polymer molecules are modelled as "finitely extensible nonlinear elastic" (FENE) dumbbells. The Oldroyd-B model is also derived from this theory where the polymer molecules are modelled as Hookean dumbbells,

with a linear intrinsic stress-strain relationship. Here we simply present the FENE-P model and its main predictions in pure shear and extensional flows (see Bird et al. (1987, 1980); Herrchen & Öttinger (1997) for detailed calculations).

The polymer contribution to the extra stress tensor writes

$$\boxed{\boldsymbol{\sigma}_p = G(f\boldsymbol{A} - \boldsymbol{\delta})} \qquad \text{where} \qquad \boxed{\overset{\triangledown}{\tau\boldsymbol{A}} + f\boldsymbol{A} = \boldsymbol{\delta}} \tag{2.44}$$

with

$$f = \left(1 - \frac{\mathrm{tr}(\boldsymbol{A})}{b}\right)^{-1} = 1 + \frac{3}{b}\left(1 + \frac{\mathrm{tr}(\boldsymbol{\sigma}_p)}{3G}\right) \tag{2.45}$$

where $\boldsymbol{A}$ is a *conformation tensor* (defined in §2.5), $\boldsymbol{\delta}$ is the unit tensor, G is the elastic modulus, τ is the (terminal) relaxation time on the polymer and b is a positive dimensionless parameter, typically larger than ten, accounting for the finite extensibility of the polymer chains. The Oldroyd-B model is recovered for infinitely extensible polymers, i.e. in the limit $b \to \infty$ ($f = 1$). At equilibrium ($\sigma_{p,ij} = 0$), equations 2.44 and 2.45 give $f_{eq} = 1 + 3/b$, $A_{ij,eq} = 0$ for $i \neq j$ and $A_{ii,eq} = 1/f_{eq}$ for $i = 1, 2, 3$.

Shear flow

For a shear flow (§2.3.2), we give the asymptotic values ($t \to +\infty$) of the stress components. We find $\sigma_{12} = \eta\dot{\gamma}$ with

$$\eta - \eta_s = 6\, G\tau\, (\tau\dot{\gamma})^{-1}\, p^{1/2}\, \sinh\left[1/3\, \mathrm{arcsinh}\left(qp^{-3/2}\right)\right] \tag{2.46}$$

where $p = b/54 + 1/18$ and $q = b\tau\dot{\gamma}/108$. The two limiting scalings are

$$\eta - \eta_s = \begin{cases} G\tau\, b/(b+3) & \text{for} \quad \tau\dot{\gamma} \to 0 \\ G\tau\, \left[(2/b)(\tau\dot{\gamma})^2\right]^{-1/3} \propto \dot{\gamma}^{-2/3} & \text{for} \quad \tau\dot{\gamma} \to +\infty \end{cases} \tag{2.47}$$

The FENE-P model predicts a shear thinning behaviour. In fact, solution 2.46 is very similar to a Carreau law 2.41 with a degree of shear thinning $n = 1/3$, a viscosity $\eta_\infty = \eta_s$ at large shear rates, a zero-shear viscosity $\eta_0 = \eta_s + \eta_p$ with

$$\eta_p \equiv \eta_0 - \eta_s = G\tau\, b/(b+3) \tag{2.48}$$

(which becomes $G\tau$ for large values of b) and a critical shear rate $\dot{\gamma}_c = \gamma_c/\tau$ where γ_c is an increasing function of b. A direct comparison with the Carreau law 2.41 suggests $a_1 \approx 2$ and $\gamma_c \propto b^{1/2}$ with a numerical prefactor close to one. This is not surprising since, as will be presented in §2.5, $b^{1/2}$ can be interpreted as the ratio of

the polymer size at full extension to its size in the coiled state at equilibrium. For a Boger fluid with a highly viscous solvent ($S \approx 1$, equation 2.30), the apparent value of n becomes 1. The other stress components are $\sigma_{22} = \sigma_{33} = 0$ and $\sigma_{11} = 2\sigma_{p,12}^2/G$, i.e. $N_2 = 0$ and

$$N_1/\dot{\gamma}^2 = 2(\eta - \eta_s)^2/G \tag{2.49}$$

which, using equation 2.47, gives the expected scaling $N_1 \propto \dot{\gamma}^2$ in the linear regime ($\dot{\gamma} \ll \dot{\gamma}_c$) and $N_1 \propto \dot{\gamma}^{2/3}$ in the nonlinear regime ($\dot{\gamma} \gg \dot{\gamma}_c$).

Extensional flow

For an extensional flow (§2.3.2), the asymptotic values ($t \to +\infty$) of the stress components are given by the following equations

$$\sigma_{p,ii} = \frac{2e_i G\tau\dot{\epsilon}}{f - 2e_i\tau\dot{\epsilon}} \quad (i = 1, 2, 3) \quad \text{and} \quad f = 1 + \frac{3}{b}\left(1 + \frac{\sigma_{p,11} + \sigma_{p,22} + \sigma_{p,33}}{3G}\right) \tag{2.50}$$

In the case of a three-dimensional extensional flow, the extensional viscosity $\eta_e \equiv (\sigma_{11} - \sigma_{22})/\dot{\epsilon}$ is given by

$$\begin{cases} (\eta_e - 3\eta_s)/G\tau = 2/(f - 2\tau\dot{\epsilon}) + 1/(f + \tau\dot{\epsilon}) \\ f^3 - [\tau\dot{\epsilon} + 1 + 3/b]\, f^2 + \left[\tau\dot{\epsilon}(1 + 3/b) - 2(\tau\dot{\epsilon})^2\right] f + 2(\tau\dot{\epsilon})^2 = 0 \end{cases} \tag{2.51}$$

for which there is no simple analytical expression. The two limiting scalings are

$$\eta_e - 3\eta_s = \begin{cases} 3G\tau\, b/(b+3) & \text{for} \quad \tau\dot{\epsilon} \to 0 \\ 2G\tau b & \text{for} \quad \tau\dot{\epsilon} \to +\infty \end{cases} \tag{2.52}$$

Equivalently, using the polymer contribution to the zero-shear viscosity $\eta_p \equiv \eta_0 - \eta_s$ (equation 2.48), we obtain

$$\frac{\eta_e - 3\eta_s}{\eta_0 - \eta_s} = \begin{cases} 3 & \text{for} \quad \tau\dot{\epsilon} \to 0 \\ 2(b+3) & \text{for} \quad \tau\dot{\epsilon} \to +\infty \end{cases} \tag{2.53}$$

Therefore, the Trouton ratio defined as $Tr \equiv \eta_e/\eta_0$ is $Tr = 3$ for $\tau\dot{\epsilon} \to 0$ and is $Tr = 3S + 2(b+3)(1-S)$ for $\tau\dot{\epsilon} \to +\infty$ where we recall that $S = \eta_s/\eta_0$. Solutions of equation 2.51 are shown in figure 2.5 along with the Oldroyd-B solution given in equation 2.39.

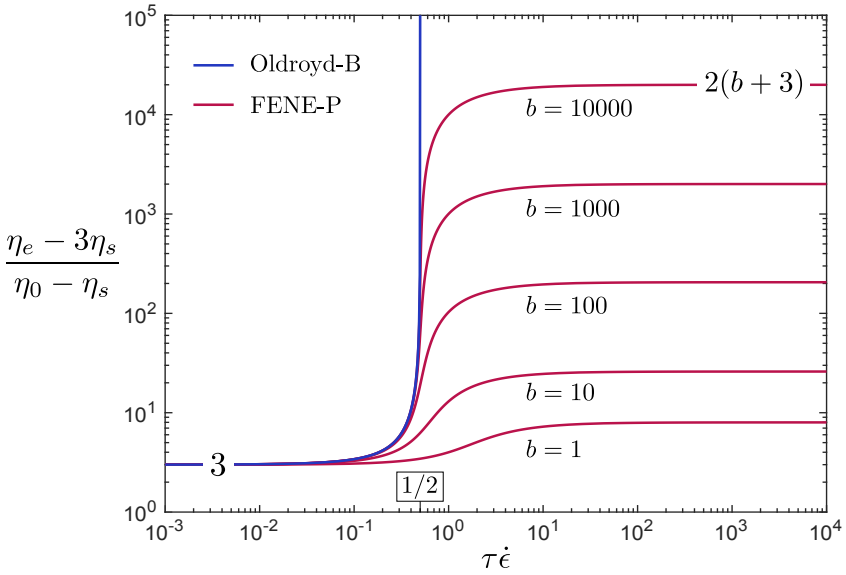

Figure 2.5 – Dimensionless polymer contribution to the extensional viscosity η_e (asymptotic value $t \to +\infty$) versus dimensionless extension rate $\tau\dot{\epsilon}$ for the Oldroyd-B (equation 2.39) model and the FENE-P (equation 2.51) model for different values of b.

The FENE-P model is more realistic than the Oldroyd-B model since shear-thinning behaviour is allowed and the extensional viscosity rises without diverging at the coil-stretch transition $\tau\dot{\epsilon} = 1/2$. It has been successfully used to describe, at least qualitatively, many physical phenomena including the breakup stage of thinning filaments (Clasen et al., 2009; McKinley, 2005). A common technique used to obtain more quantitative description is to use a *multimode FENE-P* model to allow a spectrum of relaxation times τ_i reflecting the different vibration modes of the polymer chain. This gives $\boldsymbol{\sigma}_p = \sum_i G_i(f_i \boldsymbol{A}_i - \boldsymbol{\delta})$ and $\tau_i \overset{\triangledown}{\boldsymbol{A}}_i + f_i \boldsymbol{A}_i = \boldsymbol{\delta}$ with $f_i^{-1} = 1 - \mathrm{tr}(\boldsymbol{A}_i)/b_i$. The case $f_i = 1$ gives the *multimode Oldroyd-B* model which is the tensorial version of the Generalised Maxwell model presented in §2.2. In these models, the single dumbbell model (two beads linked by one string) is replaced by a bead-spring chain model (see Anna & McKinley (2001) or (Clasen et al., 2006) for details). Another way of improving the agreement with experimental data is to use more refined constitutive equations where terms are added to the FENE-P model, like in the Bird-DeAguiar model (see Rothstein & McKinley (2001) and Bird & DeAguiar (1983) for details).

2.3.8 Other models

Many other constitutive equations have been derived to improve the Oldroyd-B model. The basic idea of such semi-empirical models is to postulate a microstructure for the polymer chains and to explore the macroscopic consequences of the polymer-flow interaction. The three main approaches are (Renardy, 2000)

- *Dilute solution theories* which treat polymer molecules individually (no interaction between molecules). Each molecule is modelled as an elastic dumbbell (one string connecting two beads) or as a bead-spring (or bead-rod) chain. The polymer-flow interaction results from the hydrodynamic viscous drag exerted on the beads by the surrounding fluid (solvent).

- *Network theories* which treat polymer molecules as a network of springs linked at junction points (interaction through entanglements). These junctions form and decay following certain statistical laws at equilibrium, contrary to a solid (rubber) where these junctions are permanent. The polymer-flow interaction results from the motion of these junctions.

- *Reptation theories* which are in between these two extremes. Polymer molecules are treated individually but their lateral motion is constrained by a "tube" formed by the other polymer molecules.

The Oldroyd-B and FENE-P dumbbell models (or bead-spring chain models for their multimode versions) are derived from dilute solution theories where the springs are respectively Hookean (Oldroyd-B) and non-Hookean (FENE-P). An example of Reptation theory is the model of Doi & Edwards (1988). An example of Network theory is the commonly used Phan-Thien-Tanner or PTT model proposed by Thien & Tanner (1977) (see also Sibley (2010)). An other useful model is the Giesekus model proposed by Giesekus (1982) to take into account the interaction between different dumbbells in the elastic dumbbell theory. Both PTT and Giesekus models add a nonlinear term to the Oldroyd-B model.

2.4 Polymers: Microscopic description

Linear polymers are long molecules formed by a large number of successive copies of a single subunit called monomer. The simplest polymer is polyethylene of formula —$[CH_2]_n$— obtained by polymerisation of ethylene monomers of formula $H_2C{=}CH_2$. Polymers are, by definition, made of more than 100 monomers while molecules with less than 100 monomers are called oligomers. Human DNA contains about 10^{10} monomers of size 0.3 nm called nucleotides, which results in a macroscopic contour length of about two meters when completely unfolded.

Polymer molecules are generally found in the form of coils, resulting in a much lower effective size. Due to the large number of possible configurations, universal laws can be found to describe polymer molecules independently of their particular chemical composition. In this section, we give an overview of the main concepts derived from the microscopic description of polymer chains in melts and in solutions.

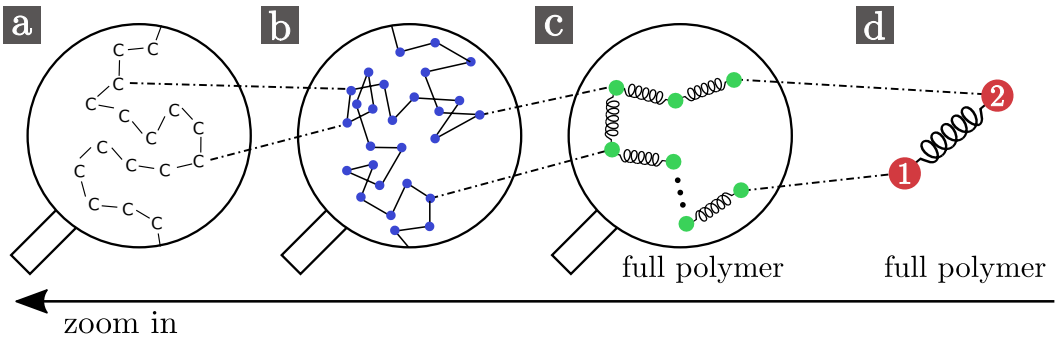

Figure 2.6 – Successive approximations of a polymer chain from the monomer scale (a) to the Kuhn length scale (b) where polymer molecules are modelled bead-rod chains, and from the bead-spring chain model (c) to the elastic dumbbell model (d).

2.4.1 Kuhn length, Flory radius and flexibility

Kuhn length

Two consecutive monomers have preferred respective orientations due to their chemical bound (which can be more or less flexible) and to the size of each monomers. Xanthan gum for example, whose monomer contains five benzene rings, has less possible orientations than polyethylene. However, there is a typical minimal distance beyond which two monomers are no longer correlated and can have arbitrary relative orientations. This length is called *Kuhn length*, or persistence length. A Kuhn segment generally contains a few monomers for flexible polymers, as shown in figure 2.6 (a to b). Hence, a polymer molecule can be seen as a succession of N Kuhn segments of length $\bar{a}$ and mass m. The molecule has a total mass mN and a *molecular weight* $M = mN\mathcal{N}_A$ where $\mathcal{N}_A$ is the Avogadro number. If $\bar{n}$ is the number of chains per unit volume, the mass concentration of polymer is $c = \bar{n}mN$.

Flory radius

The contour length of the chain is $L_{ch} = N\bar{a}$ while the radius of a polymer coil, called *Flory radius*, follows typically

$$\bar{R} \propto \bar{a}\, N^{\nu} \tag{2.54}$$

where the exponent depends on the polymer's environment. ν is often referred to as the *solvent quality exponent* or the *Flory exponent* due to the important contributions of Paul John Flory in polymer physics (Flory, 1953). $\bar{R}$ is the typical radius of the volume $4\pi\bar{R}^3/3$ effectively occupied by the chain (as represented in figure 2.7) and corresponds, with some numerical prefactor, to the polymer's radius of gyration measured from neutron scattering experiments. This effective volume has to be larger or equal to the sum of the volumes of each monomers which is proportional to

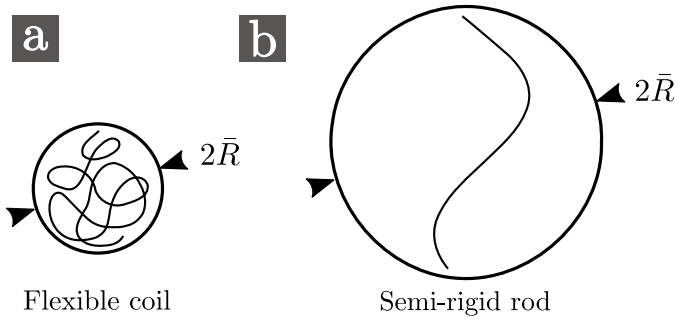

Figure 2.7 – Flexible ((a), $\chi \gg 1$) and semi-rigid ((b), $\chi \geq 1$) polymer chain.

$N\bar{a}^3$. This leads to the condition $\nu \geq 1/3$. The opposite limit is the case where the polymer chain is completely unfolded at equilibrium, i.e. $2\bar{R} = L_{ch} = N\bar{a} \Rightarrow \nu = 1$. Hence, the Flory exponent must range between $1/3 \leq \nu \leq 1$.

Flexibility

The flexibility of a polymer is linked to its extensibility defined as

$$\chi = L_{ch}/\bar{R} \tag{2.55}$$

which is $\chi \gg 1$ for flexible polymers, $\chi \geq 1$ for semi-flexible polymers and semi-rigid polymers (more rigid than semi-flexible ones), and $\chi \approx 1$ for rigid polymers (completely unfolded at equilibrium) which behave as rigid rods. In the latter case (which corresponds to $\nu = 1$), the Kuhn length is of the order of the length of the chain and a Kuhn segment contains many monomers. A flexible coil and a semi-rigid rod are schematically shown in figure 2.7.

2.4.2 Ideal chain

Random walk

The simplest model is the ideal chain (or freely-jointed chain) model which neglects any interaction between two different monomers (from the same chain or from different chains) and describes the polymer chain as a random walk of N Kuhn segments $\boldsymbol{a}_i$ of length $\bar{a}$ (see figure 2.8.a), i.e. with equiprobable orientations between two successive Kuhn segments. The *end-to-end vector* is defined as $\boldsymbol{R} \equiv \sum_{i=1}^{N} \boldsymbol{a}_i$ and we note $R = \|\boldsymbol{R}\|$. The Flory radius is given by

$$\bar{R}^2 \equiv \langle R^2 \rangle_{eq} = \sum_{i=1}^{N} \langle \boldsymbol{a}_i^2 \rangle_{eq} + 2 \sum_{i>j} \langle \boldsymbol{a}_i \cdot \boldsymbol{a}_j \rangle_{eq} \tag{2.56}$$

where $\langle \boldsymbol{a}_i \cdot \boldsymbol{a}_j \rangle_{eq} = \bar{a}^2 \delta_{ij}$ (no correlation at equilibrium) which gives

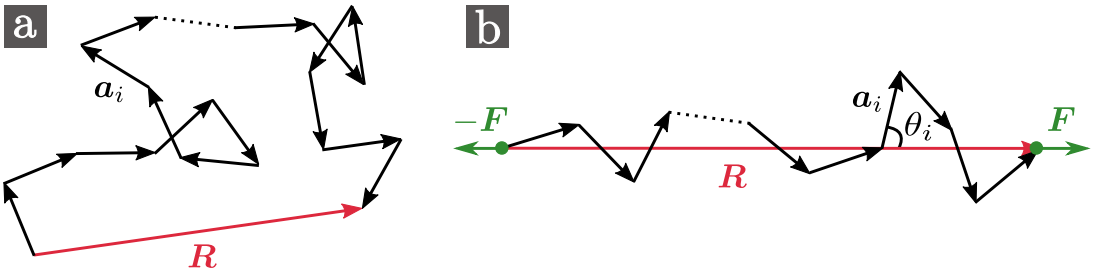

Figure 2.8 – Ideal chain. $\boldsymbol{R}$ is the end-to-end vector and $\boldsymbol{a}_i$ are the Kuhn vectors. (a): unconstrained (random walk at equilibrium) and (b): constrained by a force $\boldsymbol{F}$, each Kuhn segment $\boldsymbol{a}_i$ makes and angle θ_i with the force direction.

$$\boxed{\bar{R} = \bar{a}\sqrt{N}} \tag{2.57}$$

The Flory exponent is therefore $\nu = 1/2$ for an ideal chain and the flexibility defined in equation 2.55 is $\chi = \sqrt{N}$. All walks (micro-states) are equiprobable, but the number of walks resulting in a macro-state with end-to-end vector $\boldsymbol{R}$ is larger for lower values of R.

Restoring force

When a force $\boldsymbol{F}$ is applied to both ends of the polymer chain (see figure 2.8.b), a configuration of large end-to-end vector $\boldsymbol{R}$ is imposed and a restoring force $-\boldsymbol{F}$ arises due to the associated loss of entropy. The relation between $\boldsymbol{F}$ and $\boldsymbol{R}$ can be derived by minimising the free enthalpy of the chain (see Flory (1953) for example). The final expression for the magnitude $F = \|\boldsymbol{F}\|$ of the restoring force is

$$\boxed{F = \frac{3k_BT}{N\bar{a}^2}R = HR} \quad \text{where} \quad H = \frac{H_m}{N}, \quad H_m = \frac{3k_BT}{\bar{a}^2} \tag{2.58}$$

and is proportional to $R = \|\boldsymbol{R}\|$. This Hookean restoring force should be valid in the linear regime defined in §2.3.6 where the intrinsic deformation is much lower than the polymer contour length, i.e. when $R \ll L_{ch} = N\bar{a}^2$. This result has motivated microscopic theories where polymer chains are modelled as Hookean dumbbells with two beads connected by one spring of spring constant H (see figure 2.6.d). Since the stiffness of the full chain goes like $H \propto 1/N$, the polymer can also be modelled as a succession of $N+1$ beads connected in serie by N strings with elementary spring constant $H_m = 3k_BT/\bar{a}^2$ (see figure 2.6.c).

In the nonlinear regime ($R \leq L_{ch} = N\bar{a}^2$), the intrinsic stress-strain relationship becomes nonlinear since the polymer deformation can not exceed its contour length

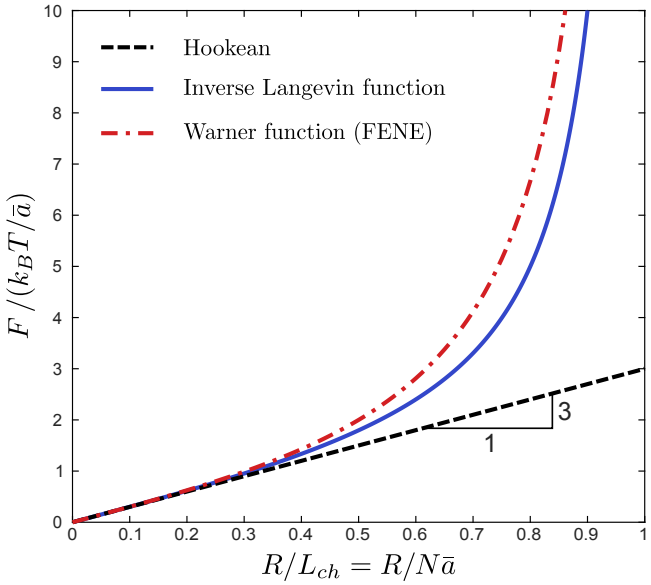

Figure 2.9 – Comparison between the Hookean function (equation 2.58), inverse Langevin function (equation 2.59) and Warner (FENE) function for the magnitude F of the polymer restoring force.

L_{ch}. A more realistic restoring force can be derived from an improved model which associates an energy cost $\boldsymbol{F}\cdot\boldsymbol{a}_i = F\bar{a}\cos\theta_i$ to the orientation of each Kuhn segment, where θ_i is the angle of the Kuhn segment $\boldsymbol{a}_i$ relative to the force $\boldsymbol{F}$. The associated Boltzmann weight is $\exp\left(-F\bar{a}\cos\theta_i/k_BT\right)$ and the norm R of the end-to-end vector is, on average, $R = N\bar{a}\langle\cos\theta_i\rangle$. The calculation gives

$$\boxed{\frac{F}{k_BT/\bar{a}} = \mathcal{L}^{-1}\left(\frac{R}{N\bar{a}}\right)} \qquad \text{with} \quad \mathcal{L}(x) = \coth x - \frac{1}{x} \tag{2.59}$$

which involves the inverse Langevin function $\mathcal{L}^{-1}$. We recover equation 2.58 in the limit $R/N\bar{a} \ll 1$ and the restoring force diverges at $R/N\bar{a} = 1$, as shown in figure 2.9. In reality, the chain breaks when F is large enough to break covalent bonds between monomers.

2.4.3 Real chain

In both polymer melts and polymer solutions, polymer chain are actually not free to adopt any conformation. Many interactions exist between two (non successive) monomers from the same chain or between two monomers from different chains. Some examples are

- Excluded volume (repulsive): two monomers can not occupy the same position in space due to the repulsion of electronic clouds (Pauli repulsion).
- Van der Waals (attractive): London, Keesom and Debye dipolar interactions.

- Electrostatic (repulsive) for polyelectrolytes which are polymers made of charged monomers.

In the case of polymer solutions, monomers also interact with the solvent molecules. All these interactions (except electrostatic) are short-range interactions. Besides, hydrodynamic long-range interactions must be added when considering the flow of polymer solutions since each monomer perturbation to the mean flow has an influence on the viscous drag experienced by other monomers. Chain-chain interactions also occur for polymer melts of large molecular weight and polymer solutions of large concentration. In both cases, the (zero-shear) viscosity stops increasing linearly with molecular weight (melts) or polymer concentration (solution) due to the friction between different chains.

When taking into account excluded volume interactions only, the statistic of a single chain is no longer Gaussian and its conformation will be that of a *self-avoiding walk*. The chain is swollen since expanded configurations are less likely to to lead to self-intersections, and the resulting Flory radius is (Larson, 1999)

$$\bar{R} \propto \bar{a}\, N^{3/5} \tag{2.60}$$

with a Flory exponent $\nu = 3/5 > 1/2$.

In polymer melts, there is no solvent. Hence, monomers only interact with other monomers. Experiments show that hydrodynamic interactions are negligible and that, more surprisingly, chains have an ideal behaviour (De Gennes (1979) p.54 and Larson (1999) p.73). A simple and comprehensive explanation is that chains must avoid self-intersections but also intersections with other chains and have therefore no tendency to expand beyond ideal behaviour since swelling would make intersections with other chains more likely to happen.

2.4.4 Polymer solutions

For polymer solutions, monomer-solvent (m-s) interactions are important and have to be compared with monomer-monomer (m-m) and solvent-solvent (s-s) interactions. At a given temperature, there are two types of solvents for a given polymer:

- Good solvent: Chains are swollen since monomers prefer contact with the solvent rather than with other monomers.
- Bad solvent: Chains are contracted since monomers prefer contact with other monomers rather than with the solvent.

A complete description taking m-s, m-m and s-s interaction can be founs in De Gennes (1979) (p.71). The interaction potential $V_{int}(r)$ between two monomers has the shape of a Lennard-Jones potential with a repulsive part due to excluded volume interactions and an attractive part due to Van der Waals interactions, both interactions being modulated by the presence of the solvent. Note that $V_{int}(r) = 0$ corresponds to an ideal chain and that a hard sphere potential corresponds to pure excluded volume interactions (see equation 2.60). To quantify the quality of the solvent, Kuhn (1934) and Flory (1949) introduced the *excluded volume parameter* $\bar{v}$ which measures the competition between attractive and repulsive interactions. It is defined as $\bar{v} = \int [1 - \exp(-V_{int}(r)/k_B T)]\, \mathrm{d}\boldsymbol{r}$ and can be written as a function of the temperature as (Oswald & Saint-Jean, 2005)

$$\bar{v} = \bar{v}_0 \left(1 - \frac{\Theta}{T}\right) \tag{2.61}$$

where $\bar{v}_0 > 0$ and Θ is a particular temperature at which $\bar{v} = 0$ which means that attractive and repulsive interactions compensate. For a given pair polymer-solvent, the properties of the solution change by varying the temperature. Good and bad solvents correspond respectively to $T > \Theta$ ($\bar{v} > 0$) and $T < \Theta$ ($\bar{v} < 0$).

Dilute solutions

For a dilute solution where chains are independent (not entangled), three regimes can be identified for electrostatically neutral polymers

- Good solvent ($T > \Theta$): $\bar{R}_d \propto \bar{a} N^{3/5}$, $\nu = 3/5$: swollen chains
- Theta solvent ($T = \Theta$): $\bar{R}_d \propto \bar{a} N^{1/2}$, $\nu = 1/2$: ideal chains
- Bad solvent: ($T < \Theta$): $\bar{R}_d \propto \bar{a} N^{1/3}$, $\nu = 1/3$: collapsed chains

where d means "dilute". On the other hand, ν is closer to 1 for polyelectrolytes (without salt) since electrostatic repulsion dominates (Colby, 2010). A proper derivation for good solvents gives $\bar{R}_d \approx (\bar{v}/\bar{a}^3)^{1/5}\, \bar{a} N^{3/5}$ (Oswald & Saint-Jean, 2005).

Critical overlap concentration

As polymer concentration c increases, the different polymer coils will eventually touch at a concentration c^* called *critical overlap concentration*, as shown schematically in figure 2.10. The dilute regime corresponds to $c < c^*$ and the semidilute regime corresponds to $c > c^*$. We recall that $c = \bar{n} m N$ where $\bar{n}$ is the number of

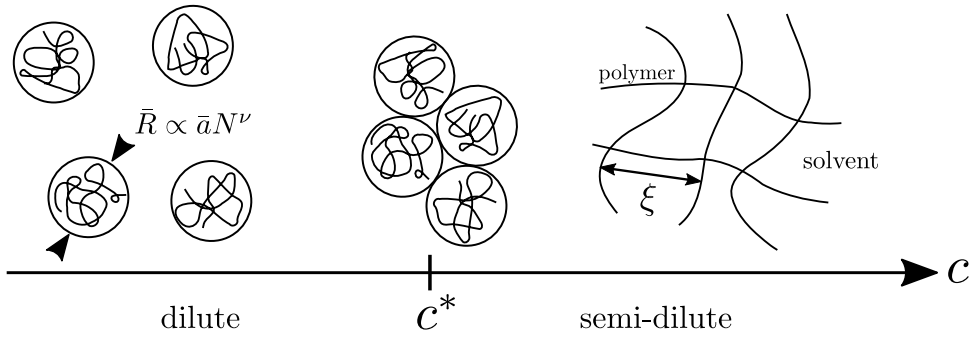

Figure 2.10 – Boundary between the dilute and semidilute regime for polymer solutions. In the semidilute regime, polymer chains are entangled and $\bar{\xi}$ is the average distance along a chain between two contacts with other chains.

chains per unit volume and that $M = mN\mathcal{N}_A$ is the molecular weight of the polymer. The volume fraction is $\phi = \bar{n}\bar{R}_d^3$ (where the numerical factor $4\pi/3$ is omitted). It must be $\phi = 1$ at $c = c^*$. Hence, we get

$$c^* \approx \frac{mN}{\bar{R}_d^3} = \frac{M}{\mathcal{N}_A \bar{R}_d^3} \qquad \Rightarrow \qquad \boxed{c^* \propto N^{1-3\nu}} \tag{2.62}$$

In practice, c^* is measured by viscosity measurements. Indeed, in the dilute regime, the properties of the solution are proportional to the concentration. In particular, the zero-shear viscosity is $\eta_0 = \eta_s(1 + [\eta]c)$ where $[\eta]$ is the *intrinsic viscosity* defined as

$$[\eta] \equiv \lim_{c \to 0} \frac{\eta_0 - \eta_s}{c\,\eta_s} \tag{2.63}$$

This result has to be compared with the viscosity predicted by Einstein's law $\eta_0 = \eta_s(1 + 2.5\phi)$ for a dilute suspension of hard spheres of volume fraction ϕ. A direct comparison suggests that $[\eta]c \approx \phi$ and in particular $[\eta]c^* \approx 1$. Physicists now agree on using the formula proposed by Graessley (1980)

$$[\eta]c^* = 0.77 \qquad \Rightarrow \qquad \boxed{[\eta] \propto N^{3\nu-1}} \tag{2.64}$$

Semidilute solutions

In the semidilute regime ($c > c^*$), polymers are entangled and form a disordered mesh of average lattice constant $\bar{\xi}$ called *correlation length* (see figure 2.10). In other words, $\bar{\xi}$ is the average distance along a chain between two contacts with other chains. De Gennes (1979) proposed a derivation based on two arguments: $\bar{\xi}$ does not depend on N (i.e. $\bar{\xi} \propto N^0$) and is equal to $\bar{R}_d$ at the critical overlap concentration $c = c^*$. Using equation 2.62, we get

$$\bar{\xi} \approx \bar{R}_d \left(\frac{c^*}{c}\right)^{\nu_{\bar{\xi}}} \qquad \text{with} \qquad \nu_{\bar{\xi}} = \frac{\nu}{3\nu - 1} \tag{2.65}$$

where the exponent is $\nu_{\bar{\xi}} = 3/4$ in good solvent ($\nu = 3/5$).

We now derive an expression of the Flory radius $\bar{R}_{sd}$ in the semidilute regime by assuming a good solvent situation. The chain can be seen as a succession of "blobs" of size $\bar{\xi}$ within which it has no contact with other chains (De Gennes, 1979). Therefore, at the $\bar{\xi}$ scale, the statistic of the chain is that of a self-avoiding walk since excluded volumes dominate ($\bar{v} > 0$) and we get $\bar{\xi} \propto \bar{a} g_{\bar{\xi}}^{3/5}$ where $g_{\bar{\xi}}$ is the number of Kuhn segment inside a blob. According to equation 2.65, we have $g_{\bar{\xi}} \propto N^0 c^{-5/4}$. The full chain can be seen as an effective chain of $N/g_{\bar{\xi}}$ Kuhn segments of size $\bar{\xi}$ which has many contacts with other chains. This is similar to polymer melts where chains are ideal since excluded volumes are screened by the presence of the other chains. Therefore, we get

$$\bar{R}_{sd} = \bar{\xi} \left(\frac{N}{g_{\bar{\xi}}}\right)^{1/2} \propto N^{1/2} c^{-1/8} \qquad \text{(good solvent)} \tag{2.66}$$

Hence, semidilute polymer solutions and polymer melts of high molecular weight are often modelled by reptation theories such as the Doi-Edward model. On the other hand, dilute polymer solutions and polymer melts of low molecular weight are modelled by dilute solution theories neglecting chain-chain interactions, such as the elastic dumbbell models discussed in the next section.

2.5 Polymers: Elastic dumbbell models

In this section, we give the important steps of the derivation of the (single mode) Oldroyd-B and FENE constitutive equations from the kinetic theory of elastic dumbbell models without (Rouse) and with (Zimm) hydrodynamic interactions. For a detailed derivation, see the chapter 13 of Bird et al. (1987). The aim of this section is to show how the macroscopic flow quantities defined in §2.3 (such as the elastic modulus G, the relaxation τ and the finite extensibility parameter b) connect with the microscopic quantities defined in the previous section §2.4.

2.5.1 General framework

Polymers are modelled by dumbbells made of two beads (1) and (2) respectively at locations $\boldsymbol{r}_1$ and $\boldsymbol{r}_2$ connected by one spring (see figure 2.6.d). The end-to-end

vector is $\boldsymbol{R} = \boldsymbol{r}_2 - \boldsymbol{r}_1$ and the velocity field of the surrounding fluid (the solvent for polymer solutions) is $\boldsymbol{u}(\boldsymbol{r}, t)$. The three forces acting on each bead $n = 1, 2$ are:

- A hydrodynamic drag force $\boldsymbol{F}_n^h = -\zeta\left(\dot{\boldsymbol{r}}_n - \boldsymbol{u}(\boldsymbol{r}_n, t)\right)$ which is proportional to the bead velocity $\dot{\boldsymbol{r}}_n = \partial_t \boldsymbol{r}_n$ relative to the velocity $\boldsymbol{u}(\boldsymbol{r}_n, t)$ of the surrounding fluid with a friction coefficient ζ. In polymer solutions, $\zeta = 6\pi\eta_s R_b$ where R_b is the bead radius.

- An elastic restoring force $\boldsymbol{F}_n^{el}$ resulting from the action of the spring. In the following, we define the *connector force* $\boldsymbol{F}^c = \boldsymbol{F}_1^{el} = -\boldsymbol{F}_2^{el}$ acting on bead (1) which points in the same direction as $\boldsymbol{R}$.

- A Brownian Langevin force $\boldsymbol{F}_n^b$ describing collisions with the molecules of the liquid (thermal fluctuations). In the following, the average of any quantity X with respect to the distribution of the realisations of collisions is noted $\langle X \rangle$. We use $\langle F_{n,i}^b(t) \rangle = 0$ and $\langle F_{n,i}^b(t) F_{m,j}^b(t') \rangle = 2\zeta k_B T\, \delta_{nm}\, \delta_{ij}\, \delta(t - t')$ which means that there is no correlation between the force acting on a bead at time t and at time $t' \neq t$ (term $\delta(t - t')$ where δ is the Dirac delta function), no correlation between the forces acting on different beads (term δ_{nm}) and no correlation between the three spatial components of the force (term δ_{ij}).

While the hydrodynamic drag force tends to stretch the dumbbell and to orient it in the direction of the flow, the elastic restoring force tends to maintain its original shape and the Brownian Langevin force tends to randomise its orientation. Neglecting the inertia of the beads, the force balance equations are

$$\boldsymbol{F}_n^h + \boldsymbol{F}_n^{el} + \boldsymbol{F}_n^b = \boldsymbol{0} \qquad n = 1, 2 \tag{2.67}$$

from which we can derive the equation of motion of $\boldsymbol{R}$.

We skip the next step which consists of deriving the diffusion equation of the configurational distribution function. The result is

$$\zeta \langle \overset{\triangledown}{\boldsymbol{R}\boldsymbol{R}} \rangle + 4\langle \boldsymbol{R}\boldsymbol{F}^c \rangle = 4k_B T \boldsymbol{\delta} \tag{2.68}$$

where $\boldsymbol{\delta}$ is the unit tensor and $[\boldsymbol{X}\boldsymbol{X}']_{ij} = X_i X_j'$ for arbitrary vectors $\boldsymbol{X}$ and $\boldsymbol{X}'$. At equilibrium (in the absence of flow), we obtain

$$\langle \boldsymbol{R}\boldsymbol{F}^c \rangle_{eq} = k_B T \boldsymbol{\delta} \tag{2.69}$$

The next step is to derive an expression of the polymer contribution to the extra stress tensor $\boldsymbol{\sigma}_p$. There are two contributions which can be understood by

considering an arbitrary plane dividing the fluid in two parts (I) and (II). If the plane is intersected by a dumbbell (one bead on each side), there is a force transmitted through the spring acting on both parts. Besides, if a bead crosses the plane, it transports some momentum from one part to the other. Since the probability of crossing the plane is proportional to the number $\bar{n}$ of dumbbells per unit volume, $\boldsymbol{\sigma}_p$ is proportional to $\bar{n}$. The final result is

$$\boldsymbol{\sigma}_p = \bar{n}\langle \boldsymbol{R}\boldsymbol{F}^c \rangle - \bar{n}k_B T\boldsymbol{\delta} \tag{2.70}$$

2.5.2 Hookean dumbbells (Rouse)

We now assume that the spring is Hookean with spring constant H, as inspired from the ideal chain model in the linear regime (see equation 2.58). We write

$$\boldsymbol{F}^c = H\boldsymbol{R} \tag{2.71}$$

When combining equations 2.68, 2.70 and 2.71, and using the fact that $\overset{\triangledown}{\boldsymbol{\delta}} = -2\boldsymbol{D}$, we recover the exact expression of the Oldroyd-B constitutive equation 2.28 where the relaxation time τ and the elastic modulus G can now be expressed as a function of microscopic quantities

$$\boxed{\tau = \frac{\zeta}{4H}} \qquad \text{and} \qquad \boxed{G = \bar{n}k_B T = \frac{c\mathcal{N}_A k_B T}{M}} \tag{2.72}$$

To summarise, the Oldroyd-B constitutive equation is a direct consequence of the Hookean dumbbell model which is a direct consequence of the ideal chain model. More visually, the take-home message is

$$\text{Ideal chain} \quad \Rightarrow \quad \text{Hookean dumbbell} \quad \Rightarrow \quad \text{Oldroyd-B}$$

We can go even further. Equation 2.69 gives

$$\langle \boldsymbol{R}\boldsymbol{R} \rangle_{eq} = \frac{k_B T}{H}\boldsymbol{\delta} \tag{2.73}$$

and the Flory radius defined as $\bar{R}^2 \equiv \langle R^2 \rangle_{eq}$ becomes $\bar{R}^2 = 3k_B T/H$. Using the expression of $H = H_m/N = 3k_B T/N\bar{a}^2$ given in equation 2.58, we recover the exact expression $\bar{R} = \bar{a}\sqrt{N}$ of the ideal chain. Furthermore, when writing $\zeta = N\zeta_m$ where ζ_m is the friction coefficient of a single monomer (or Kuhn segment), equations 2.72 and 2.58 give the (terminal) *Rouse relaxation time* (Rouse, 1953)

$$\boxed{\tau = \tau_R \propto \frac{\zeta_m\, \bar{a}^2 N^2}{k_B T} \propto N^2} \tag{2.74}$$

For polymer solutions, since $\zeta_m \propto \eta_s$, the Rouse relaxation time is proportional to the solvent viscosity η_s and is independent of the polymer concentration c. However, as will be discussed later, this result is not valid for dilute solutions (even in theta solvent where chains are ideal) due to hydrodynamic interactions between monomers which have been neglected here. The situation is different for polymer melts of low molecular weight ($M < M_e$) where hydrodynamic interactions are short-ranged since there is no solvent. Measurements indeed give $\bar{R} \propto N^{1/2}$, $\tau \propto N^2$ and $\eta_0 = G\tau \propto N$ which is compatible with an ideal chain behaviour.

2.5.3 FENE dumbbells

In the nonlinear regime, the connector force $\boldsymbol{F}^c$ must take into account the nonlinearities identified in §2.4 (see figure 2.9). In the FENE (finitely extensible nonlinear elastic) dumbbell model, we assume the form

$$\boldsymbol{F}^c = \frac{H}{1-(R/L_{ch})^2}\boldsymbol{R} \qquad \text{(FENE)} \tag{2.75}$$

which gives, using $L_{ch} = N\bar{a}$ and $H = 3k_BT/N\bar{a}^2$ (equation 2.58)

$$\boxed{\frac{F}{k_BT/\bar{a}} = \mathcal{W}\left(\frac{R}{N\bar{a}}\right)} \qquad \text{with} \quad \mathcal{W}(x) = \frac{3x}{1-x^2} \tag{2.76}$$

where the Warner function $\mathcal{W}$ is a good approximation of the inverse Langevin function $\mathcal{L}^{-1}$ introduced in equation 2.59, (see figure 2.9). The spring gets stiffer as $R = \|\boldsymbol{R}\|$ increases and diverges when approaching the chain contour length L_{ch}.

In the FENE model, the derivation of a simple constitutive equation is impossible. To solve this issue, A. Peterlin proposed to simplify the connector force as

$$\boldsymbol{F}^c = \frac{H}{1-\langle R^2/L_{ch}^2\rangle}\boldsymbol{R} \qquad \text{(FENE-P)} \tag{2.77}$$

which is known as FENE-P spring (P for Peterlin). The derivation becomes straightforward. We introduce the finite extensibility parameter b and the conformation tensor $\boldsymbol{A}$ defined as

$$\boxed{b = \frac{L_{ch}^2}{k_BT/H} = 3N} \qquad \text{and} \qquad \boxed{\boldsymbol{A} = \frac{\langle \boldsymbol{RR}\rangle}{k_BT/H} = \frac{3\langle \boldsymbol{RR}\rangle}{N\bar{a}^2}} \tag{2.78}$$

We also introduce

$$f = \left(1 - \left\langle \frac{R^2}{L_{ch}^2} \right\rangle\right)^{-1} = \left(1 - \frac{\mathrm{tr}(\boldsymbol{A})}{b}\right)^{-1} \tag{2.79}$$

since $\langle R^2 \rangle = \mathrm{tr}(\langle \boldsymbol{RR} \rangle)$. When combining equations 2.68 and 2.70 with equations 2.77 2.78 and 2.79, we finally obtain the FENE-P constitutive equation 2.44 with $\tau = \zeta/4H$ and $G = \bar{n}k_BT$ (same as equation 2.72). The finite extensibility parameter b and the Kuhn length N are simply related by a numerical constant according to equation 2.78.

Note that equation 2.69 gives $\langle R^2 \rangle_{eq} = 3k_BT/Hf_{eq}$ where $f_{eq} = 1 + 3/b$ (see equation 2.45). Hence, the Flory radius becomes $\bar{R}^2 \equiv \langle R^2 \rangle_{eq} = 3k_BT/H(1+3/b) = N\bar{a}^2(1+3/b)$. For large values of b, it becomes $\bar{R}^2 \approx N\bar{a}^2$. Hence, for flexible chains ($b = 3N \gg 1$), we get

$$b^{1/2} \approx \sqrt{3N} = \sqrt{3}\, L_{ch}/\bar{R} \tag{2.80}$$

Therefore, as announced in §2.3.7, $b^{1/2}$ is the ratio of the polymer size at full extension to its size in the coiled state at equilibrium (with a numerical constant).

2.5.4 With hydrodynamic interactions (Zimm)

In dilute polymer solutions, regardless of the quality of the solvent, these elastic dumbbell models have to be refined to include hydrodynamic interactions between the beads. The general idea is to replace the previous hydrodynamic drag force $\boldsymbol{F}_n^h$ by $-\zeta\left(\dot{\boldsymbol{r}}_n - \boldsymbol{u}(\boldsymbol{r}_n, t) - \boldsymbol{u}'(\boldsymbol{r}_n, t)\right)$ where $\boldsymbol{u}'(\boldsymbol{r}_n, t)$ is the perturbation of the flow field at the position of bead n resulting from the motion of the other bead. This was worked out by Zimm (1956) for a bead-spring chain model. The now accepted formula for the terminal *Zimm relaxation time* is (see Tirtaatmadja et al. (2006))

$$\boxed{\tau_Z = \frac{1}{\bar{\zeta}(3\nu)} \frac{[\eta] M \eta_s}{\mathcal{N}_A k_B T} \propto N^{3\nu}} \tag{2.81}$$

which is proportional to the solvent viscosity η_s and is independent of the polymer concentration c. In this formula, $\bar{\zeta}$ is the Riemann zeta function, and we have $\bar{\zeta}(3\nu) = \sum_{i=1}^{\infty} 1/i^{3\nu}$. The dependence $\tau_Z \propto N^{3\nu}$ comes from the fact that $[\eta] \propto N^{3\nu-1}$ (see equation 2.64). In theta solvent ($\nu = 1/2$), we have $\tau_Z \propto N^{3/2}$ whereas the Rouse model, which assumes an ideal chain behaviour without hydrodynamic interactions, predicts $\tau_R \propto N^2$.

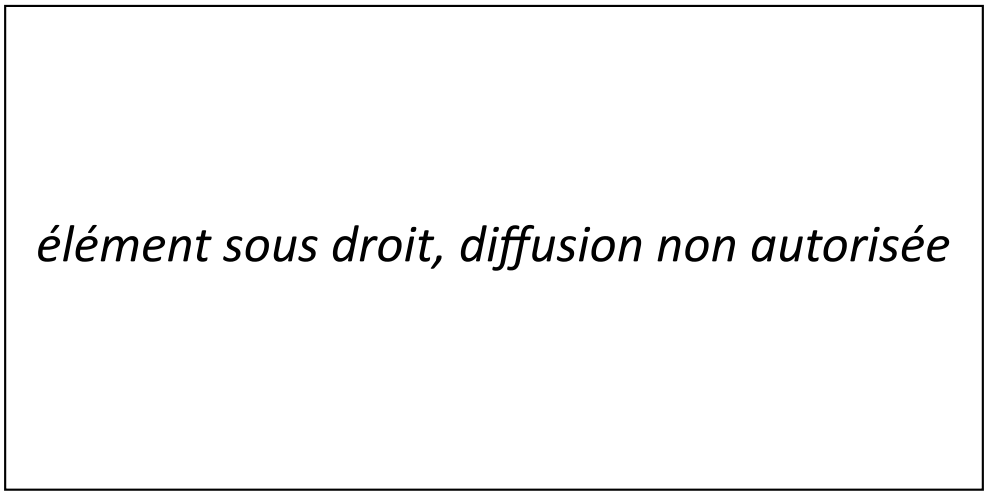

Figure 2.11 – Clean cut of a thick viscoelastic liquid flowing from a bottle into a beaker by scissors. Images taken from Boger & Walters (2012).

2.6 Unusual flows characteristics of viscoelastic liquids

In this section, we present some of the many unusual flow characteristics observed with viscoelastic liquids. Some of these particularities such as jet stabilisation and drag reduction have been used to improve industrial techniques while others such as melt fracture represent a severe limitation to industrial processes. This explains why the development of the previously presented theories, initiated in the 1930s by pioneers such as Bingham and Reiner, have been of major importance in recent history.

A classical example is the *elastic recoil* experiment shown in figure 2.11 where a viscoelastic liquid is flowing from a bottle into a beaker (liquid behaviour) and recoils back into the bottle after clean cut by scissors (solid behaviour). Here, the liquid is quite thick. Note capillary forces are also responsible of the recoil, and may become the dominant contribution, as shown by Clasen et al. (2009) for a dilute aqueous polymer solution. Here are some other examples of unusual flows.

2.6.1 Normal stress effects

Rod climbing

When a rigid rod is rotated into a viscoelastic liquid, the free surface may rise (sometimes spectacularly, see figure 2.12.a) due to the development of normal stresses in the liquid. This in not true for Newtonian liquids since the free surface is repelled by the rotating rod due to inertial effects.

Die swell

When viscoelastic liquid is extruded through a tube, the jet may rapidly swell at the outlet due to the recovery of the normal stress imparted into the tube (see figure 2.12.b). A simple image is to consider that polymer molecules are initially stretched and oriented along the shear flow inside the tube and recover a coil shape due to the change of boundary condition, thus resulting in radial expansion.

2.6.2 Extensional viscosity effects

Open siphon

When filling a syringe with a viscoelastic liquid placed in a beaker, the flow does not stop when rising the syringe above the free surface if maintaining the axial tension (depression in the syringe). This is due to the stretching of polymer molecules in the jet connecting the syringe to the beaker which produces strong extensional stresses, thus preventing breaking of the jet. The same phenomenon can be observed when replacing the syringe by a rotating drum collecting the liquid and also producing axial tension (see figure 2.13.a).

Jet stabilisation and Drag reduction

When extruding a Newtonian liquid from a tube at high velocity (high Reynolds number), addition of small amounts of high molecular weight polymers can significantly reduce the number of emitted (spray) droplets and smooth the surface of the turbulent jet (see figure 2.13.b). This stabilising effect is also used to suppress the splashing of droplets impacting on rough solid surfaces in pesticide spraying, spray coating, and inkjet printing (Crooks & Boger, 2000). Polymer additives are also used to reduce the drag in turbulent pipe flows through a rise of extensional viscosity (due to the elongation of polymer molecules) which stabilises the small-scale flow field (Virk, 1975). This effect is used to increase the flow rates of hose streams in firefighting (Chen et al., 1998).

2.6.3 Extrusion phenomena

Contraction flows

When forcing a viscoelastic liquid through a contraction (extrusion through a syringe for example), many unusual flow patterns can be observed. While Newtonian liquids exhibit vortices of modest size on both corner of the upstream part, polymer melts and solutions usually exhibit much larger (corner) vortices and even present (lip) vortices at the re-entrant corner. These phenomena are referred to as *vortex*

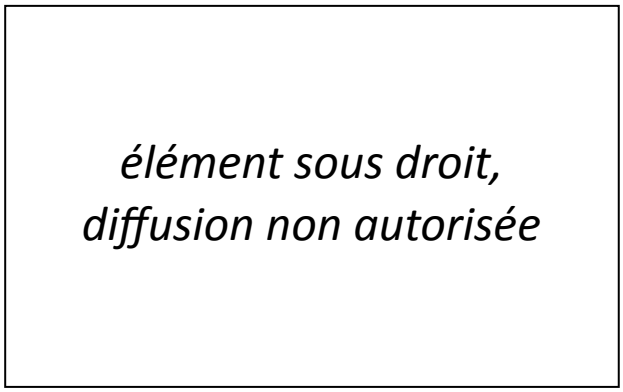

Figure 2.12 – Normal stress effects. (a): Rod climbing for a solution of polyisobutylene (B200) in polybutene. (b) Die swell from a tube for a 2.0% aqueous solution of polyacrylamide. Images taken from Boger & Walters (2012).

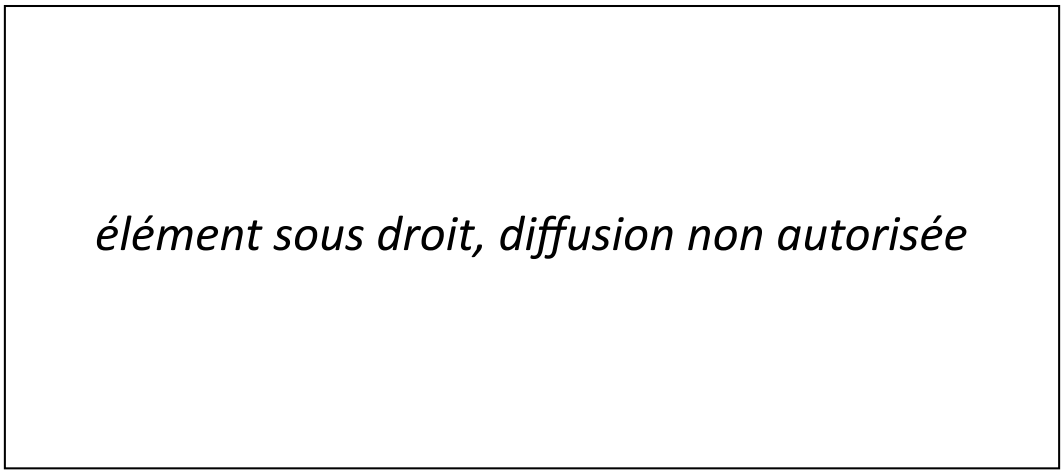

Figure 2.13 – Extensional viscosity effects (a and b). (a): Open siphon with a drum rotating above the free surface of a polyisobutylene (B200) solution in oil. (b): Jet stabilisation for a high Reynolds number capillary jet (1 m from the exit of a 0.635 cm diameter nozzle) for water (top) and a 200 ppm aqueous solution of polyethylene oxide (bottom). (c): Vortex enhancement (stationnary regime) in a 16:1 square-square contraction flow of a Boger fluid. Images taken from Boger & Walters (2012).

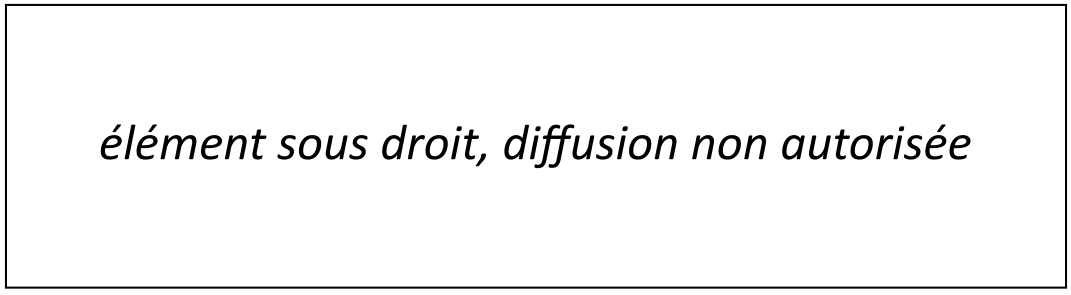

Figure 2.14 – Melt fracture. (a): Five snapshots of a polymer melt extruded from a tube at increasing flow rate from left to right. (b and c): Narrow grooves (b) and wide stripes (c) formed on the surface of a sheet of polymer solution extruded at different flow rates from slots of dimensions 3×0.3 cm (b) and 3.9×0.1 cm (c). In (c), the sheet is continuous and the stripes are simply highlighted by the photographic technique. Images taken from Morozov & van Saarloos (2007) (a) and Boger & Walters (2012) (b and c).

enhancement (see figure 2.13.c). Both vortices usually grow in size when increasing flow rate until reaching an unstable regime where the flow becomes non-stationary. The precise flow pattern depends critically on the exact experimental conditions such as the contraction geometry (axisymmetric, planar, square-square), the contraction ratio, the flow rate and the rheology of the liquid (Boger & Walters, 2012).

Melt fracture

After contraction, the liquid flows through a thin tube (axisymmetric) or a thin slot (planar) which can be long or short (a few millimetres for a syringe) before final release. The free-surface of the resulting jet (axisymmetric) or sheet (planar) often presents some irregularities, unwanted in industrial processes. Small surface defects (referred to as "sharkskin" or "loss of gloss") typically appear during extrusion of thick melts. These scratches are formed at the tube (or slot) outlet and are not related to upstream flow instabilities. On the other hand, the more severe distortions referred to as *melt fracture* are consequences of the non-stationary unstable flow patterns (jerky pulsations) developing at the contraction upstream of the tube (or slot) inlet above some critical flow rate (Piau et al., 1990) (see figure 2.14.a). Recent publications also suggest that melt fracture may be due to a nonlinear subcritical instability of the viscoelastic Poiseuille flow in the tube (or slot) initiated by perturbations of finite amplitude (Bertola et al., 2003; Morozov & van Saarloos, 2007). Figures 2.14.b and 2.14.c show the narrow vertical grooves formed on the surface of a sheet of polymer solution extruded from a slot (b) and the non-stationary wide vertical stripes appearing at larger flow rates (c). Both types of irregularities can be observed on the same sheet.

Chapter 3

Material and Methods

Contents

In this chapter, we first present the experimental set-up used in curtain experiments. The experimental results associated with this set-up will be shown in chapters 4 and 5. After describing the preparation of polymer solutions, we introduce the hydraulic loop and the slot die used to produce liquid curtains. Then we present the flow visualisation technique used to measure the curtain velocity field $U(z)$. Next, we turn our attention to the rheological characterisation of the polymer solutions, both in shear and extensional flows. This is followed by a general discussion on the different rheological parameters and by a discussion on the protocols which are adapted to solve the issue of mechanical degradation of the polymer molecules in the hydraulic loop.

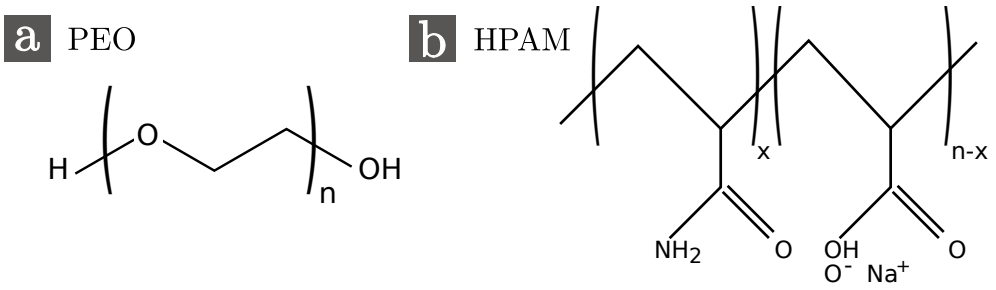

Figure 3.1 – Chemical structure of PEO (a) and of HPAM (b).

3.1 Experimental set-up

In this section, we present the experimental set-up used in curtain experiments.

3.1.1 Polymers and sample preparation

Experiments are performed with aqueous solutions of two high molecular weight polymers with different rheological behaviours. For each curtain experiment, a total mass $M_s = 5$ kg of solution is required.

We use solutions of polyethylene oxide (PEO) with an average molecular weight $M = 8 \times 10^6$ g/mol. Its chemical structure is shown in figure 3.1.a. The solvent is a Newtonian aqueous solution of polyethylene glycol (PEG) which has the same chemical structure but has a lower average molecular weight $M = 8000$ g/mol. PEG is used as a thickener, as proposed by Dontula et al. (1998); Becerra & Carvalho (2011); Karim et al. (2018b). Both polymers are provided by Sigma-Aldrich (references 372838 and P2139). In most solutions, the PEG concentration is [PEG] = 20 wt% (the mass of PEG represents 20% of the total mass of the solution) and the corresponding solvent viscosity is $\eta_s = 0.017$ Pa.s. The PEO concentration ranges between 0 (pure solvent) and 0.4 wt%. A 5 kg solution is prepared by first adding the desired mass of PEO (20 g for a 0.4 wt% PEO concentration) to 3 kg of pure water. To avoid agglomeration, the granular polymer particles are slowly added in the vortex created by a mechanical stirrer which is then used during 15 hours to ensure homogeneous mixing. Finally, another solution of 1 kg of PEG and 1 kg of water is prepared and the two solutions are mixed. The final solution is shaken for about two hours before use. Following a similar protocol, other solutions are prepared with a higher PEG concentration [PEG] = 40 wt%. The corresponding solvent viscosity is $\eta_s = 0.14$ Pa.s.

We also use solutions of partially hydrolysed polyacrylamide (HPAM), a polyelectrolyte commonly used in oil recovery provided by SNF Floerger (ref Floset 130 VG).

Molecular weight is estimated to be around $M = 15 - 20 \times 10^6$ g/mol and the hydrolysis degree is close to 30 %. At equilibrium in water, HPAM molecules are swollen due to repulsive electrostatic charges along the chain backbone and behave as semi-rigid rods, in contrast to PEO molecules which behave as flexible coils. HPAM rigidity can be tuned by adding salt to the solution. As salt is added, the repulsive interactions are screened and HPAM molecules become more flexible, i.e. their radius of gyration decreases (Chen et al., 2012; Zhang et al., 2008). This property has been used by author authors such as Cartalos & Piau (1992) and Kawale et al. (2017). In order to investigate the influence of polymer conformation on the curtain flow, we use aqueous solutions of fixed polymer concentration [HPAM] = 0.1 wt% and various salt concentrations [NaCl] ranging between 0 and 10 wt%. A 5 kg solution is prepared by adding 5 g of HPAM powder to 5 kg of pure water and shaking for 15 hours to ensure homogeneous mixing. The desired mass of salt is finally added and the final solution is shaken for a few minutes before use. The solvent viscosity is $\eta_s = 0.001$ Pa.s. Of course, when adding salt, the exact HPAM mass fraction changes since, for example, solutions referred to as 0.1 wt% HPAM solution with 1 wt% salt contain in fact 5 g of HPAM and 50 g of salt dissolved in 5 kg of water, i.e. [HPAM] = 0.099 wt% and [NaCl] = 0.99 wt%. Similarly, for the HPAM solutions referred to as 0.1 wt% HPAM solution with 10 wt% salt, the real concentrations are [HPAM] = 0.091 wt% and [NaCl] = 9.1 wt%. For simplicity, the designation of the solutions will not take this deviation into account.

As will be commented in §3.2.5, mechanical degradation occurs during shaking, as is expected from the use of a mechanical stirrer which is a high shear-rate mixing technique. Polymer chains break, resulting in a lower average molecular weight. Hence, the rheological behaviour of any newly prepared solution has to be characterised independently.

For a given solvent, density ρ and surface tension Γ, which is measured by a pendant drop method (Daerr & Mogne, 2016), were found not to depend on polymer concentration. However, it depends on PEG concentration. Values are

- $\rho = 1000$ kg/m^3 and $\Gamma = 72$ mN/m for HPAM solutions.
- $\rho = 1026$ kg/m^3 and $\Gamma = 62$ mN/m for PEO solutions (20 wt% PEG solvent).
- $\rho = 1070$ kg/m^3 and $\Gamma = 53$ mN/m for PEO solutions (40 wt% PEG solvent).

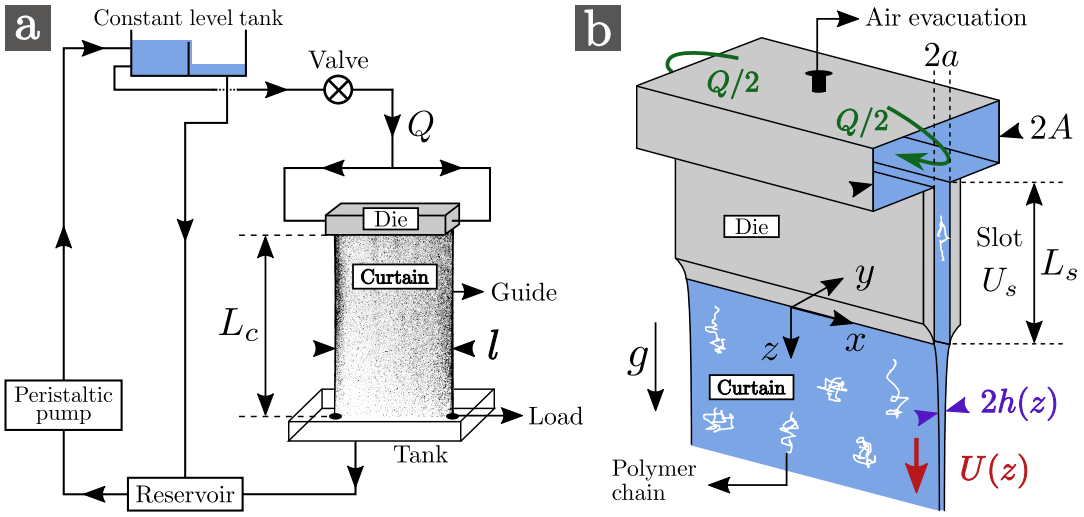

Figure 3.2 – Schematic of the hydraulic loop (a) and of the slot die (b).

3.1.2 The hydraulic loop

Most of the curtain experiments were conducted with the hydraulic loop sketched in figure 3.2.a. The polymer solution is pumped from a reservoir with a peristaltic pump up to a constant level tank, from which it flows down to a slot die by gravity. The liquid then falls vertically from the slot down to a tank, forming a rectangular curtain of width $l = 14.5$ cm and length L_c ranging between 15 cm and 200 cm. To avoid sheet retraction due to surface tension, the liquid is guided between two wires (cooking strings) held vertically with loads on the tank surface. The liquid then flows back to the reservoir, thus closing the loop.

The liquid mass flow rate Q feeding the die is controlled by a valve and is measured directly by weighing. Q is lower than the flow rate imposed by the pump, and the liquid excess flows directly from the constant level tank to the reservoir. This ensures that the liquid level, and therefore the flow rate, does not vary with time. The constant level tank is about 2 metres above the die. When the valve is completely open, it allows flow rates up to 80 g/s which is the maximum achievable water flow rate of the peristaltic pump. We define the linear flow rate (volumetric flow rate per unit width) as

$$q = \frac{Q}{\rho\, l} \tag{3.1}$$

The pulsations caused by the peristaltic pump vanish when the liquid enters the constant level tank. This ensures that the die is fed by a stationary flow. Note that the choice of a peristaltic pump, less convenient than a gear pump, was originally motivated by the constrain of minimising polymer mechanical degradation through

the hydraulic loop.

3.1.3 The die

In figure 3.2.b we present the geometry of the slot die. The liquid enters on both sides of a hollow box of width $2A = 14$ mm and then flows through a slot of length $L_s = 10$ cm, width l and thickness $2a = 1$ mm. The contraction ratio is $A/a = 14$. The air inside the die is evacuated using a small hole on top of the box. Once the die is full of liquid, the hole is closed with a screw.

The slot consists of two flat walls which were carefully designed to ensure a constant separation distance. The wall edges are bevelled to prevent any wetting of the liquid when leaving the slot. The initial curtain thickness $2h(z = 0)$ is thus expected to be equal to $2a$. Equivalently, the initial mean velocity of the curtain at the slot exit $U_0 \equiv U(z = 0)$ is expected to be equal to the mean velocity in the slot defined as $U_s = q/2a$.

3.1.4 Flow visualisation

We measure the velocity field of the curtain in the $x - z$ plane using the particle image velocimetry (PIV) technique. Polymer solutions are seeded with polyamid solid particles (PSP) of diameter 50 μm and density 1.03 g/cm^3 (provided by Dantec Dynamics) at a concentration of 0.04 wt% corresponding to a volume fraction of 4×10^{-4}. We have checked that these tracers had no influence on the rheology of the solutions. A large-angle objective is mounted on a high-speed camera which records pictures of the curtain at typically 600 frames per second with a typical spatial resolution of 60 pixels per centimetre. A typical exposire time is 500 μs. The curtain is illuminated with a white continuous light source and cross-correlation is computed over windows of size 16×16 pixels, i.e. typically 2.7×2.7 mm. Note that, due to the finite size of the PIV correlation windows and to some light reflections at the slot exit, the first value $U_1 = U(z_1)$ of the velocity field is measured at a distance $z = z_1 \approx 2.5$ mm below the slot exit. Note that we do not measure the y dependence of the flow field with the technique described in this section.

In figure 3.3.a, we show a superposition of eleven successive curtain images for a 0.2 wt% PEO solution with 20 wt% PEG solvent. Note that the falling velocity decreases down to 0 when approaching the vertical immobile guides (not visible in figure 3.3.a). This is the consequence of a boundary layer developing along the flow direction. For all the PEO and HPAM solutions used in this manuscript, curtains

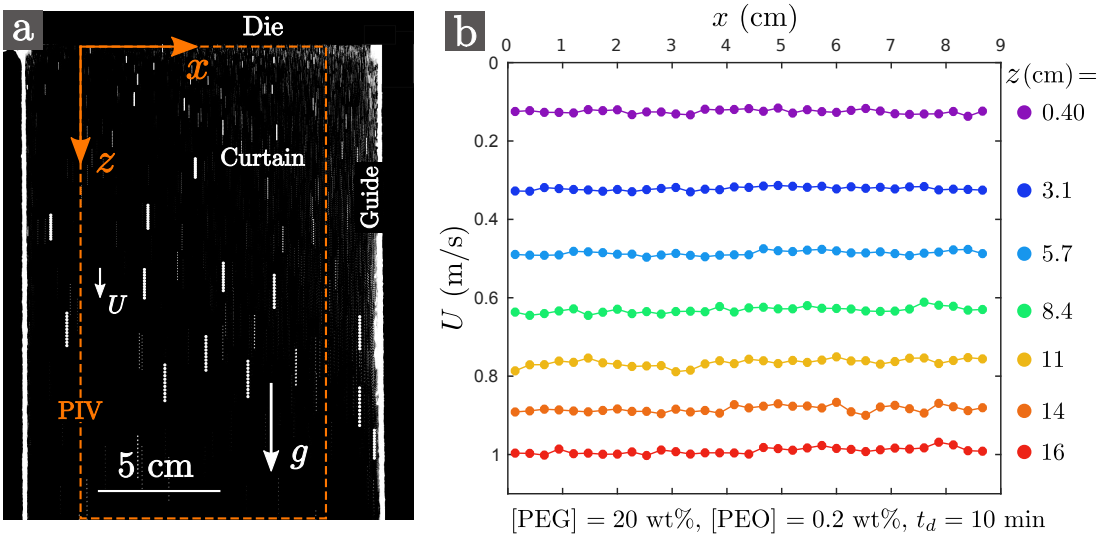

Figure 3.3 – Example of PIV measurement for a 0.2 wt% PEO solution with 20 wt% PEG solvent after ten minutes in the hydraulic loop. (a): Superposition of eleven successive PIV images where some tracers are highlighted for clarity. Due to edge effects, the correlation algorithm is applied to a domain restricted to the dashed rectangle. (b): z-component of the velocity field, i.e. $U(x, z, t)$, against the horizontal coordinate x at different distances z from the slot at an arbitrary time t. The curtain length is $L_c = 30$ cm and the linear flow rate is $q = 2.3$ cm^2/s.

are only affected within less than 2 cm from the guides at the maximum distance from the slot in the camera field, i.e. typically at $z = 20$ cm from the slot. Therefore, the image correlation algorithm is applied to a domain restricted to the central region where the flow is not affected by this edge effect (see the dashed rectangle in figure 3.3.a). This effect is much more pronounced for highly viscous Newtonian liquids. For example, we measure that the boundary layer reaches a size of about 4 cm at $z = 20$ cm for pure glycerin ($\eta \approx 1$ Pa.s), and invades the whole curtain at $z = 10$ cm for honey ($\eta \approx 10$ Pa.s). In the latter case, the velocity field $U(x, z)$ approaches a parabolic shape, i.e. a Poiseuille-like flow in which vertical wires play the role of rigid walls. Such boundary layers are also reported by Karim et al. (2018a) for Newtonian liquids.

Once a curtain is established, images of the flow are recorded during 2 seconds. An example of velocity field obtained by processing a pair of successive images is given in figure 3.3.b for a 0.2 wt% PEO solution with 20 wt% PEG solvent. We measure that the x component of the velocity field is 0, as expected. Therefore, we plot the z component $U(x, z, t)$ against x for various distances z from the slot at an arbitrary time t. As expected, the flow is fairly independent of x. Therefore, U is averaged along x at each value of z. We obtain $\langle U \rangle_x$ which is a function of z and t. Repeating this procedure for different image pairs shows that flow is

stationary. Therefore, $\langle U \rangle_x$ is averaged over 40 image pairs, equally spaced in time, and we finally obtain $U(z) \equiv \langle \langle U \rangle_x \rangle_t$. The curtain flow is stationary and translation invariant along x for most of the data presented in this manuscript. However, some exceptions are observed, as will be investigated in a separate section for clarity (see §4.1.2).

3.1.5 The accessible ranges of flow rates

For a given liquid, the maximum accessible flow rate Q_{max} feeding the die (when the valve is completely open) can either be determined by the maximum flow rate achievable by the pump (for this liquid) or by the dissipation in the slot. In the latter case, we observe that Q_{max} decreases when increasing the polymer concentration since the liquid viscosity increases. Besides, since the polymer molecules undergo a rapid strain at the slot entrance, an extra "pressure drop" can arise due to the stretching of polymer molecules, as shown by Rothstein & McKinley (1999) in the case of an axisymmetric contraction. On the other hand, the die needs to be fed with a minimum flow rate Q_{min} to prevent breaking of the sheet. We observe that Q_{min} decreases with increasing the polymer concentration, as will be discussed in §5.1. The resulting range of accessible flow rates $Q_{min} - Q_{max}$ goes from $5 - 10$ g/s for large polymer concentrations to $20 - 80$ g/s for low polymer concentrations. In the latter case, the convenient range of flow rates for flow visualisation is closer to $50 - 80$ g/s since many holes may open in the curtain at low flow rates.

For these reasons, the experiments presented in this manuscript are performed with flow rates Q ranging from 6 g/s for large polymer concentrations to 60 g/s for low polymer concentrations, i.e. the mean velocity $U_s = q/2a$ in the slot ranges between 0.04 m/s and 0.4 m/s.

3.2 Rheology of the polymer solutions

In this section, we present two distinct series of shear and extensional rheology measurements. First, in order to characterise the polymer solutions, we performed purely rheological measurements on various PEO solutions with 20 wt% PEG solvent and on 0.1% HPAM solutions with various salt concentrations at $T = 20°C$. The PEO solutions are obtained by dilution of a 0.2 wt% stock solution (except for 0.3 and 0.4 wt% solutions which are prepared independently) while HPAM solutions were obtained by addition of different salt weight fractions to samples of a 0.1 wt% HPAM stock solution. The rheological characterisation of these solutions are presented in §3.2.1, 3.2.2, 3.2.3 and 3.2.4. Then, the rheological characterisation of the specific

5 kg solution used in curtain experiments (including PEO solutions with 40 wt% PEG solvent) will be commented separately in §3.2.5.

3.2.1 Shear rheology

General principles of shear rheology

We explain how to measure experimentally the apparent shear viscosity $\eta \equiv \sigma_{12}/\dot{\gamma}$ and the first normal stress difference $N_1 \equiv \sigma_{11} - \sigma_{22}$ of a viscoelastic liquid using a shear rheometer (see notations of §2.3.2). The idea is to produce a shear flow of homogeneous shear rate and to measure the resulting torque and normal force. A common technique for producing a shear flow consists of placing the liquid between two close surfaces, one rotating at a constant angular velocity while the other is immobile.

Among the various existing geometries, we present here the cone-plate geometry schematically shown in figure 3.4. A few drops of liquid are placed at the centre of the plate before a cone of radius R_1 and angle θ_1 is placed at the appropriate vertical position where its fictional tip touches the plate. The tip of the cone is cut and the minimum distance e_1 separating the cone from the plate to avoid solid friction is called the truncation gap. The space below the cone has to be completely filled with liquid. The shear flow is produced by having the plate (or the cone) rotating at angular velocity Ω. The direction of the flow is the direction perpendicular to figure 3.4 and the direction of velocity gradient is the vertical direction. If the gap between the two surfaces is sufficiently small, i.e. if $\theta_1 \ll 1$, the flow between the cone and the plate is laminar at low angular velocities. At a distance r from the symmetry axis, the velocity of the plate is Ωr and the cone-plate gap is $r \tan\theta_1$. Therefore, the shear rate is homogeneous and writes

$$\dot{\gamma} = \frac{\Omega}{\tan\theta_1} \approx \frac{\Omega}{\theta_1} \tag{3.2}$$

The cone is equipped with sensors measuring the torque T and the normal (vertical) force F_z. The torque can be expressed as a function of the shear stress $\sigma_{12} = \eta(\dot{\gamma})\dot{\gamma}$ (which is also homogeneous) and of geometrical parameters. Assuming that $\theta_1 \ll 1$, it writes

$$T \approx \int_0^{R_1} \int_0^{2\pi} \sigma_{12}\, r^2\, \mathrm{d}\varphi\, \mathrm{d}r = \frac{2\pi R_1^3}{3}\, \sigma_{12} \tag{3.3}$$

A shear rheometer has a minimum measurable torque T_{min}. Hence, experimental data are only meaningful if $T > T_{min}$. Using equation 3.3 and $\sigma_{12} = \eta\dot{\gamma}$, this

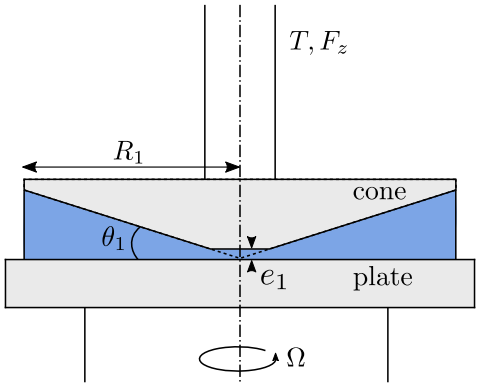

Figure 3.4 – Schematic representation of a cone-plate shear rheometer.

condition becomes

$$\eta > \eta_{min} = \frac{3T_{min}}{2\pi R_1^3 \dot{\gamma}} \propto \dot{\gamma}^{-1} \tag{3.4}$$

Concerning the normal force F_z, we can show that it is directly related to the first normal stress difference N_1, and is independent of the second normal stress difference N_2. Calculation gives (Oswald & Saint-Jean, 2005)

$$N_{1,tot} = \frac{2F_z}{\pi R_1^2} \tag{3.5}$$

However, as shown by Macosko (1994), the raw data has to be corrected by inertial effects which tend to pull the plates together. This has been shown by Lindner (2000) (page 72) who obtained negative values $N_{1,tot} < 0$ (instead of the expected 0 value) when measuring the first normal stress difference of water for shear rates $\dot{\gamma} \geq 10^3$ s^{-1}. We use the usual correction

$$N_1 = \frac{2}{\pi R_1^2}\left(F_z + 0.075\pi\rho\Omega^2 R_1^4\right) = N_{1,tot} + 0.15\rho\Omega^2 R_1^2 \tag{3.6}$$

As explained by Ewoldt et al. (2015), secondary flows and instabilities are ultimately generated at large shear rates. Hence, the flow is no longer laminar and one can no longer use equation 3.2, 3.3 and 3.6. These instabilities can either be inertial (large Reynolds number) or elastic (large Weissenberg number).

Shear rheology results

We now present shear rheology measurements performed on PEO solutions (with 20 wt% PEG solvent) and HPAM solutions. We use a strain-controlled rheometer (ARES-G2) from TA Instruments equipped with a cone-plate geometry of radius $R_1 = 25$ mm, angle $\theta_1 = 0.04$ rad and truncation gap $e_1 = 0.055$ mm. Temperature is controlled by a Peltier device. We measure the apparent shear viscosity $\eta = \sigma_{12}/\dot{\gamma}$

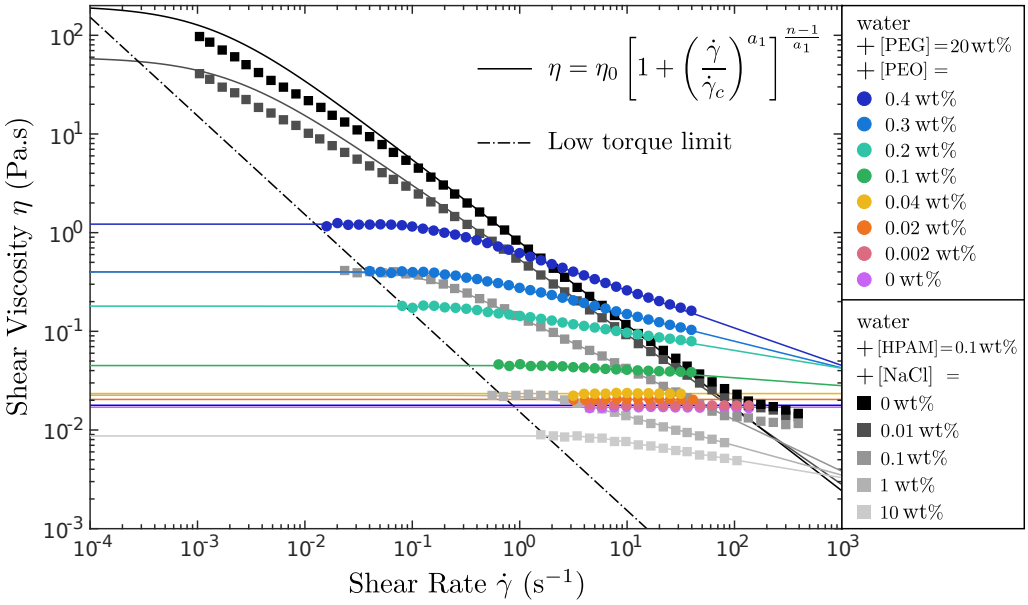

Figure 3.5 – Shear viscosity $\eta(\dot{\gamma})$ for PEO solutions with 20 wt% PEG solvent and for HPAM solutions at $T = 20°C$. Data are fitted with a Carreau law (equation 3.7). The low-torque limit is shown.

as well as the first normal stress difference $N_1 = \sigma_{11} - \sigma_{22}$. Note that it was impossible to perform satisfying small amplitude oscillatory shear (SAOS) measurements due to low solution viscosity, as also reported by other authors (Rodd et al., 2005; Oliveira et al., 2006).

We now detail the measurement protocol for measuring the apparent shear viscosity $\eta(\dot{\gamma})$. The shear rate $\dot{\gamma}$ is first increased from 10^{-3} s^{-1} to $\dot{\gamma}_{max}$, typically 100 s^{-1}, and then decreased. The overlap of both data sets indicates negligible degradation at high shear rates. Measuring $\eta(\dot{\gamma})$ for a given value of $\dot{\gamma}$ requires a minimum sampling time of 10 s to ensure steady state is achieved. $\dot{\gamma}_{max}$ is chosen to be close to the shear rate marking the onset of elastic instabilities where apparent shear-thickening is observed (Larson, 1992). Unstable data are removed. We also remove the data below the minimum measurable torque $T_{min} = 0.5$ μN.m using equation 3.4. Results are presented in figure 3.5. Since the second Newtonian plateau is not accessible by our measurement method (it is beyond the onset of the elastic instabilities), shear viscosity is fitted by a Carreau law where $\eta_\infty = 0$ (see equation 2.41). It writes

$$\eta = \eta_0 \left[1 + \left(\frac{\dot{\gamma}}{\dot{\gamma}_c}\right)^{a_1}\right]^{\frac{n-1}{a_1}} \tag{3.7}$$

where η_0 is the zero-shear viscosity, $\dot{\gamma}_c$ is the shear rate at which shear-thinning starts, a_1 is an exponent that encodes the sharpness of the transition and n is the

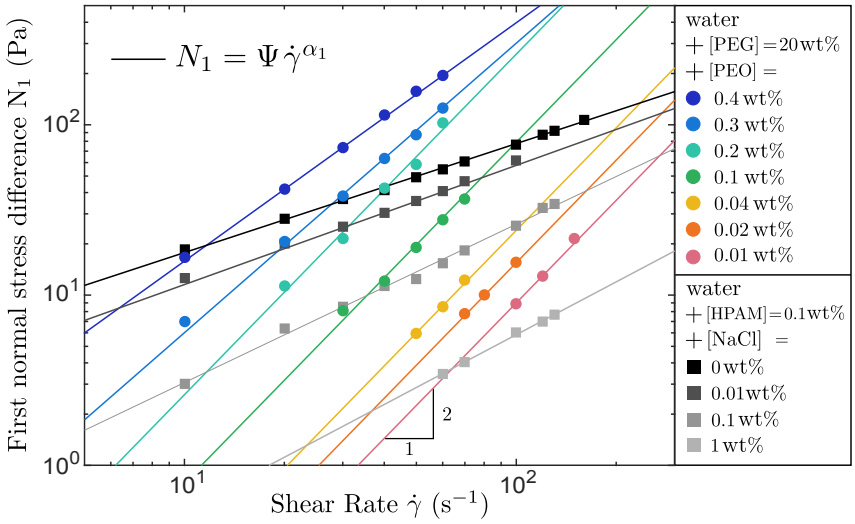

Figure 3.6 – First normal stress difference $N_1(\dot{\gamma})$ for PEO solutions with 20 wt% PEG solvent and for HPAM solutions at $T = 20°C$. Data are fitted with a power law (equation 3.8).

degree of shear thinning. a_1 is always close to 2 and other parameters are presented in table 3.1.

PEO solutions with 20 wt% PEG solvent have a constant shear viscosity ($n = 1$) up to [PEO]= 0.04 wt% beyond which shear thinning appears. Shear thinning behaviour is much more pronounced for unsalted HPAM solutions, i.e. when polymer chains are semi-rigid, with $n = 0.16$ for [NaCl]= 0 wt%. The degree of shear thinning is drastically reduced when adding salt. Note that fitting with a Carreau law fails for [NaCl]= 0 wt% and 0.01 wt% and that the Newtonian plateau is beyond the low-torque limit of the rheometer. Therefore, the corresponding values of η_0 reported in table 3.1 are merely orders of magnitude.

Normal stress measurements are performed using a specific step-by-step protocol similar to Casanellas et al. (2016) to circumvent the instrumental drift of the normal force. Each step consists in imposing a given step shear rate $\dot{\gamma}$ and then imposing a zero shear rate. Subtracting the two plateau values of the first normal stress difference gives access to the real value of $N_1(\dot{\gamma})$ after removing the contribution of fluid inertia to the normal force (equation 3.6). Results are presented in figure 3.6. Normal stress measurements are restricted to a narrow range of shear rates due to the limited resolution of the rheometer and to the onset of elastic instabilities at large shear rates. These instabilities are detected by rapid growth of both the first normal stress difference and the shear stress over time (Larson, 1992). No measurements are possible for solutions exhibiting no measurable values of N_1 below the onset of

elastic instabilities.

The data can be fitted with a power law within the measurement window

$$N_1(\dot{\gamma}) = \Psi \dot{\gamma}^{\alpha_1}. \tag{3.8}$$

Values of Ψ and α_1 are reported in table 3.1. We find $\alpha_1 = 2$ for most PEO solutions, except for the two largest concentrations. This result is consistent with the Oldroyd-B constitutive model which predicts $N_1 = 2\eta_p \tau \dot{\gamma}^2$ where τ is the relaxation time and $\eta_p = \eta_0 - \eta_s$ is the polymer contribution to the zero-shear viscosity. Therefore, when $\alpha_1 = 2$, we can define a shear relaxation time $\Psi/2\eta_p$. We also mention the more general definition $N_1/(2(\eta - \eta_s)\dot{\gamma}^2)$ which is shear rate dependent for shear-thinning solutions exhibiting a non quadratic first normal stress difference.

Note that N_1 decreased when adding salt to a HPAM solution, although chains become more flexible. This can be explained by the fact that normal stresses arise due to both single chain deformability and chain-chain interactions and that salt addition reduces the radius of gyration of the HPAM chains (Chen et al., 2012; Zhang et al., 2008), thus resulting in lower chain-chain interactions.

3.2.2 Extensional rheology

General principles of extensional rheology

Since the curtain flow is an extensional flow, we performed extensional rheology measurements. We now explain how to measure experimentally the (extensional) relaxation time and the (terminal) extensional viscosity of a viscoelastic liquid. In order to produce an extensional flow, we use the well documented filament thinning technique described by Anna & McKinley (2001). This rheometer is known in the literature as a Capillary Breakup Extensional Rheometer (CaBER). This technique is known to allow measurements of the relaxation time of very dilute polymer solutions for which neither N_1 nor SAOS measurements are accessible with a classical shear rheometer. For this reason, it has become a standard technique and is now used by many authors. A typical protocol is the following. A droplet of liquid is placed between two horizontal plates, like a drop of saliva between thumb and index. The lower plate is kept fixed and the upper plate is slowly moved upwards until the liquid bridge starts necking, at which time the plate motion is stopped (details are given later). The filament connecting the two end drops undergoes a succession of thinning regimes until final breaking. This is shown schematically in figure 3.7. The filament thinning process is recorded in order to measure the filament radius

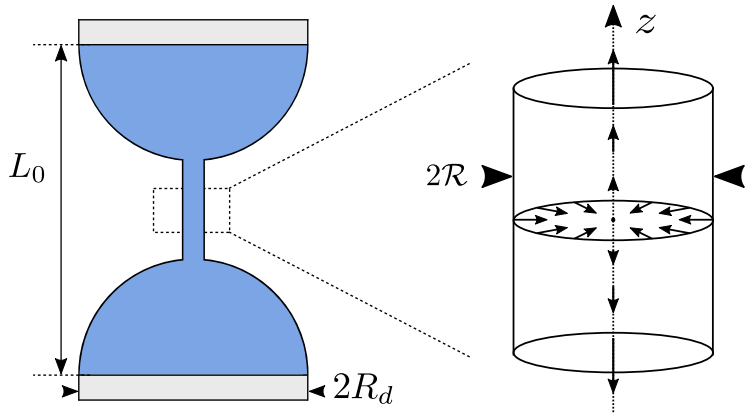

Figure 3.7 – Schematic representation of a thinning cylindrical filament.

profile $\bar{\mathcal{R}}$ at a function of time t. As shown in the following, many useful rheological information can be extracted from this experimental signal.

A global picture of the filament thinning process of complex fluids can be found in the review article published by McKinley (2005). When separating the two plates by a distance L_0, the liquid bridge (or filament) becomes unstable above a critical separation distance L_0^* where is starts necking due to capillary pressure. In dimensionless terms, the necking instability starts when reaching a critical aspect ratio $\Lambda^* = L_0^*/2R_d$ where R_d is the maximum radius of the end drops. The filament radius profile $\bar{\mathcal{R}}(z,t)$ is a function of altitude z and is not rigorously symmetric due to gravitational sagging. However, this gravitational effect is usually negligible in CaBER experiments. Hence, the altitude corresponding to the minimum filament radius is almost at the centre of the filament. This altitude is now our reference $z = 0$. We introduce the minimum filament radius $\bar{\mathcal{R}}(0,0) = \mathcal{R}_0$ at the onset of the necking instability (at time $t = 0$). Throughout the filament thinning process, this altitude corresponds to the stagnation point of a three-dimensional extensional flow. Due to capillary pressure, the liquid contained in the filament flows towards the two end drops, as shown in figure 3.7.

For slender filaments (i.e. filaments for which $\partial\bar{\mathcal{R}}/\partial z \ll 1$), mathematical analysis are often simplified by neglecting axial curvature and writing a simplified force balance equation for the minimum filament radius $\mathcal{R}(t) = \bar{\mathcal{R}}(z = 0, t)$. In this context, the extensional flow has an axial component $u_z = \dot{\epsilon} z$ and radial component $u_r = -0.5\,\dot{\epsilon} r$ where $\dot{\epsilon}$ is the extension rate. Since $u_r(r = \mathcal{R}, t)$ must be equal to $\dot{\mathcal{R}} = \mathrm{d}\mathcal{R}/\mathrm{d}t$, we get

$$\dot{\epsilon} = -\frac{2\,\dot{\mathcal{R}}}{\mathcal{R}} \tag{3.9}$$

One way of quantifying the total elongation of a fluid element after the filament has necked down to a size $\mathcal{R}$ is to use the logarithmic strain or *Hencky strain* defined as

$$\epsilon(t) \equiv \int_0^t \dot{\epsilon}(t^*)\mathrm{d}t^* = -2\ln\left(\frac{\mathcal{R}(t)}{\mathcal{R}_0}\right) \tag{3.10}$$

Taking into account inertial, capillary, viscous and elastic forces, the force balance equation writes (Tirtaatmadja et al., 2006)

$$\frac{1}{2}\rho\dot{\mathcal{R}}^2 \approx \frac{F_{ax}}{\pi\mathcal{R}^2} - \frac{\Gamma}{\mathcal{R}} - 3\eta_s\dot{\epsilon} - (\sigma_{p,zz} - \sigma_{p,rr}) \tag{3.11}$$

where ρ and Γ are the density and surface tension of the liquid, η_s is the solvent viscosity, $\sigma_{p,zz} - \sigma_{p,rr}$ is the polymeric normal stress difference, and F_{ax} is the axial tensile force in the filament. In CaBER experiments, since there is no external stretching (contrary to fibre-spinning-like experiments for example), this force F_{ax} is the force $2\pi\mathcal{R}\Gamma$ acting at the junction of the filament with the two end drops. Hence, equation 3.11 writes

$$\frac{1}{2}\rho\dot{\mathcal{R}}^2 \approx \frac{\Gamma}{\mathcal{R}} - 3\eta_s\dot{\epsilon} - (\sigma_{p,zz} - \sigma_{p,rr}) \tag{3.12}$$

Regardless of the liquid used, the first stage of the necking process (just after reaching the instability threshold L_0^*) corresponds to the exponential growth of small perturbations. According to Clanet & Lasheras (1999) and to Clasen et al. (2009), the minimum bridge radius follows $\mathcal{R}/\mathcal{R}_0 = 1 - e^{-t/\tau^*}$ where τ^* is a characteristic time scale. However, as the filament radius decreases, the dynamic of the thinning process becomes independent of the initial radius $\mathcal{R}_0$ and converges towards a self-similar behaviour with no characteristic length scale. In the following, we discuss the self-similar solutions in the case of Newtonian and viscoelastic liquids.

Newtonian liquids For a Newtonian liquid of viscosity η, close to filament breakup, two different behaviours can be observed depending on the relative importance of inertia and viscosity. When comparing the inertial (Rayleigh) time scale $(\rho\mathcal{R}^3/\Gamma)^{1/2}$ to the viscous time scale $\eta\mathcal{R}/\Gamma$, we can build the Ohnesorge number

$$Oh = \frac{\eta}{(\rho\mathcal{R}\Gamma)^{1/2}} \tag{3.13}$$

Note that Oh^2 can be seen as an inverse Reynolds number based on the capillary velocity Γ/η. If inertia overcomes gravity ($Oh \ll 1$), the force balance equation 3.12 reduces to $0.5\rho\dot{\mathcal{R}}^2 \approx \Gamma/\mathcal{R}$. On the other hand, if viscosity overcomes inertia ($Oh \gg 1$), the force balance equation 3.12 reduces to $3\eta\dot{\epsilon} \approx \Gamma/\mathcal{R}$. Therefore, the respective inertio-capillary and visco-capillary regimes write respectively

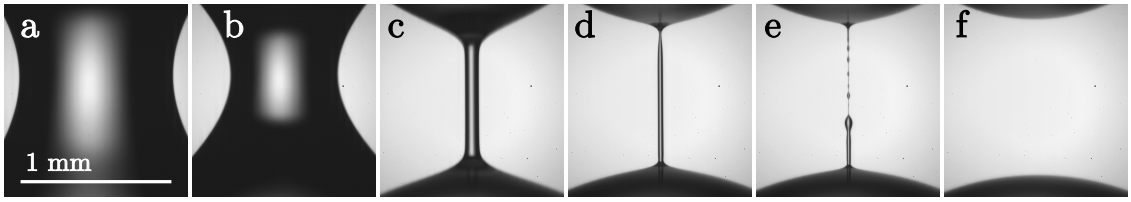

Figure 3.8 – Different stages of the thinning process of a filament made of a 0.01 wt% PEO solution with 20 wt% PEG solvent (raw images).

$$\mathcal{R}/\mathcal{R}_0 \propto \begin{cases} \left(\Gamma/\rho\mathcal{R}_0^3\right)^{1/3} (t_s - t)^{2/3} & \text{for} \quad Oh \ll 1 \\ \left(\Gamma/\eta\mathcal{R}_0\right)(t_s - t) & \text{for} \quad Oh \gg 1 \end{cases} \tag{3.14}$$

where t_s is the time at which the filament breaks (finite time singularity).

Viscoelastic liquids The end of the latter scenario is significantly altered when adding small amounts of high molecular weight polymer molecules to the liquid. A typical filament thinning sequence is shown in figure 3.8 for a 0.01 wt% PEO solution with 20 wt% PEG solvent. The slow exponential regime (stage a) is followed by a self-similar inertio-capillary ($Oh \ll 1$) or visco-capillary ($Oh \gg 1$) regime (stage between b and c) depending on the value of the Ohnesorge number which is now $Oh = \eta_0/(\rho\mathcal{R}\Gamma)^{1/2}$ where $\eta_0 = \eta_s + \eta_p$ is the zero-shear viscosity of the liquid. Then, the bridge abruptly switches to a slender filament shape at time $t = t_s$ (stage c). During this transition, elastic stresses become dominant due to the rapid stretching of polymer molecules, thus inhibiting the usual finite time singularity observed in Newtonian filaments (Amarouchene et al., 2001). During this elasto-capillary regime, this cylindrical filament (characteristic of viscoelastic liquids) thins following an exponential law. Numerical simulations using a FENE-P model (with elastic modulus G, relaxation time τ and finite extensibility parameter b) predict that the process is initially independent of the finite extensibility of the polymer chains. Therefore, predictions are initially similar to the prediction of an Oldroyd-B model. In both cases, the filament radius follows initially (McKinley, 2005; Rodd et al., 2004)

$$\frac{\mathcal{R}}{\mathcal{R}_0} \approx \left(\frac{G\mathcal{R}_0}{2\Gamma}\right)^{1/3} \exp\left(-\frac{t - t_s}{3\tau}\right) \tag{3.15}$$

Therefore, according to equation 3.9, the extension rate is initially constant and equal to

$$\dot{\epsilon} = \frac{2}{3\tau} \tag{3.16}$$

Using a multimode FENE-P model, Entov & Hinch (1997) showed that a more general analytical solution can be derived at "intermediate elastic times" (i.e. after viscous effects have become negligible and before finite polymer extensibility becomes important). For dilute solutions described by the Zimm model, Anna & McKinley (2001) showed that this solution is well approximated by equation 3.15 at "long" times when replacing τ by the terminal (longest) relaxation time of the spectrum. It means that the contribution of the higher modes rapidly decay and that all the elastic stress is ultimately carried by the mode corresponding to the longest relaxation time. Therefore, the regression of experimental data to equation 3.15 should give the Zimm longest time constant (Anna & McKinley, 2001).

The value $\tau\dot{\epsilon} = 2/3$ is larger than the coil-stretch transition value 1/2. Therefore, during this elasto-capillary regime, the polymer chains undergo progressive unravelling. The filament remains perfectly cylindrical since any localised pinching produces additional polymeric stresses which inhibits further pinching. However, when polymer chains have reached their full length, the extensional viscosity reaches a plateau value and the liquid behaves as a Newtonian liquid, allowing local pinching that typically occurs near the end drops (stage d). The filament then undergoes a Rayleigh-Plateau-like instability commonly referred to as "blistering instability" (Sattler et al., 2008, 2012; Eggers, 2014) where tiny drops are separated by micrometric sub-filaments (stage e). The simple one-dimensional force balance equation 3.12 becomes invalid. Besides, since finite extensibility effects are now important, the solution 3.15 is not valid anymore. Introducing the plateau value η_E of the extensional viscosity, the radii of sub-filaments follow $\mathcal{R} \propto (\Gamma/\eta_E)\,(t_b - t)$ where t_b is the time at which sub-filaments break (see equation 3.14). In this final regime, the extension rate $\dot{\epsilon}$ diverges towards infinity in finite time. After breaking, the two end drops are finally completely separated (stage f).

Using the force balance equation 3.12, one can estimate the normal stress difference $\sigma_{zz} - \sigma_{rr}$ in the filament. Indeed, in the elasto-capillary regime where inertia is negligible, we get

$$\frac{\Gamma}{\mathcal{R}} \approx 3\eta_s\dot{\epsilon} + (\sigma_{p,zz} - \sigma_{p,rr}) = \sigma_{zz} - \sigma_{rr} \tag{3.17}$$

where $\sigma_{zz} - \sigma_{rr} = (\sigma_{s,zz} - \sigma_{s,rr}) + (\sigma_{p,zz} - \sigma_{p,rr})$ and where $\sigma_{s,zz} - \sigma_{s,rr} = 3\eta_s\dot{\epsilon}$. Therefore, using equation 3.9, the *apparent extensional viscosity* defined as

$$\eta_{app} \equiv \frac{\sigma_{zz} - \sigma_{rr}}{\dot{\epsilon}} \tag{3.18}$$

can be estimated directly from experimentally measured quantities as

$$\eta_{app} \approx -\frac{\Gamma}{2\dot{\mathcal{R}}} \tag{3.19}$$

According to the FENE-P model described in §2.3.7 (see figure 2.5 for example), and since the extension rate diverges towards infinity near breaking, the apparent extensional viscosity is expected to reach an asymptotic value η_E called *terminal extensional viscosity* and given by

$$\eta_{app} \longrightarrow \eta_E = 3\eta_s + 2b\eta_p \tag{3.20}$$

where $\eta_p = \eta_0 - \eta_s$ by definition. In this expression, the value $b+3$ found in chapter 2 with the FENE-P model (see figure 2.5) is replaced by b in order to match the definition given by other authors (McKinley, 2005). Since we are mostly interested in the order of magnitude of b, this will have no consequences is later discussions.

Extensional rheology results

We have built a simple Capillary Breakup Extensional Rheometer (CaBER) which was used following the slow retraction method (SRM) described by Campo-Deano & Clasen (2010) in order to minimise the unwanted fluid inertia effects inherent to the classical step-strain plate separation protocol (Rodd et al., 2004). A droplet of liquid is placed between two horizontal plates of radius $R_d = 1.5$ mm (see figure 3.7). The lower plate is kept fixed and the upper plate is moved upward with a manual translation stage until the liquid bridge connecting the two end drops becomes unstable and starts necking. The initial and final plate separation distances are typically $L_{0,i} \approx 1.5$ mm and $L_{0,f} \approx 3.5$ mm, which gives initial and final aspect ratios $\Lambda_i = L_{0,i}/(2R_d) \approx 0.5$ and $\Lambda_f = L_{0,f}/(2R_d) \approx 1.2$ which is a bit larger than the critical aspect ratio Λ^*. The average rate of plate separation is 0.5 mm/s.

The filament connecting the two end drops undergoes a succession of thinning regimes until final breaking. The process is observed with a high magnification objective (allowing spatial resolution of 1 pixel per micrometre) mounted on a high-speed camera. Image processing gives access to the minimum filament radius $\mathcal{R}$ as a function of time t. Figure 3.9 displays the evolution of the filament radius $\mathcal{R}(t)$ for PEO solutions (with 20 wt% PEG solvent) and HPAM solutions along with raw filament images at four stages of thinning for one of the PEO solutions. Near breakup, $\mathcal{R}$ is the radius of the thinnest sub-filaments. Solutions are tested at room temperature $T = 20°$C.

Just after the transition to the elasto-capillary regime, we indeed observe an

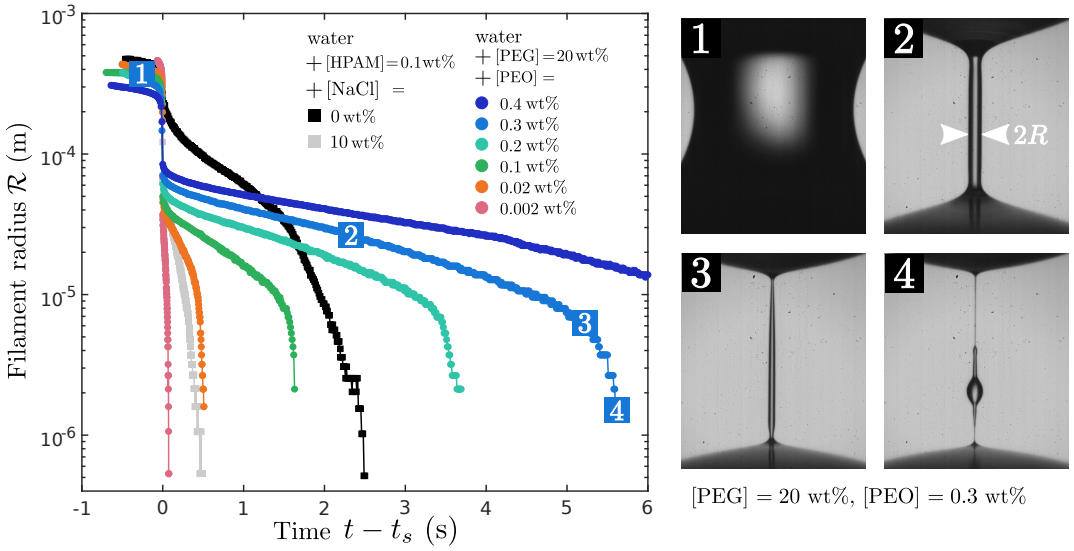

Figure 3.9 – Left: minimum filament radius $\mathcal{R}$ as a function of time $t - t_s$ where t_s marks the transition to the elasto-capillary (exponential) regime for PEO solutions with 20 wt% PEG solvent and for HPAM solutions at $T = 20°C$. Right: Four images of a filament of a 0.2 wt% PEO solution during the thinning process. These four steps are reported on the corresponding $\mathcal{R}(t)$ curve on the left.

exponential decrease of the filament radius. This regime is fitted by

$$\mathcal{R} \propto \exp\left(-t/3\tau_{fil}\right). \tag{3.21}$$

where we define τ_{fil} as the *extensional relaxation time* of the liquid. Repeating this experiment on different drops of the same liquid shows reproducible results for PEO and salted HPAM solutions. We checked that experimental parameters such as the rate of plate separation had no impact on the measured value of τ_{fil}, as also reported by Miller et al. (2009) for polymer solutions. However, unsalted HPAM solutions showed less reproducible results. One possible explanation is that solutions of rigid polymers are analogous to particle suspensions which are known to be affected by random fluctuations in the particle concentration along the filament (Mathues et al., 2015; McIlroy & Harlen, 2014). Values of τ_{fil} are reported in table 3.1 with a number of significant digits which reflects the precision of the measurement.

We show in figure 3.10 the apparent extensional viscosity η_{app} against the Hencky strain ϵ given by equations 3.19 and 3.10 respectively. Since the minimum measurable radius (before breaking) is 0.5 μm (1/2 pixel) and since the initial minimum bridge radius $\mathcal{R}_0$ (at the onset of the instability) is of order 0.4 mm, the maximum Hencky strain is $\epsilon_{max} = 13$. The plateau value η_E at large strains is estimated. Therefore, knowing η_0 and η_s from shear rheology measurements, we can use equation 3.20 as a definition for the finite extensibility parameter b, i.e.

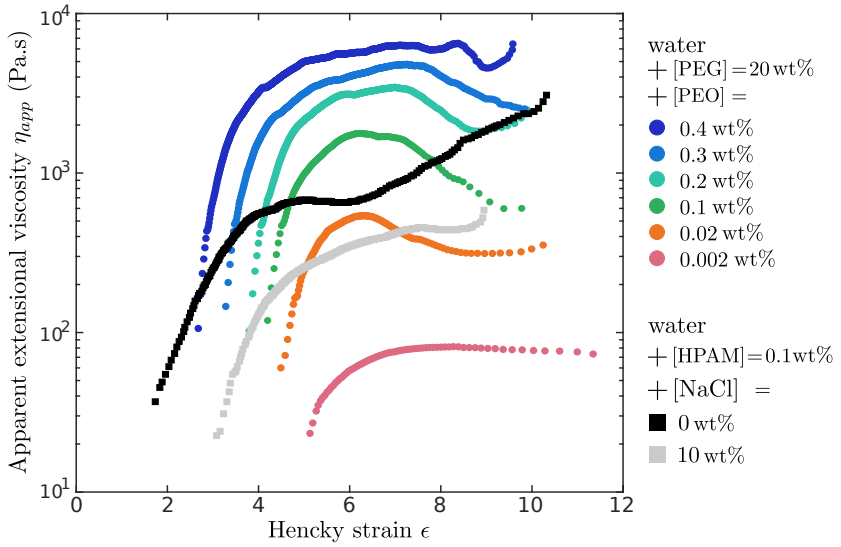

Figure 3.10 – Apparent extensional viscosity η_{app} (equation 3.19) as a function of the Hencky strain ϵ (equation 3.10) for PEO solutions with 20 wt% PEG solvent and for HPAM solutions at $T = 20°C$.

$$b \equiv \frac{\eta_E - 3\eta_s}{2(\eta_0 - \eta_s)} \tag{3.22}$$

Of course, for semidilute solutions, b has to be considered as an effective value since the FENE-P model does not take into account any chain-chain interaction. Values of η_E and b (calculated using equation 3.22) are reported in table 3.1. b ranges between 10^3 and 10^5 for flexible PEO and salted HPAM solutions but is only of order 10^0 - 10^1 for semi-rigid unsalted HPAM solutions.

3.2.3 Determination of the concentration regimes

For notation consistency, we introduce the other definition of polymer concentration $c = \rho\,[\mathrm{X}]$ (where X means PEO or HPAM) introduced in chapter 2 which is the polymer mass per unit volume, while [X] is the polymer mass fraction. Two methods can be used to determine the critical overlap concentration c^*.

Shear viscosity data In order to characterise the different concentration regimes of PEO solutions with 20 wt% PEG solvent, we show in figure 3.11.a the evolution of the polymer contribution to the zero-shear viscosity $\eta_p = \eta_0 - \eta_s$ with polymer concentration. The evolution is initially linear in the dilute regime and $\eta_p = \eta_s[\eta]c$ where $[\eta]$ is the intrinsic viscosity defined in equation 2.63. We measure $[\eta] = 0.93\ \mathrm{m^3/kg}$. Using the expression of the critical overlap concentration $c^* = 0.77/[\eta]$ by Graessley (1980), we obtain $c^* = 0.83\ \mathrm{kg/m^3}$ (equivalently 0.081 wt%). This value is consistent with the onset of shear-thinning behaviour, although the link

[PEG] wt %	[PEO] wt %	c/c^*	η_0 Pa.s	η_p Pa.s	n	$1/\dot{\gamma}_c$ s	α_1	Ψ Pa.s$^{\alpha_1}$	τ_{fil} s	η_E Pa.s	b
20	0.001	0.012	0.017	0.0002	1.0	-	-	-	0.005	3×10^1	1×10^5
20	0.002	0.025	0.017	0.0003	1.0	-	-	-	0.013	9×10^1	1×10^5
20	0.01	0.12	0.018	0.001	1.0	-	2	0.0009	0.070	4×10^2	1×10^5
20	0.02	0.25	0.020	0.003	1.0	-	2	0.0016	0.13	6×10^2	9×10^4
20	0.04	0.49	0.023	0.006	1.0	-	2	0.0024	0.19	1×10^3	8×10^4
20	0.1	1.2	0.045	0.028	0.92	0.36	2	0.0079	0.41	2×10^3	4×10^4
20	0.2	2.5	0.18	0.16	0.82	3.1	2	0.026	0.78	5×10^3	2×10^4
20	0.3	3.7	0.40	0.38	0.73	4.0	1.7	0.12	1.1	6×10^3	8×10^3
20	0.4	4.9	1.2	1.2	0.62	5.9	1.4	0.63	1.3	7×10^3	3×10^3
[HPAM] wt %	[NaCl] wt %	c/c^*	η_0 Pa.s	η_p Pa.s	n	$1/\dot{\gamma}_c$ s	α_1	Ψ Pa.s$^{\alpha_1}$	τ_{fil} s	η_E Pa.s	b
0.1	0	6.7	2×10^2	2×10^2	0.16	7×10^2	0.64	4.1	0.4	1×10^3	3×10^0
0.1	0.01	-	6×10^1	6×10^1	0.24	5×10^2	0.70	2.3	0.3	8×10^2	1×10^1
0.1	0.1	-	0.40	0.40	0.48	7.7	0.93	0.36	0.15	5×10^2	6×10^2
0.1	1	-	0.023	0.022	0.70	0.50	1.0	0.058	0.081	4×10^2	9×10^3
0.1	10	-	0.0087	0.0077	0.82	0.22	-	-	0.068	4×10^2	3×10^4

Table 3.1 – Rheological parameters of PEO solutions with 20 wt% PEG solvent (top) and salted (NaCl) HPAM solutions (bottom) at $T = 20°C$. Concentrations are in weight fraction. Shear parameters: η_0, n, $\dot{\gamma}_c$, α_1 and Ψ are such that the shear viscosity $\eta(\dot{\gamma})$ and the first normal stress difference $N_1(\dot{\gamma})$ are captured by equations 3.7 and 3.8 ($\dot{\gamma}_c$ is not measurable when $n = 1$ and N_1 is not always measurable). Values of c/c^* are shown, where $c = \rho\,[\mathrm{X}]$ (X means PEO or HPAM) and c^* is the critical overlap concentration which is $c^* = 0.83$ kg/m^3 for PEO solutions and $c^* = 0.15$ kg/m^3 for the unsalted HPAM solution. $\eta_p = \eta_0 - \eta_s$ where η_s is the solvent viscosity which is respectively 0.017 Pa.s (top) and 0.001 Pa.s (bottom). We use $\eta_p = \eta_s[\eta]c$ to determine η_p for the two smallest PEO concentrations (dilute regime) since the difference between η_0 and η_s is too small to be measured directly, where $[\eta] = 0.93$ m^3/kg is the intrinsic viscosity. Extensional parameters (CaBER): τ_{fil} is the extensional relaxation time and η_E is the terminal extensional viscosity. $b = (\eta_E - 3\eta_s)/(2\eta_p)$ is the effective value of the finite extensibility parameter.

"semidilute regime $\Leftrightarrow$ shear thinning" is far from obvious. After considering the FENE-P model (describing dilute polymer solution, i.e. $c < c^*$) in chapter 2, we already saw that finite extensibility is sufficient to lead to shear thinning behaviour even without chain-chain interaction, provided that the solvent viscosity does not "screen" intrinsic shear thinning (i.e. provided that S is not too close to 1, equation 2.30). However, shear-thinning is more likely to be observed in the semidilute regime since polymers are more likely to align along the flow and to "slide" on one another at large shear rates, thus exhibiting a lower resistance to the flow. Values of c/c^* are reported in table 3.1. Solutions are semi-dilute for $c > c^*$, as shown by the first slope change in figure 3.11.a. A second slope change is observed for the most concentrated

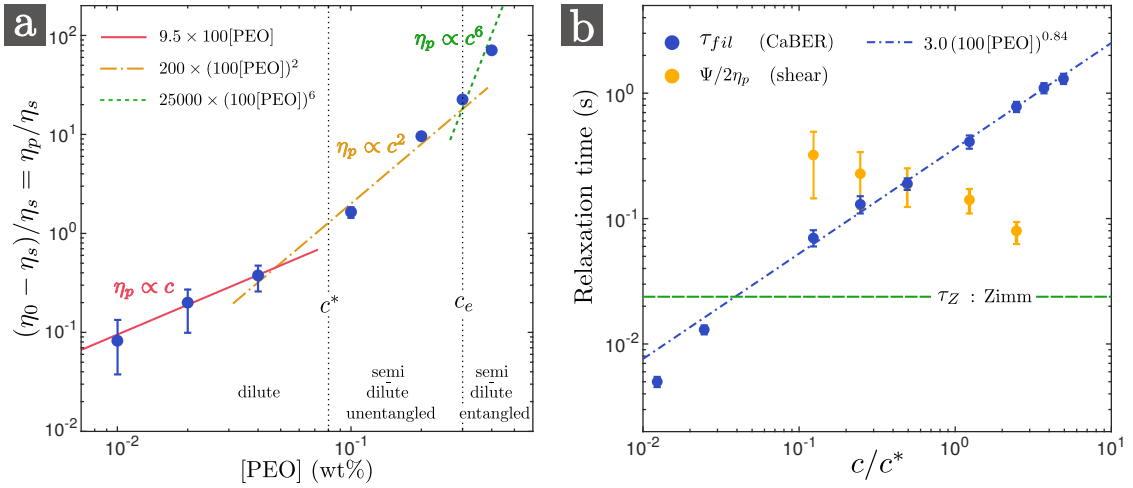

Figure 3.11 – Some data for the PEO solutions with 20 wt% PEG solvent of table 3.1. (a) Evolution of the polymer contribution to the zero-shear viscosity $\eta_p = \eta_0 - \eta_s$ (divided by the solvent viscosity η_s) with polymer concentration [PEO]. (b): Comparison of the different relaxation time estimations: $\Psi/2\eta_p$ (shear measurements for quadratic normal stress differences $N_1 = \Psi\dot{\gamma}^2$), τ_{fil} (CaBER) and $\tau_Z = 0.024$ s (Zimm theory, equation 2.81) against dimensionless polymer concentration c/c^* where $c = \rho$ [PEO] and $c^* = 0.83$ kg/m^3 is the critical overlap concentration.

solution, thus indicating a transition from the semi-dilute unentangled regime to the semi-dilute entangled regime at a concentration $c_e \approx 3$ kg/m^3 (equivalently 0.3 wt%). According to Rubinstein & Colby (2003), the different scalings are $\eta_p \propto c^{1/(3\nu-1)}$ for $c^* < c < c_e$ and $\eta_p \propto c^{3/(3\nu-1)}$ for $c > c_e$ where ν is the solvent quality (Flory) exponent. The data in figure 3.11.a can be described by the theta solvent exponents 2 and 6 ($\nu = 0.5$). However, other authors working with PEO solutions in water/glycerol mixtures reported $\nu = 0.55$ and measured the corresponding 1.54 and 4.62 exponents for η_p (Tirtaatmadja et al., 2006; Casanellas et al., 2016; Zell et al., 2010).

Mark-Houwink equation The Mark-Houwink equation is a common way to estimate the critical overlap concentration c^* which does not require intensive viscosity measurements. This equation takes the form $[\eta] = K_M\, M^{\alpha_M}$ where M is the molecular weight of the polymer and where K_M and α_M depends on the chemical nature of both polymer and solvent. We recall that $M = 8 \times 10^6$ g/mol for PEO and $M = 15 - 20 \times 10^6$ g/mol for HPAM. Investigations with PEO in various solvents (water, glycerol-water) suggest that solvent play a minor role (Tirtaatmadja et al., 2006). Using (Tirtaatmadja et al., 2006; Rodd et al., 2004)

$$[\eta] = 0.072\, M^{0.65} \qquad \text{(PEO)} \tag{3.23}$$

(where M is in g/mol and $[\eta]$ is in ml/g), we find $[\eta] = 2.2$ m^3/kg and we obtain a

value $c^* = 0.77/[\eta] = 0.35$ kg/m^3 (equivalently 0.034 wt%) which is comparable to the measured value within the experimental uncertainty reported by Tirtaatmadja et al. (2006). Besides, the discrepancy can be attributed to the mechanical breaking of polymer chains during sample preparation which results in a lower average molecular weight M_w (discussion in §3.2.5).

For HPAM chains with hydrolysis degree of 30 % in water (without salt), we can use (Wu et al., 1991; Kawale et al., 2017)

$$[\eta] = 0.022\, M^{0.74} \qquad \text{(unsalted HPAM)} \tag{3.24}$$

which gives $[\eta] = 5.0$ m^3/kg. We obtain $c^* = 0.77/[\eta] = 0.15$ kg/m^3 (equivalently 0.015 wt%). Hence, $c/c^* \approx 6.7$ for HPAM solutions without salt and polymer molecules are probably in the semi-dilute entangled regime. Since c^* increases when adding salt (Chen et al., 2012), salted solutions are expected to be less entangled.

Since $[\eta] \propto M^{3\nu-1}$ (equation 2.64), identification with the Mark-Houwink exponent leads to $\nu = 0.55$ for PEO and $\nu = 0.58$ for HPAM.

3.2.4 Discussion on the rheological parameters

We now discuss the other rheological parameters of table 3.1.

PEO solutions (with 20 wt% PEG solvent)

The CaBER extensional relaxation time τ_{fil} is compared in figure 3.11.b with the relaxation times $\Psi/2\eta_p$ calculated for PEO solutions exhibiting quadratic first normal stress differences $N_1 = \Psi\dot{\gamma}^2$ (i.e. in the dilute and semi-dilute unentangled regimes). Both quantities are plotted against c/c^*. While τ_{fil} increases with polymer concentration, $\Psi/2\eta_p$ decreases since η_p increases faster than Ψ which scales as $\Psi \propto c^{0.72}$ in the dilute regime and $\Psi \propto c^{1.5}$ in the semi-dilute unentangled regime. The link between the first normal stress coefficient Ψ and the CaBER extensional relaxation time τ_{fil} is far from obvious. An intensive study by Zell et al. (2010) involving semi-dilute PEO solutions in water-glycerol mixtures has been dedicated to this topic. The authors also report that $\Psi \propto c^{1.5}$ for $c^* < c < c_e$, as well as values of τ_{fil} much larger than $\Psi/2\eta_p$. Our experiments suggest that $\tau_{fil} \propto c^{0.84}$, which is in agreement with the exponents found by Zell et al. (2010). The authors also report an empirical relation $\Psi \propto \tau_{fil}^2$ where, surprisingly, the prefactor does not depend on polymer concentration. This is different from the microscopic predictions in the dilute regime, i.e. $\eta_p = G\tau$ (see §2.3.5) with $G = \bar{n}k_BT$ (equation 2.72, dilute regime)

and therefore $\Psi = 2nk_BT\tau^2$. Our experimental results follow the same quadratic dependence in the semi-dilute regime with a prefactor 0.06 Pa which is comparable to the prefactor reported by the authors.

Both relaxation times are compared in figure 3.11.b with the Zimm (longest) relaxation time which is given by equation 2.81. The numerical prefactor is 0.38 for $\nu = 0.5$ and 0.46 for $\nu = 0.55$ and the corresponding values of τ_Z are respectively 0.020 s and 0.024 s. The fact that τ_{fil} is larger than τ_Z in the dilute regime ($c < c^*$) has been reported by Tirtaatmadja et al. (2006) and discussed by Clasen et al. (2006). The interpretation is that polymer chain-chain interactions (neglected in the Zimm model) are not negligible during the filament thinning process since $\tau_{fil}\,\dot{\epsilon} = 2/3$ which is larger than the coil-stretch transition value 1/2 (De Gennes, 1974). The polymer chains are therefore highly extended and may overlap. Clasen et al. (2006) suggested that there must be an effective critical overlap concentration in extensional measurements which is orders of magnitude smaller than the conventional coil overlap concentration c^*. Furthermore, the authors show that τ_{fil} is larger than the longest relaxation time measured from small amplitude oscillatory shear (SAOS) experiments since intermolecular interactions are less important. The authors conclude that τ_{fil} is an effective relaxation time which is relevant in strong extensional flows. CaBER experiments have indeed been used to determine the relevant polymer time scale in many elongational flows including spraying (Keshavarz et al., 2015), jetting (Clasen et al., 2009) contraction (Rodd et al., 2005, 2007) and coating (curtain) flows (Becerra & Carvalho, 2011; Karim et al., 2018b). Note that we measure values of τ_{fil} lower than τ_Z for the two most dilute PEO solutions, as also reported by Clasen et al. (2006). The interpretation is that, for very dilute solutions, polymeric stress may be insufficient to maintain the elastocapillary balance leading to equation 3.21 and to allow an unambiguous determination of the longest relaxation time. Another possible interpretation is that our estimation of τ_Z is incorrect due to mechanical degradation during sample preparation which leads to a lower average molecular weight M_w.

We can compare the experimental values of the finite extensibility parameter b to the microscopic expression (Clasen et al., 2006)

$$b = 3\left[\frac{j(\sin(\theta/2))^2 M_w}{C_\infty M_u}\right]^{2(1-\nu)} \tag{3.25}$$

which involves the C-C bond angle $\theta = 109°$, the number of bonds j of a monomer unit with molar mass M_u and the characteristic ratio C_∞. For PEO, $j = 3$ and $C_\infty = 4.1$ (Brandrup et al., 1989). Therefore, using $\nu = 0.55$ gives a value $b =$

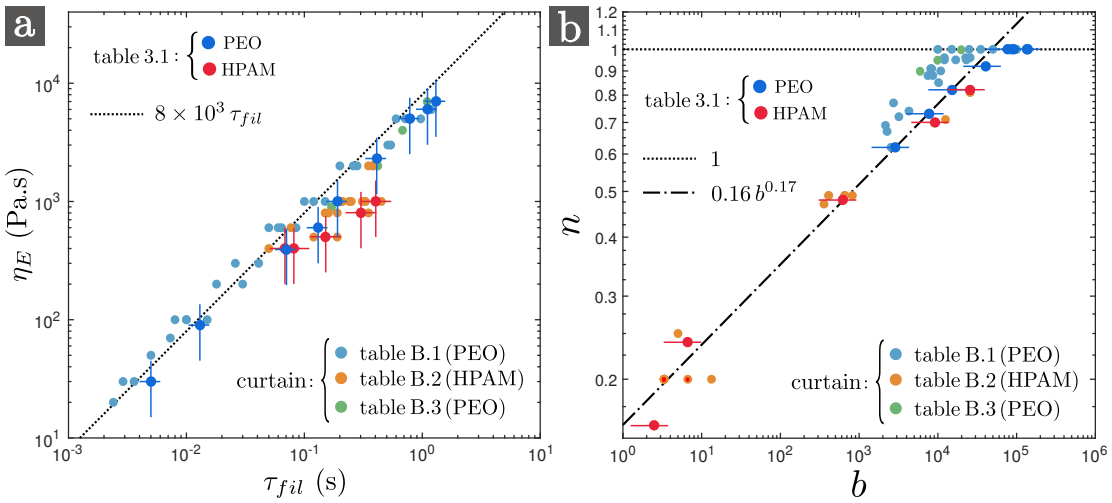

Figure 3.12 – Graphic representation of some of the rheological parameters of table 3.1 plus the rheological parameters of the solutions used in curtain experiments (see tables B.1, B.2 and B.3). (a): Terminal extensional viscosity η_E versus the extensional relaxation time τ_{fil}. (b): Degree of shear-thinning n versus the effective flexibility paramater b.

8.8×10^4 which is very close to the values measured for dilute PEO solutions. Using $\nu = 0.5$ gives a larger value $b = 2.7 \times 10^5$.

More general discussion

According to Stelter et al. (2002), the terminal extensional viscosity η_E is proportional to τ_{fil} with a prefactor which is larger for flexible polymers than for rigid polymers (see also McKinley (2005)). In figure 3.12.a, we plot η_E against τ_{fil} for both PEO and HPAM solutions (table 3.1) and we indeed find that $\eta_E \approx 8 \times 10^3\, \tau_{fil}$ for solutions of flexible chains such as PEO and salted HPAM. Lower values of η_E are found for semi-rigid (unsalted) HPAM solution. This behaviour is confirmed by experimental data with curtain solutions (not introduced yet, see tables B.1, B.2 and B.3), which are superimposed in figure 3.12.a

The data of table 3.1 also suggests a link between the degree of shear-thinning n and the effective value of the finite extensibility parameter b. In figure 3.12.b, we plot n against b and we observe a correlation between these two rheological parameters. When b increases, i.e. when the (effective) chain flexibility increases, n increases which means that the solution is less shear-thinning. Hence, rigid polymers are more likely to produce shear thinning solutions. This point has been discussed by Lindner (2000) when comparing non shear-thinning solutions of (flexible) PEO chains and shear-thinning solutions of (rigid) Xanthan chains. The experimental data suggests a relation which can be simplified to

$$n \approx \begin{cases} 0.16\, b^{0.17} & \text{for} \quad b < 5 \times 10^4 \\ 1 & \text{for} \quad b \geq 5 \times 10^4 \end{cases} \tag{3.26}$$

This behaviour is confirmed by experimental data with curtain solutions (not introduced yet, see tables B.1, B.2 and B.3), which are superimposed in figure 3.12.b. To our knowledge, this kind of relation is not mentioned in the literature. It is is not predicted by dilute polymer solutions models such as the FENE-P model which gives $\eta - \eta_s \propto \dot{\gamma}^{-2/3}$ at large shear rates, i.e. $n = 1/3$ for all values of b.

3.2.5 Mechanical degradation and adequate protocols

During preparation (see §3.1.1) of a 5 kg curtain solution, degradation of the polymer chains may occur during shaking since mechanical stirrers produce high shear rates. This is particularly true for PEO solutions since we measured that the relaxation time of two independently prepared solutions of same PEO concentration could vary by a factor of up to 4 (HPAM solution are much more reproducible). Authors working with smaller samples use generally more gentle techniques such as magnetic stirrers or (even better) roller-mixers. These techniques require longer preparation times. In our case, the rheological data presented in the previous sections which correspond to specific solutions with a particular preparation history can not be used as a reference for all other solutions. Therefore, rheological measurements are performed on any newly prepared solution. Nevertheless, the data presented in the previous sections capture the main trends and orders of magnitude. In particular, the scalings found in §3.2.4 remain true.

Mechanical degradation of the polymer chains also occur in the hydraulic loop described in §3.1.2. Indeed, in this closed-loop system, polymer chains flow many times through the peristaltic pump which was found to be the principal source of degradation. Since irreversible scission of the polymer molecules occurs at each passage through the pump, the rheological properties of the solution vary with time. Therefore, it would be incorrect to correlate curtain data with the rheological properties of the initial fresh solutions. In order to overcome this problem, we use two different experimental protocols.

Degradation protocol For the first protocol, we take advantage of degradation by proceeding as follows. A newly prepared solution is placed in the reservoir and the pump is turned on at time $t_d = 0$. Filling the loop and setting the desired flow rate takes about 1 minute. A first PIV measurement is performed, and we immediately collect a sample of the solution from the die. Without changing any

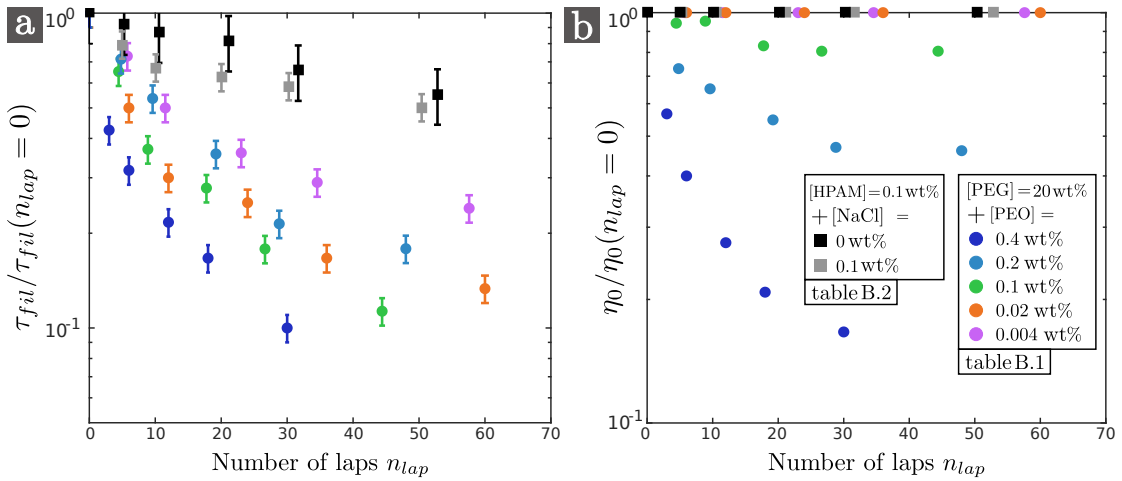

Figure 3.13 – Dependence of the extensional relaxation time τ_{fil} (a) and of the zero-shear viscosity η_0 (b) on the number of laps n_{lap} through the hydraulic loop for PEO solutions with 20 wt% PEG solvent (table B.1) and for HPAM solutions (table B.2 (top)). n_{lap} is estimated by t_dQ/M_s where t_d is the time spent since the start of the experiment, Q is the mass flow, and $M_s = 5$ kg is the mass of the solution. For each liquid, τ_{fil} and η_0 are normalised by the initial values before degradation, i.e. at $t_d = 0$.

external parameter, this procedure is repeated at times t_d = 10, 20, 40, 60 and 100 minutes. We therefore obtain six velocity profiles $U(z)$ corresponding to six degradation degrees of a given initial solution, which can be unambiguously correlated to the rheological properties of the six corresponding samples. For simplicity, the solution corresponding to the first measurement is called the fresh solution and is referred to as $t_d = 0$. Note that the flow rate Q has to be regularly readjusted because it increases naturally over time due to a decreasing dissipation in the slot.

For a solution of total mass $M_s = 5$ kg flowing with mass flow Q, the number of laps through the loop is $n_{lap} \approx t_dQ/M_s$ where t_d is the time spent since the start of the experiment. We show in figure 3.13 the extensional relaxation time τ_{fil} (a) and the zero-shear viscosity η_0 (b) as a function n_{lap} for PEO solutions with 20 wt% PEG solvent and for HPAM solutions. Values at time $t_d = 0$, 10, 20, 40, 60 and 100 minutes are normalised by the initial value before degradation, i.e. at $t_d = 0$. Since the solutions are extruded at different flow rates (see §3.1.5), the values reported in figure 3.13 correspond to different values of n_{lap}. For PEO solutions, τ_{fil} decreases by a factor of up to 10 after 100 minutes of circulation. In contrast, HPAM chains are more resistant since they deteriorate at a much lower rate. Besides, we observe that η_0 only decreases for PEO solutions which exhibit shear-thinning behaviour.

The detailed rheological parameters of all the solutions presented in figure 3.13 are summarised in tables B.1 and B.2 (top). Shear thinning PEO solutions become

less shear thinning during degradation, i.e. n increases. Note that an extra HPAM solution is presented in table B.2 (bottom): starting from a fresh unsalted HPAM solution, five PIV measurements are performed at arbitrary times, each measurement corresponding to a particular salt concentration which is achieved by adding a particular salt quantity to the solution. Samples are again collected at each step and shear and extensional rheological measurements are performed on each sample. Since polymer degradation is slow for HPAM solutions, we ensure that the drastic modifications of the rheological parameters reported table B.2 (bottom) are mostly due to salt addition.

Degradation-free protocol A second protocol is used when investigating the role of external parameters such as the curtain length (§4.2.1), the flow rate (§4.2.2) or the die geometry (§4.4.3). In this case, solutions must have the exact same rheological properties for each measurement. Instead of using the peristaltic pump, the liquid is poured manually from a bucket directly into a tank placed at two metres above the die and drilled with a hole on the lower side. A constant flow rate is ensured by keeping a constant liquid level in the tank. With 5 kg of liquid, this protocol is only possible if the time to perform a controlled experiment is less than the time to empty the bucket. This degradation-free protocol was used with the PEO solutions with 40 wt% PEG solvent presented in table B.3, which have a fairly constant shear viscosity ($n \approx 1$) and large extensional relaxation times, and with the PEO solution of table B.4. We checked that the shear and extensional rheological parameters do not vary during experiments.

Temperature Curtain experiments are performed at room temperature, which could vary between 20°C and 30°C from day to day. Since temperature is not imposed in our "home-made" CaBER rheometer, the extensional rheology measurements are always performed a few minutes after curtain experiments and in the same room for maximum accuracy on extensional parameters. For the liquids of tables B.3 and B.4, the temperature of the curtain room was imposed for shear rheology measurements. However, for the liquids of tables B.1 and B.2, shear rheology measurements were performed at a temperature $T = 20$°C which was not necessarily the room temperature. We measured on similar solutions that the variation of the viscosity parameters η_0, n and $\dot{\gamma}_c$ is very weak within this temperature range (the zero-shear viscosity η_0 typically decreases by a factor of only 1.1 when raising the temperature from 20°C to 30°C, while n and $\dot{\gamma}_c$ remain unchanged). Hence, we can reasonably use the 20°C values reported in tables B.1 and B.2. However, values of the first normal stress difference could vary significantly (by a factor 2). Hence, values of α_1 and Ψ are only reported for the liquids of tables B.3 and B.4. These

values will be used for investigating die swell (§4.1.3 and §4.4.1) and the impact of die geometry on the curtain flow (§4.4.3).

Chapter 4

Curtain flow

Contents

In this chapter, we first present the three important experimental specificities of viscoelastic liquids in the context of curtain flows. These specificities are a dramatic shift of the velocity field $U(z)$ towards sub gravity accelerations, the apparition of a flow instability for the most shear-thinning solutions, and a swelling of the curtain at the slot exit. Then, focusing on the first specificity, we investigate the role of curtain length, flow rate and rheological properties on the velocity field. Then, after deriving a general force balance equation of the curtain flow, we identify a master curve of viscoelastic curtains by analogy with Newtonian curtains. Next, we investigate the influence of the pre-shear inside the slot on the curtain flow. Finally, we present an attempt of theoretical description using the Oldroyd-B model.

4.1 General observations

4.1.1 A dramatic shift towards sub gravity accelerations

To identify the specificity of polymer solutions in the context of curtain flows, we have performed a first series of experiments with three different liquids. The first one (1) is the Newtonian 20 wt% PEG solvent of viscosity $\eta = 0.017$ Pa.s. The second one (2) is a fresh ($t_d = 0$ min) 0.2 wt% PEO solution with 20 wt% PEG solvent (table B.1). Its zero-shear viscosity is $\eta_0 = 0.12$ Pa.s, ten times larger than the pure solvent (1). The third one (3) is pure glycerin, a Newtonian liquid with a measured viscosity $\eta = 1.5$ Pa.s, a hundred times larger than the shear viscosity of liquid (1), and density $\rho = 1250$ kg/m^3. Note that we used a different setup for glycerin since, due to a strong viscous dissipation in the hydraulic loop, the maximum accessible flow rate is well below the minimum flow rate required to create a continuous curtain. Glycerin is placed in a reservoir connected to the die and a large enough flow rate is enforced by applying a constant air flow on the top of the reservoir.

In figure 4.1, we plot the square U^2 of the falling velocity of these liquids as a function of the distance z from the slot. All three curtains have the same length $L_c = 30$ cm and start from comparable initial velocities U_1 ranging between 0.07 m/s for glycerin (3) and 0.2 m/s for the PEG solvent (1). We recall that $U_1 = U(z_1)$ is the liquid velocity at $z_1 \approx 2.5$ mm from the slot exit (see §3.1.4) while $U_0 = U(z = 0)$ is the liquid velocity at the slot exit. The local acceleration of the liquid is given by $U\mathrm{d}U/\mathrm{d}z$ which is half the local slope of the $U^2(z)$ curve. For both Newtonian curtains (1) and (3), we observe that this acceleration is equal to g far from the slot exit.

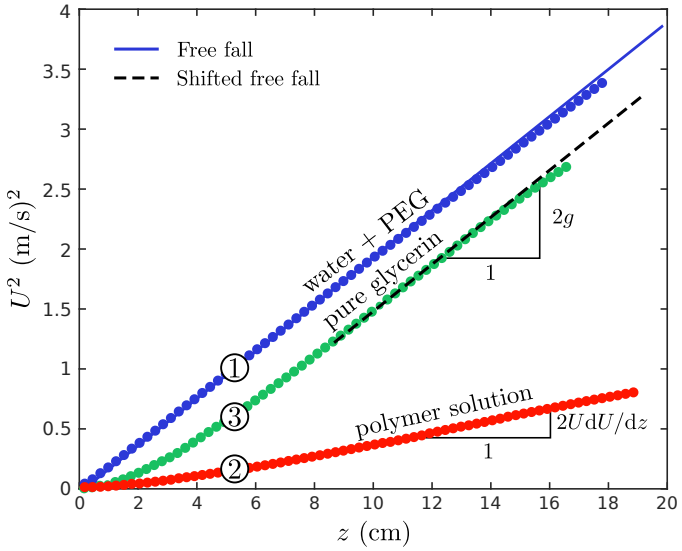

Figure 4.1 – Square U^2 of the falling velocity as a function of the distance z from the slot for two Newtonian curtains (1) and (3), a 20 wt% PEG solution and pure glycerin of viscosities $\eta = 0.017$ Pa.s and $\eta = 1.5$ Pa.s respectively, and for a fresh ($t_d = 0$ min) 0.2 wt% PEO solution (2) with 20 wt% PEG solvent of zero-shear viscosity $\eta_0 = 0.12$ Pa.s (table B.1). The curtain length is $L_c = 30$ cm and the initial velocity U_1 at $z_1 \approx 2.5$ mm from the slot exit is 0.2 m/s, 0.13 m/s and 0.07 m/s for liquids (1), (2) and (3) respectively. The local acceleration of the liquid is $U\mathrm{d}U/\mathrm{d}z$.

More precisely, the fall of the low-viscosity Newtonian liquid (1) is very well captured by a free-fall, i.e. $U^2 = U_0^2 + 2gz$, whereas the acceleration of glycerin reaches the asymptotic value g at about 10 cm from the slot. These results are in agreement with the theory of viscous Newtonian curtains derived in chapter 1 according to which viscous forces are negligible far downstream from the slot. Indeed, the length of the sub-gravitational part of the flow is of order $z_v = ((4\eta/\rho)^2/g)^{1/3}$ (equation 1.3), respectively 0.077 cm and 1.4 cm for liquids (1) and (3), with a prefactor which is about 7 for low initial velocities $U_0 \ll \sqrt{gz_v}$ (see §1.1.3). In particular, we measure $U_0 = 0.05$ m/s from the glycerin curtain movie, which gives $U_0/\sqrt{gz_v} \approx 0.14 < 1$. Hence, according to the theory, the length of the sub-gravitational part of the flow should be about $7\,z_v \approx 10$ cm which is in agreement with the experimental results.

In contrast, the PEO solution falls at much lower velocities than the two others, despite the fact that its zero-shear viscosity is one order of magnitude smaller than the viscosity of glycerin. More precisely, the acceleration at $z = 14$ cm from the slot is $U\mathrm{d}U/\mathrm{d}z = 2.5$ m/s^2 $< g$ despite the fact that the viscous length $z_v = ((4\eta_0/\rho)^2/g)^{1/3}$ is only 0.28 cm based on the zero-shear viscosity. Therefore, viscoelastic curtain flows are not captured by the Newtonian curtain theory.

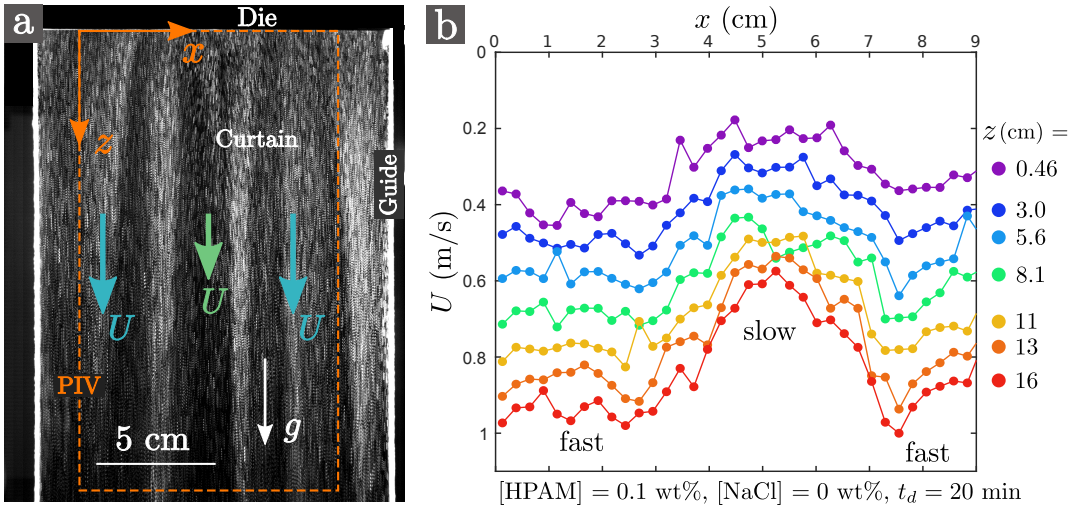

Figure 4.2 – Example of PIV measurement for a degraded ($t_d = 20$ min) 0.1 wt% unsalted HPAM solution (table B.2). (a): Superposition of six successive PIV images. The correlation algorithm is applied to a domain restricted to the dashed rectangle. (b): z-component of the velocity field, i.e. $U(x, z, t)$, against the horizontal coordinate x at different distances z from the slot at an arbitrary time t. The curtain length is $L_c = 30$ cm and the linear flow rate is $q = 3.1$ cm^2/s.

4.1.2 Unstable flow for the most shear-thinning solutions

We observed that the curtain flow is not always stationary and translation invariant along the x horizontal direction as displayed in figure 4.2. Indeed, for some solutions, the curtain flow is unstable and presents a time-dependent varicose mode along x. More precisely, at a given time, the extrusion velocity of the liquid is found to depend on the position x along the slot, producing a modulation of the thickness of the curtain. This is illustrated by the vertical dark and bright stripes in figure 4.2.a for an unsalted HPAM solution. This is one of the most extreme cases of unstable curtain flow. The wavelength and the typical time of evolution of the pattern are of the order of a few centimetres and a few tens of seconds respectively. The corresponding velocity field $U(x, z, t)$ is presented in figure 4.2.b at an arbitrary time t. The dark and bright stripes are associated with flow regions with characteristic velocities respectively slower and faster than the average velocity. For example, at a distance $z = 16$ cm from the slot, the liquid velocity ranges between 0.6 m/s and 1 m/s which corresponds to a variation of $\pm 25\%$ around the average value $\langle U \rangle_x = 0.85$ m/s. The time variation of the average velocity $\langle U \rangle_x$ is presented in figure 4.3.a: it is fairly independent of time. Hence, we can reasonably define an average flow $U(z) = \langle \langle U \rangle_x \rangle_t$ obtained after averaging $\langle U \rangle_x$ over time, as presented in figure 4.3.b.

As salt is added to an initially unsalted HPAM solution, the amplitude of the

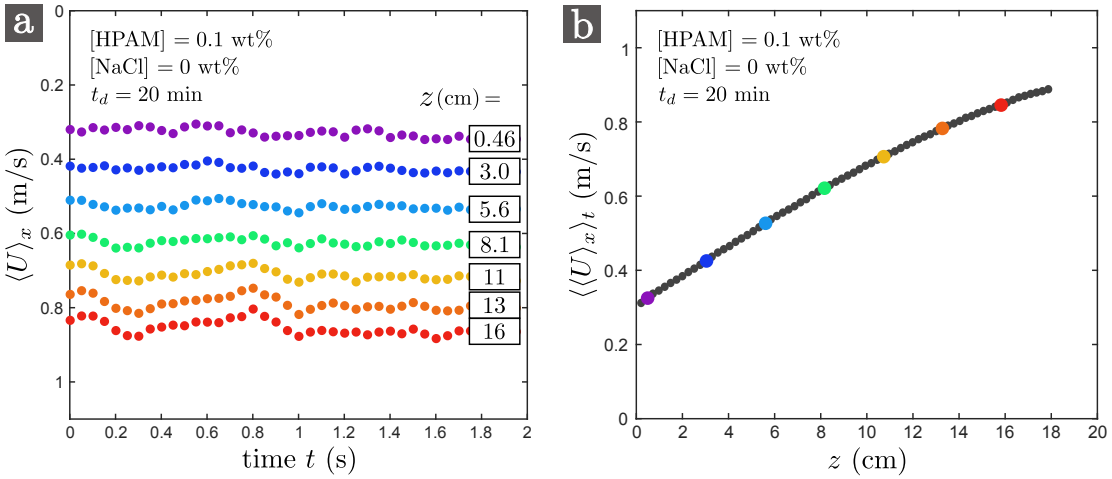

Figure 4.3 – (a): Velocity $\langle U \rangle_x$ averaged over x versus time t (for a two seconds PIV movie) and at different distances z from the slot. Time $t = 0$ s corresponds to the data of figure 4.2.b. (b): Velocity $\langle \langle U \rangle_x \rangle_t$ averaged over x and t versus z. The big coloured dots correspond to the values of figure a.

instability decreases. It disappears for [NaCl] ≥ 1 wt%. Besides, for PEO solutions with 20 wt% PEG solvent (table B.1), the curtain flow is weakly unstable for the highest concentration [PEO] = 0.4 wt%. However, as the polymer chains break due to mechanical degradation, the amplitude of the velocity variation decreases. It disappears for $t_d \geq 40$ min. All other solutions in table B.1 produce a stable curtain, as well as every PEO solution with 40 wt% PEG solvent (table B.3).

Within our experimental range of rheological parameters and flow rates, the only solutions producing an unstable flow have a degree of shear-thinning $n < 0.70$ or, equivalently, an effective finite extensibility $b < 2 \times 10^3$. Neither the zero-shear viscosity η_0 nor the extensional relaxation time τ_{fil} does provide such a clear separation between stable and unstable curtains. This aspect of our work will be developed in §5.2 when focusing on the curtain stability. Besides, in chapter 6 which will be dedicated to the visualisation of the flow upstream of the slot, we give experimental evidence that the flow instability observed in these curtains is in fact generated at the planar contraction prior to entering the slot. This contraction instability is characterised by a variation of the local velocity along the slot, thus leading to overfed and underfed regions generating a modulation of the thickness and velocity field of the downstream curtain. For now, concerning this chapter, whatever the curtain (stable or unstable) we focus on the mean flow $U(z) = \langle \langle U \rangle_x \rangle_t$.

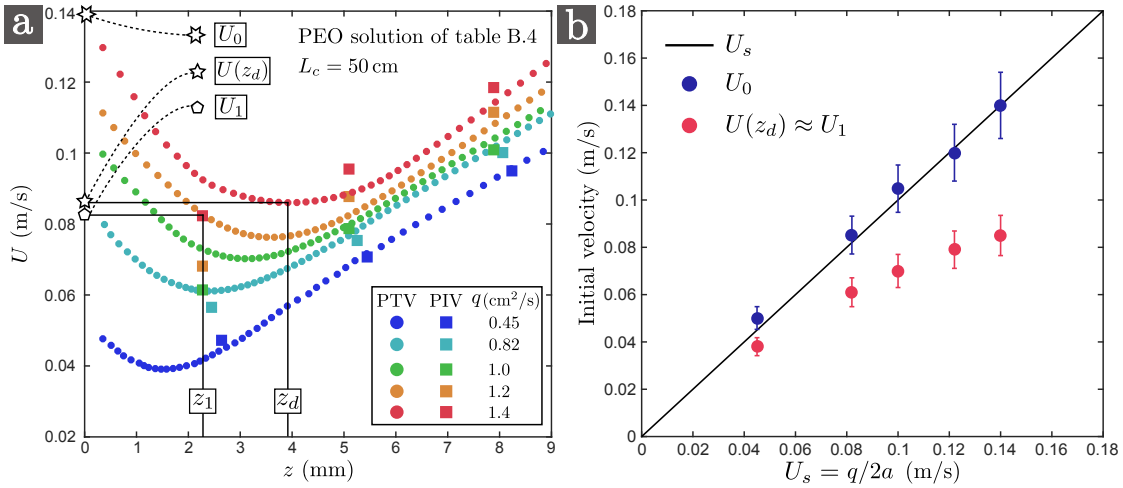

Figure 4.4 – (a): Velocity field $U(z)$ at the slot exit measured from single particle tracking velocimetry (PTV) for the PEO solution of table B.4 extruded at different flow rates q ranging between 0.45 cm^2/s and 1.4 cm^2/s. The curtain swells since the mean velocity decreases from U_0 at $z = 0$ to $U(z_d)$ at a distance z_d from the slot exit. U_0 is estimated by extrapolation the PTV data. The PIV velocity fields are also shown for comparison, the first value U_1 corresponding to $z_1 \approx 2.5$ mm. To guide the eye, z_1, z_d, U_0, U_1 and $U(z_d)$ are shown for the data corresponding to $q = 1.4$ cm^2/s (red symbols). (b): The corresponding values of U_0 and $U(z_d)$ are plotted against the mean velocity $U_s = q/2a$ inside the slot.

4.1.3 Die swell

We recall that the first value $U_1 = U(z_1)$ measured by PIV corresponds to the velocity at $z_1 \approx 2.5$ mm from the slot exit, whereas the mean velocity in the slot can be estimated as $U_s = q/2a$ where q is the measured linear flow rate and $2a$ is the slot thickness. Values of both U_s and U_1 are reported in tables B.1, B.2 and B.3 for the corresponding curtains experiments. We observe that U_1 is systematically smaller than U_s, except for HPAM curtains, and that the ratio $\xi = U_s/U_1$ is up to 2 and increases with polymer concentration. Observations with the naked eye confirm that the curtain rapidly swells at the slot exit. This is not due to a wetting effect, as expected from the design of the die where the wall edges are bevelled (figure 3.2.b).

In order to estimate the velocity profile $U(z)$ in this region, we can use the particle tracking velocimetry (PTV) technique within the first millimetres of the flow, i.e. we track the position of singles particles after leaving the slot. Image processing is performed "manually". Results are presented in figure 4.4.a for the PEO solution of table B.4 extruded at different flow rates. The liquid velocity first decreases from $U_0 = U(z = 0)$ at the slot exit to a minimum value at $z = z_d$ before finally increasing, where z_d increases from 1.5 mm to 4 mm when increasing the flow rate. This is reminiscent of the delayed die swell effect (Boger & Walters, 2012; Delvaux & Crochet, 1990). PIV measurements are not able to capture this behaviour since

cross-correlation is computed over centimetric windows. However, a superposition of the PIV velocity profiles in figure 4.4.a shows an acceptable agreement between the first value U_1 measured from PIV and the minimum velocity $U(z_d)$ measured from particle tracking: $U(z_d) = U_1$ with less than 15% error. The values of U_0 and $U(z_d)$ are reported in figure 4.4.b as a function of the mean velocity U_s in the slot. As expected, $U_0 = U_s$. Besides, the swelling ratio $\xi = U_s/U_1$ increases when increasing the flow rate. In the following, z_d and $U(z_d)$ are approximated by z_1 and U_1 for the sake of simplicity.

4.2 The influence of experimental parameters

4.2.1 The influence of the curtain length

To investigate the role of the curtain length L_c on the flow, we perform experiments with L_c ranging from 15 cm to 200 cm. To achieve such measurements, we use a two-floor room: the liquid is poured from the top floor and reaches the die hanging from the ceiling of the bottom floor. After extrusion, the liquid is stopped at the desired distance L_c from the slot by a 20×10 cm horizontal plastic plate and finally falls into a reservoir. The vertical wires guiding the flow pass through two small holes drilled on the plastic plate to ensure that all the liquid is stopped. The camera only records the first 32 centimetres of the fall. Only the most elastic solutions could form a 2 meters continuous curtain. On the other hand, curtains made of solutions with low polymer concentration usually break before reaching the plastic plate. Near the breaking zone, some curtains may even adopt a sinuous flag-like motion. We suspect that this is due to the shear instability with the surrounding air described by Dombrowski & Johns (1963) and Villermaux & Clanet (2002).

For these experiments, we use the PEO solutions with 40 wt% PEG solvent presented in table B.3 along with the degradation-free protocol presented in §3.2.5 to ensure that L_c is the only varying parameter for a given solution. We only consider the curtains reaching the plastic plate without breaking. Some results are presented in figure 4.5 for [PEO] = 0.2 wt% (a) and [PEO] = 0.024 wt% (b). In the first case, longer curtains fall clearly faster than shorter ones, i.e. the velocity U is larger at a any distance z from the slot. The liquid vertical velocity has to vary from the imposed initial velocity $U(0) = U_0$ at the slot exit to $U(L_c) = 0$ when impinging onto the motionless plastic plate where the curtain flow turns into a plane stagnation flow. Everyday experience with jets of tap water suggests that the presence of a horizontal solid surface only affects the liquid flow within a few millimetres before impact. However, as suggested in the curtain-like experiment of figure 2.11 (elastic recoil,

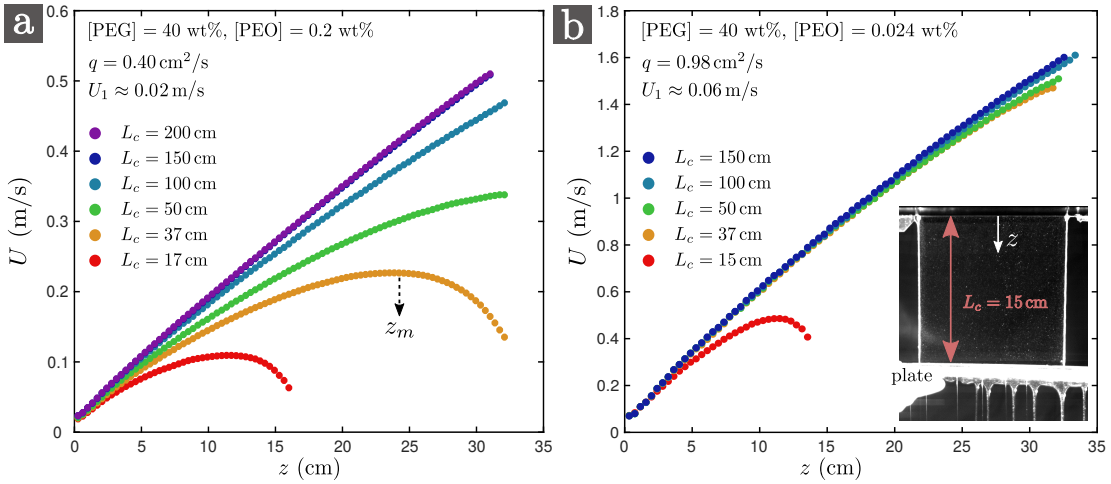

Figure 4.5 – Velocity field $U(z)$ for $z \leq 32$ cm for curtains of lengths L_c ranging between 15 cm and 200 cm. The liquid falls onto a motionless horizontal plate (see inset on the right) and reaches a maximum velocity at a distance z_m from the slot. The liquids are respectively 0.2 wt% (a) and 0.024 wt% (b) PEO solutions with 40 wt% PEG solvent (table B.3). They are respectively extruded at flow rates $q = 0.40$ cm^2/s and 0.98 cm^2/s. The liquid velocity U_1 at $z_1 \approx 2.5$ mm from the slot is respectively 0.02 m/s and 0.06 m/s.

first image), "thick" viscoelastic liquids start "spreading" much further upstream. In other words the curtain thickness (resp. the curtain velocity) starts increasing (resp. decreasing) at a much larger distance from the plate. Indeed, for the liquid of figure 4.5.a with extensional relaxation time $\tau_{fil} = 1.1$ s, the presence of the plate clearly affects the flow on a much larger scale: for $L_c = 37$ cm, the liquid velocity first increases and reaches a maximum value at $z = z_m \approx 25$ cm before decreasing, i.e. the curtain starts to get thicker at a distance $L_c - z_m \approx 12$ cm from the impact. As the plate is moved downwards, the flow field near the slot exit converges towards a universal behaviour which is no longer influenced by the presence of the plate: there is no difference between $L_c = 150$ cm and $L_c = 200$ cm within the first 32 centimetres of the fall in figure 4.5.a. This is even more visible for the solution used in figure 4.5.b which has a lower extensional relaxation time $\tau_{fil} = 0.17$ s since the liquid velocity $U(z)$ is almost the same for all curtain lengths, except for $L_c = 15$ cm.

4.2.2 The influence of the flow rate

To investigate the role of the flow rate, we perform experiments using the degradation-free protocol presented in §3.2.5 to ensure that q is the only varying parameter for a given solution. The test liquid is the PEO solution presented in table B.4 which is close to (but not exactly the same as) the degraded ($t_d = 100$ min) 0.4 wt% PEO solution with 20 wt% PEG solvent presented in table B.1. The liquid is extruded at different flow rates q ranging between 0.45 cm^2/s and 1.4 cm^2/s. In figure 4.6.a,

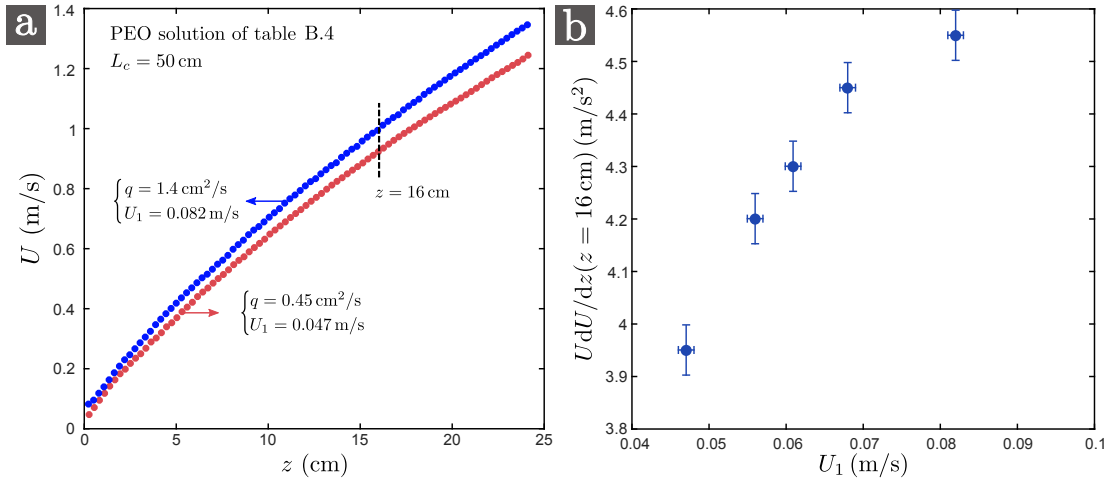

Figure 4.6 – (a): Velocity field $U(z)$ for the PEO solution of table B.4 extruded at flow rates $q = 0.45$ cm^2/s and 1.4 cm^2/s. The liquid velocity U_1 at $z_1 \approx 2.5$ mm from the slot is respectively 0.047 m/s and 0.082 m/s. (b): Local acceleration $U\mathrm{d}U/\mathrm{d}z$ at an arbitrary distance $z = 16$ cm from the slot versus initial velocity U_1. The curtain length is $L_c = 50$ cm.

we report the velocity field $U(z)$ for these two flow rates. U increases slightly faster when increasing the flow rate. To quantify this effect, values of the liquid acceleration $U\mathrm{d}U/\mathrm{d}z$ at an arbitrary distance $z = 16$ cm from the slot are reported in figure 4.6.b as a function of the initial velocity U_1 (after swelling). The local acceleration is increased by a factor 1.2 when U_1 is increased by a factor 1.7. The same trend is observed for all solutions, including HPAM solutions.

4.2.3 The influence of the rheological properties

To investigate the role of the rheological properties, we show in figure 4.7.a the square $U^2(z)$ of the velocity field for the six 0.1 wt% PEO solutions with 20 wt% PEG solvent presented in table B.1. These measurements are performed with the degradation protocol presented in §3.2.5 and each solution corresponds to a specific degradation time. All six curtains share the same initial velocity $U_1 \approx 0.17$ m/s at $z_1 \approx 2.5$ mm from the slot and the same curtain length $L_c = 30$ cm. These specific solutions are almost non shear-thinning ($n \approx 0.96$) and have similar shear viscosities. In particular, the three last solutions have the same values of both $\eta_0 = 0.029$ Pa.s and $\eta_p = 0.012$ Pa.s. However, we observe that the liquid acceleration increases with degradation time. This suggests that neither η_0 nor η_p does fully control the curtain flow and that other rheological parameters are to be taken into account to rationalise the curtain data. The same conclusion can be drawn for the 0.02 wt% and 0.004 wt% PEO solutions of table B.1 for which degradation has no impact on the shear viscosity (results not shown).

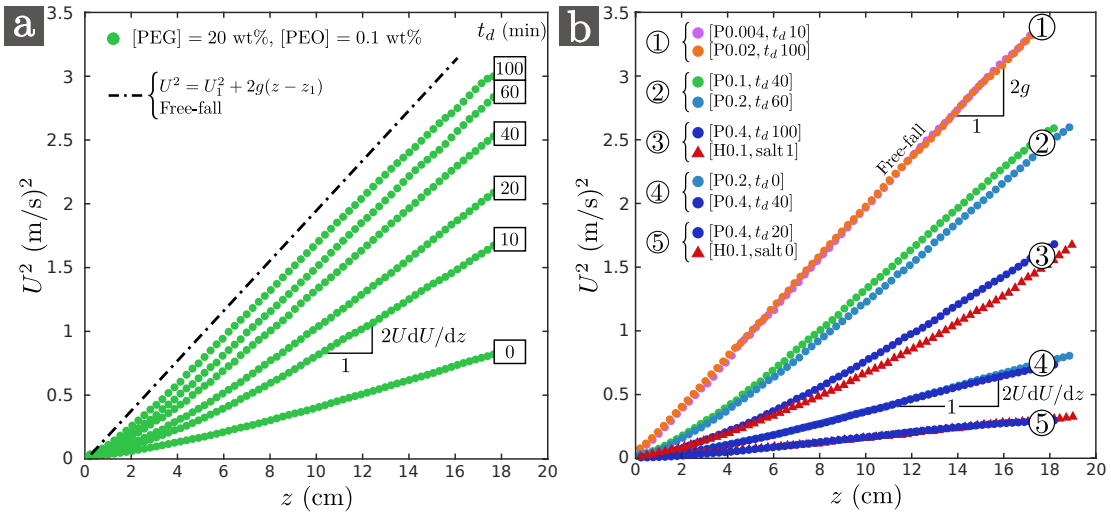

Figure 4.7 – Dependence of the velocity field $U(z)$ on the rheological properties of the solution. (a): $U^2(z)$ for the 0.1 wt% PEO solutions with 20 wt% PEG solvent (table B.1) for all degradation times $t_d = 0$ to 100 min. All solutions are almost non shear-thinning fluids of comparable zero-shear viscosity $\eta_0 \approx 0.03$ Pa.s and have comparable initial velocities $U_1 \approx 0.17$ m/s at $z_1 \approx 2.5$ mm from the slot. A free-fall is shown for comparison. (b): $U^2(z)$ for five pairs of solutions (1), (2), (3), (4) and (5) from tables B.1 and B.2 (bottom) which are referred to as follows: [P0.2, t_d 60] corresponds to a 0.2 wt% PEO solution (with 20 wt% PEG solvent) with degradation time $t_d = 60$ min and [H0.1, salt 1] corresponds to a 0.1 wt% HPAM solution with salt concentration [NaCl] = 1 wt%. Within each pair, both solutions share similar initial velocities U_1 and comparable extensional relaxation times ranging between $\tau_{fil} = 0.0073-0.008$ s (1) to $\tau_{fil} = 0.38-0.5$ s (5). The curtain length is $L_c = 30$ cm for both figures.

In figure 4.7.b, we plot the square $U^2(z)$ of the velocity field for various PEO and HPAM solutions from tables B.1 and B.2 (bottom). The curtain length is $L_c = 30$ cm and we choose five pairs of solutions such that both solutions within each pair share comparable extensional relaxation times τ_{fil} and initial velocities U_1. The results suggest that the liquid fall is mostly influenced by the value of τ_{fil} since the flow of both solutions within each pair is very similar. More precisely, the flow of solutions (1), which have low extensional relaxation times $\tau_{fil} = 7-8$ ms, is well captured by a free fall with constant acceleration $g = 9.81$ m/s^2, whereas other solutions with larger values of τ_{fil} fall with sub-gravitational accelerations. In the latter case, note that the local acceleration $U\mathrm{d}U/\mathrm{d}z$ is an increasing function of z. These results are consistent with the recent results of Karim et al. (2018b) who also measured free-falls for curtains made of PEO solutions with extensional relaxation times $\tau_{fil} \leq 7.3$ ms.

Note that η_0 and η_p vary significantly for the pair (3) in figure 4.7.b. This example reinforces the idea that shear viscosity does not fully control the curtain flow.

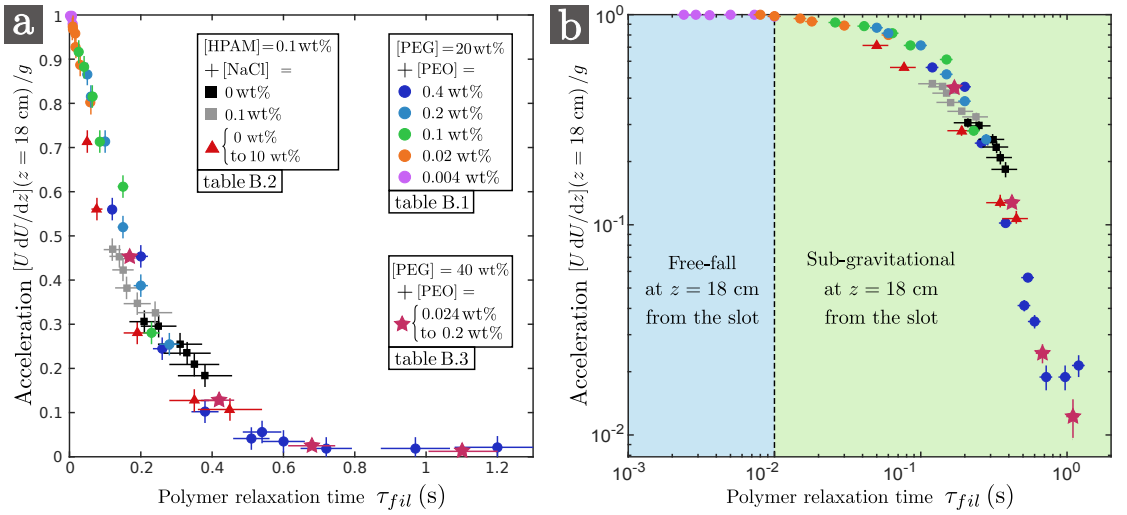

Figure 4.8 – Dimensionless acceleration $[U\mathrm{d}U/\mathrm{d}z]/g$ at $z = 18$ cm from the slot against polymer extensional relaxation time τ_{fil} in lin-lin (a) and log-log (b) scales for all the solutions of tables B.1 (PEO) and B.2 (HPAM), for which the curtain length is always $L_c = 30$ cm, and for all PEO the solutions of tables B.3 when the curtain length is also $L_c = 30$ cm. Note that another 0.4 wt% PEO solution with 20 wt% PEG solvent was prepared and that the curtain flow was measured at $t_d = 0$, 5, 10, and 20 minutes in order to fill the high relaxation time region of the curve.

The flexibility of the polymer chains also appears to play no major role since values of the effective finite extensibility b (and of the degree of shear-thinning n) are very different for the solutions of pair (5). To confirm these ideas, we gather all the data corresponding to $L_c = 30$ cm in figure 4.8 where the acceleration at a given (arbitrary) distance $z = 18$ cm from the slot is plotted against τ_{fil}. We observe a good collapse of the data although neighbouring points in the plot can correspond to very different values of the other rheological parameters. This result confirms that curtain data can be fairly rationalised using only the extensional relaxation time τ_{fil} measured from CaBER experiments. The deviations can be explained by the differences in flow rates: curtains extruded at lower flow rates have a slightly lower acceleration (§4.2.2). Note that some of the data in figure 4.8 correspond to the unstable curtains mentioned in §4.1.2 and blend with the stable curtain data, which suggests that this instability does not affect significantly the average velocity field $U(z) = \langle\langle U\rangle_x\rangle_t$.

According to figure 4.8.b, solutions with relaxation times $\tau_{fil} \leq 10$ ms have an acceleration $U\mathrm{d}U/\mathrm{d}z = g$ at $z = 18$ cm from the slot exit. In fact, for some of these solutions, the local liquid acceleration is less than g close to the slot and reaches the free-fall value g at $z < 18$ cm. This is reminiscent of the flow of pure glycerin reported in figure 4.1, which suggests that g is also the asymptotic value of the

liquid acceleration for viscoelastic curtains. However, due to the finite length of the curtain, many liquids are stopped before reaching the free-fall behaviour. This is particularly true for solutions with high relaxation times $\tau_{fil} \approx 1$ s which fall with very low accelerations $U\mathrm{d}U/\mathrm{d}z \approx 0.1$ m/s$^2 \ll g$ at $z = 18$ cm from the slot exit.

4.3 Characterisation of the average velocity field

4.3.1 General overview of the problem

Before focusing on the description of the curtain flow, we would like to give in this section a general overview of the different types of flows involved in this problem, as we did in §1.1 for Newtonian curtains. Here we will focus on viscoelastic liquids.

General description The liquid first experiences a planar contraction of ratio A/a at the slot entrance (figure 3.2.b). The mean liquid velocity on the centre line $y = 0$ switches from about $q/2A$ in the hollow box to $U_s = q/2a$ inside the slot in a characteristic time a/U_s, where q is the linear flow rate and $2a$ is the slot thickness. Then, a Poiseuille flow is established in the slot due to the development of a viscous boundary layer along the walls. At the slot exit, the wall boundary condition switches to a free-surface boundary condition, i.e. zero shear stress at the liquid-air interface. Hence, due to viscous diffusion, the Poiseuille flow switches to a plug flow, as illustrated in figure 4.9. U is the mean vertical velocity averaged over the curtain thickness. After initial swelling at the slot exit, the curtain thickness decreases since fluid particles are now accelerated by gravity. Since the liquid may develop some resistance to gravitational forces, the local mean acceleration $U\mathrm{d}U/\mathrm{d}z$ may be initially less than g. The asymptotic free-fall regime where $U\mathrm{d}U/\mathrm{d}z = g$ is reached when inertia overcomes the resistance of the liquid.

Viscoelastic liquids For all solutions used in our experiments, the time scale a/U_s of the planar contraction is shorter than the extensional relaxation time τ_{fil}. Hence, the polymer molecules undergo a rapid strain of Hencky strain $\epsilon \approx \ln(A/a) = 2.6$ (equation 3.10). Significant extensional stresses may arise due to this sudden polymer elongation. However, the time L_s/U_s spent by the liquid inside the slot is generally longer than τ_{fil}. Therefore, the polymeric stress developed by the liquid at the slot entrance is expected to relax towards the asymptotic Poiseuille flow value before leaving the slot.

For a Newtonian liquid, due to the development of a viscous boundary layer along the slot walls, a fully developed Poiseuille flow is expected to be established

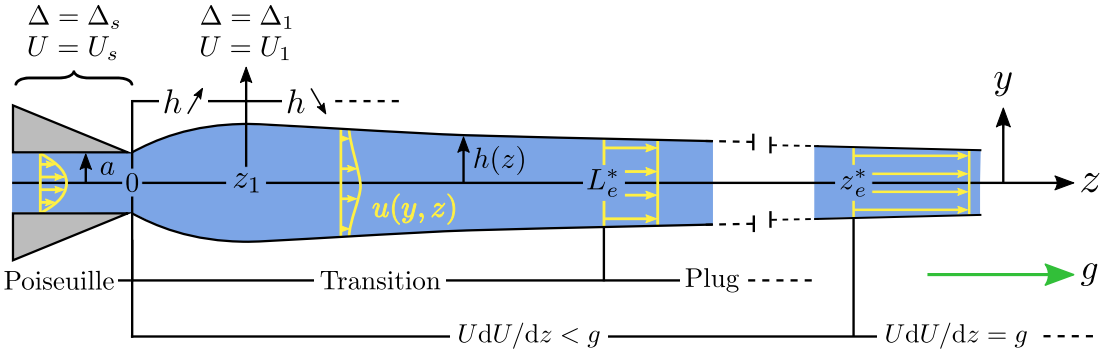

Figure 4.9 – Sketch of an infinitely long viscoelastic curtain (cross-sectional view). During the swelling at the slot exit, the mean liquid velocity U and the mean normal stress difference $\Delta = \sigma_{zz} - \sigma_{yy}$ averaged over the curtain thickness switch respectively from U_s and Δ_s to U_1 and Δ_1 at $z_1 \approx 2.5$ mm from the slot exit. The local vertical velocity field $u(y, z)$ switches from a Poiseuille flow inside the slot to a plug flow at a distance $z = L_e^*$ from the slot. In parallel, the mean velocity field $U(z)$ is characterised by a transition from a sub-gravitational regime to an asymptotic free-fall regime at a distance $z = z_e^*$ from the slot.

at a distance from the slot inlet which scales as $L_v = Re\, a$ from the slot, where $Re = \rho U_s a/\eta$ is a Reynolds number. The prefactor for the effective establishment is typically less than one (Kays et al., 2005). For the viscoelastic liquids used in our experiments, the Reynolds number ranges between 0.03 and 10 based on the zero-shear viscosity. Hence, L_v ranges between 0.01 mm and 5 mm which is much smaller than the slot length $L_s = 10$ cm. This suggests that a fully developed Poiseuille flow is established long before the slot exit, as confirmed by direct visualisation.

We recall that z_v^* ("v" for "viscous") is the distance from the slot exit at which a Newtonian curtain reaches the asymptotic free-fall value (given in equation 1.28). Using analogous notations for viscoelastic curtains, let z_e^* ("e" for "elastic") be the distance from the slot at which the local acceleration of the liquid reaches the asymptotic value g. We showed in sections 4.1.1 and 4.2.3 that this transition length can be much larger than what could be expected from the theory of Newtonian curtains, i.e. $z_e^* \gg z_v^*$, and that it was mainly determined by the value of the extensional relaxation time τ_{fil} of the polymer solution. Of course, regardless of the liquid rheology, this discussion only makes sense if the curtain length is larger than this transition length, i.e. $L_c > z_e^*$ or $L_c > z_v^*$, otherwise the curtain flow would turn into a plane stagnation flow before reaching the free-fall regime.

Direct visualisation of the y dependence of the curtain flow is quite difficult. Therefore, to estimate the length L_e^* at which the plug flow is fully established in the case of viscoelastic liquids, we visualised the flow of some PEO solutions when

issuing from a nozzle of diameter 1 mm. For the degraded ($t_d = 100$ min) 0.1 wt% PEO solution with 20 wt% PEG solvent, we measure $L_e^* \approx 1.2$ cm although the transition to free-fall is out of frame in curtain experiments, i.e. $z_e^* > 18$ cm. Hence, provided that the order of magnitude of L_e^* is comparable in the curtain, we can reasonably assume that the plug flow is established much sooner than the free-fall regime, i.e. $L_e^*/z_e^* \ll 1$. We shall mention that our measurements suggest an influence of elasticity on the Poiseuille to plug transition: L_e^* is larger than what could be expected from the theory of Newtonian curtains. Further analysis is required to characterise this effect.

In this manuscript, we focus on the transition from the sub-gravitational regime to the free-fall regime. In particular, we wish to characterise the sub-gravitational regime in the case of a viscoelastic curtain and to express z_e^* as a function of the parameters of the problem.

4.3.2 Newtonian master curve

Before investigating the structure of the flow of viscoelastic curtains, we check that the master curve identified in §1.1.3 for Newtonian curtain gives correct predictions. We recall that the analysis of the Taylor equation 1.14 predicted that, when the downstream boundary condition does not affect the flow (i.e. when the curtain length L_c is much larger than the characteristic length $z_v = ((4\eta/\rho)^2/g)^{1/3}$ of the transition from the sub-gravitational regime to the free-fall regime), the velocity field $U(z)$ of a Newtonian curtain was given by

$$\bar{U}(\bar{z}) = M_v\left(\bar{z} + M_v^{-1}(\bar{U}_0)\right) \tag{4.1}$$

where $\bar{z} = z/z_v$ and $\bar{U} = U/U_v$, where z_v and $U_v = \sqrt{g\,z_v}$ are the characteristic length and velocity scales of the problem. In this formula, M_v is a master curve characterised by an initial viscous regime $M_v(\bar{z}) = \bar{z}^2/2$ (gravity is balanced by viscous dissipation) and an asymptotic inertial regime $M_v(\bar{z}) = \sqrt{2\,(\bar{z} - s_{v,0})}$ where $s_{v,0} \approx 2.8$ (gravity is balanced by the fluid inertia). Basically, equation 4.1 predicts that for any solution $\bar{U}(\bar{z})$ with initial velocity $\bar{U}_0$, the curve will collapse on the master curve $M_v(\bar{z})$ after translation along the $\bar{z}$ axis by a distance $M_v^{-1}(\bar{U}_0)$ on the right, where M_v^{-1} is the functional inverse of M_v.

For the glycerin curtain flow presented in figure 4.1, we have $z_v = 1.4$ cm (which is smaller than the curtain length $L_c = 30$ cm) and $U_0 = 0.05$ m/s which gives $\bar{U}_0 = U_0/\sqrt{gz_v} = 0.14$ and $M_v^{-1}(\bar{U}_0) = 0.55$. Therefore, shifting the dimensionless curve $\bar{U}(\bar{z})$ by a distance 0.55 on the right makes the experimental data collapse on

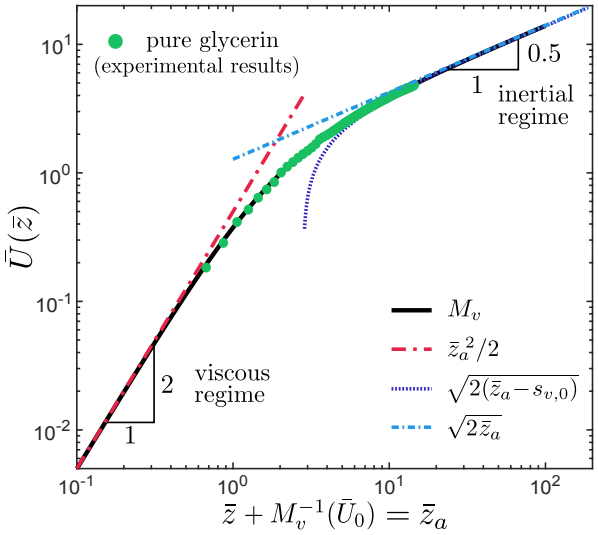

Figure 4.10 – Superposition of the experimental velocity field of the pure glycerin curtain of figure 4.1 ($\bar{U}_0 = 0.14$) and of the Newtonian master curve shown previously in figure 1.3.b. The master curve M_v is characterised by an initial sub-gravitational viscous regime and an asymptotic free-fall regime (equation 1.25).

the master curve, as shown in figure 4.10 in log-log scale. In fact, we tried to observe a fully developed the viscous regime (equation 1.26) using honey but the boundary layer developing along the guides had unfortunately completely invaded the curtain after 4 cm of fall (see discussion in §3.1.4). Glycerin was a good compromise: it is viscous enough to observe the intermediate inertio-viscous regime and inviscid enough to measure the flow over a considerable distance without guide effects.

4.3.3 Viscoelastic scaling

As will be presented in §4.3.4, many aspects of the Newtonian curtains theory presented in the previous section are analogous to the description of viscoelastic curtains. Hence, in order to find the appropriate length and velocity scales of viscoelastic curtains, we first use the general force balance equation 1.14 derived in §1.1.2. Then, a simple model giving the same result is presented. We recall that for Newtonian curtains, the mean normal stress difference was simply $\Delta = 4\eta \mathrm{d}U/\mathrm{d}z$. In the case of a viscoelastic liquid however, a more general constitutive equation must be used to close the system. An attempt of closure using the Oldroyd-B model will be provided in §4.5. Note that equation 1.14 can reasonably be used for the curtains presented in this manuscript since the local slenderness ratio $|\mathrm{d}h/\mathrm{d}z|$ is less than one. The data of figure 4.4 are a typical example where $\mathrm{d}h/\mathrm{d}z$ goes from $+0.1$ at $z = 0$ to a minimum value of about -0.06 after die swell, and is of order -10^{-4} at $z = 20$ cm from the slot.

Force balance equation We can use equation 1.14 to find the appropriate scalings of viscoelastic curtain flows without specifying any particular form of the constitutive equation. We know from the experimental results of §4.2.3, that the extensional relaxation time τ_{fil} of the solution is of primary importance. Therefore, let us write equation 1.14 in a Lagrangian form where we introduce time

$$t = \int_0^z \frac{\mathrm{d}z^*}{U(z^*)} \tag{4.2}$$

We obtain

$$\frac{\mathrm{d}U}{\mathrm{d}t} = g + \frac{1}{\rho}\frac{\mathrm{d}}{\mathrm{d}t}\left(\frac{\Delta}{U}\right) \tag{4.3}$$

which can be integrated into

$$U - U_1 = g(t - t_1) + \frac{1}{\rho}\left(\frac{\Delta}{U} - \frac{\Delta_1}{U_1}\right) \tag{4.4}$$

where subscript $_1$ refers to any altitude z_1. Introducing τ_{fil} which is the natural (longest) time scale of the polymers, we obtain the dimensionless force balance equation

$$\frac{U - U_1}{g\tau_{fil}} = \frac{t - t_1}{\tau_{fil}} + \frac{\Delta}{\rho g U \tau_{fil}} - \frac{\Delta_1}{\rho g U_1 \tau_{fil}} \tag{4.5}$$

This equation suggests that the natural velocity scale of the flow is

$$U_e = g\tau_{fil} \tag{4.6}$$

Therefore, the natural length scale of the flow is $z_e = U_e\,\tau_{fil}$ which gives

$$z_e = g\tau_{fil}^2 = U_e^2/g \tag{4.7}$$

Simple model The characteristic length scale z_e can also be derived by simple physical arguments. If a polymer molecule follows a free-fall trajectory $U \propto \sqrt{2gz}$, it experiences a spatially decreasing strain-rate field $\dot{\epsilon} = \mathrm{d}U/\mathrm{d}z \propto \sqrt{g/2z}$. It is known that polymer chains go through the coil-stretch transition when they are stretched faster that their natural relaxation rate, i.e. when $\tau_{fil}\,\dot{\epsilon}$ is larger than $1/2$ if taking τ_{fil} as the relevant polymer relaxation time (De Gennes, 1974). Therefore, when considering the free-fall expression of $\dot{\epsilon}(z)$, the polymer chains are expected to exhibit large extensional viscosities as long as $z < z_e = g\tau_{fil}^2$ (without prefactor).

4.3.4 A master curve for viscoelastic curtains

By analogy with Newtonian curtains, we can now use the scalings 4.6 and 4.7 to identify the master curve of the viscoelastic curtain flow. First, we plot $U(z)/U_e$ as a function of $(z - z_1)/z_e$ where $z_1 \approx 2.5$ mm (not shown). We obtain similar curves which, like in figure 1.3.a, seem to rescale on a unique master curve after translation along the horizontal axis. Indeed, when shifting each curve by a certain dimensionless distance z_{shift}, we obtain a good collapse of the velocity profiles with less than 20% error, as shown in figure 4.11.a in log-log scale. Our experimental data covers seven decades in z/z_e.

Master curve

We introduce dimensionless variables

$$\hat{z} = z/z_e \qquad \text{and} \qquad \hat{U} = U/U_e \tag{4.8}$$

The master curve $M_e(\hat{z})$ is characterised by two regimes:

$$M_e(\hat{z}) = \begin{cases} K\hat{z}^{\alpha} & \hat{z} \ll 1 : \text{ elastic regime} \\ \sqrt{2\,(\hat{z} - s_{e,0})} & \hat{z} \gg 1 : \text{ inertial regime} \end{cases} \tag{4.9}$$

where $K = 1.3 \pm 0.2$ and $\alpha = 0.92 \pm 0.02$. Note that we only consider in figure 4.11.a the experimental data which are presumably not influenced by the downstream boundary condition. This includes the unstable (modulated) HPAM curtains mentioned in §4.1.2, showing that the instability does not affect the average velocity field. This result also confirms that the shear rheology parameters such as η_0, η_p and n play no major role in the description of the curtain flow, as well as the flexibility parameter b. We measure that M_e^2 reaches an oblique asymptote of equation $M_e^2 = 2(\hat{z} - s_{e,0})$ in the free-fall regime where $s_{e,0} = 6 \pm 2$.

The value of z_{shift}, which is specific to each velocity field, is presented in figure 4.11.b as a function of the dimensionless initial velocity

$$\hat{U}_1 = \hat{U}(\hat{z}_1) = \frac{U_1}{U_e} \tag{4.10}$$

where $U_1 = U(z_1)$. We measure that $z_{shift} \approx (\hat{U}_1/K)^{1/\alpha}$ for low initial velocities $\hat{U}_1 \ll 1$ and that $z_{shift} \approx \hat{U}_1^2/2$ for large initial velocities $\hat{U}_1 \gg 1$, which suggests that $z_{shift} = M_e^{-1}(\hat{U}_1)$. Finally, we can write that

$$\boxed{\hat{U}(\hat{z}) = M_e\left(\hat{z} - \hat{z}_1 + M_e^{-1}(\hat{U}_1)\right)} \tag{4.11}$$

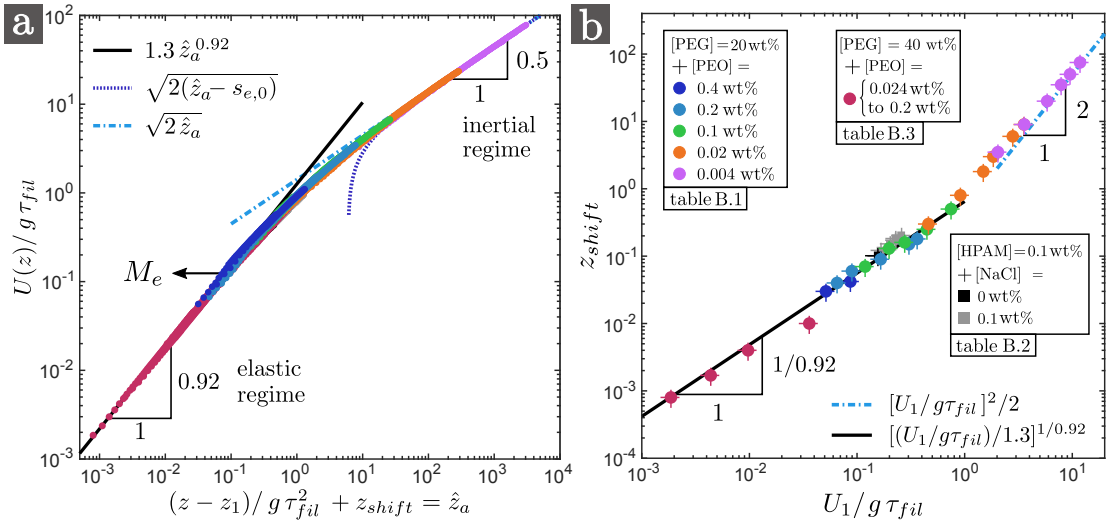

Figure 4.11 – (a): Master curve of viscoelastic curtains. Dimensionless velocity field $U(z)/g\tau_{fil}$ against $(z-z_1)/g\tau_{fil}^2 + z_{shift}$ in log-log scale, where $z_1 \approx 2.5$ mm, and where each curve is translated by a distance z_{shift} in order to rescale all the data on a single curve. The master curve M_e is characterised by an initial sub-gravitational elastic regime and an asymptotic free-fall regime (equation 4.9). (b): When plotting z_{shift} against $U_1/g\tau_{fil}$, we find that $z_{shift} = M_e^{-1}(U_1/g\tau_{fil})$. We only consider the curtain flows which are presumably not influenced by the downstream boundary condition. For the PEO solutions with 40 wt% PEG solvent of table B.3, we only take the longest curtains, for example $L_c = 200$ cm for the data of figure 4.5.a. Besides, for the PEO and HPAM solutions of tables B.1 and B.2 (top) which correspond to curtains of length $L_c = 30$ cm, we show the velocity profile for $z < 20$ cm only for the solutions with extensional relaxation times $\tau_{fil} \leq 0.2$ s since the experiments reported in §4.2.1 suggest that the effect of the downstream boundary condition is out of frame.

This formula is completely analogous to the Newtonian curtain flow since equation 4.1 also gives $\bar{U}(\bar{z}) = M_v\left(\bar{z} - \bar{z}_1 + M_v^{-1}(\bar{U}_1)\right)$ for any altitude $z_1 \geq 0$. However, since the die swell flow for $0 < z < z_1$ is not captured by equation 4.9, equation 4.11 is only valid for $z \geq z_1$. In particular, $\hat{U}(\hat{z}) \neq M_e\left(\hat{z} + M_e^{-1}(\hat{U}_0)\right)$ where $\hat{U}_0 = U_0/U_e$.

According to equations 4.11 and 4.9, we can show that the elastic regime only exists if U_1 is much smaller than U_e, i.e. $\hat{U}_1 \ll 1$. This important result can be summarised as

- $\hat{U}_1 \ll 1 \quad \Rightarrow \quad$ elastic regime for $\hat{z} \ll 1$ and inertial regime for $\hat{z} \gg 1$
- $\hat{U}_1 \gg 1 \quad \Rightarrow \quad$ inertial regime only

If $U_1 \ll U_e$ (equivalently $\hat{U}_1 \ll 1$), according to equations 4.9 and 4.11, the elastic regime of the flow ($z \ll z_e$) writes

$$\hat{U}(\hat{z}) = K\left(\hat{z} - \hat{z}_1 + \left(\frac{\hat{U}_1}{K}\right)^{1/\alpha}\right)^{\alpha} \tag{4.12}$$

and corresponds to negligible inertia in the force balance equation 1.14. Note that only two curtains exhibit such a fully developed elastic regime: the 0.2 and 0.11 wt% PEO solutions with 40 wt% PEG solvent (table B.3). For these solutions, the curtain flow is the same within the first 30 cm of the fall for both $L_c = 1.5$ m and 2 m which suggests that the flow has become independent of the downstream boundary condition (figure 4.5.a). However, $z_e = g\tau_{fil}^2$ is respectively $z_e = 12$ m and $z_e = 4.5$ m. Hence, we are not in the ideal limit $L_c \gg z_e$. Therefore, it is not excluded that the data corresponding to the elastic regime in figure 4.11.a are still a bit sensitive to the downstream boundary condition. If that is the case, a curtain of length $L_c \gg z_e$ would potentially exhibit an elastic regime with a value of α closer to 1. Of course, achieving such curtains is very difficult in practice since they would probably break before reaching the free-fall regime due to the shear instability mentioned in §4.2.1.

Note that the transition to plane stagnation flow discussed in §4.2.1 for viscoelastic curtains is analogous to the Newtonian case. In both figures 4.5 and 1.2, the liquid velocity first increases, reaches a maximum value at some distance z_m from the slot, and finally decreases down to $U(L_c) = 0$. Provided that the analogy remains true, we speculate that the presence of the plate affects the viscoelastic curtain flow within a distance from the plate which is of order z_e.

Regardless of the value of the initial velocity, in the inertial regime, again using equations 4.11 and 4.9, the dimensionless velocity field writes

$$\hat{U}(\hat{z}) = \sqrt{\hat{U}_1^2 + 2(\hat{z} - \hat{z}_1 - s_e)} \tag{4.13}$$

where $s_e = s_{e,0} + \hat{U}_1^2/2 - M_e^{-1}(\hat{U}_1)$. In the case of a negligible initial velocity $U_1 \ll U_e$, this regime is reached for $z \gg z_e$. On the other hand, for initial velocities $U_1 \gg U_e$, inertia dominates over elastic forces even close to the slot and the flow is well approximated by a free-fall $U^2 = U_1^2 + 2g(z - z_1)$ since s_e goes to zero.

In figure 4.12.a and 4.12.b, we present respectively the dimensionless extension rate $\dot{\epsilon}\tau_{fil}$ where $\dot{\epsilon} = \mathrm{d}U/\mathrm{d}z$ and the dimensionless acceleration $[U\mathrm{d}U/\mathrm{d}z]/g$ as a function of $\hat{z} - \hat{z}_1 + z_{shift}$. The experimental data collapse on master curves which correspond to M_e' and $M_e\, M_e'$ respectively, where $'$ denotes spatial derivation $\mathrm{d}/\mathrm{d}\hat{z}$. According to figure 4.12.a, the extension rate is of the order of $1/\tau_{fil}$ in the elastic regime $z \ll z_e$. More precisely, $\dot{\epsilon}\tau_{fil}$ weakly decreases and is initially larger than the

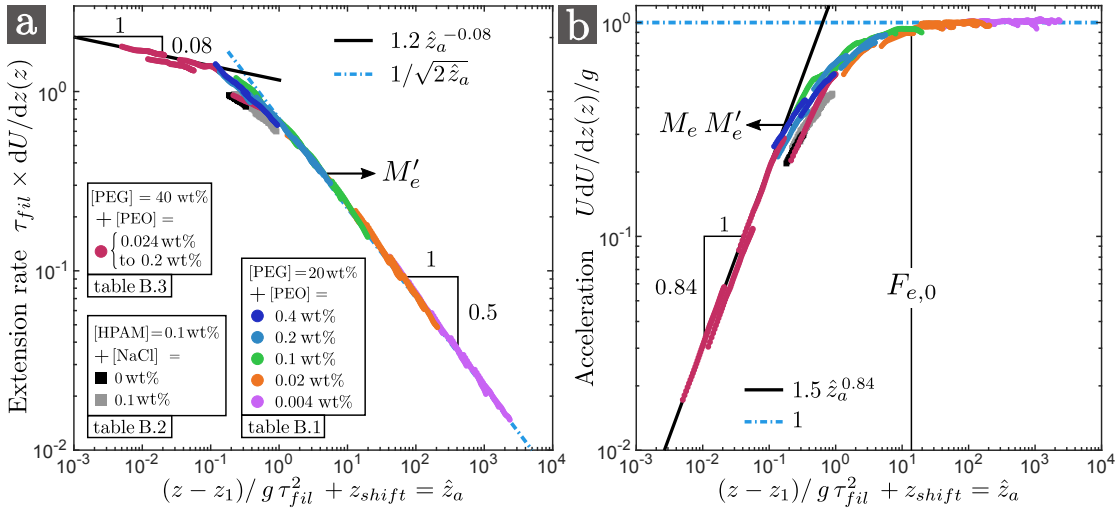

Figure 4.12 – (a) Dimensionless extension rate $\tau_{fil}\,\mathrm{d}U/\mathrm{d}z(z)$ and (b) dimensionless acceleration $U\mathrm{d}U/\mathrm{d}z(z)/g$ versus $(z - z_1)/z_e + z_{shift}$ for the curtains of figure 4.11. The master curve M_e reaches the asymptotic free-fall regime at z/z_e about $F_{e,0} = 12 \pm 5$ since $M_e\, M'_e(F_{e,0}) = 0.95$, where 0.95 is an arbitrary value close to 1.

coil-stretch transition value 1/2. This result is reminiscent of the filament thinning experiment described in §3.2.2 for which $\dot{\epsilon}\,\tau_{fil} = 2/3$ in the elastic regime. Physically, polymer chains are therefore expected to unravel in the elastic regime since $\tau_{fil}\,\dot{\epsilon} = O(1)$, and to return progressively to a coil state in the inertial regime where $\tau_{fil}\,\dot{\epsilon}$ decreases and becomes $\ll 1$.

Polymer extension in the elastic regime

We can now give a physical argument for the absence of finite extensibility effects in the curtain flow. First we need to estimate the total Hencky strain ϵ_e accumulated by the polymer chains in the elastic regime. We use the following high estimation

$$\epsilon_e - \epsilon_1 \approx \int_{t(z_1)}^{t(z_e)} \dot{\epsilon}\mathrm{d}t = \int_{z_1}^{z_e} \mathrm{d}U/U = \ln\left(\frac{U(z_e)}{U_1}\right) \tag{4.14}$$

We assume that the Hencky strain after swelling ϵ_1 is less than ϵ_e since polymer chains are expected to unravel more in the curtain extensional flow than in the slot shear flow. Using equation 4.12 and taking $\alpha = 1$ for simplicity, we find $U(z) \approx U_1 + K(z - z_1)/\tau_{fil}$ and therefore $U(z_e) \approx U_1 + KU_e$ assuming $z_1 \ll z_e$. Finally, we get $\epsilon_e \approx \ln(1 + K/\hat{U}_1)$. This value has to be compared to the critical Hencky strain ϵ^* above which the polymer deformation saturates to its maximum value. It can be estimated from CaBER data shown in figure 3.10. We get $\epsilon^* \approx 6$ for PEO and salted HPAM solutions and $\epsilon^* \approx 4$ for unsalted HPAM solutions. The condition for no finite extensibility effect writes $\epsilon_e \ll \epsilon^*$, i.e. polymer chains must not reach their maximum length during the elastic regime. After injecting the estimation of

ϵ_e, the condition becomes $\hat{U}_1 \gg K/(\exp(\epsilon^*) - 1)$ which is 2×10^{-3} for PEO and salted HPAM solutions and 2×10^{-2} for unsalted HPAM solutions. This condition is fulfilled in most experiments (see values of $\hat{U}_1$ in figure 4.11.b) and the finite extensibility parameter b does not play a major role.

Length of the sub-gravitational regime

We can now derive an expression of the length z_e^* of the sub-gravitational part of the curtain introduced in §4.3.1. Let us define this length as $U\mathrm{d}U/\mathrm{d}z(z = z_e^*) = 0.95g$ where 0.95 is an arbitrary value close to 1 and let $F_{e,0}$ be such that $M_e\, M_e'(\hat{z} = F_{e,0}) = 0.95$. We obtain $F_{e,0} = 12 \pm 5$ (figure 4.12.b). Therefore, according to equation 4.11, we have

$$z_e^* = F_e \times z_e \qquad \text{with} \qquad F_e = F_{e,0} + \hat{z}_1 - M_e^{-1}(\hat{U}_1) \tag{4.15}$$

where the prefactor F_e is a decreasing function of the initial velocity.

4.3.5 An elasticity number

We have characterised the curtain flow of both Newtonian and viscoelastic liquids. In particular, the length of the sub-gravitational part of the curtain is given respectively by z_v and z_e (equations 1.17 and 4.7) with prefactors which are decreasing functions of the initial velocity. For a given viscoelastic liquid with zero-shear viscosity η_0, density ρ and extensional relaxation time τ_{fil}, we define a dimensionless number

$$El = \left(\frac{z_e}{z_v}\right)^{1/2} = \frac{\tau_{fil}\, g^{2/3}}{(4\eta_0/\rho)^{1/3}} \tag{4.16}$$

which measures the relative importance of elastic to viscous effects in the curtain flow. In the general case, the exact definition of the elasticity number is the ratio between the Weissenberg number $Wi = \tau U/L$ (equation 2.26) and the Reynolds number $Re = \rho UL/\eta$ (equation 2.31) defined in chapter 2, where U and L are characteristic velocity and length scales. The resulting number is independent of velocity and writes

$$El = \frac{Wi}{Re} = \frac{\tau\, \eta}{\rho L^2} \tag{4.17}$$

Hence, the dimensionless number defined in equation 4.16 is an elasticity number based on the viscous length scale $z_v = ((4\eta_0/\rho)^2/g)^{1/3}$ and on the extensional relaxation time τ_{fil}.

Values of *El* are reported in tables B.1, B.2 and B.3. As expected, it is larger than one since $z_e \gg z_v$ in our experiments, except for solutions with low polymer concentrations exhibiting a free-fall, for which both z_e and z_v are less than a few millimetres. When adding polymer molecules to a viscous Newtonian solvent with a large value of z_v, we can expect a transition from the viscous regime described in §4.3.2 with exponent 2 (equation 1.26) to the elastic regime described in §4.3.4 with exponent $\alpha = 0.92$ (equation 4.12) when *El* becomes larger than one.

4.4 Elastic stress at the slot exit

In this section, we address the question of the origin of the elastic stress in the curtain. In the previous section, we have assumed that it comes mostly from the stretching of polymer molecules in the curtain, especially in the elastic regime where $\tau_{fil}\,\dot{\epsilon} = O(1)$. However, one other possible origin lies is the initial stretching (or "pre-shear") of polymer molecules in the slot, which may lead to unrelaxed stress on top of the curtain. We start this discussion by investigating the die swell ratio.

4.4.1 The die swell ratio

The liquid swells at the slot exit due to the recovery of the elastic strain imparted into the die. In the theory of Tanner (1970, 2005), and Huang & White (1979), the swelling ratio is

$$\xi = \frac{U_s}{U_1} = \left[1 + \frac{3-m}{m+1}\left(\frac{N_1}{2\sigma}\right)_w^2\right]^{1/4} \tag{4.18}$$

where $N_1 = \sigma^*_{zz} - \sigma^*_{yy}$ and $\sigma = \sigma^*_{yz}$ are respectively the normal stress difference and the shear stress, m is such that $N_1 \propto \sigma^m$, and subscript $_w$ indicates that N_1 and σ are to be taken at the wall of the slot, i.e. at $y = a$. Note that $\boldsymbol{\sigma}^*$ is the local stress tensor. This formula, which was developed for melts, has also been used in the context of polymer solutions (Allain et al., 1997). Let us compare the experimental data presented in figure 4.4 for the PEO solution of table B.4 with Tanner's prediction 4.18. Since the wall shear rate $\dot{\gamma}_w \sim U_s/a$ is larger than the shear rate $\dot{\gamma}_c = 3\ \mathrm{s}^{-1}$ at which shear-thinning starts, the Carreau law 3.7 can be reduced to an Ostwald power law $\sigma = K_0\dot{\gamma}^n$ with $K_0 = \eta_0/\dot{\gamma}_c^{n-1}$ and the wall shear rate can be simplified to

$$\dot{\gamma}_w = \frac{2n+1}{n}\,\frac{U_s}{a} \tag{4.19}$$

With U_s ranging between 0.045 and 0.14 m/s and $n = 0.81$, we find that $\dot{\gamma}_w$ ranges

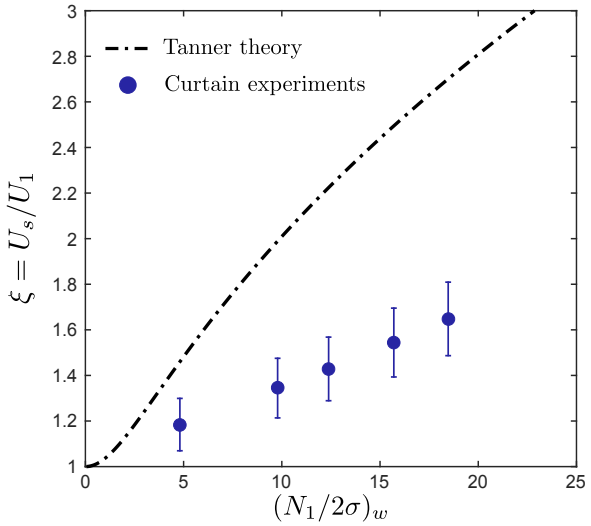

Figure 4.13 – Comparison between the experimental die swell ratio $\xi = U_s/U_1$ for the data of figure 4.4 and the values predicted by Tanner's unconstrained recovery theory (equation 4.18) where we use $(N_1)_w = N_1(\dot{\gamma}_w) = \Psi\dot{\gamma}_w^{\alpha_1}$ and $(\sigma)_w = \sigma(\dot{\gamma}_w) = K_0\dot{\gamma}_w^n$ where $\dot{\gamma}_w$ is the wall shear rate (equation 4.19). Since $N_1 \propto \sigma^m$, we use $m = \alpha_1/n$.

between 290 and 900 s^{-1}. We can reasonably use the parameters of table B.4 since shear rheology measurements are performed for shear rates up to 500 s^{-1} which is close to $\dot{\gamma}_w$.

The experimental die swell ratio ξ is shown in figure 4.13 along with the predictions of equations 4.18 and 4.19. The theory clearly overpredicts the die swell ratio. This is not surprising since the unconstrained recovery theory of Tanner is only valid if the extruded sheet is load-free, i.e. in the absence of tensile stress. A correction has been proposed in the context of fibre spinning (White & Roman, 1976) (which is equivalent to film casting) but not in the context of free jets or curtains subjected to gravity only. The die swell ratio is generally assumed to be only slightly modified by gravity for free jets (Richardson, 1970). However, in the planar case, Huang & White (1979) report significant discrepancies between Tanner's theory and their experimental results when extruding melts from slit dies into ambient air, like in figure 4.13. They report that Tanner's law was recovered when extruding into a bath of silicone oil with the same density, in which case the curtain no longer necks down after swelling due to gravity (i.e. h and U are constant). In the latter case, according to the force balance equation 1.14 without inertia, Δ must therefore be constant. In the theory of Tanner, it is assumed that most fluid particles "rapidly" switch from the state of fully developed flow in the slot to a state of zero stress measured relative to atmospheric pressure as datum. Here, "rapidly" means that the time needed to clear the exit zone is short compared to the polymer relaxation time, i.e. $U_s\tau_{fil}/a \gg 1$ which is the case in figure 4.13. In other words, the mean

normal stress difference Δ defined in §1.1.2 in equation 1.13 switches from a value Δ_s inside the slot to a value $\Delta_1 = \Delta(z_1)$ after swelling (figure 4.9) which is $\Delta_1 = 0$ in the absence of gravity. The discrepancy in figure 4.13 suggests that $\Delta_1 \neq 0$ in the presence of an axial tension due to gravity.

These results suggest that the elastic stress imparted into the die may have an effect on the curtain flow downstream. In order to quantify this effect, we now compare the value of the mean normal stress difference Δ_s inside the die and Δ_1 after swelling.

4.4.2 Mean normal stress difference before and after swelling

Before swelling

Δ_s can be estimated analytically. We consider a shear-thinning fluid following an Ostwald power law $\sigma = K_0\dot{\gamma}^n$ for simplicity. Assuming a fully developed Poiseuille flow, a classical calculation shows that the local velocity inside the slot is

$$u(y) = U_s \frac{2n+1}{n+1}\left[1 - \left(\frac{\mid y \mid}{a}\right)^{1+\frac{1}{n}}\right] \tag{4.20}$$

where $U_s = q/2a$, from which equation 4.19 is recovered. Using $N_1 = \Psi\dot{\gamma}^{\alpha_1}$ and $\dot{\gamma} = \mathrm{d}u/\mathrm{d}y$. we find

$$\Delta_s = \frac{1}{a}\int_0^a N_1 \,\mathrm{d}y = \frac{n}{\alpha_1 + n}\left(\frac{2n+1}{n}\right)^{\alpha_1} \Psi \left(\frac{U_s}{a}\right)^{\alpha_1}. \tag{4.21}$$

Note that for an Oldroyd-B fluid (for which $n = 1$ and $\alpha_1 = 2$), we can easily show that a parabolic flow $u(y)$ is an exact solution. We obtain equation 4.20 with prefactor 3/2. The constitutive equation gives the following local stress components: $\sigma^*_{yz} = (\eta_s + \eta_p)\dot{\gamma}(y)$ and $\sigma^*_{zz} - \sigma^*_{yy} = 2\eta_p\tau[\dot{\gamma}(y)]^2$ where $\dot{\gamma} = \mathrm{d}u/\mathrm{d}y$. This means that the normal stress at a distance y from the symmetry axis ($y = 0$) only depends on the local velocity gradient. In particular, the polymer molecules are not deformed at $y = 0$ (since $\dot{\gamma} = 0$) and are elongated close to the wall where the shear rate is maximum.

After swelling

Viscoelastic liquid Now we show how to obtain the value of the mean normal stress difference Δ_1 after swelling based on the Lagrangian force balance equation derived in §1.1.2.

We know from figure 4.12.a that the extension rate goes to 0 far from the slot for an infinitely long curtain. Therefore, we can reasonably assume that the mean normal stress difference Δ becomes negligible in the asymptotic free-fall regime. In particular, in the free-fall regime, according to equation 4.5 where we choose to start from $z_1 \approx 2.5$ mm, the curtain velocity U reaches an oblique asymptote of equation

$$\frac{U - U_1}{g\tau_{fil}} = \frac{t - t_1}{\tau_{fil}} - A_e \tag{4.22}$$

where

$$A_e = \frac{\Delta_1}{\rho g U_1 \tau_{fil}} = \frac{\Delta_1}{\rho U_1 U_e} = \frac{\hat{\Delta}_1}{\hat{U}_1} \tag{4.23}$$

where

$$\hat{\Delta}_1 = \frac{\Delta_1}{\Delta_e} \tag{4.24}$$

and

$$\Delta_e = \rho g z_e = \rho U_e^2 = \rho (g\tau_{fil})^2 \tag{4.25}$$

which is the natural scaling for Δ in the force balance equation 1.14 for a low viscosity elastic liquid.

To estimate A_e, we plot $(U - U_1)/g\tau_{fil}$ as a function of $(t - t_1)/\tau_{fil}$, as shown in figure 4.14.a for some liquids with extensional relaxation times τ_{fil} ranging between 0.008 s and 0.68 s. Since we could not always observe the asymptotic free-fall regime, we use the master curve M_e identified in figure 4.11.a to extend the experimental data and we fit the free-fall regime by an oblic asymptote to obtain the value of A_e (figure 4.14.a). In order to validate this method, we performed an additional experiment where a long curtain is observed at various vertical positions to obtain a more complete velocity field $U(z)$. The extensional relaxation time of this liquid (which is close to the degraded ($t_d = 100$ min) 0.4 wt% PEO solution with 20 wt% PEG solvent presented in table B.1) was $\tau_{fil} = 0.1$ s. Unfortunately, the curtain spontaneously breaks at $z \approx 100$ cm due to the shear instability mentioned in §4.2.1 and we can still not observe the free-fall regime since $z_e^* \approx 120$ cm. However, the flow for $z \leq 100$ cm fits perfectly onto the master curve M_e, and the data presented in figure 4.14.a are comparable to the data corresponding to the almost same liquid observed for $z \leq 20$ cm, which validates the method presented here to estimate A_e.

Values of A_e are presented in figure 4.14.b for various solutions as a function

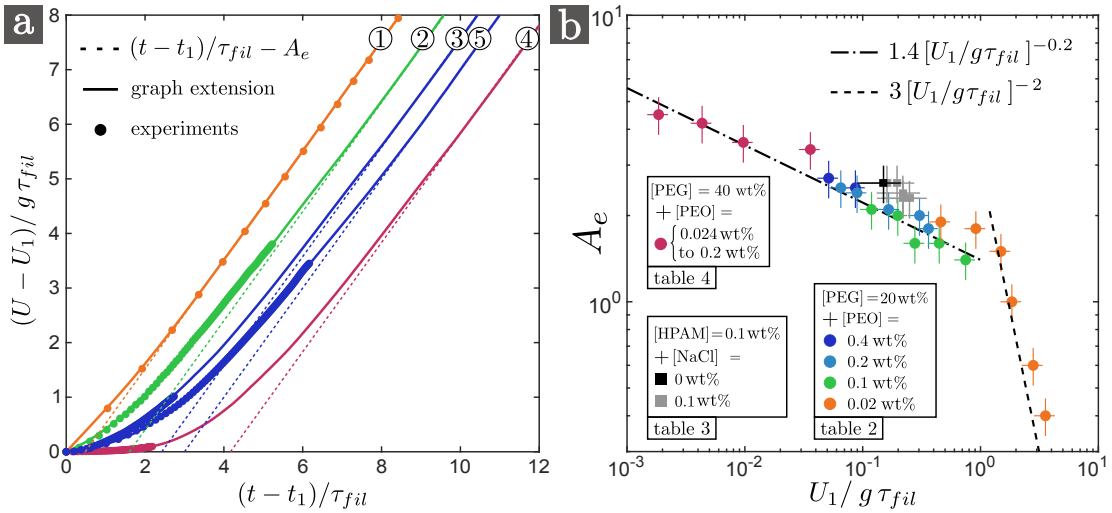

Figure 4.14 – (a): $(U-U_1)/g\tau_{fil}$ versus $(t-t_1)/\tau_{fil}$, where subscript $_1$ refers to the altitude $z_1 \approx 2.5$ mm and t is the Lagrangian time (equation 4.2), for five liquids. Liquid 1: degraded ($t_d = 100$ min) 0.02 wt% PEO solution with 20 wt% PEG solvent (table B.1), Liquid 2: degraded ($t_d = 60$ min) 0.1 wt% PEO solution with 20 wt% PEG solvent (table B.1), Liquid 3: degraded ($t_d = 100$ min) 0.4 wt% PEO solution with 20 wt% PEG solvent (table B.1), Liquid 4: 0.11 wt% PEO solution with 40 wt% PEG solvent (table B.3). The curtain length L_c is 30 cm for liquids 1, 2 and 3 and is 200 cm for liquid 4. Liquid 5: liquid close to liquid 3 for $L_c = 100$ cm and observed at various vertical positions to obtain a more complete velocity field $U(z)$. The experimental data is extended with the master curve M_e (figure 4.11) and the free-fall regime is fitted by equation 4.22. (b): Values of A_e versus $U_1/U_e = U_1/g\tau_{fil}$ for some of the liquids of figure 4.11.

of the dimensionless initial velocity $\hat{U}_1 = U_1/U_e$. It ranges from $A_e = 4.5$ for the solution with the largest relaxation time to negligibly small values $A_e < 0.4$ for the solutions with low extensional relaxation times which are almost immediately in the free-fall regime after leaving the slot. For $\hat{U}_1 \leq 1$, the experimental data are well captured by

$$A_e \approx 1.4\,\hat{U}_1^{-0.2} \tag{4.26}$$

which, according to equation 4.23, gives finally

$$\Delta_1 \approx 1.4\,\rho g^{1.2} U_1^{0.8} \tau_{fil}^{1.2} \tag{4.27}$$

A different behaviour is observed for $\hat{U}_1 \geq 1$. The slope switches from about -0.2 to about -2 (see figure 4.14).

Newtonian liquid As we now show, this result is analogous to Newtonian curtains for which die swell can be neglected (Tanner, 2000). Since there is no internal relaxation time, the mean normal stress difference instantaneously switches from $\Delta_s = 0$ inside the slot to a value $\Delta_0 = \Delta(z = 0)$ at the slot exit. Since we know

the constitutive equation, the derivation is straightforward. According to equation 1.16, Δ_0 is given by

$$\Delta_0 = 4\eta \left.\frac{\mathrm{d}U}{\mathrm{d}z}\right|_{z=0} \tag{4.28}$$

In dimensionless form, we obtain

$$\bar{\Delta}_0 = \bar{U}'(\bar{z}=0) \qquad \text{where} \qquad \bar{\Delta} = \frac{\Delta}{\Delta_v} \tag{4.29}$$

and

$$\Delta_v = \rho g z_v = \rho U_v^2 = \rho(4\eta g/\rho)^{2/3} \tag{4.30}$$

which is the natural scaling for Δ in the force balance equation 1.14 for a viscous Newtonian liquid. Equations 1.26 and 4.29 gives

$$\bar{\Delta}_0 = (2\,\bar{U}_0)^{1/2} \qquad \text{for} \quad \bar{U}_0 \ll 1 \tag{4.31}$$

which, in dimensional variable, gives

$$\Delta_0 = 2\sqrt{2}\,\rho\,(gU_0\eta/\rho)^{0.5} \tag{4.32}$$

We can also define

$$A_v = \frac{\Delta_0}{\rho U_0 U_v} = \frac{\bar{\Delta}_0}{\bar{U}_0} \tag{4.33}$$

and we obtain

$$A_v = \sqrt{2}\,\bar{U}_0^{-1/2} \qquad \text{for} \quad \bar{U}_0 \ll 1 \tag{4.34}$$

where the exponent -0.5 is larger (in absolute value) than the exponent -0.2 found in the viscoelastic case. Note that for $\bar{U}_0 \gg 1$, in which case the curtain flow is a free-fall even close to the slot, we have

$$\bar{\Delta}_0 = 1/\bar{U}_0 \qquad \text{and} \qquad A_v = \bar{U}_0^{-2} \qquad \text{for} \quad \bar{U}_0 \gg 1 \tag{4.35}$$

which is analogous to the $\hat{U}_1 \geq 1$ part of the curve of figure 4.14.b.

Physical meaning In order to get more information about the physical meaning of Δ_1, we can use the integrated force balance equation 4.4 which we write here in its Eulerian form for more clarity

$$2h_1\Delta_1 - 2h\Delta = \rho q(U_1 - U) + 2\rho g \int_{z_1}^{z} h(z^*)\mathrm{d}z^* \tag{4.36}$$

where $2h_1 = 2h(z_1) = q/U_1$. Note that, when plotting the right-hand side of this equation, we always find a positive value (not shown), unless the flow is a free-fall in which case it is equal to 0. Hence, $h_1\Delta_1 \geq h\Delta$. In the elastic regime ($z \ll z_e$), the inertia term is negligible and the weight of the curtain between z_1 and z is supported by the difference between the contact forces $2h_1\Delta_1$ and $2h\Delta$ acting respectively on the upper and lower side. This shows that Δ_1 is the mean normal stress difference which is necessary to bear the weight of the sub-gravitational part of the curtain. We can derive the previous results for viscoelastic liquids by neglecting inertia and returning to the Lagrangian description. In the elastic regime ($t \ll \tau_{fil}$), using $q = 2hU$ and the definition of time (see equation 4.2), we obtain

$$\frac{\Delta_1}{U_1} - \frac{\Delta}{U} \approx \rho g(t - t_1) \tag{4.37}$$

Assuming that Δ becomes negligible at the transition to free-fall ($t \approx \tau_{fil}$) and that $t_1 \ll \tau_{fil}$, we find that

$$\Delta_1 \propto \rho g U_1 \tau_{fil} \tag{4.38}$$

with a prefactor A_e which must be a decreasing function of the dimensionless initial velocity $\hat{U}_1$ since the length of the sub-gravitational part of the curtain is $z_e^* = F_e \times z_e$ where F_e is a decreasing function of $\hat{U}_1$. In particular, as expected from the discussion about Tanner's theory, $\Delta_1 = 0$ in the absence of gravity. The exact same reasoning can lead to an analogous conclusion for Newtonian curtains.

Comparison between Δ_s and Δ_1

For the experiments presented so far, using equations 4.21 and 4.23, we obtain

$$\frac{\Delta_1}{\Delta_s} = \left[\frac{n}{\alpha_1 + n}\left(\frac{2n+1}{n}\right)^{\alpha_1}\right]^{-1} \frac{A_e\, \rho g \tau_{fil} U_1}{\Psi\,(U_s/a)^{\alpha_1}}. \tag{4.39}$$

Estimating A_e by the method presented in this section, we find $\Delta_1/\Delta_s = O(1)$. More precisely, it decreases from 2.5 to 0.5 for the liquid of table B.4 used in figures 4.4 and 4.13 when increasing the flow rate, and it is equal to 0.6 ± 0.1 for all PEO solutions with 40 wt% PEG solvent of table B.3. In the latter case, the elastic stress rapidly decreases when leaving the slot as the polymer chains undergo a rapid strain $\epsilon = \ln(U_1/U_s) = -\ln(\xi) < 0$ during swelling. However, in the presence of gravity, the sheet is not load-free and the swelling ratio is less than expected since some elastic stress $\Delta_1 \neq 0$ has to bear the weight of the sub-gravitational part of the

curtain. In other words, the polymer chains can not recover their equilibrium shape after swelling.

The last question which remains unanswered is the link between Δ_1 and Δ_s. Since the experiments presented so far indicate that $\Delta_1/\Delta_s = O(1)$, one might think that Δ_1 is intrinsically linked to Δ_s. If so, the origin of the polymeric stress would lie in the shear deformation of the polymer chains in the slot, in which case the length z_e^* of the sub-gravitational regime would be a function of Δ_s. In particular, a curtain of vanishing slot velocity U_s would exhibit no sub-gravitational elastic regime (although $U_1 \ll g\tau_{fil}$) since Δ_s, and therefore Δ_1, would be arbitrarily small. However the fact that we find $\Delta_1/\Delta_s = O(1)$ might also be a coincidence. To answer this question, we need to compare the flow of two curtains made of the same liquid but with radically different values of Δ_s. According to equations 4.21 and 4.27, changing the slot thickness $2a$ while keeping the same initial velocity U_1 is a good solution: if Δ_1 does not change while Δ_s changes, it means that the origin of the polymeric stress lies in the extensional deformation of polymer molecules once in the free-surface curtain. If so, the description of the flow provided in 4.3.4 is universal and the master curve M_e does not depend on the pre-shear history upstream of the curtain.

4.4.3 The influence of the die geometry

In order to check if Δ_1 is intrinsically linked to Δ_s or not, i.e. whether or not the curtain flow is affected by the history of polymer deformations upstream of the curtain, we compare the flow of two curtains of same length and made of the same liquid (table B.4).

Slot Die The first curtain is extruded from the slot die of figure 3.2.b where the slot thickness $2a = 1$ mm. The flow rate is $q = 1.4$ cm^2/s, the mean velocity is $U_s = q/2a = 0.14$ m/s in the slot and $U_1 = 0.085$ m/s at $z_1 = 2.5$ mm from the slot exit, after an initial swelling of ratio $\xi = U_s/U_1 = 1.6 > 1$.

Inclined plane The second curtain is formed using a second "die" presented in figure 4.15.a where the liquid flows freely along an inclined plane before forming a vertical curtain when falling off the edge. Imposing a flow rate $q^\star = 0.85$ cm^2/s $< q$, we measure that the thickness of the liquid layer flowing down the plane is $2a^\star = 2.5$ mm $> 2a$, which gives a mean velocity $U_s^\star = q^\star/2a^\star = 0.034$ m/s $< U_s$. We measure that the mean vertical velocity is $U_1^\star = 0.088$ m/s $\approx U_1$ at 3 mm from the edge of the plane. Therefore, the thickness of the liquid rapidly decreases by a factor

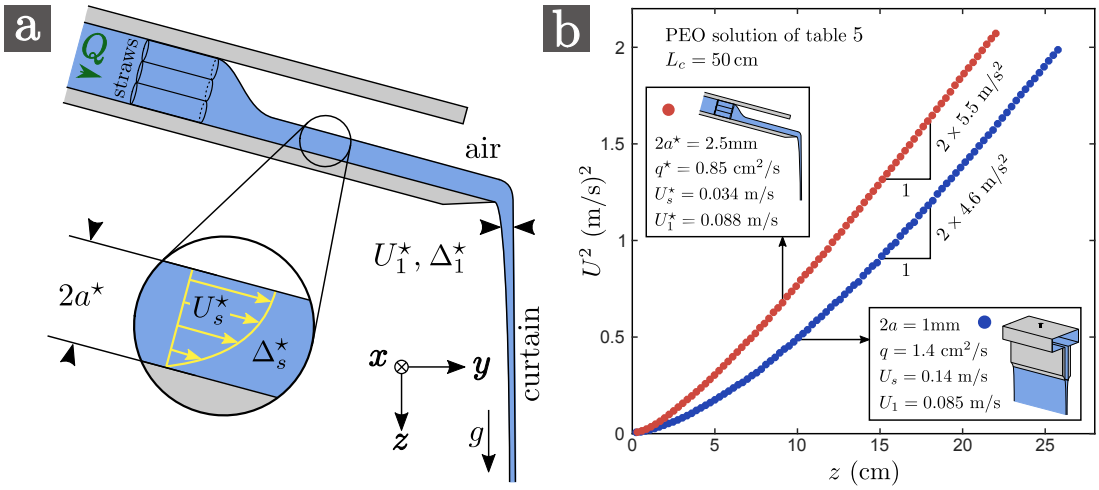

Figure 4.15 – (a): Sketch of a curtain formed when a liquid layer of thickness $2a^\star$ falls off the edge of an inclined plane with mass flow Q. A grid of straws is used to homogenise the flow in the x direction and the linear flow rate is $q = Q/\rho l$ where l is the curtain width. Guides are used to avoid sheet retraction. (b): Using the PEO solution of table B.4, comparison of the squared velocity field $U^2(z)$ of the curtain formed using the inclined plane and using the slot die of figure 3.2.*b*. Both curtains start with comparable initial velocities U_1 and share the same length $L_c = 50$ cm. The typical shear rate is $U_s/a = 280$ s^{-1} in the slot but is only only $U_s^\star/2a^\star = 14$ s^{-1} along the inclined plane, i.e. 20 times less.

$\xi^\star = U_s^\star/U_1^\star = 0.39 < 1$ at the edge of the plane. The swelling observed for the slot die is now replaced by a contraction.

As presented in figure 4.15.b, the flows of these two curtains are slightly different. The liquid velocity, which is initially comparable since $U_1^\star \approx U_1$, increases a bit faster when falling off the edge of the plane than when being extruded from the slot. For example, the liquid acceleration is respectively 5.5 m/s^2 and 4.6 m/s^2 at $z = 18$ cm. Therefore, the flow of the curtain falling of the inclined plane does not perfectly collapse on the master curve M_e identified in figure 4.11.a. Let us estimate Δ_s and Δ_1 for these two curtains.

We find $\Delta_s \approx 690$ Pa for the slot die (equation 4.21). For the inclined plane, we estimate the mean normal stress difference $\Delta_s^\star$ developed by the liquid when flowing down the plane using equation 4.21 where a is replaced by $2a^\star$ since the flow is a semi-Poiseuille. We find $\Delta_s^\star \approx 1.6$ Pa which is much less than Δ_s. In fact, the general formula for the ratio between $\Delta_s^\star$ and Δ_s depends only on flow parameters. We find

$$\frac{\Delta_s^\star}{\Delta_s} = \left(\frac{U_s^\star}{U_s} \times \frac{a}{2a^\star}\right)^{\alpha_1} = \left(\frac{q^\star}{q} \times \frac{a^2}{2(a^\star)^2}\right)^{\alpha_1} \approx 2 \times 10^{-3} \ll 1 \qquad (4.40)$$

This result suggests that the effect of Δ_s on the curtain flow identified in figure 4.15.b is actually very weak. Indeed, despite a much different flow upstream of the curtain, the curtain flows are quite comparable. In particular, $z_e = g\tau_{fil}^2$ is still the appropriate scaling for the length of the sub-gravitational regime. Therefore, the mean normal stress difference Δ_1 developed a few millimetres below slot or below the edge of the plane respectively must be comparable in both experiments. Using the method described in §4.4.2, we find $A_e \approx 3.4$ for the slot die and $A_e^\star \approx 2.1$ for the inclined plane. In the latter case, note that this estimation is based on comparisons with other curtain flows (of similar extensional relaxation time) extruded from the slot die since the master curve can not be used to extend the experimental data. We find respectively $\Delta_1 \approx 460$ Pa and $\Delta_1^\star \approx 300$ Pa which are indeed comparable, i.e.

$$\frac{\Delta_1^\star}{\Delta_1} = \frac{A_e^\star}{A_e} \approx 0.6 \tag{4.41}$$

For the slot die, the polymeric stress decreases during swelling and $\Delta_1/\Delta_s \approx 0.7 < 1$. However, for the inclined plane, the polymeric stress increases during the contraction at the edge of the plane and $\Delta_1^\star/\Delta_s^\star \approx 180 > 1$. In fact, in both cases, the polymer molecules undergo a rapid strain $\epsilon = \ln(U_1/U_s)$ which is $-0.50 < 0$ for the slot and which is $0.95 > 0$ for the inclined plane. According to figure 3.10, such strains can indeed cause significant modifications of the polymeric stress.

Summary To summarise, the mean normal stress difference switches from a value Δ_s inside the die to a value Δ_1 at the die exit, where Δ_1 is of order $\rho g U_1 \tau_{fil}$ independently of the flow history inside the die, with a prefactor A_e which is a decreasing function of the initial velocity. However, since the flow is slightly modified when changing Δ_s, the prefactor also depends on the die geometry and is an increasing function of Δ_s. The length z_e^* of the sub-gravitational regime is of order $g\tau_{fil}^2$ with a prefactor F_e which is a decreasing function of the initial velocity and which is also an increasing function of Δ_s. In simple words, polymeric stresses in the curtain are mostly due to the extensional stretching of polymer molecules in the curtain (where $\tau_{fil}\,\dot{\epsilon} = 0(1)$ in the elastic regime), with a small correction due to the "pre-shear" in the die.

4.5 Theoretical description using Oldroyd-B

In this section, we provide an attempt of analytical description of the viscoelastic curtain flow using the Oldroyd-B model. This choice is motivated by the simplicity of the model and by the fact that, as suggested by experimental results, the extensional relaxation time is the only relevant rheological parameter. Indeed, a

more realistic model would involve at least one other rheological parameter such as the finite extensibility parameter b in the FENE-P model. As will be developed, some assumptions lead to a simple analytical expression which roughly captures the trends observed in the experimental data, with discrepancies which will be discussed. Hence, we do not mean to say in this section that the Oldroyd-B model is the right model, and we rather investigate the implications of the model in order to derive the basic ideas which will be necessary for a more refined description.

4.5.1 Set of equations

The general force balance equation 1.14 has to be coupled with a constitutive equation giving an expression of the mean normal stress difference Δ defined by equation 1.13. Assuming a fast convergence towards the plug flow, we assume that (at first order) the flow will be well captured by neglecting any y dependence in the constitutive equation, i.e. by treating the flow as a pure planar extensional flow, as done by Taylor when deriving the Newtonian Taylor equation 1.5. Using the Oldroyd-B model (with elastic modulus G and relaxation time τ), since the local extension rate is $\dot{\epsilon}(z) = \mathrm{d}U/\mathrm{d}z$, the components of the mean extra stress tensor $\boldsymbol{\sigma}$ are (assuming a pure planar extensional flow)

$$\sigma_{zz} = 2\eta_s \frac{\mathrm{d}U}{\mathrm{d}z} + \sigma_{p,zz} \qquad \text{and} \qquad \sigma_{yy} = -2\eta_s \frac{\mathrm{d}U}{\mathrm{d}z} + \sigma_{p,yy} \tag{4.42}$$

where (according to equation 2.36 where $\mathrm{d}/\mathrm{d}t$ is replaced by $U\mathrm{d}/\mathrm{d}z$)

$$\begin{cases} \tau U \dfrac{\mathrm{d}\sigma_{p,zz}}{\mathrm{d}z} + \sigma_{p,zz}\left(1 - 2\tau \dfrac{\mathrm{d}U}{\mathrm{d}z}\right) = 2\eta_p \dfrac{\mathrm{d}U}{\mathrm{d}z} \\ \tau U \dfrac{\mathrm{d}\sigma_{p,yy}}{\mathrm{d}z} + \sigma_{p,yy}\left(1 + 2\tau \dfrac{\mathrm{d}U}{\mathrm{d}z}\right) = -2\eta_p \dfrac{\mathrm{d}U}{\mathrm{d}z} \end{cases} \tag{4.43}$$

where η_s is the solvent viscosity and where $\eta_p = G\tau$. The mean normal stress difference is

$$\Delta = \sigma_{zz} - \sigma_{yy} = 4\eta_s \frac{\mathrm{d}U}{\mathrm{d}z} + (\sigma_{p,zz} - \sigma_{p,yy}) \tag{4.44}$$

No simple equation for $\sigma_{p,zz} - \sigma_{p,yy}$ can be derived by subtracting or adding equations 4.43. Therefore, using equations 1.14, 4.42 and 4.43, the complete set of equations describing the curtain flow are

$$\boxed{\begin{cases} U\dfrac{\mathrm{d}U}{\mathrm{d}z} = g + \dfrac{4\eta_s U}{\rho}\dfrac{\mathrm{d}}{\mathrm{d}z}\left(\dfrac{1}{U}\dfrac{\mathrm{d}U}{\mathrm{d}z}\right) + \dfrac{U}{\rho}\dfrac{\mathrm{d}}{\mathrm{d}z}\left(\dfrac{\sigma_{p,zz}-\sigma_{p,yy}}{U}\right) \\ \tau U\dfrac{\mathrm{d}\sigma_{p,zz}}{\mathrm{d}z} + \sigma_{p,zz}\left(1 - 2\tau\dfrac{\mathrm{d}U}{\mathrm{d}z}\right) = 2\eta_p\dfrac{\mathrm{d}U}{\mathrm{d}z} \\ \tau U\dfrac{\mathrm{d}\sigma_{p,yy}}{\mathrm{d}z} + \sigma_{p,yy}\left(1 + 2\tau\dfrac{\mathrm{d}U}{\mathrm{d}z}\right) = -2\eta_p\dfrac{\mathrm{d}U}{\mathrm{d}z} \end{cases}} \tag{4.45}$$

The first equation is general while the two others are the expressions of the normal stresses given by the Oldroyd-B model assuming a pure planar extensional flow. Note that, as expected, the Newtonian Taylor equation 1.5 is recovered when $\tau = 0$ by replacing η by $\eta_0 = \eta_s + \eta_p$.

We have obtained a system of three ordinary differential equations describing the evolution of the velocity $U(z)$ and the evolution of the polymeric normal stresses $\sigma_{p,zz}(z)$ and $\sigma_{p,yy}(z)$. Since the first equation involves a second derivative $\mathrm{d}^2U/\mathrm{d}z^2$ due to the solvent term, four boundary conditions are required. This is two times more than for Newtonian curtains. Here are four possible boundary conditions: one for the initial velocity and one for each initial polymeric normal stress components (three upstream boundary conditions) plus one describing the downstream boundary condition (plane stagnation flow, film casting or free-fall, see §4.3.2). Since die swell is not captured by the force balance equation, the three upstream boundary conditions should be evaluated at a distance $z = z_1$ from the slot exit. In the following, we note

$$U(z_1) = U_1, \qquad \sigma_{p,zz}(z_1) = \sigma_{p,zz,1} \qquad \text{and} \qquad \sigma_{p,yy}(z_1) = \sigma_{p,yy,1} \tag{4.46}$$

The system 4.45 can be written in terms of dimensionless variables

$$\hat{z} = z/z_e, \qquad \hat{U} = U/U_e \qquad \text{and} \qquad \hat{\sigma}_{p,ii} = \sigma_{p,ii}/\Delta_e \qquad (i = y, z) \tag{4.47}$$

where we recall that

$$z_e = g\tau^2, \qquad U_e = \sqrt{gz_e} = g\tau \qquad \text{and} \qquad \Delta_e = \rho U_e^2 = \rho g z_e = \rho(g\tau)^2 \tag{4.48}$$

We obtain

$$\boxed{\begin{cases} \hat{U}\dfrac{\mathrm{d}\hat{U}}{\mathrm{d}\hat{z}} = 1 + \dfrac{S}{El^3}\hat{U}\dfrac{\mathrm{d}}{\mathrm{d}\hat{z}}\left(\dfrac{1}{\hat{U}}\dfrac{\mathrm{d}\hat{U}}{\mathrm{d}\hat{z}}\right) + \hat{U}\dfrac{\mathrm{d}}{\mathrm{d}\hat{z}}\left(\dfrac{\hat{\sigma}_{p,zz} - \hat{\sigma}_{p,yy}}{\hat{U}}\right) \\ \hat{U}\dfrac{\mathrm{d}\hat{\sigma}_{p,zz}}{\mathrm{d}\hat{z}} + \hat{\sigma}_{p,zz}\left(1 - 2\dfrac{\mathrm{d}\hat{U}}{\mathrm{d}\hat{z}}\right) = \dfrac{1-S}{2El^3}\dfrac{\mathrm{d}\hat{U}}{\mathrm{d}\hat{z}} \\ \hat{U}\dfrac{\mathrm{d}\hat{\sigma}_{p,yy}}{\mathrm{d}\hat{z}} + \hat{\sigma}_{p,yy}\left(1 + 2\dfrac{\mathrm{d}\hat{U}}{\mathrm{d}\hat{z}}\right) = -\dfrac{1-S}{2El^3}\dfrac{\mathrm{d}\hat{U}}{\mathrm{d}\hat{z}} \end{cases}} \tag{4.49}$$

where

$$\boxed{S = \frac{\eta_s}{\eta_s + \eta_p} = \frac{\eta_s}{\eta_0}} \qquad \text{and} \qquad \boxed{El = \frac{\tau\, g^{2/3}}{(4\eta_0/\rho)^{1/3}}} \tag{4.50}$$

where El is the elasticity number defined with τ_{fil} in equation 4.16.

4.5.2 Three hypothesis

At this point, one important hypothesis can be made to simplify the problem:

- *Hypothesis 1*: Elasticity dominates over viscosity, i.e. $El \gg 1$

This hypothesis is motivated by the fact that, as suggested by experimental results, η_0 is does not play a major role. For example, for the 0.2 wt% PEO solution with 40 wt% PEG solvent of table B.3 which showed a fully developed elastic regime in the master curve (figure 4.11), we have $El = 37$ and therefore $1/El^3 = 2.0 \times 10^{-5} \ll 1$. Hence, for this liquid and many others, is seems reasonable to neglect the term on the right-hand side of the last two equations 4.49, as well as the solvent term in the first equation.

At this point, it can be useful to turn to the Lagrangian description by introducing time t (defined in equation 4.2) in order to replace $U\mathrm{d}/\mathrm{d}z$ by $\mathrm{d}/\mathrm{d}t$, or equivalently $\hat{U}\mathrm{d}/\mathrm{d}\hat{z}$ by $\mathrm{d}/\mathrm{d}\hat{t}$ where

$$\hat{t} = t/\tau \tag{4.51}$$

In Lagrangian description, the extension rate $\dot{\epsilon} = \mathrm{d}U/\mathrm{d}z$ becomes $\dot{\epsilon} = (1/U)\mathrm{d}U/\mathrm{d}t$. In dimensionless form, $\mathrm{d}\hat{U}/\mathrm{d}\hat{z}$ (which is equal to $\tau\dot{\epsilon}$) becomes $(1/\hat{U})\mathrm{d}\hat{U}/\mathrm{d}\hat{t}$. In particular, the two last equations 4.49 become

$$\begin{cases} \dfrac{\mathrm{d}\hat{\sigma}_{p,zz}}{\mathrm{d}\hat{t}} + \hat{\sigma}_{p,zz}\left(1 - \dfrac{2}{\hat{U}}\dfrac{\mathrm{d}\hat{U}}{\mathrm{d}\hat{t}}\right) = 0 \qquad \Rightarrow \qquad \dfrac{\hat{\sigma}_{p,zz}}{\hat{\sigma}_{p,zz,1}} = \left(\dfrac{\hat{U}}{\hat{U}_1}\right)^2 e^{-(\hat{t}-\hat{t}_1)} \\ \dfrac{\mathrm{d}\hat{\sigma}_{p,yy}}{\mathrm{d}\hat{y}} + \hat{\sigma}_{p,yy}\left(1 + \dfrac{2}{\hat{U}}\dfrac{\mathrm{d}\hat{U}}{\mathrm{d}\hat{t}}\right) = 0 \qquad \Rightarrow \qquad \dfrac{\hat{\sigma}_{p,yy}}{\hat{\sigma}_{p,yy,1}} = \left(\dfrac{\hat{U}}{\hat{U}_1}\right)^{-2} e^{-(\hat{t}-\hat{t}_1)} \end{cases} \tag{4.52}$$

where $t_1 = t(z_1)$. This results suggests that, provided that $\sigma_{p,yy,1} \ll \sigma_{p,zz,1}$, then $\sigma_{p,yy} \ll \sigma_{p,zz}$ at all later times. This is our third hypothesis

- *Hypothesis 2*: The axial tension dominates, i.e. $\sigma_{p,yy} \ll \sigma_{p,zz}$

This hypothesis has also been successfully used by Clasen et al. (2009) to find the simple solution $\mathcal{R} \propto \exp(-t/3\tau)$ (equation 3.15) in the filament thinning problem. Since the solvent term has been neglected through hypothesis 1, we obtain

$$\Delta \approx \sigma_{p,zz} \tag{4.53}$$

Finally, under hypothesis 1 and 2, the system becomes simply

$$\begin{cases} \hat{U}\dfrac{\mathrm{d}\hat{U}}{\mathrm{d}\hat{z}} = 1 + \hat{U}\dfrac{\mathrm{d}}{\mathrm{d}\hat{z}}\left(\dfrac{\hat{\Delta}}{\hat{U}}\right) \\ \hat{U}\dfrac{\mathrm{d}\hat{\Delta}}{\mathrm{d}\hat{z}} + \hat{\Delta}\left(1 - 2\dfrac{\mathrm{d}\hat{U}}{\mathrm{d}\hat{z}}\right) = 0 \end{cases} \tag{4.54}$$

and only requires two boundary conditions (for example: the initial velocity $\hat{U}_1$ and the initial mean normal stress difference $\hat{\Delta}_1$). The initial values $\sigma_{p,zz,1}$ and $\sigma_{p,yy,1}$ have been replaced by Δ_1. More importantly, one boundary condition has been removed when neglecting the solvent term in the force balance equation. Therefore, if considering that U_1 and Δ_1 can be any arbitrary value, it becomes impossible to control the downstream boundary condition. Although it is clear that the initial velocity U_1 can be imposed arbitrarily by varying the flow rate, the status of Δ_1 as a valid boundary condition is not yet clear.

Let us clarify this point with the theory of Newtonian curtains developed in §4.3.2. We know that the initial mean normal stress difference $\bar{\Delta}_0$ is equal to the initial slope of the velocity profile $\bar{U}'(\bar{z} = 0)$ (see equation 4.29). If the downstream boundary condition is not specified, the value of C in Clarke's solution 1.19 can be positive (film casting) negative (plane stagnation flow) or equal to 0 (infinite curtain converging towards a free-fall). Therefore, the exact value of $\bar{\Delta}_0$ depends on the upstream and downstream boundary conditions. Considering the case of a

convergence towards a plane stagnation flow for example ($C < 0$), there is no experimental control on $\bar{\Delta}_0$ since it is fixed by the initial velocity $\bar{U}_0$ and by the curtain length $\bar{L}_c$. When $C = 0$, $\bar{\Delta}_0$ is a (decreasing) function of $\bar{U}_0$ only (see §4.4.2).

For viscoelastic curtains however, it would seem reasonable to assume that Δ_1 can be varied arbitrarily, independently of (for example) the curtain length. The data of figure 4.15 indeed suggests that, for a given initial velocity U_1 and a given curtain length L_c, the initial mean normal stress difference Δ_1 (after swelling) is a (weak) function of the mean normal stress difference Δ_s developed inside the slot. Hence, if the value of Δ_1 is not directly encoded by U_1 and by the downstream boundary condition (contrary to the Newtonian case), then one boundary condition is missing in equation 4.54.

4.5.3 Analytical solution

General expression

Let us continue the calculation to see where the two hypothesis are taking us. In Lagrangian form, equation 4.54 becomes

$$\begin{cases} \dfrac{\mathrm{d}\hat{U}}{\mathrm{d}\hat{t}} = 1 + \dfrac{\mathrm{d}}{\mathrm{d}\hat{t}}\left(\dfrac{\hat{\Delta}}{\hat{U}}\right) \quad \Rightarrow \quad \hat{U} - \hat{U}_1 = \hat{t} - \hat{t}_1 + \dfrac{\hat{\Delta}}{\hat{U}} - \dfrac{\hat{\Delta}_1}{\hat{U}_1} \\ \dfrac{\mathrm{d}\hat{\Delta}}{\mathrm{d}\hat{t}} + \hat{\Delta}\left(1 - \dfrac{2}{\hat{U}}\dfrac{\mathrm{d}\hat{U}}{\mathrm{d}\hat{t}}\right) = 0 \quad \Rightarrow \quad \dfrac{\hat{\Delta}}{\hat{\Delta}_1} = \left(\dfrac{\hat{U}}{\hat{U}_1}\right)^2 e^{-(\hat{t}-\hat{t}_1)} \end{cases} \tag{4.55}$$

which finally gives a simple analytical expression

$$\boxed{\hat{U} - \hat{U}_1 = \frac{\hat{t} - \hat{t}_1 - A_e\left[1 - e^{-(\hat{t}-\hat{t}_1)}\right]}{1 - Xe^{-(\hat{t}-\hat{t}_1)}}} \tag{4.56}$$

or equivalently

$$\boxed{\hat{U} = \frac{\hat{t} - \hat{t}_1 - A_e + \hat{U}_1}{1 - Xe^{-(\hat{t}-\hat{t}_1)}}} \tag{4.57}$$

where

$$\boxed{A_e = \frac{\hat{\Delta}_1}{\hat{U}_1}} \quad \text{and} \quad \boxed{X = \frac{A_e}{\hat{U}_1} = \frac{\hat{\Delta}_1}{\hat{U}_1^2}} \tag{4.58}$$

where $\hat{\Delta}_1 = \Delta_1/\Delta_e$ and $\Delta_1 = \Delta(z_1)$. The definition of A_e matches the definition of equation 4.23. At infinity ($\hat{t} \to +\infty$), this solution reaches an oblique asymptote of

equation

$$\hat{U} - \hat{U}_1 = \hat{t} - \hat{t}_1 - A_e \tag{4.59}$$

which is exactly the free-fall anticipated in equation 4.22. This is not surprising since the only hypothesis used to write equation 4.22 was that Δ becomes negligible in the free-fall regime ($\hat{t} \gg 1$). Indeed, according to equation 4.55, this hypothesis is valid for an Oldroyd-B fluid.

Avoiding the divergence

The denominator of the right-hand side of equation 4.57 becomes 0 at a time $\hat{t}_{div}$ given by

$$\hat{t}_{div} - \hat{t}_1 = \ln(X) \tag{4.60}$$

which is positive is $A_e > \hat{U}_1$ (i.e. if $X > 1$). If the denominator goes to zero, the solution diverges in finite time, unless the numerator is also 0 at time $\hat{t}_{div}$. Using equation 4.57 and 4.60, the latter condition writes

$$\boxed{\ln X - \hat{U}_1 (X - 1) = 0} \tag{4.61}$$

Let X^* be a solution of this equation. A trivial solution is $X^* = 1$ and the nontrivial solution is a decreasing function of $\hat{U}_1$ with no simple analytical expression. More precisely, $X^* > 1$ if $\hat{U}_1 < 1$ and $X^* < 1$ if $\hat{U}_1 > 1$. Therefore, the only way to have a nondiverging solution using equation 4.57 is to restrict the value of A_e (and thus the value of $\hat{\Delta}_1$) to a very specific value $A_e^* = \hat{U}_1 X^*$ which is a function of the initial velocity $\hat{U}_1$. Therefore, with our hypothesis, $\hat{\Delta}_1$ can not be arbitrary.

In order to obtain the Eulerian solution, one must reintroduce the distance z from the slot which writes

$$z - z_1 = \int_{t_1}^{t} U(t^*)\,\mathrm{d}t^* \qquad \Leftrightarrow \qquad \hat{z} - \hat{z}_1 = \int_{\hat{t}_1}^{\hat{t}} \hat{U}\left(\hat{t}^*\right)\,\mathrm{d}\hat{t}^* \tag{4.62}$$

Combining with the solution 4.57, we get

$$\hat{z} - \hat{z}_1 = \int_0^{\hat{t}-\hat{t}_1} \frac{T - A_e + \hat{U}_1}{1 - X e^{-T}}\,\mathrm{d}T \tag{4.63}$$

which has no simple analytical expression.

In figure 4.16.a, we present the velocity field $\hat{U}$ predicted by equation 4.57 as a

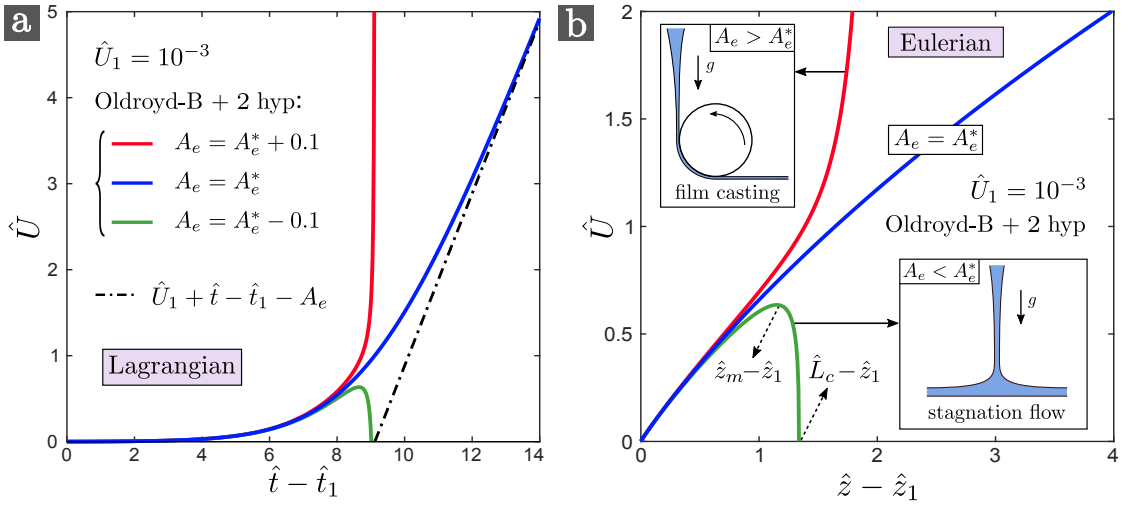

Figure 4.16 – Velocity field $\hat{U}$ against $\hat{t} - \hat{t}_1$ (a) (Lagrangian description, equation 4.57) and against $\hat{z} - \hat{z}_1$ (b) (Eulerian description, equations 4.57 and 4.62) for an initial velocity $\hat{U}_1 = 10^{-3}$ and for $A_e = A_e^*(\hat{U}_1) \approx 9.1191$ (infinite curtain converging to a free-fall), $A_e = A_e^* - 0.1$ (the velocity reaches a maximum value at a distance $\hat{z}_m$ from the slot and turns into a plane stagnation flow when impacting a flat surface at a distance $\hat{L}_c$ from the slot) and for $A_e = A_e^* + 0.1$ (the velocity diverges and becomes arbitrarily large, like in film casting experiments).

function of time for an initial velocity $\hat{U}_1 = 10^{-3}$ and for three different values of A_e. Figure 4.16.b is the Eulerian version, where the velocity field is plotted against the distance from the slot instead of time using equation 4.62. When $A_e = A_e^*$ (the solution of equation 4.61), the solution converges to the free-fall oblique asymptote. However, for $A_e > A_e^*$, the solution diverges in finite time, which allows arbitrary large values of the velocity at a given distance from the slot. Moreover, for $A_e < A_e^*$, the velocity reaches a maximum value at a distance $\hat{z}_m$ from the slot before decreasing down to $\hat{U} = 0$ at a distance $\hat{L}_c$ from the slot. These three scenarios are reminiscent to the Newtonian scenarios discussed in figure 1.2.a. Hence, the Oldroyd-B model also predicts the three types of downstream boundary conditions discussed in §4.3.2 depending on the value of A_e:

- $A_e = A_e^*$: Infinite curtain converging to a free-fall
- $A_e > A_e^*$: Film casting experiment
- $A_e < A_e^*$: The flow turns into a plane stagnation flow

Comparison with experimental results

Values of A_e^* (solution of equation 4.61) are plotted against $\hat{U}_1$ in figure 4.17.a. This theoretical curve is compared with the experimental data of figure 4.14.b. The

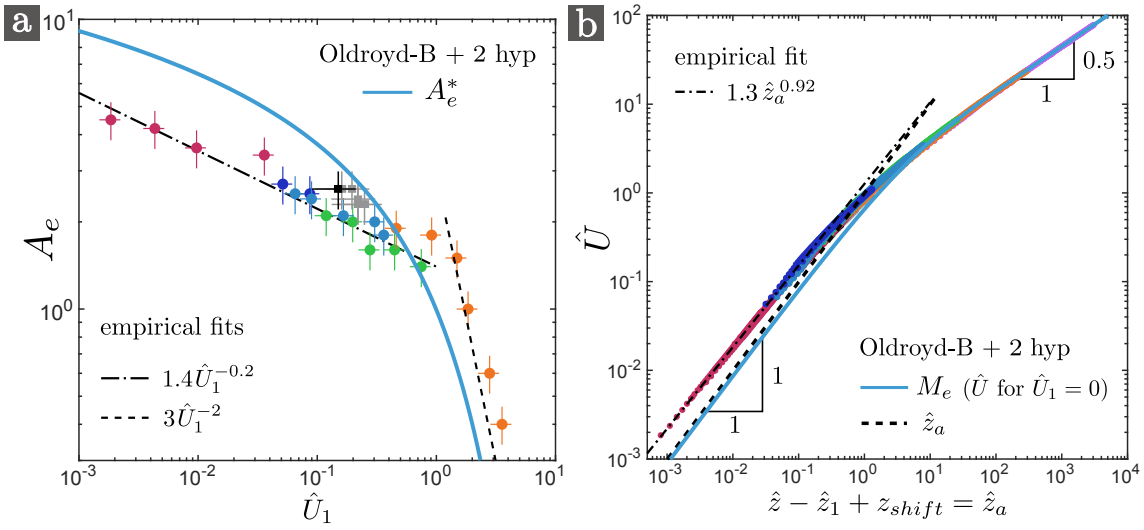

Figure 4.17 – (a) Solution A_e^* of equation 4.61 compared with the experimental data of figure 4.14.b. (b) Master curve M_e (solution $\hat{U}$ (equation 4.57) for $\hat{U}_1 = 0$ and $A_e = A_e^*$ in Eulerian description using equation 4.62), compared with the experimental data of figure 4.11.a. In practice, it is impossible to impose $\hat{U}_1 = 0$ rigorously. Therefore, we chose a value $\hat{U}_1 \lll 1$ and we check that choosing an other value (ten times lower or ten times larger for example) has no consequence on the shape of the analytical curve in the domain of figure (b).

orders of magnitude are recovered, as well as the decreasing behaviour. However, A_e^* overestimates the experimental values for low initial velocities $\hat{U}_1 < 1$. Note that this comparison relies on an implicit third hypothesis which is that the relaxation time τ of the Oldroyd-B model is rigorously equal to the extensional relaxation time τ_{fil} measured in CaBER experiments, i.e.

- *Hypothesis 3*: The relevent Oldroyd-B relaxation time is $\tau = \tau_{fil}$ (CaBER)

Indeed, the dimensionless quantities in figure 4.17.a are $A_e = \Delta_1/\rho g U_1 \tau_{fil}$ and $\hat{U}_1 = U_1/g\tau_{fil}$ for the experimental data and are $A_e = \Delta_1/\rho g U_1 \tau$ and $\hat{U}_1 = U_1/g\tau$ for the theoretical data. We recall that, when using a multimode Oldroyd-B constitutive equation with a Zimm spectrum of relaxation times to model the filament thinning process, the filament radius decreases as $\exp(-t/3\tau)$ in the elastic regime at "long times", where τ (model) is the longest relaxation time corresponding to the slowest mode (the contribution of the other modes becomes negligible, see discussion in §3.2.2). Hence, it corresponds to the value τ_{fil} measured in CaBER experiments. For the viscoelastic curtain problem, experimental results suggested that τ_{fil} was also the relevant time scale.

In figure 4.17.b, the experimental master curve $M_{e,\text{exp}}$ of figure 4.11.a is compared with the theoretical master curve $M_{e,\text{th}}$ corresponding to the particular solution of

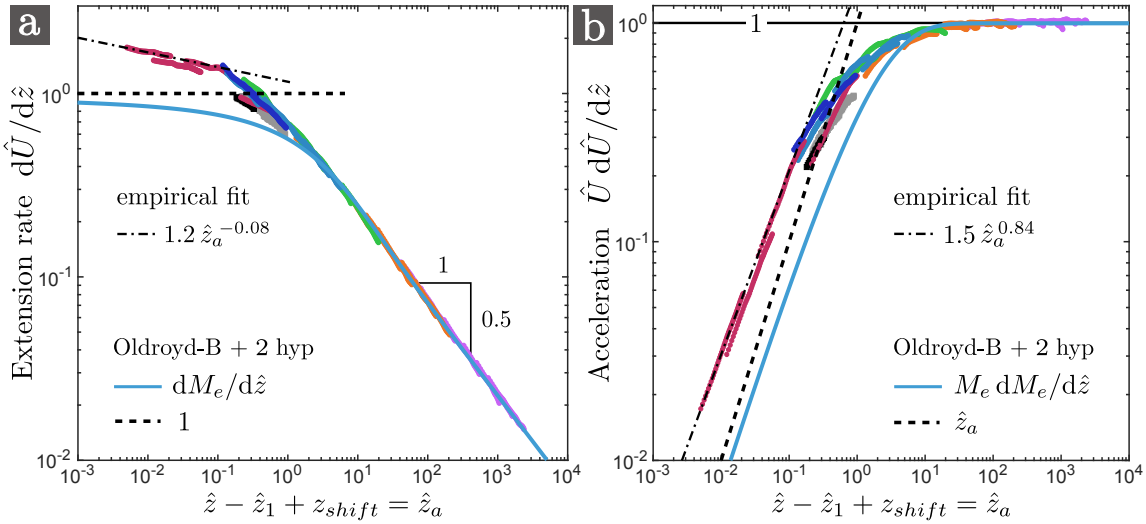

Figure 4.18 – Extension rate $\mathrm{d}M_e/\mathrm{d}\hat{z}$ (a) and acceleration $M_e\,\mathrm{d}M_e/\mathrm{d}\hat{z}$ (b) for the master curve M_e of figure 4.17.b, compared respectively with the experimental data of figure 4.12.a and 4.12.b.

equations 4.57 and 4.62 for $\hat{U}_1 = 0$ and $A_e = A_e^*$. With the Oldroyd-B model, we obtain two distinct regimes: an elastic regime for $\hat{z} \ll 1$ and an inertial free-fall regime for $\hat{z} \gg 1$. We remind the expression of the master curve found in §4.3.4:

$$M_e(\hat{z}) = \begin{cases} K\hat{z}^\alpha & \hat{z} \ll 1 : \text{ elastic regime} \\ \sqrt{2\,(\hat{z} - s_{e,0})} & \hat{z} \gg 1 : \text{ inertial regime} \end{cases} \tag{4.64}$$

The experimental data suggested that $K = 1.3 \pm 0.2$ and $\alpha = 0.92 \pm 0.02$, as well as $s_{e,0} = 6 \pm 2$. However, in spite of the reasonable order-of-magnitude agreement in figure 4.17.b, the Oldroyd-B model underestimates the liquid velocity in the elastic regime, with a maximum difference of about 100 % (a factor 2). Moreover, a careful examination of $M_{e,\mathrm{th}}$ reveals that there is no clear power law such as $K\hat{z}^\alpha$ in the elastic regime. However, as $\hat{z}$ decreases, we observe that $M_{e,\mathrm{th}}(\hat{z})$ gets closer and closer to $\hat{z}$. The experimental data are better described by the theory in the free-fall regime. Note that, when plotting $M_{e,\mathrm{th}}^2$, we find a free-fall oblique asymptote of equation $2\,(\hat{z} - s_{e,0})$ where $s_{e,0} \approx 3.3$ which is not too bad given the experimental error bar.

We show in figures 4.18.a and 4.18.b the extension rate $\mathrm{d}M_{e,\mathrm{th}}/\mathrm{d}\hat{z}$ and the acceleration $M_{e,\mathrm{th}}\,\mathrm{d}M_{e,\mathrm{th}}/\mathrm{d}\hat{z}$ of the master curve respectively, compared to the experimental data of figures 4.12.a and 4.12.b. In both cases, the Oldroyd-B theory underestimates the experimental data in the elastic regime. Note that the extension rate seems to have a limiting value 1 for low $\hat{z}$, i.e.

$$\lim_{\hat{z}\to 0} \frac{\mathrm{d}M_{e,\mathrm{th}}}{\mathrm{d}\hat{z}} = 1 \tag{4.65}$$

Besides, note that the master curve acceleration reaches 0.95 at $\hat{z} = F_{e,0} \approx 12$, which is in excellent agreement with the experimental value 12 ± 5 found in §4.3.4.

According to equation 4.65, in the Oldroyd-B theory, the extension rate $\mathrm{d}\hat{U}/\mathrm{d}\hat{z}$ goes to 1 for $\hat{U}_1 \to 0$ and $\hat{z} \ll 1$ (elastic regime). To understand how this result in consistent with previous results, let us write the mean normal stress difference $\hat{\Delta}$ as a function of $\hat{U}$ and $\mathrm{d}\hat{U}/\mathrm{d}\hat{z}$ only. When eliminating the $\mathrm{d}\hat{\Delta}/\mathrm{d}\hat{z}$ term from equations 4.54, we obtain

$$\hat{\Delta} = \hat{U}\frac{1 - \hat{U}\dfrac{\mathrm{d}\hat{U}}{\mathrm{d}\hat{z}}}{1 - \dfrac{\mathrm{d}\hat{U}}{\mathrm{d}\hat{z}}} \qquad \Leftrightarrow \qquad \Delta = \rho g \tau \hat{U}\frac{1 - \dfrac{U}{g}\dfrac{\mathrm{d}U}{\mathrm{d}z}}{1 - \tau\dfrac{\mathrm{d}U}{\mathrm{d}z}} \tag{4.66}$$

which gives $\hat{\Delta} > 0$ since both the numerator and the denominator are positive. Taking $\hat{z} = \hat{z}_1$ in equation 4.66, we obtain an expression of $\hat{\Delta}_1$, and therefore of A_e which becomes

$$A_e = \frac{\hat{\Delta}_1}{\hat{U}_1} = \frac{1 - \hat{U}_1 \left.\dfrac{\mathrm{d}\hat{U}}{\mathrm{d}\hat{z}}\right|_{\hat{z}_1}}{1 - \left.\dfrac{\mathrm{d}\hat{U}}{\mathrm{d}\hat{z}}\right|_{\hat{z}_1}} \tag{4.67}$$

For $\hat{U}_1 \to 0$, if $\mathrm{d}\hat{U}/\mathrm{d}\hat{z}|_{\hat{z}_1}$ goes to 1, the numerator goes to 1 while the denominator goes to zero. Therefore, A_e goes to $+\infty$, which is consistent with the prediction on $A_e^*(\hat{U}_1)$ (see figure 4.17.a and equation 4.61).

Discrepancies

The above results are encouraging since the Oldroyd-B theory, despite of its simplicity, is able to capture the main experimental trends and orders of magnitudes. Therefore, the analytical solution 4.57 is a good starting point for any more refined theoretical description. We now discuss the discrepancies between this model and the experimental results. Three interpretations can be proposed:

1. One of the three hypothesis leading to the solution 4.57 is not valid.

2. The Oldroyd-B model is not appropriate.

3. The experimental data in the elastic regime are still a bit influenced by the downstream boundary condition.

The third interpretation is tempting since it would explain why the experimental velocity exponent is $\alpha = 0.92 < 1$ in the elastic regime while it is closer to one in the Oldroyd-B theory. Indeed, as already commented in figure 4.5, the velocity field $U(z)$ becomes less and less concave as the curtain length L_c increases, thus suggesting "$\alpha \to 1$" when $L_c \gg z_e$. However, according to this interpretation, the experimental velocities should be lower than the theoretical ones, which is the contrary of what is observed in figure 4.17.b. Therefore, this interpretation alone is not sufficient.

An other major problem of this theory is that, contrary to the experimental results presented in §4.4.3, the solution 4.57 does not allow a dependence of the initial mean normal stress difference Δ_1 on the mean normal stress difference Δ_s developed upstream of the curtain. Hence, an interesting possibility is to release the first hypothesis $El = \infty$ to allow one more boundary condition arising from the solvent term. Besides, although the single mode Oldroyd-B model may lead to qualitative predictions in viscoelastic flows, a multimode Oldroyd-B model if often used to obtain a more quantitative agreement with experimental results. We are not yet sure of what would be the analytical implications of these two possibilities. In particular, we are not sure of weather or not the analytical solution will give larger or lower velocities. Both possibilities of improvement will be explored in the future.

4.6 Partial conclusion

In this chapter, we presented the first intensive experimental investigation of the role of viscoelasticity in the extensional flow of a sheet - or curtain - of low-viscosity liquid falling freely from a slot at constant flow rate. Contrary to film casting, gravity is the only source of axial tension. The mean liquid velocity $U(z)$, where z is the distance from the slot exit, is measured for polymer solutions with various rheological behaviours. We show that the flow is mostly influenced by the value of the extensional relaxation of the polymers, characterised by the time τ_{fil} measured with a CaBER rheometer. If the liquid initial velocity U_1 after swelling is such that $U_1 \ll g\tau_{fil}$, gravity is initially balanced by the elastic stresses arising from the stretching of polymer molecules. In this elastic regime, the liquid acceleration $U\mathrm{d}U/\mathrm{d}z$ is less than the gravitational acceleration g. However, inertia finally dominates over elasticity far from the slot and the liquid acceleration reaches the

asymptotic free-fall value g. Polymer molecules initially unravel in the elastic regime since $\tau_{fil}\,\mathrm{d}U/\mathrm{d}z = O(1)$, and return progressively to a coil state in the inertial free-fall regime where $\tau_{fil}\,\mathrm{d}U/\mathrm{d}z \ll 1$. The length of the sub-gravitational part of the curtain is $z_e^* = F_e \times z_e$ where $z_e = g\tau_{fil}^2$ and where F_e is a decreasing function of $U_1/g\tau_{fil}$. In particular, the flow is a free-fall even close to the slot if $U_1 \gg g\tau_{fil}$. When considering the flow far from the impingement zone, we show that the velocity field $U(z)$ rescales on a master curve, like for Newtonian liquids of dynamic viscosity η and density ρ where the flow is initially dominated by viscous dissipation if the initial velocity is less than $U_v = \sqrt{gz_v}$ where $z_v = ((4\eta/\rho)^2/g)^{1/3}$.

We show that the flow is only weakly influenced by the history of polymer deformations in the die upstream of the curtain. More precisely, the polymeric stresses in the curtain are mostly due to the extensional stretching of polymer molecules in the curtain, with a small correction due to the "pre-shear" in the die. In particular, the mean normal stress difference Δ switches from a shear value Δ_s inside the slot to an extensional value $\Delta_1 = A_e\,\rho g U_1 \tau_{fil}$ after swelling which is needed to bear the weight of the sub-gravitational part of the curtain, where A_e is a decreasing function of $U_1/g\tau_{fil}$.

Chapter 5

Curtain stability

Contents

In this chapter, we wish to characterise the curtain stability. This aspect is of major importance regarding industrial processes such as curtain coating since, if the curtain spontaneously breaks during the process, a large area of the substrate will remain "dry" (uncoated). One of the questions which originally motivated this thesis is whether or not the addition of polymer molecules to a Newtonian coating liquid could stabilise the curtain by reducing the frequency of such spontaneous breaking events. Besides, we measure the dependence of the minimum flow rate Q_{min} (below which the curtain spontaneously breaks in the form of equidistant jets) on the rheological properties of the polymer solutions. As mentioned at the end of chapter 1, contrary to the "velocity field" aspect of viscoelastic curtains investigated in chapter 4, which had not been explored in the past, the stability aspect has already received some attention in recent literature, mostly from the group of Marcio S. Carvalho (Becerra & Carvalho, 2011; Karim et al., 2018b). These aspects will be investigated in §5.1.

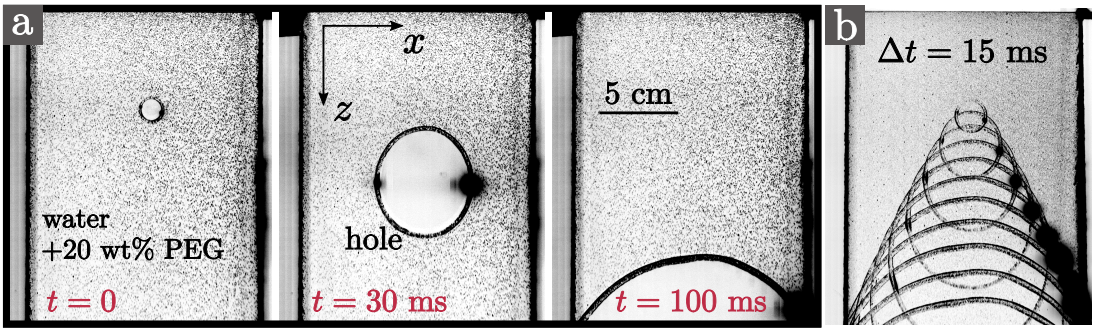

Figure 5.1 – Time evolution of a hole forming spontaneously in a curtain of 20 wt% PEG solvent with flow rate $q = 3.3$ cm^2/s and length $L_c = 30$ cm. The hole is advected by the flow (self-healing). (b): Image superposition.

Furthermore, if the curtain thickness is modulated at the slot exit due to an extrusion instability, the thickness of the coating layer may be irregular. When there is no choice but using a viscoelastic liquid which is particularly prone to this type of elastic instability, this destabilising mechanism can become a major limitation for industrial applications. This aspect, which was already mentioned in §4.1.2, will be investigated in more details in §5.2.

5.1 Spontaneous breaking of the liquid sheet

In this section, we investigate the influence of elasticity on the stability of the curtain in terms of spontaneous hole opening events. Here, we only consider the stability of the liquid sheet a as physical object, meaning that a continuous sheet is a stable state while a broken sheet is an unstable state. We are not yet considering the stability of the flow discussed in §4.1.2 and all the liquids used in this section produce "stable" (or "smooth") curtains, in the sense that the flow is not modulated in the horizontal direction.

5.1.1 Dynamics of hole opening

In figures 5.1.a and 5.1.b, we show the time evolution of a hole forming spontaneously in a Newtonian curtain of 20 wt% PEG solvent. Such a hole can be generated by impurities in the liquid such as bubbles which are inevitably generated in the hydraulic loop. The hole in figure 5.1 is advected by the flow while growing in size and the liquid is collected in a rim at the edge of the hole.

We briefly recall the results mentioned in §1.2 for liquids of negligible viscosity and elasticity. If capillary forces are only balanced by inertia, the local retraction

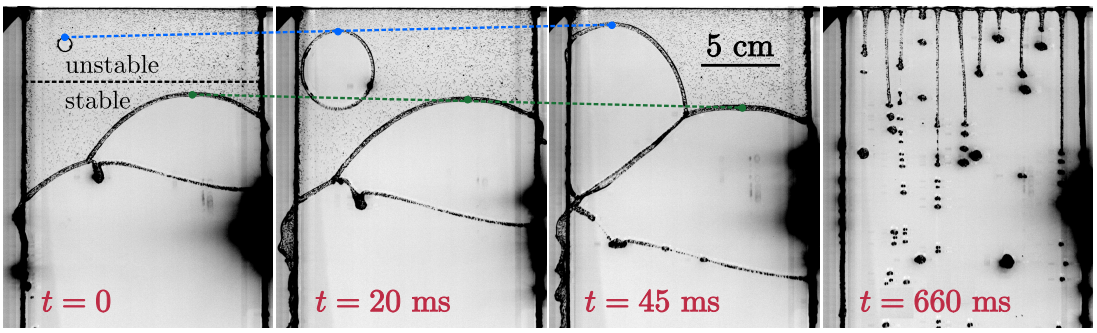

Figure 5.2 – Time evolution of two holes forming spontaneously in a curtain of degraded (t_d = 100 min) 0.004 wt% PEO solution with 20 wt% PEG solvent with flow rate $q \approx$ 1.5 cm^2/s and length L_c = 30 cm. The upper edge of one of the holes moves downwards while the other moves upwards and causes the breaking of the sheet. It can be interpreted as the fact that the Weber number (equation 5.2) is less than one close to the slot (unstable zone) where the second hole formed. An arbitrary line is traced between the two holes to illustrate the separation between the unstable zone and the stable zone.

speed of the sheet (i.e. the velocity of the rim) in the reference frame of the moving liquid is the Taylor-Culick velocity

$$V = \sqrt{\frac{\Gamma}{\rho h}} \tag{5.1}$$

Hence, the part of the liquid rim corresponding to the upper edge of the hole grows at velocity $V - U$ in the reference frame of the laboratory, where $V(z)$ is calculated based on the local curtain thickness $2h(z)$ and where $U(z)$ is the local velocity of the surrounding liquid. This local competition can be written in terms of a local Weber number

$$We = \left(\frac{U}{V}\right)^2 = \frac{\rho h U^2}{\Gamma} = \frac{\rho q U}{2\Gamma} \tag{5.2}$$

which can be less than one close to the slot and become larger than one downstream. Therefore, if a hole opens at an altitude where $We > 1$, i.e. where advection is faster than the hole opening process, it will be carried away by the flow, like in figure 5.1. This process is often referred to as "self-healing". However, if a hole opens in the unstable part of the curtain where $We < 1$, the upper edge of the hole propagates upwards and stops when reaching the slot whereas the lower end propagates downwards, in which case the curtain is finally split into two parts delimited by a rim which takes the form of an arch. A comparable scenario is shown in figure 5.2 (the flow rate is so low that instead of a single arch, we end up with a set of jets). Hence, there is a separation between an unstable zone upstream ($We < 1$) and a stable zone downstream ($We > 1$).

If the Weber number is larger than one everywhere, i.e. if the initial velocity $U_s = q/2a$ at the slot exit (of thickness $2a$) is larger than the value of V at the slot exit, any hole should be advected by the flow. Equivalently, the linear flow rate q has to be larger than a critical value

$$q_\Gamma = \sqrt{\frac{4a\Gamma}{\rho}} \tag{5.3}$$

This description does not take die swell into account and one could argue that U_1 is the velocity which has to be larger than V. This gives a larger critical flow rate $q_\Gamma = (4a\xi\Gamma/\rho)^{1/2}$ where $\xi = U_s/U_1$ is the die swell ratio.

In the following, we show that two different scenarios are observed when increasing of decreasing the flow rate (hysteretic behaviour). Hence, two different flow rates can be experimentally measured: the critical flow rate q_c above which a curtain forms when increasing q (§5.1.2), and the minimum flow rate q_{min} below which the curtain breaks when decreasing the flow rate (§5.1.3).

5.1.2 Critical flow rate

In figure 5.3.a, we show the different regimes observed when increasing the flow rate. First (step 1), droplets are periodically emitted from equally spaced spots along the slot. In the case of a polymer solution, these drops can be connected by filaments (Clasen et al., 2009). Then, the liquid falls in the form of equally spaced continuous jets (step 2). The transition from dripping to jetting is described by Clanet & Lasheras (1999) in the case of a single Newtonian jet issuing from a nozzle. The distance between two jets is typically captured by the value $2\pi\sqrt{2}(\Gamma/\rho g)^{1/2}$ expected from the Rayleigh-Taylor instability theory which is of order 2 cm for PEO solutions (Fermigier et al., 1992; Brunet et al., 2007). As the flow rate is further increased, neighbouring jets merge and form thicker jets until the arches are finally advected and a continuous sheet of liquid suddenly emerges from the slot (step 3) at a critical flow rate q_c which is measured.

Values of the ratio q_c/q_Γ are reported in figure 5.3.b for the five degraded (t_d = 100 min) PEO solutions with 20 wt% PEG solvent (table B.1). Results are reproducible and are plotted against the extensional relaxation time τ_{fil}. We measure that $q_c/q_\Gamma \approx 0.8$ for all solutions. Note that taking die swell into account, we obtain a value of q_c/q_Γ closer to 0.7. This shows that the arches indeed detach from the slot when the extrusion velocity becomes of the order of the Taylor-Culick

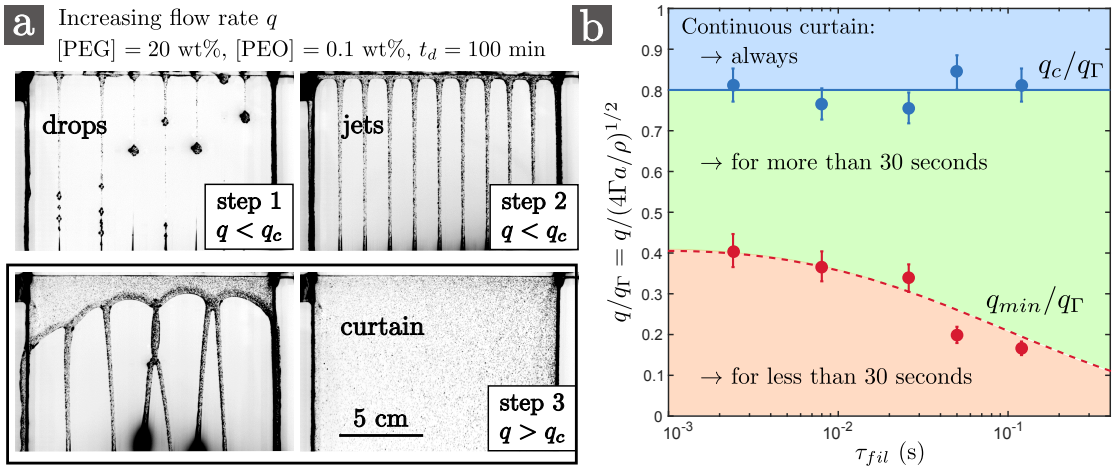

Figure 5.3 – (a): Different regimes observed when increasing the flow rate from 0 to 6 cm^2/s for the degraded ($t_d = 100$ min) 0.1 wt% PEO solution with 20 wt% PEG solvent (table B.1). (b): Critical flow rate q_c (above which any hole is advected by the flow) and minimum flow rate q_{min} (required to maintain a continuous curtain for more than 30 seconds), divided by $q_\Gamma = (4a\Gamma/\rho)^{1/2}$, against the extensional relaxation time τ_{fil} for the five degraded ($t_d = 100$ min) PEO solutions with 20 wt% PEG solvent (table B.1). $q_\Gamma = 3.5$ cm^2/s and curtain length is $L_c = 30$ cm.

velocity and suggests that elastic forces have a negligible influence on the retraction speed of the hole. The fact that q_c is not rigorously equal to q_Γ may be due to the weight of the rim pulling arches downwards and shows that the classical criterion based on the Weber number can be refined. Instead of a simple balance between the liquid inertia pulling the arch downwards and surface tension pulling it upwards, one could add the rim weight pulling the arch downwards to obtain a more complex dimensionless number which is equal to one at the boundary between the unstable zone (close to the slot) and the stable zone. However, since the weight of the rim increases with time during hole expansion, the derivation is not trivial. Inspiration can be drawn from the calculation of Clanet & Lasheras (1999) in the context of free jets. See Roche et al. (2006) for more advanced discussions on rim weight effects in the context of liquid curtains.

5.1.3 Minimum flow rate

Starting from $q > q_c$, nothing special happens when decreasing the flow rate below q_c and the curtain generally remains continuous for a long time. However, since holes are continuously generated in the curtain, the curtain will finally break when a hole eventually opens close enough to the slot where $We < 1$, i.e. where the upper edge of a hole propagates upwards. Hence, as proposed by Becerra & Carvalho (2011), we define the minimum flow rate q_{min} above which the liquid sheet remains continuous for more than a certain amount of time, for example 30 seconds since liquid depos-

ition on a substrate takes a few seconds in curtain coating. We measure q_{min} as follows. Starting from a continuous curtain, the flow rate q is slowly decreased step by step, each step lasting 30 seconds, until the curtain breaks at $q = q_{min}$. We obtain reproducible values of q_{min}. The ratio q_{min}/q_Γ is reported in figure 5.3.b. Values of q_{min} decrease from 1.3 cm^2/s for the 0.004 wt% PEO solution (which is also the value measured with the pure solvent) to 0.58 cm^2/s for the 0.4 wt% PEO solution, i.e. q_{min} decreases by a factor 2.2. Therefore, curtain coating can be performed at lower flow rates when adding polymer molecules to the liquid, as already shown by Becerra & Carvalho (2011) and Karim et al. (2018b) with similar measurements.

The value of q_{min} is linked to the frequency of spontaneous hole opening events in the curtain. Holes are mostly generated far from the slot where the curtain is thin. Curtain are indeed often continuous close to the slot but constantly punctured downstream, as is commonly observed in water fountains. The frequency of hole opening events must depend on the concentration of impurities in the liquid, which is not controlled in our experiment. We measure that this frequency decreases when increasing the extensional relaxation time of the solution. Typically, for the 0.02 wt% PEO solution with 20 wt% PEG solvent (table B.1) extruded at flow rate $q = 1.7$ cm^2/s with curtain length $L_c = 30$ cm, the frequency of spontaneous hole opening events decreases from about one hole per minute before degradation ($t_d = 0$ min) to ten holes per second after $t_d = 100$ minutes of degradation, most of them being generated more than 10 cm below the slot. The latter case is reminiscent of the curtain shown in figure 5.2 which is riddled with holes. For such curtains, the velocity field $U(z)$ for $z < 20$ cm can only be measured after raising the flow rate up to 3.4 cm^2/s, as mentioned in §3.1.5 when discussing the accessible ranges of flow rates. Indeed, the hole opening frequency decreases when increasing the flow rate since the curtain becomes thicker everywhere.

We conclude that polymer addition greatly enhances the stability of the curtain by reducing the frequency of spontaneous hole opening events. Since these events are generally consequences of the bursting of bubbles in the liquid, this result can be interpreted as a greater resistance of the liquid sheet to bubble bursting. We speculate that two liquid layers separating a bubble on both sides from the ambient air undergo an extensional flow and are therefore more difficult to break due to the elastic stresses arising from the stretching of polymer molecules, like in the filament thinning experiment where breaking is inhibited by the presence of polymer molecules. This interpretation is consistent with the experiments conducted by Karim et al. (2018b) which consist of applying a local disturbance on the curtain with an air jet blown through a needle. Indeed, since Newtonian curtains break

much more easily than viscoelastic curtains, the authors concluded that the growth rate of any disturbance leading to the formation of a hole is delayed by polymer addition.

5.2 Modulated curtains

In this section, we turn our attention to another aspect of the curtain stability issue which is the possibility of the development of a modulated curtain, as already mentioned in §4.1.2. In a nutshell, for the most shear thinning solutions, the curtain flow is unstable and presents a time-dependent varicose mode along the horizontal direction x. More precisely, at a given time, the extrusion velocity of the liquid is found to depend on the position x along the slot, producing a modulation of the thickness of the curtain. Hence, the curtain organises in a succession of vertical thick and thin bands (or stripes) where the liquid velocity is respectively larger and lower than the averages value $\langle U \rangle_x$. The modulation of the sheet has a centimetric length scale, meaning that the typical distance between two thick bands is of a few centimetres.

This instability may belong to the family of melt-fracture phenomena described in §2.6. However, it is not exactly similar to the extrusion instability reported by Boger & Walters (2012) (see figure 2.14.c) where, to quote the author, the wide vertical bands "are not stationary but travel from the middle to both sides, i.e. they are generated sequentially at the middle and annihilated at the edges". We did not observe such behaviour in our experiments where the thick bands are generated at "random" (unpredictable) positions along the slot. Besides, in our experiments, new bands emerge continuously from the slot and "die" (disappears spontaneously) after a few tens of seconds without travelling along x in their lifetime. Hence to our knowledge, this particular instability has not yet been mentioned in the literature. This section is dedicated to a more extensive exploration of this phenomenon with a purely empirical approach.

5.2.1 Empirical description

A direct visualisation of the difference between a modulated and a smooth (unmodulated) curtain is presented in figure 5.4. The liquid is a 0.1 wt% HPAM solution before (a) and after (b) salt addition. These pictures are extracted from experiments performed on the solutions presented in table B.5 where salt is added step by step to an initially unsalted HPAM solution using the degradation protocol presented in §3.2.5. A PIV measurement is performed at each step and is correlated to the

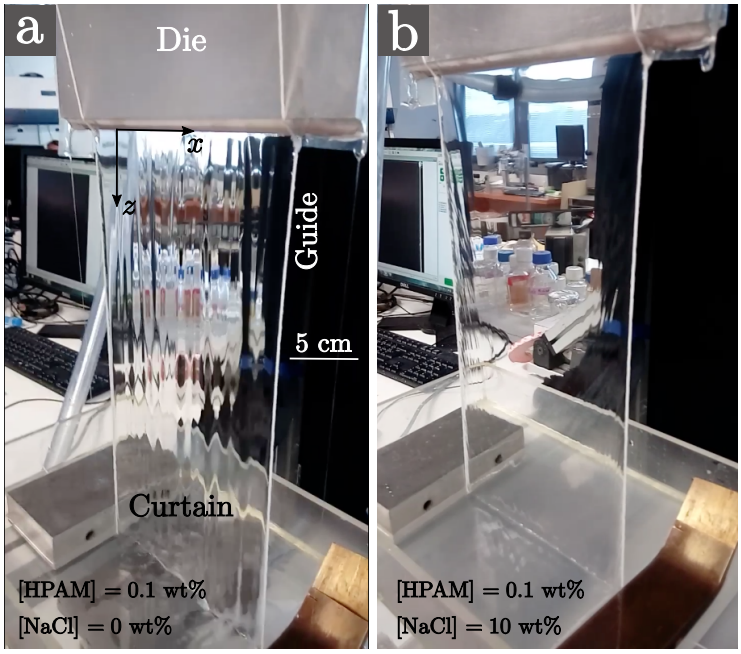

Figure 5.4 – Modulated (a) and smooth (b) curtains observed when extruding an unsalted (a) and a salted (b, [NaCl] = 10 wt%) 0.1 wt% HPAM solution (see table B.5). In (a), the curtain organises in a succession of vertical thick and thin bands where the liquid is respectively faster and slower than average.

rheology of a sample of liquid collected simultaneously, exactly like for the liquids of table B.2 (bottom). We choose to use the liquids of table B.5 to characterise the curtain modulation. The thickness modulation of the curtain (succession of thick and thin vertical bands) is illustrated by the deformation of the background when looking through the transparent sheet. The PIV measurements corresponding to these curtains are very similar to the ones already shown in figure 3.3 (smooth curtain) and figure 4.2 (modulated curtain).

Velocity distribution

We now describe this instability in more details. In figures 5.5.a and 5.6.a, we present the velocity field $U(x,z,t)$ of an unsalted 0.1 wt% HPAM solution against the distance z from the slot at 42 different horizontal positions x_i (along the slot) at arbitrary times t^* (figures 5.5.a) and $t^*+1.2$ s (figures 5.6.a). These figures contain the same information as figure 4.2.b where $U(x,z,t)$ is plotted against x for different z. At each distance z from the slot, the average velocity $\langle U\rangle_x$ is computed and is compared to its time average $\langle\langle U\rangle_x\rangle_t$ defined in §3.1.4 which is the velocity field $U(z)$ discussed in chapter 4. As already discussed in figure 4.3, $\langle U\rangle_x \approx \langle\langle U\rangle_x\rangle_t$ at all times which means that the average flow $\langle U\rangle_x$ is fairly independent of time.

We now discuss the distribution of the velocity field $U(x,z,t)$ around its mean value $\langle U\rangle_x$ at a given time. As illustrated in figures 5.5.a and 5.6.a, U ranges between a minimum and maximum value U_{min} and U_{max} which are both increasing functions

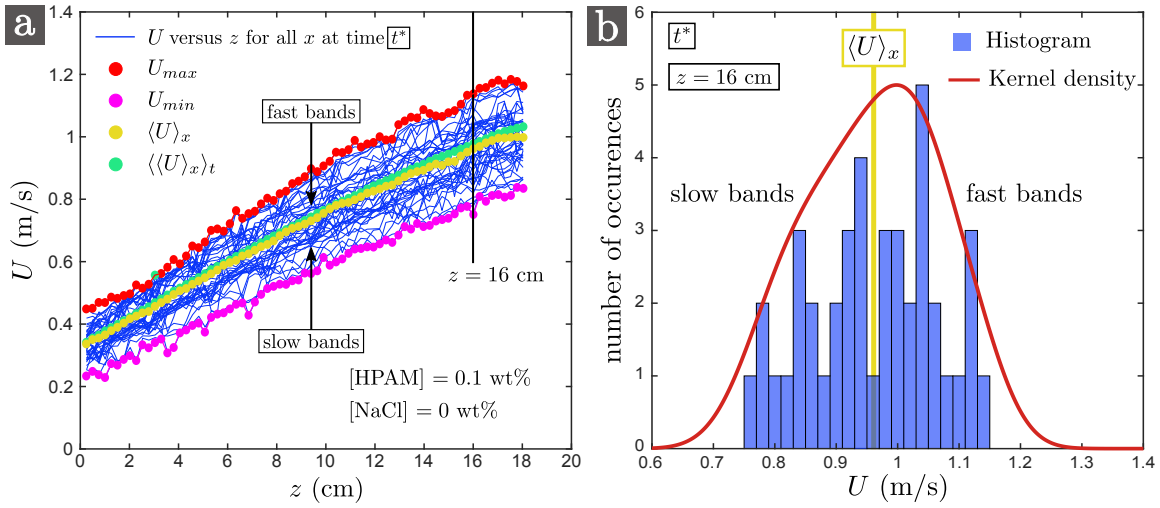

Figure 5.5 – (a): z-component of the velocity field, i.e. $U(x, z, t)$, against the distance z from the slot at 42 different horizontal positions x_i (along the slot) at an arbitrary time t^* for an unsalted 0.1 wt% HPAM curtain (see table B.5) of length $L_c = 30$ cm. The difference between two successive positions is $x_{i+1} - x_i = 2.7$ mm (the size of a PIV correlation window). At a given distance z from the slot, the velocity along x ranges between U_{min} and U_{max} with an average value $\langle U\rangle_x$. Each blue curve is either above or below the average curve, meaning that the curtain organises in a horizontal succession of fast vertical "bands" and slow ones. The time average $\langle\langle U\rangle_x\rangle_t$ defined in §3.1.4 is also shown. (b): Histogram of the velocity distribution at an arbitrary distance $z = 16$ cm from the slot. The kernel density estimation (KDE) is also shown. The KDE is normalised for an easier comparison with the histogram.

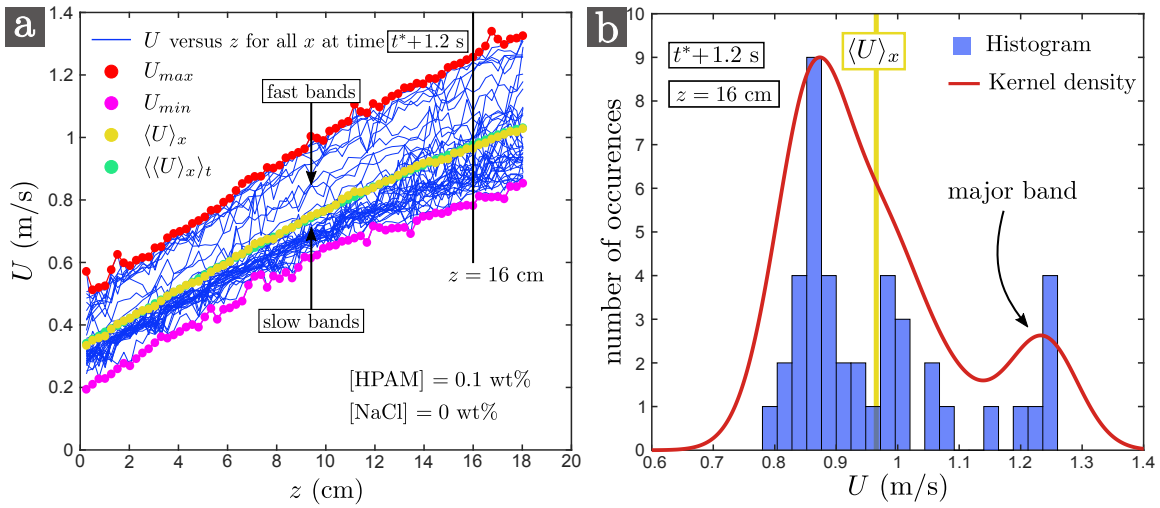

Figure 5.6 – Same as figure 5.5 but 1.2 seconds later. The velocity field (a) and the histogram (b) show the appearance of a band of fluid which is much faster than the others ("major band") and which can clearly be identified in the curtain movie.

of z. At each position x_i, the velocity curve $U(x_i, z, t)$ versus z is either below of above the mean curve $\langle U \rangle_x$, which means that the liquid within each vertical band is either systematically faster or slower than the average flow.

Typical flow pattern As observed in 5.5.a, the velocity distribution is often fairly symmetric around the average value and is quite narrow, meaning that there are no "extremely fast" or "extremely slow" flow regions. This is illustrated in figure 5.5.b by the histogram of the velocity distribution at an arbitrary distance $z = 16$ cm from the slot, superimposed to its associated kernel density estimation (KDE). The KDE has only one peak corresponding to the average velocity $\langle U \rangle_x$.

Atypical flow pattern However, as shown in figures 5.6.a and b, for the same liquid at a different time, the distribution can be wider and the KDE can even display other secondary peaks (here one) corresponding to atypically fast or slow flow regions. In the case of an atypically fast flow region, curtain movies reveal the existence of a band of fluid ("major band" in figure 5.6) which is faster (and also thicker) than the other fast bands. Such bands are often wider than the others (larger extension in the x direction). On the other hand, in the case of an atypically slow flow region, curtain movies reveal the existence of a band of fluid which is slower (and also thinner) than the other slow bands, sometimes so thin that almost no PIV tracers can be found in this region. This scenario corresponds to the velocity field presented in figure 4.2. The latter scenario often leads to curtain breaking (spontaneous hole opening event), as will be discussed in §5.2.2.

As will be discussed in chapter 6, this curtain modulation is the consequence of a flow instability at the inlet of the slot (planar contraction) which results in the formation of overfed and underfed spots x_i along the slot. For the downstream curtain, this leads to a the formation of thick-and-fast bands (overfed spots) and thin-and-slow ones (underfed spots).

HPAM: The influence of salt concentration

In figure 5.7, we present the average velocity $\langle \langle U \rangle_x \rangle_t$ of three 0.1 wt% HPAM solutions with different salt concentrations. The fact that the velocity increases when increasing the salt concentration comes from a reduction of the extensional relaxation time τ_{fil}. To compare the relative amplitudes of the curtain modulation, we plot the time averages $\langle U_{min} \rangle_t$ and $\langle U_{max} \rangle_t$ of the minimum and maximum velocities U_{min} and U_{max} defined in figures 5.5.a and 5.6.a. Clearly, the curtain flow is less and less modulated as salt is added to the solution, i.e. the velocity distribution narrows

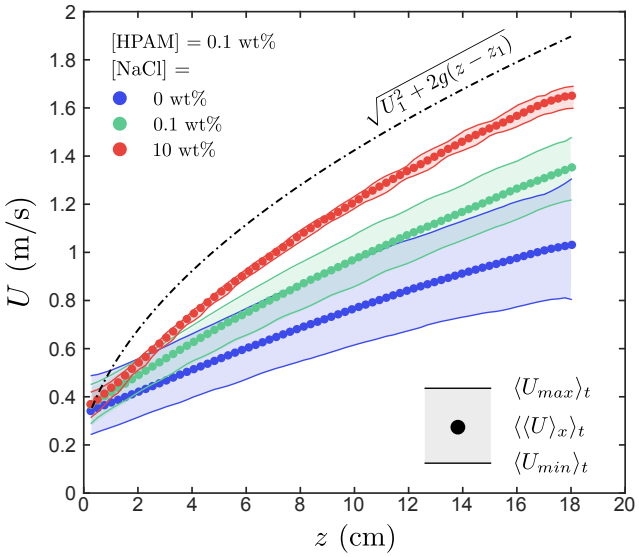

Figure 5.7 – Amplitude of the velocity distribution for three 0.1 wt% HPAM solutions with different salt concentrations (see table B.5). The average velocity $\langle \langle U \rangle_x \rangle_t$ is compared to the time averages or the $\langle U_{min} \rangle_t$ and $\langle U_{max} \rangle_t$ of the minimum and maximum velocities U_{min} and U_{max} defined in figures 5.5.a and 5.6.a. The curtain length is $L_c = 30$ cm

down with the addition of salt. In fact, for [NaCl] = 1 wt% (not shown) and 10 wt%, the velocity profile is similar to the one shown in figure 3.3 which means that the curtain flow can be considered as stationary and translation invariant along x. The slight variation around $\langle \langle U \rangle_x \rangle_t$ is mainly due to small measurements errors.

In order to characterise the velocity distribution associated to different liquids, we introduce the standard deviation σ_U defined as

$$\sigma_U = \sqrt{\left\langle (U - \langle U \rangle_x)^2 \right\rangle_x} \tag{5.4}$$

which is a function of z and t. The time-averaged standard deviation $\langle \sigma_U \rangle_t$ is plotted against z in figure 5.8.a for the HPAM solutions of table B.5 (data of figure 5.7). It is an increasing function of z, which means that the velocity distribution gets wider far from the slot. This could have been anticipated by noticing that U_{min} and U_{max} "get away" from the average velocity curve in figures 5.5.a and 5.6.a and in figure 5.7. In order to estimate the amplitude of the velocity variation relatively to the average flow, we plot in figure 5.8.b the relative width of the velocity distribution defined as $\langle \sigma_U / \langle U \rangle_x \rangle_t$. It is close to $\langle \sigma_U \rangle_t / \langle \langle U \rangle_x \rangle_t$. It decreases with z since the increasing tendency of $\langle \langle U \rangle_x \rangle_t$ overcomes the decreasing tendency of $\langle \sigma_U \rangle_t$. The relative modulation amplitude decreases from more than 10 % for the unsalted HPAM solution to about 0.60 % (far from the slot) for the largest salt concentrations for which the flow is not modulated. The small 0.60 % error represents the small experimental

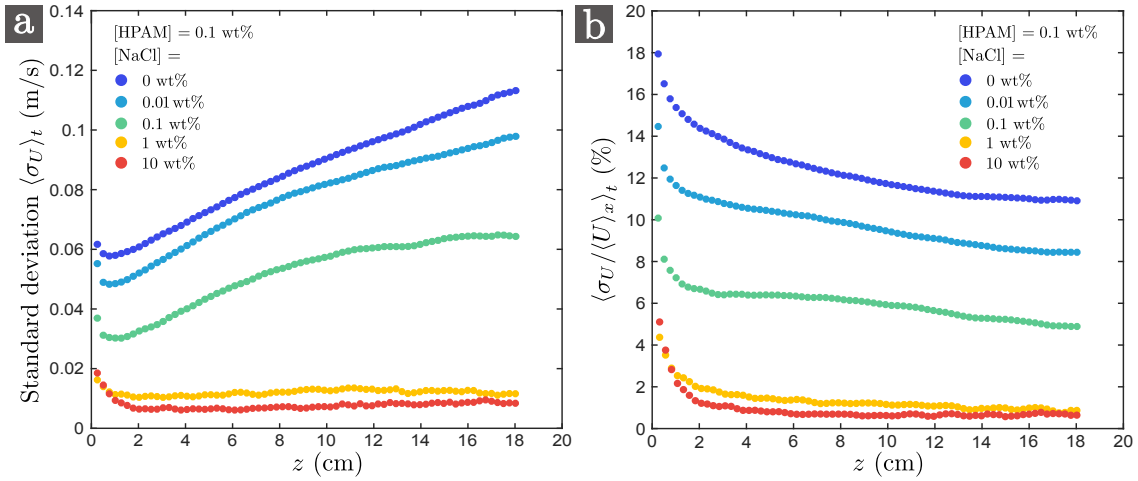

Figure 5.8 – (a) Time-averaged standard deviation $\langle\sigma_U\rangle_t$ (equation 5.4) against z for the HPAM solutions of table B.5. (b): Relative modulation amplitude $\langle\sigma_U/\langle U\rangle_x\rangle_t$ for the same liquids. The curtain length is $L_c = 30$ cm

errors in velocity measurements.

Note that $\langle\sigma_U\rangle_t$ slightly decreases close to the slot (see figure 5.8.a for $z \gtrsim z_1$). The reason is quite subtle. We recall that the flow has a y dependence, especially close to the slot where the Poiseuille flow inside the slot has not completely switched to a plug flow, as shown in the general overview of figure 4.9. Hence, PIV tracers at $y \approx 0$ (in the slot) exit the slot with a larger velocity than those at $y \approx \pm a$. In curtain movies, we clearly observe different "layers" of tracers of different velocities close to the slot exit. This results in a greater difficulty for the PIV correlation algorithm to estimate the velocity in this region, i.e. the measured velocity distribution is artificially slightly wider than expected. This is a pure limitation of our measurement method and is not related to any modulation of the flow along x. According to the data of figure 5.8.b, for the unmodulated curtains, this effect leads to an extra error of about 4 % (to be added to the 0.60 % experimental errors) in estimating the flow field in the first two centimetres of the flow (in particular in estimating U_1). This is small enough not to weaken the validity of the results presented in chapter 4.

HPAM: The influence of the flow rate

The influence of flow rate q on the modulation amplitude was investigated with unsalted HPAM solutions. A direct observation suggests that modulated curtains are smoother (less modulated) at lower flow rates, i.e. the background is less deformed when looking through the curtain. If $2h(x, z, t)$ is the local value of the curtain thickness and σ_h is the standard deviation of the thickness distribution, our

guess is that the amplitude $\langle \sigma_h / \langle h \rangle_x \rangle_t$ of the thickness modulation decreases when decreasing the flow rate. Since no direct thickness measurement was performed, this result is a conjecture. This scenario is reminiscent of the melt fracture phenomena reported by Morozov & van Saarloos (2007) (figure 2.14.a) for jets extruded from a tube and by Boger & Walters (2012) (figure 2.14b and c) for sheets extruded from a slot. In both cases, the amplitude of the thickness modulation is an increasing function of the flow rate. However, contrary to these analogous examples, we did not detect smooth curtains in the low flow rate limit. Indeed, as explored in §5.1.3, there is a minimum flow rate q_{min} below which the curtain rapidly breaks (in less than 30 seconds), thus forbidding the exploration of lower flow rates.

Different behaviours were observed when examining the velocity field of HPAM curtains extruded at different flow rates. When decreasing q, both narrower and wider velocity distributions could be observed. In the latter case, curtain movies reveal very slow bands of liquid connecting faster bands (atypical flow pattern). These slow bands seem to be almost not fed at all by the slot and are more likely to break due to spontaneous hole initiation (as will be developed in §5.2.2). However, the amplitude and duration of this phenomenon could vary from one curtain movie to an other, resulting in different values of both $\langle \sigma_U \rangle_t$ and $\langle \sigma_U / \langle U \rangle_x \rangle_t$ for two movies of the same curtain extruded at the same flow rate. Indeed, curtains are filmed during two seconds (at 600 frames per second) while the time of evolution of the band pattern is of few tens of seconds. Hence, two different movies (of duration two seconds) will potentially exhibit different band patterns. Therefore, although curtain movies are long enough to estimate roughly the width of the time-averaged velocity distribution, they are not long enough to obtain reproducible results.

Attempt of bifurcation diagram

In order to determine the role of rheological parameters in the appearance of the curtain modulation, we gather data extracted from many curtains in figure 5.9 where both $\langle \sigma_U \rangle_t$ (a) and $\langle \sigma_U / \langle U \rangle_x \rangle_t$ (b) (measured at an arbitrary distance $z = 16$ cm from the slot) are plotted versus $1 - n$ where n is the degree of shear thinning (see equation 3.7). There is clearly a correlation between the amplitude of the modulation and the degree of shear thinning. The only curtains exhibiting a modulation are the HPAM solutions with low salt concentrations and the 0.4 wt% PEO solution with 20 wt% PEG solvent at low degradation times. More generally, according to figure 5.9, the curtain becomes unstable for $n < n_c$ in the range of investigates flow rate , where the "instability threshold" is approximately $n_c = 0.72$. According to the correlation identified in figure 3.12.b between n and the effective value b of the

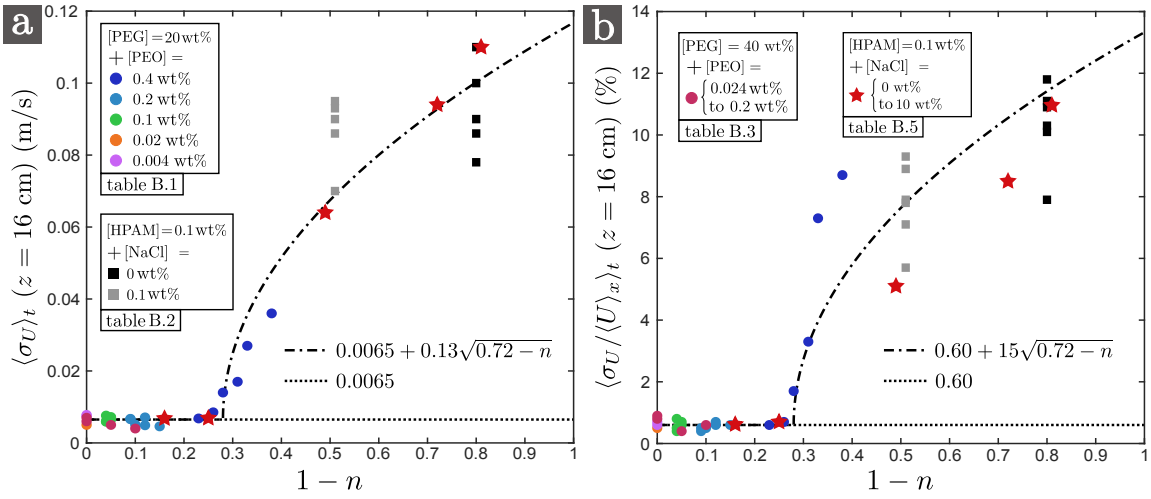

Figure 5.9 – Bifurcation diagram. Amplitudes $\langle \sigma_U \rangle_t$ (a) and $\langle \sigma_U / \langle U \rangle_x \rangle_t$ (b) of the modulation at an arbitrary distance $z = 16$ cm from the slot versus $1 - n$ where n is the degree of shear thinning (see equation 3.7) for the liquids of table B.1, B.2 (top), B.3 and B.5 corresponding to the data of figure 5.8. The modulation amplitude starts increasing for $n < 0.72$. A square root fit is drawn in both cases. The curtain length is $L_c = 30$ cm except for the PEO solutions with 40 wt% PEO solvent (table B.3) for which the curtain is not modulated for all curtain lengths L_c ranging between 15 cm and 200 cm.

finite extensibility parameter, this is equivalent of saying that the curtain becomes unstable for b smaller than a critical value b_c, i.e. for the most rigid polymers. Plotting the modulation amplitude against b suggests $b_c \approx 3 \times 10^3$.

We present in figure 5.9 an tentative of fit with a square root law of the type $B_0 + A_m\sqrt{n_c - n}$ which corresponds to a supercritical pitchfork bifurcation. B_0 is simply the amplitude of the measurement errors and A_m is a fitting parameter. Although the agreement is not too bad, the experimental data are too scattered to conclude on any particular law. The scatter in the data comes probably from the lack of reproducibility mentioned earlier. For example, the six unsalted HPAM solutions of table B.2 (top) are extruded at similar flow rates q ranging between 2.9 cm^2/s and 3.1 cm^2/s and there is no correlation between $\langle \sigma_U \rangle_x$ and the degree of degradation. Hence, for this set of curtains, the scatter in the data can hardly be attributed to the effect of flow rate of to the effect of other rheological parameters. Note that plotting the same data against the extensional relaxation time τ_{fil} (for example) does not provide such a clear separation between stable and unstable (modulated) curtains. In particular, the PEO solutions with 40 wt% PEG solvent have large extensional relaxation times but are almost non shear-thinning fluids ($n \geq 0.9$) exhibiting no curtain modulation.

5.2.2 Impact on curtain stability

Dynamics of hole opening

The modulation of the curtain has a strong impact on the curtain stability in terms of spontaneous hole opening events. Indeed, thin bands are quite fragile, especially in an extreme cases where a band of liquid seems to be almost not fed at all (atypical flow pattern). Hence, hole initiations are more frequent in modulated curtains since a bubble ending up in a thin band is more likely to burst than in a smooth curtain extruded at the same flow rate. Besides, since the liquid velocity is lower in such bands, the time spent by the bubble in the curtain (before advection in the reservoir) is larger and it has more time available to burst. Moreover, due to the reduction of the curtain thickness in thin bands, the local Taylor-Culick velocity $V(x,z,t) = \sqrt{\Gamma/\rho h(x,z,t)}$ can be much larger than its average value

$$\langle V \rangle_x = \sqrt{\frac{\Gamma}{\rho \langle h \rangle_x}} \tag{5.5}$$

Besides, the advection is reduced since the local velocity $U(x,z,t)$ of the surrounding liquid is smaller in thin bands. Combining both effects, the local Weber number $We = (U/V)^2$ can be quite small in thin bands, i.e. smaller than the ratio of the averaged velocities defined as a "mean Weber number"

$$\langle We \rangle_x = \left(\frac{\langle U \rangle_x}{\langle V \rangle_x} \right)^2 = \frac{\rho \langle h \rangle_x \langle U \rangle_x^2}{\Gamma} \tag{5.6}$$

which is also $\langle We \rangle_x = \rho q \langle U \rangle_x / 2\Gamma$ when assuming that $2\langle h \rangle_x \langle U \rangle_x = q$, by analogy with smooth curtain for which $2hU = q$.

In figure 5.10, we present two scenarios observed in a curtain of unsalted HPAM solution with concentration close to 0.1 wt% extruded at a flow rate $q = 3.8$ cm^2/s. In both cases (a and b), a hole is initiated in a very thin band (atypical flow pattern and low local Weber number) and the upper edge of the hole initially propagate upwards. This initial phase can be seen as a "fracture" developing along a "weak" part of the curtain. In both cases (a and b), the thin band upstream of the hole disappears at some point due to the natural evolution of the band pattern (whose time scale is of the order of a few tens of seconds). Hence, the upper edge of the hole may propagate upwards or downwards depending on the new value of the local Weber number. In the first case (a), it reaches the slot and the hole finally invades the whole curtain, resulting in a permanent arch (rim) of liquid. The curtain is irreversibly broken. However, in the second case (b), the hole is finally advected by the flow (self-healing). Generally speaking, since the average Weber number $\langle We \rangle_x$

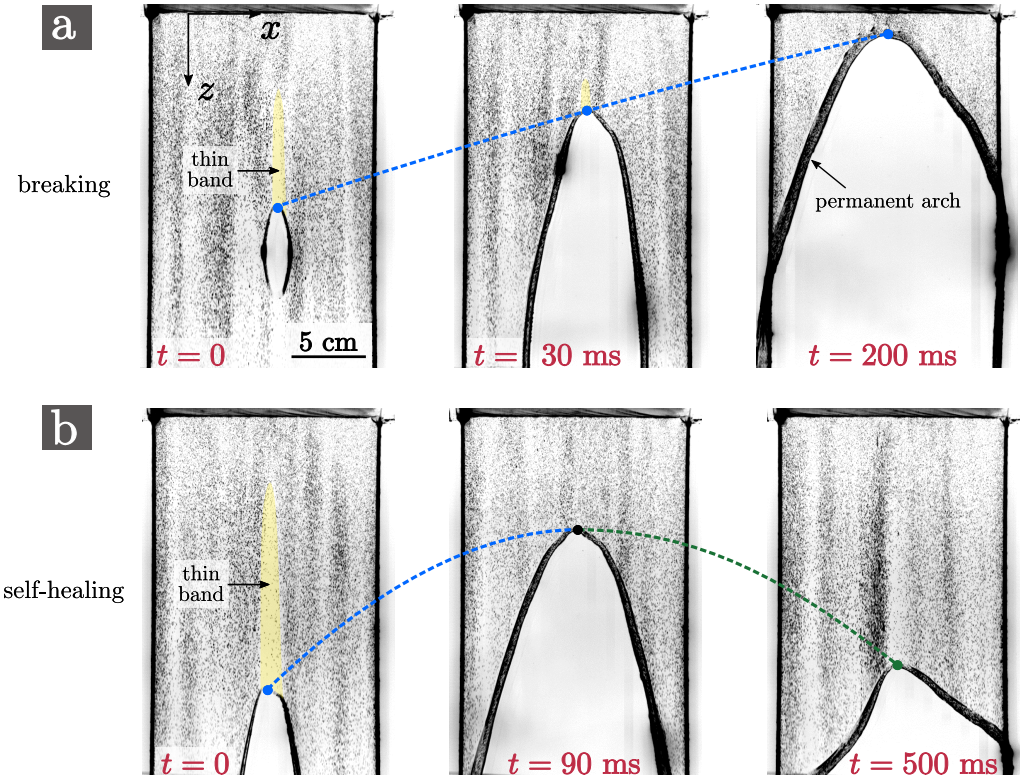

Figure 5.10 – Two different scenarios after a spontaneous hole opening event in a given modulated curtain. The hole is generally initiated in a thin band where the local Taylor-Culick velocity V is large and the local liquid velocity U is low. Therefore, the upper edge of the hole initially propagates upwards. When the thin band upstream of the hole disappears due to the natural evolution of the band pattern, the upper edge of the hole may go on propagating upwards and cause irreversible breaking of the curtain (a), or start propagating downwards, in which case the hole is finally advected (b). The liquid is an unsalted HPAM solution with concentration 0.08 wt% (early experiment) extruded at a flow rate $q = 3.8$ cm^2/s. The curtain length is $L_c = 30$ cm.

is lower close to the slot, a hole is more likely to reach the slot (and therefore to break the curtain) if the initial "fracture" along the thin band takes the hole to a vertical position z close to 0. The self-healing scenario, where the hole goes "up and down", is frequently observed in modulated curtains. However, it is never observed in smooth curtains since there is a clear altitude separating the unstable zone close to the slot from the unstable zone downstream.

We can estimate the thickness of the thin band in figure 5.10.a. For simplicity, we assume that the dynamic of hole opening is only influenced by capillarity and inertia without any effect of the weight of the rim, so that the velocity of the upper edge of the hole is $v_{hole} = V - U$ where V and U are the local values in the thin band. We show in figure 5.11 the time evolution of the altitude of the upper edge of the hole following hole initiation. The hole velocity is initially constant and equal

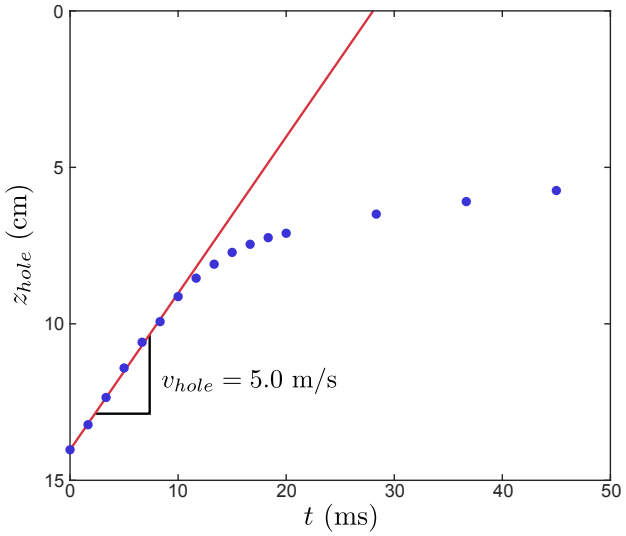

Figure 5.11 – Altitude of the upper edge of the hole in figure 5.10.a, a few milliseconds after initiation of the hole, measured from the curtain movie. $z = 0$ corresponds to the altitude of the slot exit.

to $v_{hole} = 5.0$ m/s within the first 10 ms. It decreases after this initial phase due to a change in surrounding geometry: the portion of liquid upstream of the hole is now thicker. According to particle tracking velocimetry (PTV), the local liquid velocity in the thin band is $U = 1.1$ m/s during this initial phase, which gives $V = v_{hole} + U = 6.1$ m/s and $We = (U/V)^2 = 0.033 \leq 1$: the hole propagates upwards. Hence, using equation 5.1, we get $2h = 2\Gamma/\rho V^2 = 3.9$ μm. We now compare this to the average curtain thickness. According to PIV measurement, the average velocity at the altitude of hole initiation is $\langle U \rangle_x = 1.8$ m/s, about two times more than in the thin band. Hence, assuming that $2\langle h \rangle_x \langle U \rangle_x = q$, we get $2\langle h \rangle_x = 0.21$ mm $= 210$ μm which is 50 times more than in the thin band. We can calculate that the average Weber number at this altitude is $\langle We \rangle_x = \rho q \langle U \rangle_x / 2\Gamma = 4.8 > 1$ which means that the hole would be advected by the flow without curtain modulation.

Critical and minimum flow rate

For modulated curtains, we can also measure the critical flow rate q_c defined in §5.1.2. We recall that, starting from a broken curtain at low flow rate, the flow rate is increased until the last arch detaches from the slot. For example, the arch in figure 5.10.a (last picture) will remain as long as the flow rate $q = 3.8$ cm^2/s is kept constant, but it will detach from the slot and be advected after increasing the flow rate above a critical value q_c. The minimum flow rate q_{min} below which the curtain spontaneously breaks in less than 30 seconds is also measured. Results corresponding to the 0.1 wt% HPAM solutions of table B.5 are presented in figure 5.12 as a function of $1 - n$. We recall that the data corresponding to $n < 0.72$ (equivelently,

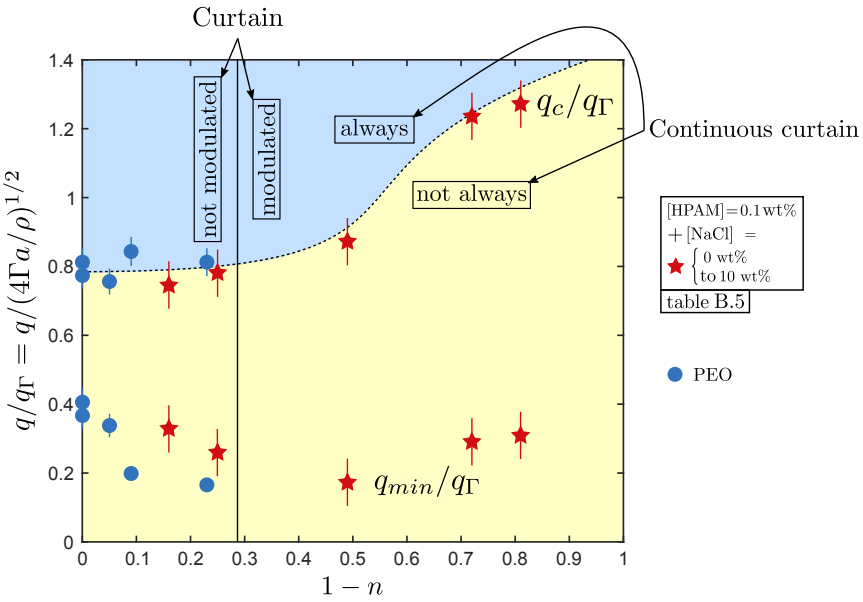

Figure 5.12 – Critical flow rate q_c (above which any hole is advected by the flow) and minimum flow rate q_{min} (required to maintain a continuous curtain for more than 30 seconds), divided by $q_\Gamma = (4a\Gamma/\rho)^{1/2}$, against $1-n$ (n being the degree of shear-thinning) for the five degraded ($t_d = 100$ min) PEO solutions with 20 wt% PEG solvent of table B.1 ($q_\Gamma = 3.5$ cm^2/s, data of figure 5.3.b) and for the 0.1 wt% HPAM solutions of table B.5 ($q_\Gamma = 3.8$ cm^2/s). The curtain length is $L_c = 30$ cm.

$1-n > 0.28$) correspond to modulated curtains (see bifurcation diagram in figure 5.9). The data corresponding to the degraded PEO solutions of figure 5.3.b (for which curtains are smooth) are also shown. Both q_{min} and q_c are normalised by $q_\Gamma = (4a\Gamma/\rho)^{1/2}$ which is 3.8 cm^2/s for the HPAM solutions and 3.5 cm^2/s for the PEO solutions. Note that the data are not plotted against the extensional relaxation time τ_{fil} contrary to figure 5.3.b.

As expected, $q_c/q_\Gamma \approx 0.8$ below the instability threshold. However, for $n < 0.72$, we measure larger critical flow rates, up to $q_c/q_\Gamma \approx 1.3$, which means that the flow rate has to be increased above the usual value to detach the arch from the slot. To understand this, let us consider that, at a given time, the position of the highest point of a permanent arch it x_a. Direct observation reveals that the horizontal position x_a of the arch usually coincide with an underfed spot along the slot, i.e. there is usually a thin band upstream of the arch. As the band pattern evolves, the thin band corresponding to this spot may disappear, in which case the horizontal position x_a of the arch spontaneously changes to match the position of a new underfed spot. During such transitions, the arch may be transiently advected by the flow since the inertia of the liquid leaving the slot becomes larger, thus resulting in an oscillatory vertical motion of the arch. This scenario is commonly observed with HPAM solu-

tions but is never observed for smooth PEO curtains for which arches are quite still. For the arch of figure 5.10.a (last picture), PIV reveals that the average velocity at the slot exit is $\langle\langle U\rangle_x\rangle_t = 0.40$ m/s $(= U_1)$ which means that the average Weber number is $\langle\langle We\rangle_x\rangle_t = \rho q\langle U\rangle_x/2\Gamma = 1.0$. Hence, when adding the weight of the rim pulling the arch downwards, we understand that the arch can only "survive" as long as its horizontal position coincides with an underfed spot where the Weber number is locally less than one. According to this interpretation, the particular rheology of the liquid is not the direct cause of the unusually high value of q_c. High values of q_c are rather a direct consequence of the curtain modulation, which is itself probably a consequence of the liquid rheology.

Figure 5.12 also suggests that q_{min} is larger than expected for modulated curtains. Indeed, the unsalted HPAM values (for which $1 - n$ is large) correspond to the largest extensional relaxation times $\tau_{fil} \approx 0.3$ s. Hence, following the trend in figure 5.3.b, we expect values of q_{min}/q_Γ lower than 0.2 in the absence of modulation since the largest PEO extensional relaxation time in the plot is 0.12 s (less than 0.3 s). Nonetheless, we find $q_{min}/q_\Gamma \approx 0.3 > 0.2$ for unsalted HPAM curtains. This result suggests that, due to the presence of fragile thin bands, modulated curtains break more easily than smooth curtains at a given flow rate and for the same value of τ_{fil}.

5.2.3 The influence of the die geometry

With the intuition that the curtain modulation is a consequence of a flow instability at the planar contraction upstream of the slot, we predict that the length L_s of the slot may affect the amplitude of the curtain modulation. Indeed, if the width of the velocity distribution decreases inside the slot, we should observe an increase of the curtain modulation amplitude when shortening the slot.

We examine the role of the die geometry by performing experiments with an unsalted 0.1 wt% HPAM solution extruded from two different dies. The first die is the usual die presented in figure 3.2.b with a slot of thickness $2a = 1$ mm and length $L_s = 10$ cm. The other die presented in figure 5.13.a consists of a hollow cylinder drilled with a slot of same thickness $2a^\star = 1$ mm. The slot has a much shorter length $L_s^\star = 4$ mm. In fact, this type of die is much more common than the die of figure 3.2.b which was specifically designed for us, in particular to ensure that the time L_s/U_s spent by the liquid in the slot is longer than its extensional relaxation time τ_{fil} (see discussion in §4.3.1).

Figure 5.13.b displays the amplitude $\langle\langle\sigma_U/U\rangle_x\rangle_t$ of the velocity modulation meas-

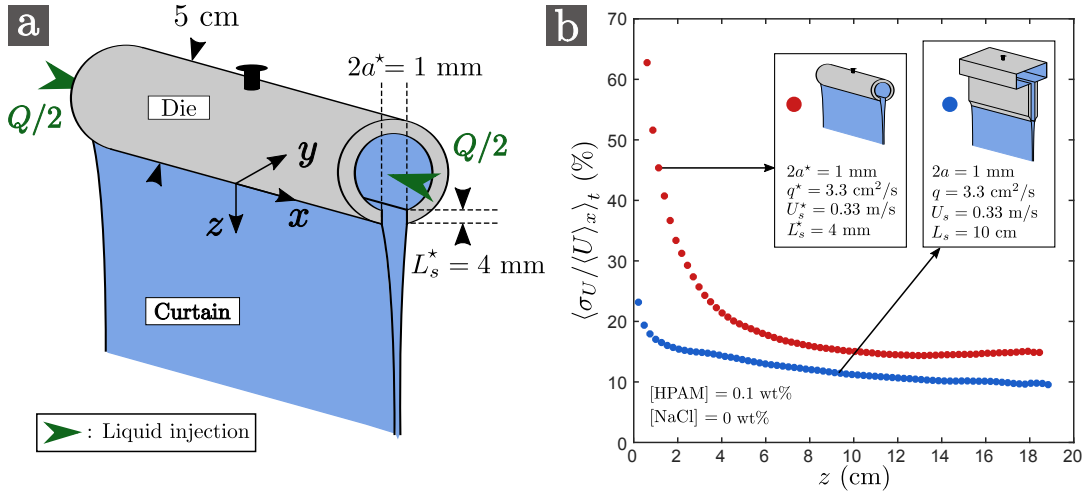

Figure 5.13 – (a) Sketch of a curtain extruded from a cylindrical die drilled with a slot of thickness $2a^\star = 1$ mm and length $L_s^\star = 4$ mm on its lower side. (b): Comparison of the relative modulation amplitude $\langle\sigma_U/\langle U\rangle_x\rangle_t$ for an unsalted 0.1 wt% HPAM solution extruded from this cylindrical die and from the usual die of slot length $L_s = 10$ cm presented in figure 3.2.b at the same flow rate $q = q^\star = 3.3$ cm^2/s. The curtain length is $L_c = 30$ cm.

ured on curtains extruded from the two dies at the same flow rate $q = 3.3$ cm^2/s. We obtain larger values for the cylindrical die, which suggests that shortening the slot exacerbates the curtain modulation. In particular, we obtain $\langle\langle\sigma_U/U\rangle_x\rangle_t > 50\%$ close to the slot exit, which is much larger than any of the values reported in previous examples using the usual die. Our interpretation is that the flow, which has a wide velocity distribution at the slot inlet, quietens down inside the slot. Hence, for the short slot, the curtain velocity distribution at the slot exit is closer to the characteristic velocity distribution at the contraction. This point is confirmed by direct visualisation of the flow. Indeed, for the cylindrical die, we observe fast portions of liquid erupting from the slot at unpredictable positions x. This often leads to the formation of "fingers" (or "spurts") of liquid within the curtain, i.e. thick portions of liquid generally evolving into thick bands. This is illustrated by the curtain pictures of figure 5.14 extracted from the image sequences used for figure 5.13.b.

Some details can be discussed regarding the data of figure 5.13.b. Although the flow rates are she same ($q = 3.3$ cm^2/s), which means that the average velocity inside the slot is the same and is equal to $\langle\langle U\rangle_x\rangle_t = U_s = q/2a = 0.33$ m/s, we measure that the initial average velocity at $z_1 \approx 2.5$ mm from the slot exit is $U_1 = \langle\langle U\rangle_x\rangle_t = 0.35$ m/s for the usual die and $U_1^\star = 0.18$ m/s $< U_1$ for the cylindrical die. A possible interpretation is that, the curtain swells (on average) for the short slot while, as mentioned in §4.1.3, is does not swell (on average) for HPAM curtains extruded from the usual long-slot die. Indeed, as discussed for example by

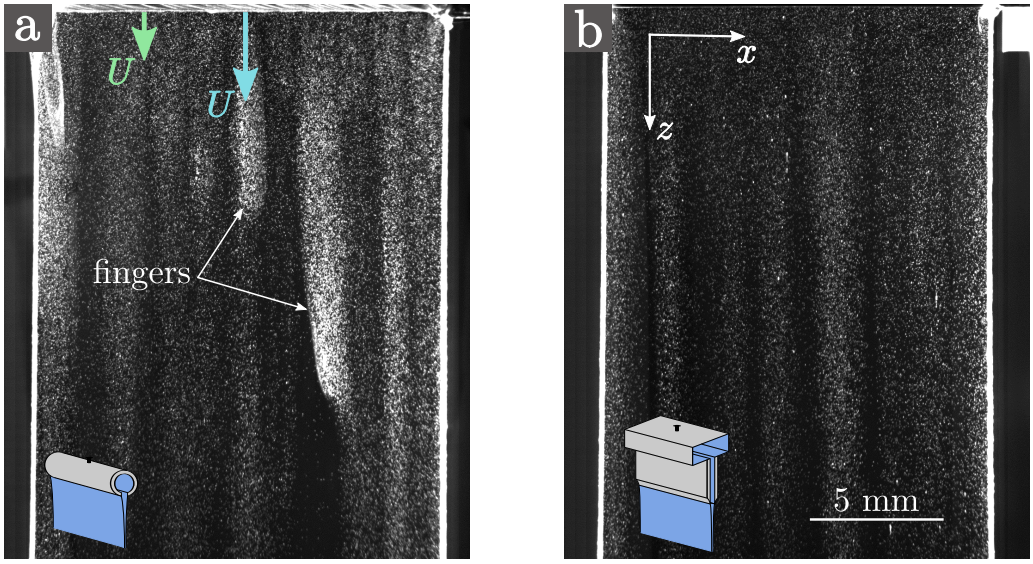

Figure 5.14 – Typical flow patterns for an unsalted 0.1 wt% HPAM solution (the same in (a) and (b)) extruded from the short-slot cylindrical die of figure 5.13.a (a) and from the usual long-slot die of figure 3.2.b (b) at the same flow rate $q = 3.3$ cm^2/s. In the first case, fast portions of liquid erupt from the slot, leading to the formation of thick "fingers" of liquid within the curtain. Images are extracted from the image sequences used for figure 5.13.b. The curtain length is $L_c = 30$ cm.

Kiriakidis & Mitsoulis (1993), it is well known that the swelling ratio increases when the slot aspect ratio $L_s/2a$ decreases. Since, the slot exit is not bevelled (contrary to the usual die), wetting at is also a possible interpretation. Since U_1 is not the same for both dies, the amplitude of the modulation may be affected, as discussed in §5.2.1. However, it is clear from direct observation (figure 5.14) that the curtain behaves differently for the cylindrical die, and the large values of $\langle\langle\sigma_U/U\rangle_x\rangle_t$ can not simply be attributed to a lower initial velocity. For example, the absolute width $\langle\langle\sigma_U\rangle_x\rangle_t$ of the velocity distribution at $z = 16$ cm from the slot exit is 0.12 m/s for the cylindrical die and 0.09 m/s for the usual die. Hence, the large relative value $\langle\langle\sigma_U/U\rangle_x\rangle_t \approx \langle\langle\sigma_U\rangle_x\rangle_t/\langle\langle U\rangle_x\rangle_t$ does not come from a lower value of the average velocity $\langle\langle U\rangle_x\rangle_t$. In fact, we chose to have the same value of U_s instead of the same value of U_1 because, as will be developed in chapter 6, the amplitude of the flow instability at the planar contraction is known to be a function of the Weissenberg number $Wi = \tau U_s/a$ where τ is a polymer relaxation time.

Finally, we shall mention here that original results were obtained when using the inclined plate technique described in figure 4.15.a to produce a curtain out of an unsalted 0.1 wt% HPAM solution. If the liquid velocity along the plane is large enough, the liquid forms a nice continuous sheet in the form of an arc with no abrupt transition to a vertical curtain when reaching the end of the plane. In this

case, the sheet is perfectly smooth, i.e. not modulated at all along x. However, at lower velocities, we observe the abrupt transition shown in figure 4.15.a where the free-surface has a high curvature at the end of the plane. In this case, the vertical curtain is modulated, like after extrusion through a die. However, there is no apparent modulation of the liquid film flowing down the plane, and the destabilisation emerges at the high curvature point at the end of the plane, with the formation of "ribs" at the free-surface. Similar ribs can be observed simply by pouring a HPAM solution from a beaker. This phenomenon may belong to the family of interfacial viscoelastic instabilities (described for example by Graham (2003)) arising from the combination of large tangential tension and surface curvature and leading to unstable stress gradient along the free-surface. Of course, such ribs were not observed for the PEO solution used in figure 4.15.b. Much more work would be needed to characterise this effect.

In the next chapter, focusing on the modulation of curtains extruded from a die, we present some visualisations of the planar contraction flow upstream of the slot.

Chapter 6

Planar contraction flow

Contents

In this section, we present visualisations of the flow upstream of the slot, where the liquid is forced to flow through an abrupt planar contraction. Since the die used in curtain experiments is made of opaque metal, another die of similar slot thickness and contraction ratio has been designed using Plexiglas. These experiments confirm

a correlation between the modulations observed in the curtains described in §5.2 and the presence of a flow instability at the slot inlet.

We begin by introducing the results found in the literature concerning axisymmetric and planar contraction flows of viscoelastic liquids. Then we present the experimental set-up which was developed specifically for this flow visualisation, as well as the rheology of the test liquids, before finally presenting our results.

6.1 State of the art

6.1.1 General context

The viscoelastic entry flow problem has a rich history and has received a particular attention in the experimental and numerical community in the last decades. It has been selected by the computational rheology community as a core problem for testing algorithms due to the diversity and complexity of the associated flow patterns. Three orifice configurations are generally considered, as shown in figure 6.1, in both axisymmetric and planar geometries. The upstream part, which corresponds generally to a fully developed Poiseuille flow in a channel of size A, is followed by a constriction of size a and length L_s. The contraction ratio is defined as $\beta \equiv A/a$. Depending on the particular orifice configuration, the flow can either expand in a new channel of size A (figure 6.1.a: contraction-expansion), or leave the contraction and be exposed to ambient air (figure 6.1.b: free curtain (planar) or free jet (axisymmetric)). The contraction can also have an infinite length (figure 6.1.c: entry in an infinite slot (planar) or in an infinite capillary (axisymmetric)). The last configuration is of particular interest for numerical studies. Note that contraction flows have both a shear component, due to the presence of walls, and an extensional component due to rapid increase of the velocity at the contraction inlet. Before the existence of filament thinning techniques, this flow had even been considered for measurements of the extensional viscosity of polymer solutions (Binding & Walters, 1988).

Most experimental studies have been focusing on the characterisation of the flow pattern at the contraction using PIV techniques. Early photographs of viscoelastic entry flow patterns, in both axisymmetric and planar geometries, have been gathered in the reference book "Rheological phenomena in focus, volume 4" by Boger & Walters (2012), Chapter 3: "Contraction and expansion flows". Some experimental studies have also addressed the question of the pressure drop arising from the presence of the contraction by measuring the pressure difference $P_1 - P_2$ between two planes

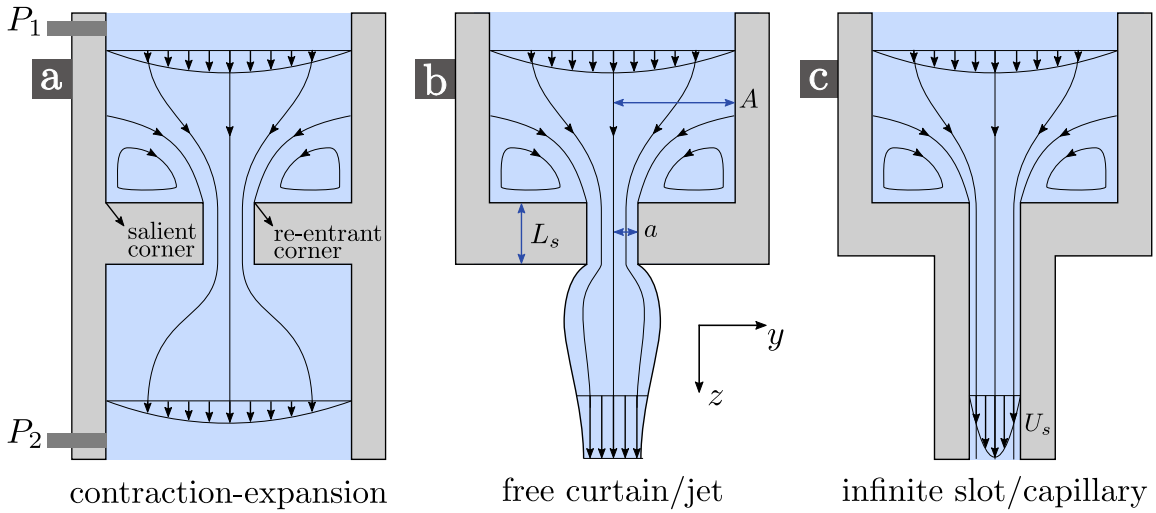

Figure 6.1 – Side view of three orifice configurations considered in the literature for (axisymmetric and planar) contraction flows. (a): contraction-expansion, (b): free curtain (planar) or free jet (axisymmetric), (c): entry in an infinite slot (planar) or in an infinite capillary (axisymmetric). In the planar case, the thickness of the upstream channel is A and the thickness and length of the slot are a and L_s. The mean velocity increases from $q/2A$ to $U_s = q/2a$ in the slot, where q is the linear flow rate. In the first configuration (a), pressure measurements are often performed upstream (P_1) and downstream (P_2) of the contraction.

far upstream and far downstream of the contraction in a contraction-expansion configuration.

Dimensionless group

For a viscoelastic liquid, the flow characteristics depend on the Reynolds and Weissenberg numbers which are usually defined as

$$Re = \frac{\rho U_s a}{\eta^*} \qquad \text{and} \qquad Wi = \frac{\tau^* U_s}{a} \tag{6.1}$$

where ρ is the fluid density, η^* is a characteristic shear viscosity and τ^* is a characteristic relaxation time. Since the mean flow velocity switches from the upper channel value (which is $q/2A$ in the planar case, where q is the linear flow rate) to the contraction value U_s ($=q/2a$ in the planar case) in a characteristic time $\sim a/U_s$, the Weissenberg number is in fact the ratio of a polymer relaxation time and a flow timescale. This flow timescale is the characteristic residence time in the contraction region, as well as the inverse of the characteristic shear rate $\dot{\gamma}^*$ in the contraction which is given by

$$\dot{\gamma}^* = \frac{U_s}{a} \tag{6.2}$$

In the planar case, the local value $\dot{\gamma} = \mathrm{d}u/\mathrm{d}y$ of the shear rate for a fully developed

Poiseuille flow can be calculated from equation 4.20. Other dimensionless numbers may be considered for a given viscoelastic liquid, such as the finite extensibility parameter b of the FENE-P model, or the experimentally measured degree of shear-thinning n.

Reynolds number When calculating the Reynolds number, many authors choose to define the characteristic shear viscosity as $\eta^* = \eta(\dot{\gamma}^*)$ where η is the apparent shear viscosity measured with a shear rheometer (McKinley et al., 1991; Chiba et al., 1990). Other authors choose the zero-shear viscosity, i.e. $\eta^* = \eta_0$, which is an equivalent definition for non shear-thinning fluids (Walters & Rawlinson, 1982; Rothstein & McKinley, 2001; Rodd et al., 2005).

Weissenberg number When calculating the Weissenberg number, two different approaches have been considered. Many authors have used the following definition

$$Wi = \tau^*(\dot{\gamma}^*)\,\dot{\gamma}^* \qquad \text{with} \qquad \tau^*(\dot{\gamma}^*) = \frac{\Psi_1(\dot{\gamma}^*)}{2\eta(\dot{\gamma}^*)} \tag{6.3}$$

where Ψ_1 is the first normal stress coefficient defined as $\Psi_1 \equiv N_1/\dot{\gamma}^2$ where N_1 is the first normal stress difference measured with a shear rheometer (McKinley et al., 1991; Walters & Rawlinson, 1982; Rothstein & McKinley, 1999; Cartalos & Piau, 1992; Piau et al., 1990). Among these authors, some add a numerical prefactor ($\dot{\gamma}^* = 8U_s/a$ for axisymmetric contractions) to their definition $\dot{\gamma}^*$ to account for larger shear rates close to the walls (Cartalos & Piau, 1992; Piau et al., 1990). Other authors choose the zero-shear-rate relaxation time $\tau_0 = \Psi_{10}/2\eta_0$ where Ψ_{10} is the constant value approached by Ψ_1 at small shear rates (Rothstein & McKinley, 2001). Both definitions are equivalent for non shear-thinning fluids exhibiting quadratic normal stresses $N_1 \propto \dot{\gamma}^2$. The second approach in more recent studies (Rodd et al., 2005, 2007) was to use the extensional relaxation time τ_{fil} measured in CaBER experiments as a characteristic relaxation time, i.e.

$$Wi = \frac{\tau_{fil}\, U_s}{a} \tag{6.4}$$

This choice is motivated by the extensional component of the flow which is due to rapid increase of the velocity at the contraction inlet where polymer chains undergo a transient elongation. Indeed, polymers chains may unravel partially depending on the magnitude of the Weissenberg number: if $\tau_{fil} \ll a/U_s$, the polymer relaxation overcomes stretching and the liquid behaves almost as a Newtonian liquid, whereas if $\tau_{fil} \gg a/U_s$, polymer chains undergo a rapid Hencky strain equal to $\ln(\beta^2)$ in the axisymmetric case and to $\ln(\beta)$ in the planar case (Rothstein & McKinley, 1999).

This difference in the amplitude of polymer elongation is one of the reasons for the many differences between axisymmetric and planar contractions.

6.1.2 Axisymmetric contraction

Non shear-thinning fluids without inertia

The laminar flow of a Newtonian liquid is characterised by the presence of a weak recirculating vortex in the salient corner, upstream of the contraction plane, called corner vortex or "Moffatt eddy" (Moffatt, 1964). In an axisymmetric contraction, this vortex takes the form of a torus. This weak corner vortex can also be observed at low Weissenberg numbers for viscoelastic liquids. As the Weissenberg number is increased, two distinct scenarios have been identified for non shear-thinning fluids ($n = 1$) with negligible inertia ($Re \ll 1$) at a given contraction ratio β (see pictures of Boger & Walters (2012) and Rothstein & McKinley (1999)).

• In a nutshell, for some elastic fluids, the size of the corner vortex increases, i.e. it grows radially inward toward the re-entrant corner while growing axially outward. This flow regime is steady in time until reaching a critical Weissenberg number Wi_c marking the onset of a flow instability: the corner vortex become asymmetric and precesses (oscillates) in the azimuthal direction at a frequency which increases with Wi, i.e. fluid elements follow a helical path into the orifice (Rothstein & McKinley (1999), $Wi_c \approx 2.8$ for $\beta = 4$). More dramatic unsteady patterns are observed at very large Weissenberg numbers (Boger & Walters, 2012).

• A second scenario is observed for other elastic fluids at the same contraction ratio: the size of the corner vortex decreases while a separate, distinct "lip vortex" appears near the re-entrant corner and expands in the radial direction until "devouring" the corner vortex. This flow becomes unsteady in time above some critical Weissenberg number: the size of the lip vortex oscillates with a regular period (Boger & Walters, 2012; McKinley et al., 1991). These oscillations can only be observed in a certain range of contraction ratios (McKinley et al. (1991) proposed $2 \leq \beta \leq 5$) and the flow remains steady for larger contraction ratios. More complex behaviours are observed at large Weissenberg numbers.

Since, in both cases, the resulting vortex (corner or lip) is much larger than the Newtonian Moffatt eddy, these phenomena are commonly referred to as "vortex enhancement" and are attributed to elastic effects. An example is shown in figure 2.13.c. In the case of a free jet orifice configuration (see figure 6.1.b), it has been shown that the oscillations observed in the unsteady regime were responsible for the

strong surface defects observed in the downstream extruded jet and referred to as "melt-fracture" (Piau et al., 1990).

In parallel, beyond a critical Weissenberg number which is smaller than Wi_c, the measured pressure drop becomes larger than the pressure drop predicted by the Newtonian theory. This extra pressure drop is associated with the strong extensional flow near the contraction inlet but could not be predicted by numerical computations using simple (Oldroyd-B) dumbbell models (Rothstein & McKinley, 1999).

Shear-thinning fluids with inertia

Fluid inertia and shear-thinning effects can alter the vortex growth scenario. Many authors have reported that, while elasticity encourages vortex growth, inertia tends to decrease the size of the vortex by pressing the vortex in the outer (salient) corner, resulting in a divergence of the streamlines towards the walls of the tube, thus leading to more complex flow patterns where a stagnant zone may be present in the central region near the contraction entry (Boger & Walters, 2012; Raiford et al., 1989; Kim-e et al., 1983). Calculations by (Kim-e et al., 1983) also suggest that shear-thinning decreases the size of the vortex and increases entrance pressure losses.

6.1.3 Planar contraction

Corner and lip vortices may also be observed on both sides of a planar contraction (two separated sets of vortices are formed instead of the recirculating torus observed in axisymmetric contractions). However, different pattern evolution scenarios have been reported. A comprehensive review of the different vortex growth scenarios in planar contractions has been proposed by Rodd et al. (2005).

Early works showed that non shear-thinning fluids exhibiting vortex enhancement in axisymmetric contractions may exhibit no evident vortex activity in planar contractions, while shear-thinning fluids usually exhibit vortex enhancement in both axisymmetric and planar contractions (Walters & Rawlinson, 1982; Evans & Walters, 1986, 1989). An other generally accepted idea is that, for a given shear-thinning liquid with negligible inertia, the existence of lip vortices depends on the contraction ratio. For example, for an aqueous solution of polyacrylamide (PAA) with large polymer concentration, while the corner vortex grows in size when increasing the Weissenberg number for $\beta = 4$, a lip vortex appears, grows, and ultimately "devours" the corner vortex for $\beta = 16$ (Boger & Walters, 2012). However, using a less concentrated aqueous solution of polyacrylamide with contraction ratio $\beta = 4$, a lip vortex is visible, proving that the vortex enhancement mechanism is a very

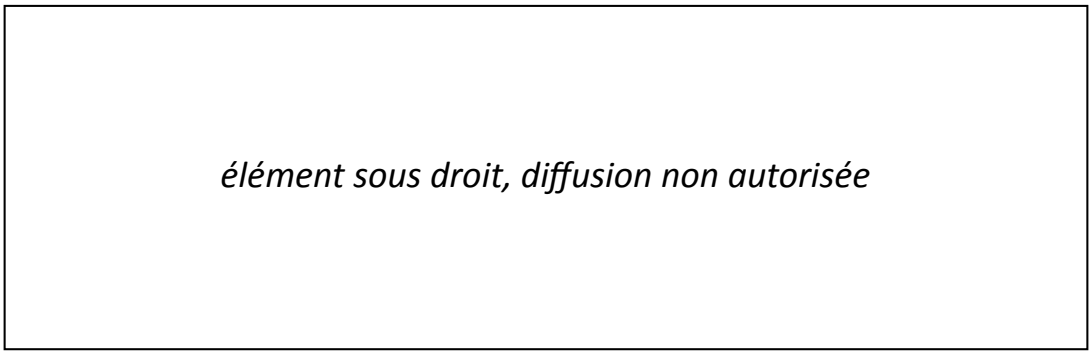

Figure 6.2 – 3-dimensional flow structure observed by Chiba et al. (1990, 1992) at large flow rate for a shear-thinning aqueous PAA solutions with low concentration. (a): Schematic representation. (b): side view ($z-y$ plane) and (c): front view ($z-x$ plane) close to the wall: appearance of counter rotating Görtler-like vortex tubes.

complicated function of flow rate, material properties and contraction ratio (Boger & Walters, 2012). In the latter case, inertia finally comes into play: the vortex size now decreases significantly when increasing the flow rate, and divergent streamlines are ultimately observed, like in the axisymmetric case. Such inertial damping and diverging streamlines, as well as the selection between corner and lip vortices, has been reproduced numerically by Purnode & Crochet (1996) using a FENE-P model.

At large flow rates, unstable flows can be observed, like in axisymmetric contractions. Using a micro-fabricated planar contraction ($\beta = 16$) and aqueous PEO solutions with almost constant shear viscosity, Rodd et al. (2005) reported that the onset of elastic instabilities, manifested by fluctuations in the local velocities near the contraction, occur above a critical Weissenberg number $Wi_{crit} \approx 50$ for Reynolds numbers less than 40.

More surprisingly, although the flow is 2-dimensional at sufficiently low flow rates, Chiba et al. (1990, 1992) obtained experimental evidence for the existence of a nontrivial 3-dimensional flow structure appearing at large flow rates using shear-thinning aqueous PAA solutions with low polymer concentration (i.e., subjected to inertial effect and therefore exhibiting divergent streamlines). This "anomalous flow pattern" is characterised by a modulation along the neutral x direction which is shown schematically in figure 6.2.a, along with flow visualisations in the $z-y$ plane (figure 6.2.b) and in a $z-x$ plane parallel and close to the side wall (figure 6.2.c). The divergence of the streamlines and the y asymmetry of the flow are clear in figure 6.2.b. Note that figure 6.2.b corresponds to a regime where the vortices have disappeared due to inertia. When (corner or lip) vortices are present, the unsteady nature of the flow is characterised by a periodic and alternative growth and decay

of the vortices present on both sides. Figure 6.2.c shows a multiple cellular structure along x where "bundle-like" streamlines are generated near the salient corners. These streamlines move back and forth along x due to the alternative growth and decay of the (corner or lip) vortices (not visible in the figure). Based on these visualisations, the authors conclude on the existence of counter rotating vortex tubes consisting in Görtler-like vortices with almost rectangular cross sections. Görtler vortices are counter rotating longitudinal vortices that appear in a boundary layer flow along a concave wall due to destabilising centrifugal forces. According to the authors interpretation, such tubes are generated by a decrease in radius of the main flow curvature which is due to the diverging streamlines. Such flow structure might possibly result in a velocity variation along the slot. However, since the authors used a long slot (large L_s) and did not investigate the structure of the downstream curtain, we do not know if such 3-dimensional flow structure in the contraction region can result in a modulation of the curtain velocity field along x.

In parallel of the appearance of these different flow patterns, the measured pressure drop may be affected by the presence of polymers. Different behaviours have been reported: while Nigen & Walters (2002) measured no extra pressure losses (i.e. no difference between a Newtonian liquid and a non shear-thinning liquid of same shear viscosity), Rodd et al. (2005) reports extra pressure losses, like in axisymmetric contractions.

Conclusion A rich variety of flow structures are observed in both axisymmetric and planar abrupt contractions. To quote Xue et al. (1998), "it is impracticable, or even impossible to get the whole picture about the flow behaviour of viscoelastic fluids in such complex flow from existing experimental results". In other words, the exact observed flow patterns are so dependent on the exact contraction ratio, flow rate and liquid rheological properties (for example through Re, Wi and n) that formulating any general law is quite difficult. In the following, we report new phenomena which, in the case of HPAM solutions, are linked to the modulation of the curtain flow after extrusion through the slot (discussed in chapter 5).

6.2 Experimental set-up

6.2.1 The die

We present in figure 6.3 the experimental set-up which was developed specifically for the visualisation of the flow upstream of the slot. The liquid is poured in a container

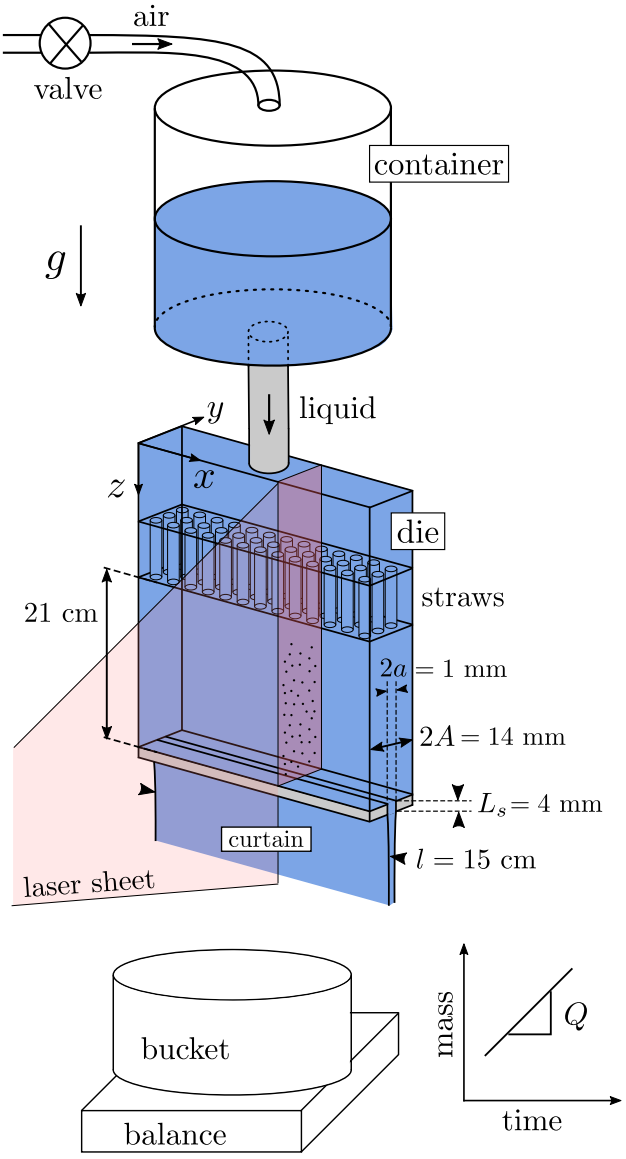

Figure 6.3 – Experimental set-up for visualisations of the flow structure upstream of the slot. The flow is illuminated by a laser sheet. We visualise the flow along two different planes: a $z-y$ plane situated at a few centimetres from the side wall (side view, shown in this figure) and the $z-x$ plane situated along the slot ($y = 0$) which is the plane of symmetry of the die (front view).

connected to a rectangular die of height 30 cm, inner width $l = 15$ cm and inner thickness $2A = 14$ mm presenting a short slot ($L_s = 4$ mm) of thickness $2a = 1$ mm. The slot thickness $2a$ and the contraction ratio $\beta = A/a = 14$ are the same as the die used in previous curtain experiments (see figure 3.2.b). We are in the situation of figure 6.1.b: after exiting the slot, depending on the flow rate, the liquid forms either a free curtain (large flow rate) or an array of jets (low flow rate). Since the liquid from the container enters at the centre of the die ($x = 0$), an array of straws of length 5 cm and diameter close to $2A/3 \approx 4.6$ mm is placed in the die at 21 cm from the slot in order to homogenise the flow along x.

6.2.2 Flow control

In order to avoid mechanical degradation of the polymer chains, the liquid flow is not controlled by a pump but by applying an air flow on top of the container. The detailed procedure is as follows. First, the die is sealed by fixing a plastic plate below the slot using a "clamp" (or "jaw"). Then, a polymer solution of total mass $M_s = 5$ kg is poured into the container: it fills the die and about 2/3 of the container. The container is then sealed using a specific lid, winded by a soft o-ring, which is pressed against the container in order to obtain an airtight set-up. The lid is then connected to a pressurised filtered air system by an adequate hole. The air flow is controlled by a valve. While the valve is closed, the die is released (i.e. the plastic plate is removed): some liquid flows outside of the die until reaching a steady state where the liquid weight is supported by the air depression on top of the container. The slot is thin enough to avoid air entering the die (no Rayleigh-Taylor instability). Hence, the liquid flow can be adjusted by opening the valve.

The liquid is collected by a bucket placed on a balance which is connected to the computer. Using a Matlab code, we have a real-time access to the mass $m_s(t)$ measured by the balance. The signal is differentiated to obtain the instantaneous mass flow rate $Q = \mathrm{d}m_s/\mathrm{d}t$. We checked that, for a given valve opening, the measured liquid flow rate is constant. The time window for flow visualisation is limited by the time needed to empty the die-container system. It is equal to M_s/Q which ranges typically between 30 s for $Q = 150$ g/s and 16 min for $Q = 5$ g/s.

6.2.3 Flow visualisation

The liquid is seeded with polyamid solid particles (PSP) of diameter 20 μm and density 1.03 g/cm^3 (provided by Dantec Dynamics) at a concentration of 0.009 wt%. A laser sheet is used to illuminate the flow along a desired plane and a high speed camera records the flow at about 100 images per second during typically 8 seconds. We visualise the flow along two different planes: one $z - y$ plane situated at a few centimetres from the side wall (side view, as shown in figure 6.3) and the $z - x$ plane along the slot ($y = 0$) which is the plane of symmetry of the die (front view). In the latter case, the curtain flow is also visible since the curtain is also illuminated by the laser.

The vertical flow velocity switches from about $U_u = q/2A$ ("u" for upstream) in the die to about $U_s = q/2a$ ("s" for slot) in the slot where $q = Q/\rho l$ is the linear flow rate. Typical orders of magnitude for $q = 3$ cm^2/s are $U_u = 0.02$ m/s and $U_s = 0.3$ m/s. Unfortunately, the laser sheet we had at our disposal was not strong

enough to allow sufficiently low camera exposure times for resolving the flow near the contraction with a PIV technique (tracers look like streaks instead of points). This problem is even more dramatic in the case of HPAM solutions which (as will be presented below) exhibit surprisingly large velocities. In contrast, the light source used in earlier curtain experiments (mentioned in 3.1.4) was powerful enough to allow sufficiently short exposure times (typically 500 μs) for the resolution of velocities $U > U_s$ in the curtain. This problem will be solved for future experiments. The results presented in this chapter are in fact preliminary results where the structure of the flow is investigated using image superpositions to visualise the pathlines of the tracers, which correspond to the flow streamlines in steady regimes. In all the experiments presented below, the thickness of the viscous boundary layer developing along the side walls (situated at $x = \pm l/2$) never exceeds 2 cm. Side views are always performed sufficiently far from the side walls to avoid this edge effect.

6.3 Test liquids

We choose to define the Weissenberg number as $Wi = \tau_{fil}\, U_s/a$ (equation 6.4) where τ_{fil} is the extensional relaxation time measured with a CaBER rheometer, as defined by Rodd et al. (2005). We know that it is an important parameter since elastic instabilities usually arise above a critical Weissenberg number. However, since the results of §5.2 suggest that the degree of shear-thinning n is of primary importance when investigating the onset of modulated curtain flows, we use four PEO and HPAM solutions with different values of n and with similar extensional relaxation times τ_{fil} which cover comparable ranges of Weissenberg numbers.

6.3.1 Rheological parameters

The four recipes and the corresponding solvent viscosities η_s, density ρ and surface tension Γ are given in table 6.1. The first three solutions, which we refer to as P1, P2 and P3, are PEO solutions with respective PEG concentrations 40 wt% (P1), 20 wt% (P2) and 0 wt% (P3). Note that the reported solvent viscosity $\eta_s = 0.12$ Pa.s for solution P1 is lower than the value reported in §3.1.1 $\eta_s = 0.14$ Pa.s for similar solutions. This is due to the fact that the temperature dependence of the solvent viscosity becomes non negligible for solvents with such large PEG concentrations. The two measured values correspond to different room temperatures: the experiments reported in this chapter were performed at a room temperature $T = 27°$C for this specific solution P1 while the experiments reported in previous chapters with

Liquid	[PEG] wt%	[PEO] wt%	[HPAM] wt%	[NaCl] wt%	η_s Pa.s	ρ kg/m^3	Γ mN/m
P1	40	0.02	0	0	0.12	1070	53
P2	20	0.05	0	0	0.017	1026	62
P3	0	0.36	0	0	0.001	1000	72
H1	0	0	0.1	0.2	0.001	1000	72

Table 6.1 – Composition of the four liquids P1, P2, P3 and H1 used in this chapter. η_s, ρ and Γ are the respective solvent viscosity, solution density and solution surface tension.

Liquid	η_0 Pa.s	η_p Pa.s	n	$1/\dot{\gamma}_c$ s	τ_{fil} s	η_E Pa.s	b	Wi	Re
P1	0.13	0.01	1.0		0.17	8×10^2	4×10^4	10 - 160	0.12 - 1.9
P2	0.019	0.002	0.97	0.1	0.10	7×10^2	2×10^5	8 - 220	1.2 - 33
P3	0.15	0.15	0.57	0.71	0.088	6×10^2	2×10^3	7 - 170	0.76 - 74
H1	0.11	0.11	0.56	2	0.13	8×10^2	4×10^3	7 - 160	1.0 - 33

Table 6.2 – Rheological parameters of the solutions P1, P2, P3 and H1 introduced in table 6.1. The first columns are similar to table 3.1. The range of Weissenberg $Wi = \tau_{fil} U_s/a$ and Reynolds $Re = \rho U_s a/\eta(\dot{\gamma}^*)$ (where $\dot{\gamma}^* = U_s/a$) numbers experimentally investigated are shown.

the solutions of table B.3 were performed at a lower room temperature closer to 23°C. The last solution, which we refer to as H1, is a 0.1 wt% HPAM solution with 0.2 wt% salt.

The rheological properties of these four solutions are reported in table 6.2. We checked that they do not vary in the course of an experimental session by measuring the rheological properties of a sample of fresh solution and a sample of solution collected after experiments. Since the room temperature could vary between 26°C and 30°C from day do day, CaBER experiments are once more performed in the same room as curtain experiments (a few minutes after) and shear rheology experiments were performed by imposing the room temperature to the rheometer. The extensional relaxation time ranges between 0.088 s and 0.17 s. The apparent shear viscosity of each liquid is shown in figure 6.4.a. Solutions P1 and P2 are almost non shear-thinning fluids $n \approx 1$ while solutions P3 and H1 are shear thinning with $n \approx 0.57$.

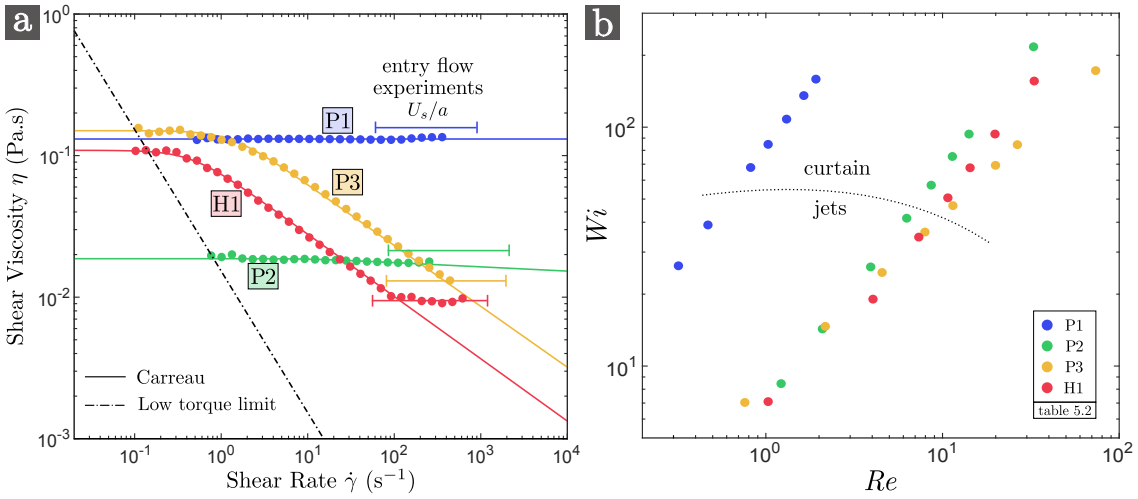

Figure 6.4 – (a): Apparent shear viscosity of the solutions P1, P2, P3 and H1 presented in tables 6.1 and 6.2. The low torque limit is shown, as well as the range of experimentally achieved values of $\dot{\gamma}^* = U_s/a$ which is a characteristic shear rate in the slot. The data are fitted by a Carreau law (equation 3.7). (b): Explored regions in the $Wi - Re$ space for solutions P1, P2, P3 and H1. The data corresponding to sufficiently large flow rates for the formation of a curtain are shown (a line is drawn to guide the eye).

6.3.2 Range of Weissenberg and Reynolds numbers

Each solution is extruded at linear flow rates q ranging typically between 0.3 cm^2/s and 10 cm^2/s. Hence, the mean velocity in the slot $U_s = q/2a$ ranges between 0.03 m/s and 1 m/s and the Weissenberg number $Wi = \tau_{fil} U_s/a$ ranges between 7 and 220. We define the Reynolds number as $Re = \rho U_s a/\eta(\dot{\gamma}^*)$ where $\dot{\gamma}^* = U_s/a$ (see equations 6.1 and 6.2). In figure 6.4.a, we show the different ranges of shear rates $\dot{\gamma}^*$ achieved in the slot for the four solutions. For solution P1, $\eta(\dot{\gamma}^*)$ is simply η_0. For solution P2, we use the Carreau law 3.7 for $\eta(\dot{\gamma}^*)$, unless we obtain values lower that the solvent viscosity η_s, in which case we choose $\eta = \eta_s$. For solution P3, we also use the Carreau law (it gives values larger than η_s). For solution H1, we observe the second Newtonian plateau $\eta_\infty = 0.0091$ Pa.s which is larger than η_s. Therefore, we use the Carreau law for $\eta(\dot{\gamma}^*)$, unless we obtain values lower than η_∞, in which case we choose $\eta = \eta_\infty$. The range of Weissenberg and Reynolds number explored for each solution is shown in table 6.2: we are in conditions similar to Rodd et al. (2005). A graphic representation of this is provided in figure 6.4.b where each experimental measurement is placed in the $Wi - Re$ space. The data corresponding to sufficiently large flow rates for the formation of a curtain are shown.

6.4 Flow patterns

Before showing the different flow patterns, we shall mention a difficulty in defining the onset of instabilities for our particular set-up. Since we use a free-curtain configuration instead of the more classical contraction-expansion or infinite slot configurations (see figure 6.1), the flow upstream of the slot is not translation invariant along x at low flow rates (in particular $q < q_{min}$) where the liquid leaving the slot forms an array of jets instead of a continuous liquid sheet (see figure 5.3.a). Indeed, at low flow rates, we observe that the flow upstream of the slot "focuses" on the different spots x_i corresponding to jets near the contraction, while the flow far upstream from the contraction (when leaving the array of straws) is perfectly 2-dimensional (i.e. translation invariant along x outside of the boundary layers) for the four solutions. In other words, the tracer pathlines start pointing towards the positions x_i of the jets a few centimetres from the contraction plane. Therefore, it is possible to observe a transition from a 3-dimensional flow at low flow rates to a 2-dimensional flow at $q \geq q_c$, i.e. when a continuous curtain is finally formed (this will be true for solutions P1, P2 and P3 only). In fact, the flow becomes 2-dimensional at lower flow rates closer to q_{min} since a short liquid sheet is usually formed within the first millimetres below the slot before separating into jets. Since this 3-dimensional effect is simply due to our choice of configuration and is not at all a consequence of elastic effects (it is also observed with pure water), we will consider that the onset of elastic instability corresponds to the onset of time-dependent flow patterns and not to the onset of x-dependent flow patterns.

This 3-dimensional effect at low flow rates has a consequence on the side view visualisation (along a $z - y$ plane) since different flow patterns may be observed depending on the arbitrary position x_i of the laser sheet: higher velocities will be measured upstream of a jet. In future experiments, one possible idea to get rid of this uninteresting 3-dimensional effect is to immerse the lower part of the die in a bath containing the same liquid. We speculate that the flow will become 2-dimensional at low flow rates since jets are no longer formed below the slot. Of course, this would take us away from our original question which is: are curtain modulations linked or not to a flow instability upstream of the slot? To answer this question, we need to see both the curtain and the contraction flow at the same time.

6.4.1 Non shear-thinning PEO solutions P1 and P2

For the whole range of flow rates investigated, solutions P1 and P2 exhibit steady flow patterns with a symmetry axis at the position $y = 0$ of the slot. The tracers

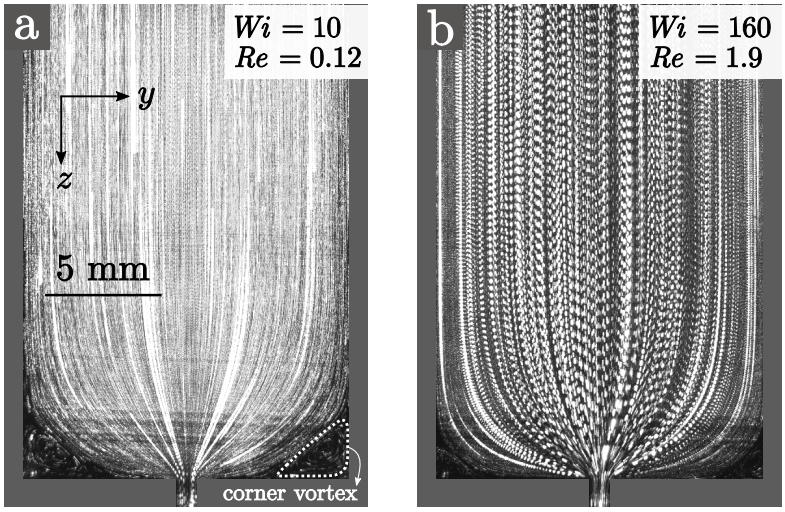

Figure 6.5 – Side view of the flow pattern for solution P1 extruded at the lowest flow rate (a) $q = 0.29$ cm^2/s and the largest flow rate (b) $q = 4.7$ cm^2/s. The respective Weissenberg and Reynolds numbers are shown. These images are obtained by superposition of successive images.

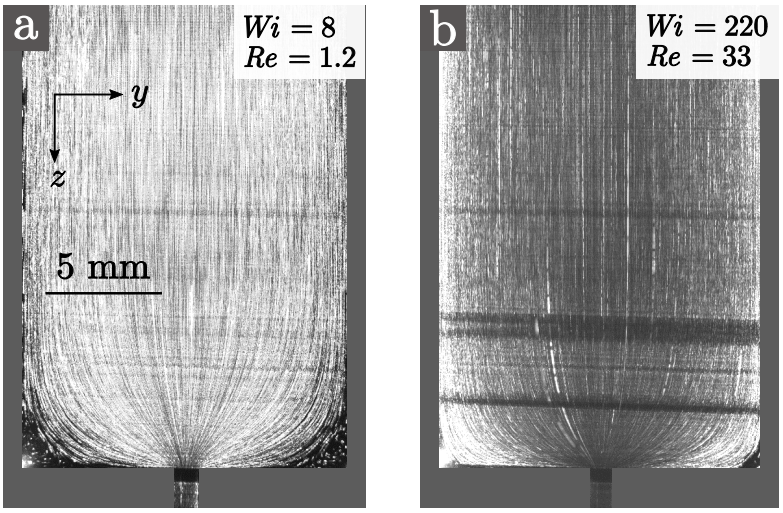

Figure 6.6 – Side view of the flow pattern for solution P2 extruded at the lowest flow rate (a) $q = 0.42$ cm^2/s and the largest flow rate (b) $q = 11$ cm^2/s. The respective Weissenberg and Reynolds numbers are shown. These images are obtained by superposition of successive images.

pathlines correspond to the flow streamlines. These patterns are shown in figures 6.5 (P1) and figures 6.6 (P2) at a low flow rate (a: array of jets) and large flow rate (b: continuous curtain). The corresponding Weissenberg and Reynolds numbers are indicated. Our results differ from the results of Rodd et al. (2005) who reports unsteady and asymmetric flows for $Wi > Wi_{crit}$ where $Wi_{crit} \approx 50$ (with the same definition of the Weissenberg number) using a planar contraction of comparable ratio $\beta = 16$ for the same range of Reynolds numbers. The explanation lies probably in the fact that these authors, due to the constrains of micro-fabricated

geometries, use a slot of limited aspect ratio $l/2a = 2$ for which edge effects are not negligible, whereas we use a slot of much larger aspect ratio $l/2a = 150$. Indeed, as discussed in §6.2.3, the size of the boundary layer developing along the side walls is small compared to the channel width l in our case. Our contraction is therefore closer to the ideal planar contraction of infinite aspect ratio. Furthermore, no trace of 3-dimensional structure has been observed in the curtain regime (large flow rate) for these solutions. This is consistent with the fact that the downstream curtain is not modulated.

Note that the velocity field $u(y, z)$ in the upstream channel depends only on y far from the contraction plane and is well captured by a parabolic law, which means that the flow rapidly reaches a fully developed Poiseuille state after leaving the array of straws. This results comes from preliminary PIV measurement (not shown) which can only be performed far from the contraction for reasons mentioned in §6.2.3.

Note also that small corner vortices are observed in the salient corners. Their size slightly decreases when increasing the flow rate (this is usually attributed to the inertia of the flow). Hence, we do not observe the vortex enhancement phenomenon. This is consistent with the results obtained by Walters & Rawlinson (1982); Evans & Walters (1986, 1989) who report low vortex activity for planar contractions of non shear-thinning fluids.

6.4.2 Shear-thinning PEO solution P3

In contrast, solution P3 exhibits more complex flow patterns. These patterns are shown in figures 6.7 for different flow rates. A large lip vortex is visible for the lowest flow rate (a) and we speculate that the usual growing sequence reported in the literature would have been observed at lower increasing flow rates. The size of this lip vortex rapidly decreases (b) and divergent streamlines are finally observed (c), which attests a competition between elasticity and inertia. A similar sequence is for example reported by Boger & Walters (2012) (p. 61). For the first flow rates (a), (b) and (c), the flow is steady and presents a symmetry axis at the position $y = 0$.

The flow becomes both unsteady and asymmetric at a critical flow rate q_{crit} ranging between 2.7 cm^2/s and 3.9 cm^2/s, as shown in figure 6.7 (d), (e) and (f) which correspond to flow rates $q \geq 3.9$ cm^2/s. These images are comparable to the results of Chiba et al. (1990, 1992) shown in figure 6.2.b. Besides, for these three last images (for which a curtain is formed below the slot), a front view reveals a

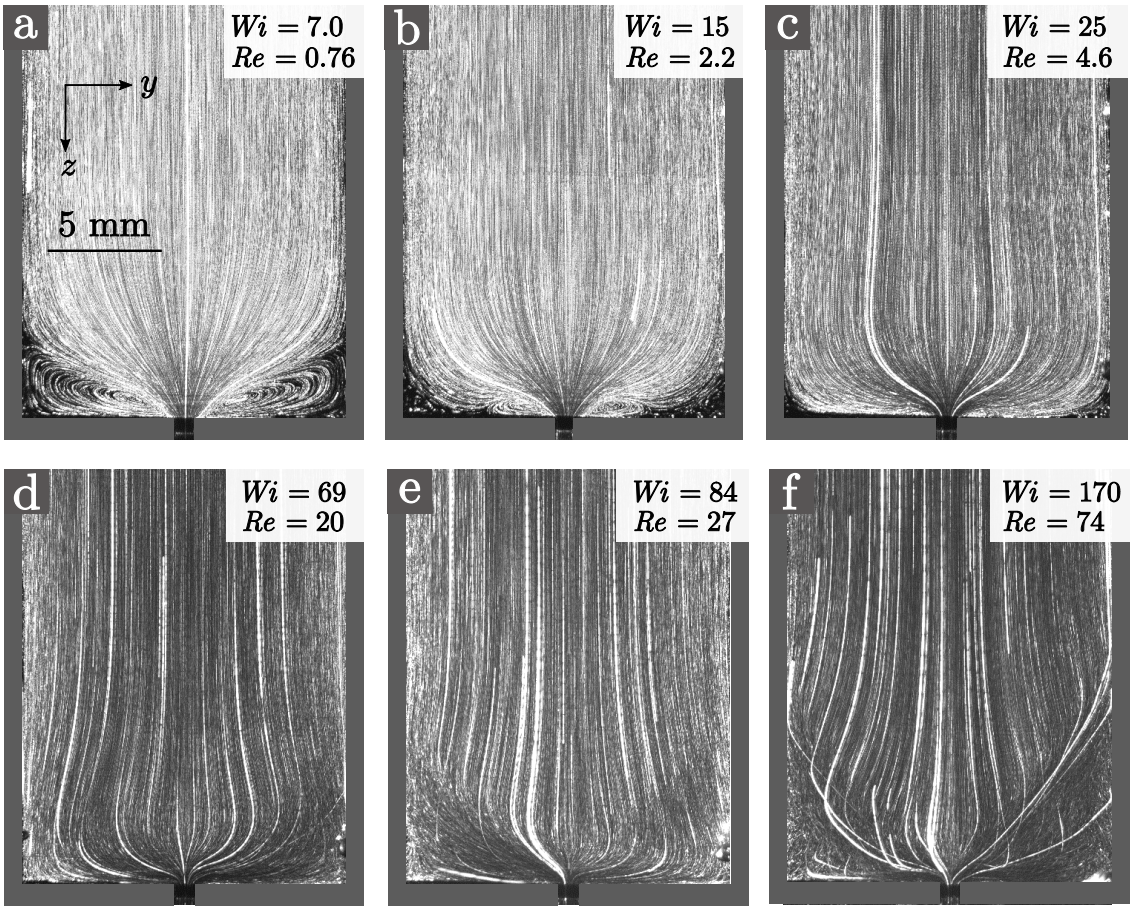

Figure 6.7 – Side view of the flow pattern for solution P3 extruded at flow rates $q = 0.40$ cm^2/s (a), $q = 0.83$ cm^2/s (b), $q = 1.4$ cm^2/s (c), $q = 3.9$ cm^2/s (d), $q = 4.8$ cm^2/s (e), $q = 9.8$ cm^2/s (f). The respective Weissenberg and Reynolds numbers are shown. These images are obtained by superposition of successive images.

very weak tendency to 3-dimensionality with particles moving along x just before entering into the contraction (a few millimetres before the contraction plane). This effect is not shown since it is hardly noticeable with an image superposition. A possible explanation is that our $z-x$ plane corresponds to the slot position ($y = 0$) whereas the front view images of Chiba et al. (1990, 1992) shown in figure 6.2.c correspond to a plane close to the wall situated at $y = \pm A$ where this 3-dimensional structure may be more visible.

No trace of curtain modulation is visible for the largest flow rates, although the flow upstream of the slot is unsteady and weakly 3-dimensional. Since solution P3 has a degree of shear thinning $n = 0.56$, this result is in contradiction with the results presented in §5.2 which suggested that, in this range of flow rates, curtains become modulated for $n < 0.72$. In fact, PEG-free PEO solutions like solution P3 had not been tested in previous chapters, and the only PEO curtains presenting

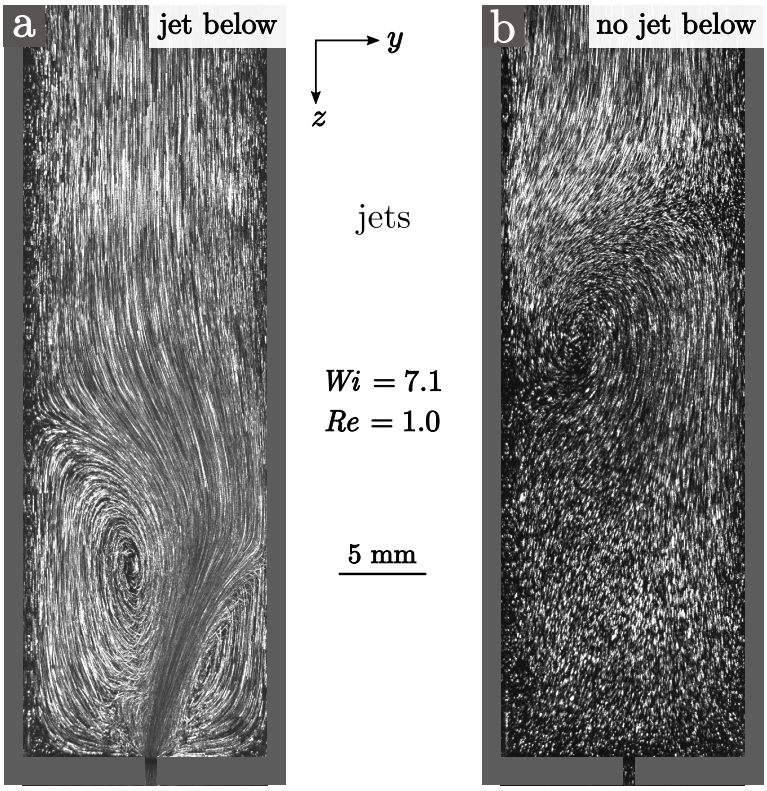

Figure 6.8 – Side view of the flow pattern for solution H1 extruded at flow rate $q = 0.27$ cm^2/s $< q_{min}$ where the x position of the laser sheet matches (a) or does not match (b) the position of a jet below the slot. The respective Weissenberg and Reynolds numbers are shown. These images are obtained by superposition of successive images.

a modulation were some 0.4 wt% PEO solutions with 20 wt% PEG solvent. This point will be examined in a more general discussion in §6.5.

6.4.3 Shear-thinning HPAM solution H1

Flow patterns

Solution H1 exhibits incredibly complex flow structures, even at the lowest tested flow rates, i.e. the flow is strongly unsteady, asymmetric and 3-dimensional. The corresponding curtains are all modulated. Hence, the critical flow rate q_{crit} marking the onset of unsteady flow patterns is below our minimum flow rate which is 0.27 cm^2/s.

Figures 6.8, 6.9 and 6.10 show different flow patterns observed at different flow rates where jets (figure 6.8) and (modulated) curtains (figures 6.9 and 6.10) are formed below the slot. Note that in figure 6.8, there is actually only one jet formed below the slot instead of the classical full array of equidistant jets. This behaviour is often observed with HPAM solutions and we did not find explanations for this in the literature. Figure 6.8.a corresponds to a typical flow pattern observed upstream of this jet while figure 6.8.b displays a typical flow pattern when there is no jet below the position x_i of the laser sheet. Figures 6.9 and 6.10 correspond to different typical flow patterns upstream of the curtain at a particular position x_i at

two different arbitrary times (a and b).

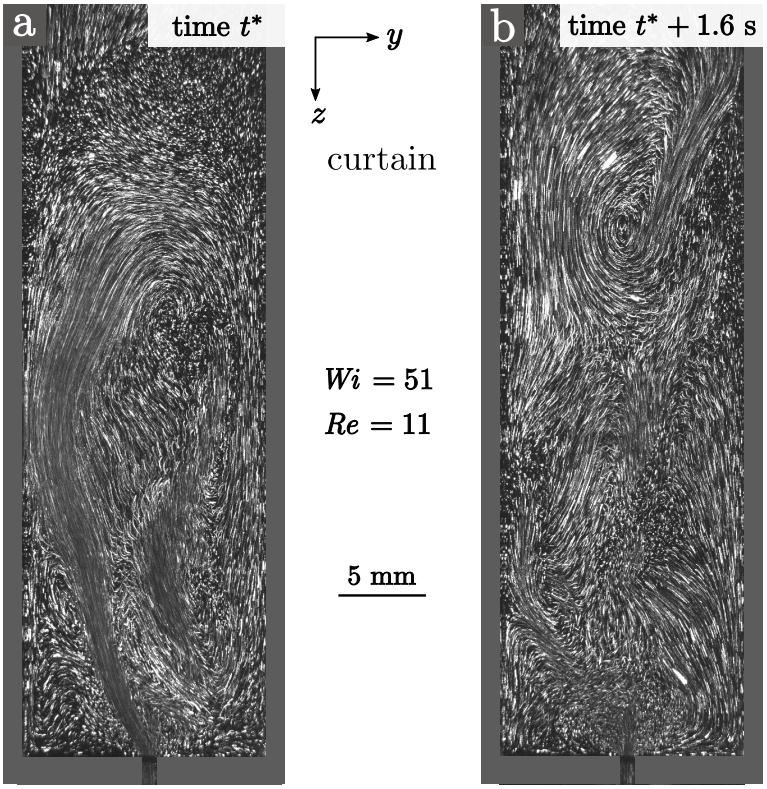

Figure 6.9 – Side view of the flow pattern for solution H1 extruded at flow rate $q = 2.0$ cm^2/s (a curtain is formed below the slot) at two arbitrary times t^* and $t^* + 1.6$ s. The respective Weissenberg and Reynolds numbers are shown. These images are obtained by superposition of successive images.

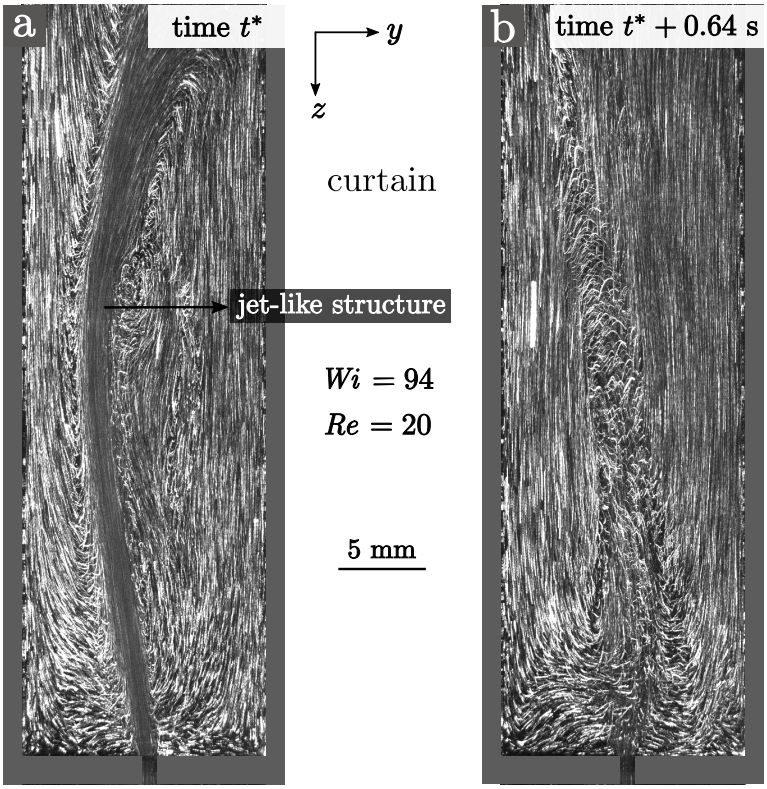

Figure 6.10 – Side view of the flow pattern for solution H1 extruded at flow rate $q = 2.0$ cm^2/s (a curtain is formed below the slot) at two arbitrary times t^* and $t^* + 0.64$ s. The respective Weissenberg and Reynolds numbers are shown. These images are obtained by superposition of successive images.

Figures 6.8.a and 6.8.b are quite different. Figure 6.8.a shows an asymmetric vortex structure upstream of the jet while figure 6.8.b shows no obvious structure near the contraction. In particular, the velocity of the tracers inside the slot is almost 0 in figure 6.8.b since there is no jet to be "fed" with liquid at this particular position x_i. A comparable 3-dimensional effect was observed with the previous solutions P1, P2 and P3 (which exhibit an array of almost equidistant jets like in figure 5.3.a), but with a quite reduced intensity, meaning that the tracer pathlines start pointing towards the jet positions much closer to the contraction plane than with solution H1.

In fact, an analogous 3-dimensional effect was observed with solution H1 at large flow rates where a modulated curtain is formed beneath the slot. This is illustrated by the different structures observed at a particular position x_i in figures 6.9.a and 6.9.b and in figures 6.10.a and 6.10.b. In both cases, figure (a) shows a long jet-like structure in the upstream channel, feeding the slot (at this particular position x_i) with high liquid velocity, while figure (b) reveal no such jet-like structure, the slot (at the same position, a few tens of second later) being fed with liquid with a much more modest velocity. In other words, if $U_s = q/2a$ is the mean velocity in the slot in the case of a purely 2-dimensional flow, the position x_i is alternatively overfed (a: $U > U_s$) and underfed (b: $U < U_s$). The time of evolution of the flow structure if of the order of a few tens of seconds. Contrary to figure 6.8, this 3-dimensional structure is not trivial since it is not a consequence of the destabilisation of the downstream curtain into jets.

These observations suggest that the modulation of the curtain thickness and velocity field along x is related to the 3-dimensional flow structures observed in figures 6.9 and 6.10. This is validated by front visualisation of the flow in the $z - x$ plane where the laser sheet is placed at the position of the slot ($y = 0$). An example is shown in figure 6.11: there is a remarkable continuity between the flow in the upper channel and the flow in the curtain: the thick-and-fast bands of the modulated curtain are simply the continuation of the long jet-like structures in the die. This explains why the characteristic time of evolution of the band pattern in the curtain is the same as the time of evolution of the flow in the upper channel. Note that, due to a short exposure time used for the front view of solution H1, it was quite difficult to obtain a meaningful image superposition, although the die-curtain continuity is quite clear when watching the movie. For this reason, figure 6.11 corresponds to an experiment with an unsalted 0.1 wt% HPAM solution filmed at a longer exposure time. The exact shape of the flow patterns observed for these two liquids are different (the velocity distribution is narrower for solution H1, as suggested by figure 5.8) but both flows have the same intrinsic unsteady, asymmetric and 3-dimensional

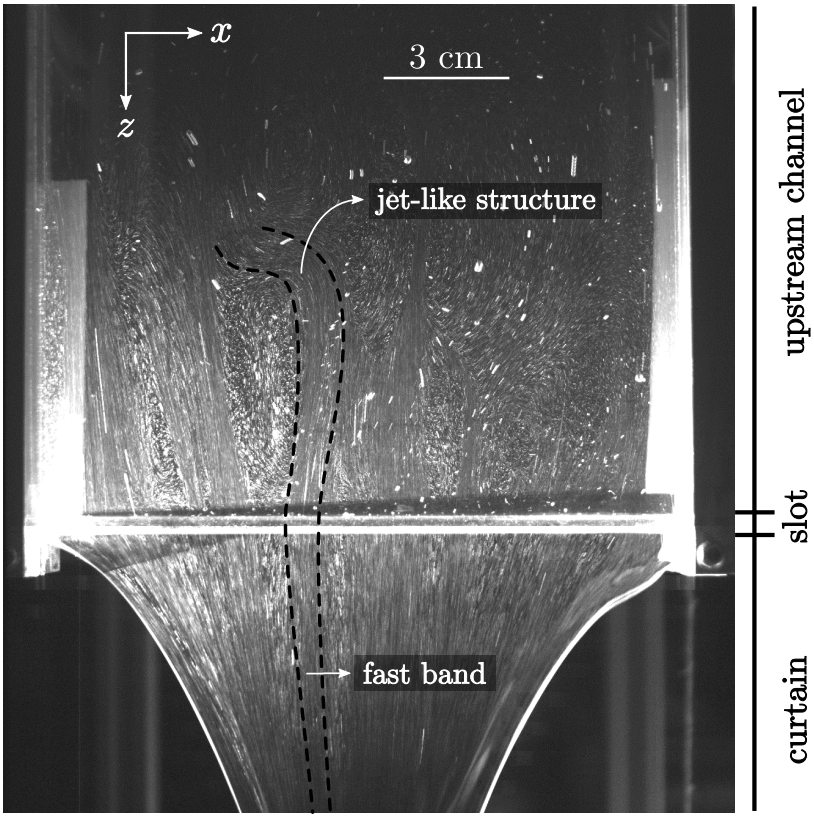

Figure 6.11 – Front view of the flow pattern for an unsalted 0.1 wt% HPAM solution (the nature of the flow patterns are similar to those observed for solution H1). A curtain is formed below the slot. Note that no guides were used to enforce a rectangular curtain shape in this chapter for practical reasons (observations suggests that it does not affect the flow inside the die). There is a continuity between the flow in the upper channel and the flow in the curtain: the thick-and-fast bands of the modulated curtain are simply the continuation of the long jet-like structures within the die.

characteristics. In the future, in order to obtain even more meaningful images, we plan to change the lighting of the curtain by using the powerful light source used in curtain experiments (see figure 4.2.a for example), while illuminating the die with a more powerful laser sheet.

Size of the recirculation area

From the movies, we observe that the flow in the die is only perturbed (i.e. unsteady, asymmetric and 3-dimensional) within a restricted area upstream of the contraction plane., i.e. the flow is usually unperturbed (i.e. steady, symmetric and 2-dimensional) when leaving the array of straws situated at 21 cm from the contraction plane. We note L_{rc} the length of this area along the vertical direction z. In the case of solution P3, the length of the perturbed area is of the order of the upper channel thickness, i.e. $L_{rc} \approx 2A$ (see figure 6.7). However, according to figures 6.8, 6.9, 6.10 and 6.11, the perturbed area is much longer for solution H1.

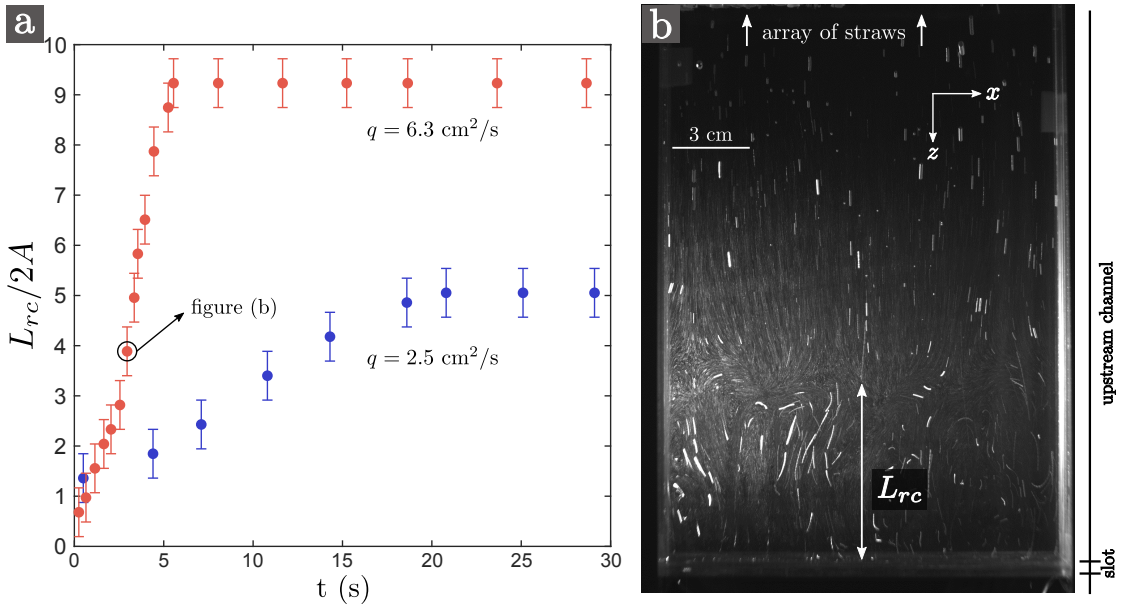

Figure 6.12 – (a): Time evolution of the dimensionless size $L_{rc}/2A$ of the perturbed recirculation area when initiating a sudden flow of flow rate $q = 2.5$ cm^2/s ($Wi = 67$ and $Re = 14$) and $q = 6.3$ cm^2/s ($Wi = 160$ and $Re = 34$) for the solution H1. (b): Example of flow pattern during the transient rising of the perturbed recirculation area for $q = 6.3$ cm^2/s at a time reported in figure (a).

In order to estimate L_{rc}, we performed a serie of experiments with solution H1 where, starting from equilibrium ($q = 0$), a flow of linear flow rate $q > 0$ is rapidly initiated. We then observe that the recirculating perturbed area, which is initially restricted to the neighbourhood of the contraction plane, grows in size an invades a long part of the upstream channel. The time evolution of the length $L_{rc}(t)$ of this perturbed area can be estimated. Results are presented in figure 6.12.a for two different flow rates $q = 2.5$ cm^2/s and $q = 6.3$ cm^2/s. After initial rising, the perturbed recirculating area reaches a plateau value $L_{rc,\infty}$ which is an increasing function of the flow rate. In dimensionless values, we find $L_{rc,\infty}/2A = 5$ for the low flow rate and $L_{rc,\infty}/2A = 9$ for the large flow rate. We also observe that the transient rising phase of the perturbed front is shorter (about 6 s) for the large flow rate than for the low flow rate (for which it lasts about 21 s).

Such surprisingly long recirculation areas have also been reported by Cartalos & Piau (1992) in both steady (long steady vortices) and unsteady regimes for HPAM solutions extruded from an axisymmetric contraction. Note that their solvent is much more viscous, resulting is solutions of zero-shear viscosity $\eta_0 \approx 1$ Pa.s and therefore in lower Reynolds numbers. They report $Re \leq 2$ while the results of figure 6.12 correspond to $Re > 10$.

Analogous phenomena

Analogous large jet-like structures have been observed in different situations. In particular, in the movie presented by Salipante et al. (2016) at the 69th Annual Meeting of the APS Division of Fluid Dynamics called "Jetting Flow of a Shear Banding Fluid" (video available on YouTube), the authors report the existence of a very similar unsteady jetting structures in shear banding worm-like micellar solutions upstream of a progressive contraction in a micro-fabricated channel. This phenomenon is characterised by the existence of a self-contained portion of the channel where the fluid velocity is much greater than the surroundings, like in our pictures of HPAM solutions upstream of a planar contraction (figures 6.10 and 6.11). Authors also report the existence of such phenomena even in the absence of a contraction in rectangular micro-fabricated ducts with shear banding worm-like micellar solutions (Salipante et al., 2017; Haward et al., 2014). According to the authors, the existence of such jets relies on the existence of plateau in the (shear rate) - stress ($\dot{\gamma}$ - σ) curve, which is a characteristic of shear banding fluids. Hence, HPAM solutions (exhibiting no shear banding properties) are not expected to form the same flow structure. However, since both fluids exhibit both elastic and shear-thinning properties, an analogy between the patterns observed with worm-like micellar solutions and with HPAM solutions is not excluded.

Analogous elastic instabilities have also been reported by Kawale et al. (2017) with HPAM solutions forced through a controlled porous media made of pillars in a micro-fabricated channel. Here, the flow presents stationary "dead zones" of immobile liquid upstream of the pillars while the flow is strongly unsteady at large Weissenberg numbers and is characterised by fast portions of liquid sneaking between the pillars. In particular, the size of the dead zones is an increasing function of $1 - n$, thus suggesting that flow inhomogeneities are correlated to shear-thinning behaviour.

These comparisons suggest that the provocatively complex flow pattern observed with our HPAM solution is principally driven by elastic and shear-thinning effects. In the examples presented above and in our experiments, fast jets of fluid erupt within a quasi immobile surrounding liquid. We can imagine a simple mechanism for this instability: fast portions of liquid correspond to regions of highly stretched material where polymer molecules align along the flow, thus resulting in lower flow resistance which enhances further concentration of the fluid motion within the jet.

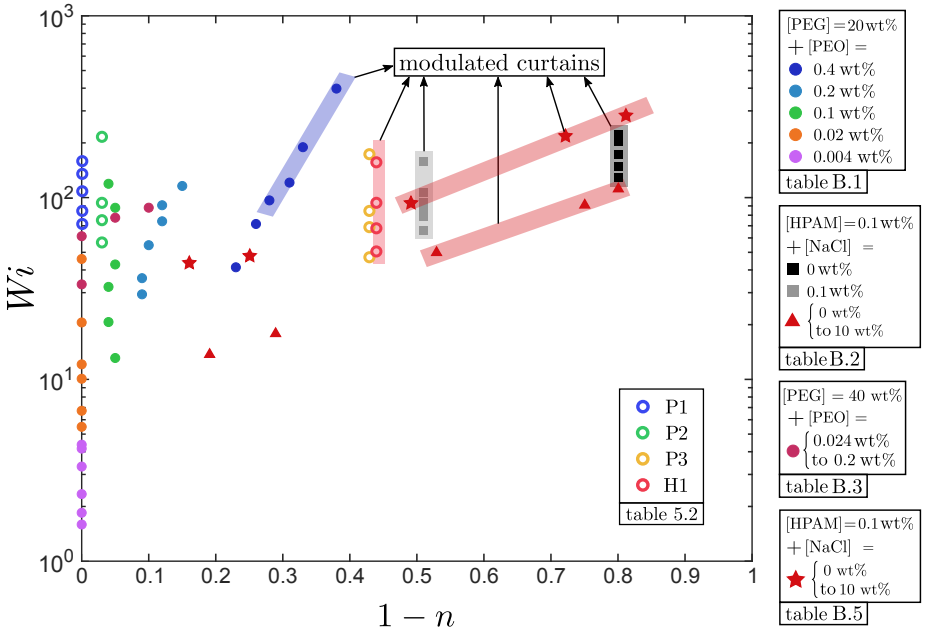

Figure 6.13 – Phase diagram of the modulated and smooth curtains in the $Wi - n$ space. The curtain data corresponding to solutions P1, P2, P3 and H1 (table 6.2) are superposed to the data corresponding to the PEO and HPAM solutions used in previous chapters (tables B.1, B.2, B.3). Most of these previous data correspond to the data of figure 5.9.

6.5 Onset of curtains modulation

Now that we know that the curtain modulation is linked to 3-dimensional unsteady flow patterns in the die, we can discuss the onset of curtain modulation in terms of Weissenberg numbers which is known to be an important parameter for describing the onset of elastic instabilities in contractions. Since we know from figure 5.9 that shear-thinning plays a major role, modulated and smooth curtains are gathered in a $Wi - n$ phase diagram in figure 6.13. As anticipated in figure 5.9, most modulated curtains are found at $n < 0.72$. Of course, for a given highly shear-thinning fluid, smooth curtains are to be expected at low Weissenberg numbers (low flow rates) since the onset of elastic instabilities usually correspond to a critical flow rate. Such low-flow-rate curtain visualisations are unfortunately hindered by the existence of a critical flow rate below which the curtain rapidly breaks into an array of jets. This explains why the low Wi region of the map 6.13 is empty. Indeed, if q_{min} is the minimum linear flow rate to form a curtain, the minimum achievable Weissenberg number is $q_{min}\tau_{fil}/2a^2$ (see equation 6.4 with $U_s = q/2a$).

The only data preventing us from drawing any line separating modulated and smooth curtain in figure 6.13 is the data of solution P3, which is very similar to solution H1 (same n and same range of Wi). For both solutions, unsteady and 3-dimensional flow structures are observed in the die. However, this 3-dimensional

character is much more pronounced for solution H1, thus leading to clearly observable modulation in the curtain flow. Understanding the striking difference between these two behaviours is not trivial at all. In particular, as shown in figure 6.4.b, both solutions correspond to comparable Reynolds numbers. Hence, adding a third Re axis to figure 6.13 will not separate the P3 data from the H1 data.

In the next section, we sum up the results obtained in this manuscript concerning modulated curtains and we present some perspectives for future works aiming at a finer characterisation of the onset of curtain modulation.

6.6 Partial conclusions and perspectives

In this chapter, the behaviour of three PEO solutions P1, P2 and P3 and one HPAM solution H1 extruded through a planar contraction of ratio $\beta = 14$ has been investigated. In particular, the critical linear flow rate marking the onset of elastic instabilities in the die, characterised by unsteady flow patterns, has been investigated, as well as the appearance of 3-dimensional flow patterns presenting a modulation along the neutral direction x. These experiments aimed at identifying the origin of the thickness and velocity modulation of some curtains emerging from the slot which, as discussed in §5.2, seemed to appear for highly shear-thinning solutions.

While solutions P1 and P2 present no elastic instability and no curtain modulation for the largest tested flow rate, solution P3 presents an elastic instability above a critical flow rate but presents no observable curtain modulation. In contrast, solution H1 presents strong elastic instabilities, even at the lowest tested flow rate, as well as modulation in the downstream curtain. Our experiments bring to light a correlation for this HPAM solution between the modulation of the curtain and the unsteady and 3-dimensional nature of the flow upstream of the contraction. More precisely, thick-and-fast bands of the modulated curtain are simply the continuation of long jet-like structures in the die which are initiated at the contraction plane and grow in size when imposing a sudden flow rate. This is reminiscent of the experiments conducted by Piau et al. (1990) who clearly showed that melt fracture phenomena observed for jets extruded from an axisymmetric contraction above some critical flow rate are caused by the onset and downstream transport of unstable phenomena occurring within the extensional flow upstream of the orifice. In our case, a planar contraction leads to a modulation of the liquid velocity along the slot, thus resulting in the appearance of spots which are overfed (jet-like structure upstream and thick band downstream) and underfed with liquid. To our knowledge,

such behaviour has not yet been reported in the literature.

One question is still open: which phenomenon is the consequence of the other? In order to prove that the curtain modulation is the consequence (and not the cause) of the flow instability in the die, future works should focus on visualising the flow upstream of the planar contraction in submerged conditions (as done by Piau et al. (1990)) where the liquid leaving the slot no longer presents a free surface and flows directly into a bath of the same liquid. If the flow is still unsteady and 3-dimensional, it will mean that the flow instability comes from the planar contraction and not from any destabilisation of the free surface of the curtain.

Furthermore, the results reported in this work and gathered in figure 6.13 show that the critical Weissenberg number marking the onset of curtain modulation (which, according to the data of solution P3, is not exactly the same as the critical Weissenberg number marking the onset of flow instabilities in the die) is a complex function of the experimental parameters. Our results suggest a general trend: highly shear thinning liquids have a greater tendency to produce modulated curtains at a given Weissenberg numbers than weakly shear thinning liquids. However, other parameters must play a role. The Reynolds number can not be one of them since solutions L3 and H1 share comparable values of Re while exhibiting very different behaviours. Future works should focus on identifying these parameters. An answer may lie in a finer rheological description of solutions L3 and H1.

General conclusion

In this thesis, we have experimentally investigated the role of viscoelasticity on the flow and stability of a liquid curtain falling freely from a slot at constant flow rate. Extruded liquids were dilute and semi-dilute solutions of flexible polyethylene oxide (PEO) and solutions of semi-rigid partially hydrolysed polyacrylamide (HPAM) whose rigidity could be tuned by salt addition. These solutions exhibit significant elasticity while having relatively low shear viscosities, contrary to the polymer melts used in the analogous film casting problem where inertia and gravity are negligible. Significant deviations from the classical free-fall law (valid for low-viscosity Newtonian curtains) were observed and quantified by velocimetry measurements. Moreover, addition of flexible polymer molecules was shown to stabilise the liquid sheet while addition of semi-rigid polymer molecules was shown to trigger a flow instability resulting in a varicose modulation of the curtain which may ultimately lead to a destabilisation of the liquid sheet. We now summarise these different experimental results before drawing outlooks for future investigations.

Curtain flow

We measured the local vertical velocity $U(z)$ of the liquid as a function of the distance z from the slot exit. Experiments reveal the existence of an initial regime where fluid particles accelerate at a rate lower than gravitational acceleration g. This regime had not been observed before. This elastic regime is characterised by a balance between gravity and the elastic stresses arising from the stretching of polymer molecules in the curtain. As the liquid velocity increases, inertia finally dominates over elasticity and the classical free-fall behaviour is recovered (inertial regime). We show that the flow is mostly influenced by the value of the extensional relaxation time τ_{fil} of the solution measured by a filament thinning technique and that the length of the elastic regime scales as $z_e = g\tau_{fil}^2$. The elastic regime is characterised by strong stretching of polymer molecules where the local extension rate $\dot{\epsilon} = \mathrm{d}U/\mathrm{d}z$ is of order $1/\tau_{fil}$. This result is analogous to viscous Newtonian curtains for which the length beyond which inertia overcomes viscous dissipation is

given by $z_v = ((4\eta/\rho)^2/g)^{1/3}$ for a liquid of viscosity η and density ρ. While this viscous length is generally much smaller than the curtain length in typical curtain coating experiments, the elastic length z_e can be larger than the curtain length for viscoelastic coating liquids. By analogy with the Newtonian curtain theory (which we revised to extract a Newtonian master curve), we show that the viscoelastic velocity profiles fall on a master curve for sufficiently long curtains which are not influenced by the downstream boundary condition. Furthermore, we show that the history of shear deformations in the slot has a weak impact on the curtain dynamic.

Curtain stability

Two aspects of curtain stability have been investigated: the stability of the sheet in terms of spontaneous hole opening events and the stability of the flow with respect to elastic instabilities.

• We find than adding small amounts of flexible polymer molecules to a Newtonian solvent greatly enhances the stability of the sheet by reducing dramatically the typical frequency of hole opening events. Besides, the minimum flow rate q_{min} (below which the curtain spontaneously break into jets) is reduced, thus allowing the formation of continuous sheets at lower flow rates. These effects have already been observed by other authors. However, the critical flow rate q_c above which the curtain forms is shown not to depend on polymer concentration, which suggests that the dynamic of sheet retraction is mostly influenced by capillarity and inertia and is not greatly influenced by elastic stresses.

• However, when adding semi-rigid polymer molecules to a Newtonian solvent, we show that the curtain flow undergoes an elastic instability which is characterised by a varicose modulation of the curtain. This effect had not been observed before. The amplitude of the modulation seems to correlate with to the degree of shear-thinning of the solution. In particular, the strong modulation observed for highly shear-thinning unsalted HPAM solutions disappears after adding salt to the solution. This modulation has a dramatic influence on the stability of the sheet since holes are more easily initiated in the fragile thin zones of the sheet and are more likely to propagate towards the slot since capillary forces dominate. This modulation is shown to be linked to an elastic instability observed inside the die upstream of the slot where the liquid is forced through an abrupt planar contraction. For a HPAM solution with sufficiently low salt concentration, the flow inside the die is highly unsteady, asymmetric and 3-dimensional. We observe jet-like structures where liquid velocity is much larger than the surrounding liquid. Below a jet-like

structure, the slot is overfed with liquid, resulting in a thick and fast band of liquid in the downstream curtain, whereas underfed spots along the slot result in thin and slow bands.

Perspectives

A quantitative analytical description of the curtain flow is still missing. Although a simple Oldroyd-B approach appears to provide a qualitative agreement with the experimental results, more work is needed to obtain quantitative predictions. One possible approach is to use a multimode description of the polymer relaxation while keeping τ_{fil} as the longest time scale.

More experimental work is also needed to fully characterise the complex flow behaviours observed for shear-thinning solutions at the slot inlet. In order to avoid the uninteresting 3-dimensional effects arising at low flow rates from the destabilisation of the downstream curtain into jets, future experiments should be performed with a die submerged in a bath of polymer solution. Besides, a more refined rheological characterisation of the polymer solutions is needed to conclude about the onset of elastic instabilities in the die since no clear criterion could be derived with available data including the Weissenberg and Reynolds numbers and the degree of shear-thinning.

In order to extend our experimental description, one could measure the velocity field of a viscoelastic jet extruded from a hole. This problem is analogous to liquid curtains and should present a similar scaling of the distance from the nozzle beyond which inertia overcomes elasticity. However, due to the strong radial curvature of the jet surface, capillary forces should be taken into account. Some inspiration can be found in the experimental study of Clasen et al. (2009) on the jetting–dripping transition in flows of polymer solutions.

Bibliography

Abramowitz, M. & Stegun, I. A. (1964). *Handbook of mathematical functions: with formulas, graphs, and mathematical tables*, volume 55. Courier Corporation. (page 10)

Aidun, C. K. (1987). Mechanics of a free-surface liquid film flow. *Journal of applied mechanics*, 54(4), 951–954. (page 1, 8, 197, 206)

Alaie, S. M. & Papanastasiou, T. C. (1991). Film casting of viscoelastic liquid. *Polymer Engineering & Science*, 31(2), 67–75. (page 2, 18)

Allain, C., Cloitre, M., & Perrot, P. (1997). Experimental investigation and scaling law analysis of die swell in semi-dilute polymer solutions. *Journal of non-newtonian fluid mechanics*, 73(1-2), 51–66. (page 108)

Alves, M. A. & Poole, R. J. (2007). Divergent flow in contractions. *Journal of non-newtonian fluid mechanics*, 144(2-3), 140–148. (page 36)

Amarouchene, Y., Bonn, D., Meunier, J., & Kellay, H. (2001). Inhibition of the finite-time singularity during droplet fission of a polymeric fluid. *Physical Review Letters*, 86(16), 3558. (page 73)

Anna, S. L. & McKinley, G. H. (2001). Elasto-capillary thinning and breakup of model elastic liquids. *Journal of Rheology*, 45(1), 115–138. (page 28, 41, 70, 74, 210)

Becerra, M. & Carvalho, M. S. (2011). Stability of viscoelastic liquid curtain. *Chemical Engineering and Processing: Process Intensification*, 50(5), 445–449. (page 2, 19, 20, 60, 81, 131, 135, 136, 220)

Bertola, V., Meulenbroek, B., Wagner, C., Storm, C., Morozov, A., & Bonn, W. v. D. (2003). Experimental evidence for an intrinsic route to polymer melt fracture phenomena: A nonlinear instability of viscoelastic poiseuille flow. *Physical review letters*, 90(11), 114502. (page 58)

Bertram, A. (2005). *Elasticity and plasticity of large deformations*. Springer. (page 33)

Bertram, A. & Glüge, R. (2015). *Solid mechanics*. Springer. (page 33)

Binding, D. M. & Walters, K. (1988). On the use of flow through a contraction in estimating the extensional viscosity of mobile polymer solutions. *Journal of Non-Newtonian Fluid Mechanics*, 30(2-3), 233–250. (page 154)

Bird, R. B., Armstrong, R. C., Hassager, O., & Curtiss, C. (1987). *Dynamics of Polymeric Liquids-Volume 2: Kinetic Theory*. John Wiley and Sons Inc., New York, NY. (page 39, 50)

Bird, R. B. & DeAguiar, J. R. (1983). An encapsulted dumbbell model for concentrated polymer solutions and melts i. theoretical development and constitutive equation. *Journal of non-newtonian fluid mechanics*, 13(2), 149–160. (page 41)

Bird, R. B., Dotson, P. J., & Johnson, N. L. (1980). Polymer solution rheology based on a finitely extensible bead—spring chain model. *Journal of Non-Newtonian Fluid Mechanics*, 7(2-3), 213–235. (page 39)

Boger, D. V. & Walters, K. (2012). *Rheological phenomena in focus*, volume 4. Elsevier. (page 55, 57, 58, 92, 137, 143, 154, 157, 158, 159, 168, 222)

Brandrup, J., Immergut, E. H., Abe, E. A. G. A., & Bloch, D. R. (1989). *Polymer handbook*, volume 7. Wiley New York etc. (page 81)

Brown, D. R. (1961). A study of the behaviour of a thin sheet of moving liquid. *Journal of fluid mechanics*, 10(2), 297–305. (page 1, 2, 7, 8, 15, 16, 205)

Brunet, P., Flesselles, J.-M., & Limat, L. (2007). Dynamics of a circular array of liquid columns. *The European Physical Journal B*, 55(3), 297–322. (page 134)

Campo-Deano, L. & Clasen, C. (2010). The slow retraction method (srm) for the determination of ultra-short relaxation times in capillary breakup extensional rheometry experiments. *Journal of Non-Newtonian Fluid Mechanics*, 165(23-24), 1688–1699. (page 75)

Cartalos, U. & Piau, J. M. (1992). Creeping flow regimes of low concentration polymer solutions in thick solvents through an orifice die. *Journal of non-newtonian fluid mechanics*, 45(2), 231–285. (page 61, 156, 174, 222)

Casanellas, L., Alves, M. A., Poole, R. J., Lerouge, S., & Lindner, A. (2016). The stabilizing effect of shear thinning on the onset of purely elastic instabilities in serpentine microflows. *Soft matter*, 12(29), 6167–6175. (page 69, 79)

Chen, E. B., Morales, A. J., Chen, C. C., Donatelli, A. A., Bannister, W. W., & Cummings, B. T. (1998). Fluorescein and poly (ethylene oxide) hose stream additives for improved firefighting effectiveness. *Fire Technology*, 34(4), 291–306. (page 56)

Chen, P., Yao, L., Liu, Y., Luo, J., Zhou, G., & Jiang, B. (2012). Experimental and theoretical study of dilute polyacrylamide solutions: effect of salt concentration. *Journal of molecular modeling*, 18(7), 3153–3160. (page 61, 70, 80)

Chiba, K., Sakatani, T., & Nakamura, K. (1990). Anomalous flow patterns in viscoelastic entry flow through a planar contraction. *Journal of Non-Newtonian Fluid Mechanics*, 36, 193–203. (page 156, 159, 168, 169, 222)

Chiba, K., Tanaka, S., & Nakamura, K. (1992). The structure of anomalous entry flow patterns through a planar contraction. *Journal of non-newtonian fluid mechanics*, 42(3), 315–322. (page 159, 168, 169, 222)

Clanet, C. & Lasheras, J. C. (1999). Transition from dripping to jetting. *Journal of fluid mechanics*, 383, 307–326. (page 72, 134, 135)

Clarke, N. S. (1966). A differential equation in fluid mechanics. *Mathematika*, 13(1), 51–53. (page 1, 10, 12, 206)

Clarke, N. S. (1968). Two-dimensional flow under gravity in a jet of viscous liquid. *Journal of Fluid Mechanics*, 31(3), 481–500. (page 1, 10, 12, 206)

Clasen, C., Bico, J., Entov, V. M., & McKinley, G. H. (2009). Gobbling drops: the jetting–dripping transition in flows of polymer solutions. *Journal of fluid mechanics*, 636, 5–40. (page 10, 41, 55, 72, 81, 121, 134, 181)

Clasen, C., Plog, J. P., Kulicke, W.-M., Owens, M., Macosko, C., Scriven, L. E., Verani, M., & McKinley, G. H. (2006). How dilute are dilute solutions in extensional flows? *Journal of Rheology*, 50(6), 849–881. (page 41, 81)

Colby, R. H. (2010). Structure and linear viscoelasticity of flexible polymer solutions: comparison of polyelectrolyte and neutral polymer solutions. *Rheologica Acta*, 49(5), 425–442. (page 48)

Crooks, R. & Boger, D. V. (2000). Influence of fluid elasticity on drops impacting on dry surfaces. *Journal of Rheology*, 44(4), 973–996. (page 56)

Culick, F. E. C. (1960). Comments on a ruptured soap film. *Journal of applied physics*, 31(6), 1128–1129. (page 16, 218)

Daerr, A. & Mogne, A. (2016). Pendent_drop: an imagej plugin to measure the surface tension from an image of a pendent drop. *Journal of Open Research Software*, 4(1). (page 61)

De Gennes, P.-G. (1974). Coil-stretch transition of dilute flexible polymers under ultrahigh velocity gradients. *The Journal of Chemical Physics*, 60(12), 5030–5042. (page 36, 81, 102, 211)

De Gennes, P.-G. (1979). *Scaling concepts in polymer physics*. Cornell university press. (page 47, 48, 49, 50)

Delvaux, V. & Crochet, M. J. (1990). Numerical simulation of delayed die swell. *Rheologica acta*, 29(1), 1–10. (page 92)

Doi, M. & Edwards, S. F. (1988). *The theory of polymer dynamics*, volume 73. oxford university press. (page 42)

Dombrowski, N. & Johns, W. R. (1963). The aerodynamic instability and disintegration of viscous liquid sheets. *Chemical Engineering Science*, 18(3), 203–214. (page 93)

Dontula, P., Macosko, C. W., & Scriven, L. E. (1998). Model elastic liquids with water-soluble polymers. *AIChE journal*, 44(6), 1247–1255. (page 60)

Eggers, J. (2014). Instability of a polymeric thread. *Physics of Fluids*, 26(3), 033106. (page 74, 211)

Entov, V. M. & Hinch, E. J. (1997). Effect of a spectrum of relaxation times on the capillary thinning of a filament of elastic liquid. *Journal of Non-Newtonian Fluid Mechanics*, 72(1), 31–53. (page 28, 74, 211)

Evans, R. E. & Walters, K. (1986). Flow characteristics associated with abrupt changes in geometry in the case of highly elastic liquids. *Journal of Non-Newtonian Fluid Mechanics*, 20, 11–29. (page 158, 168)

Evans, R. E. & Walters, K. (1989). Further remarks on the lip-vortex mechanism of vortex enhancement in planar-contraction flows. *Journal of non-newtonian fluid mechanics*, 32(1), 95–105. (page 158, 168)

Ewoldt, R. H., Johnston, M. T., & Caretta, L. M. (2015). Experimental challenges of shear rheology: how to avoid bad data. In *Complex Fluids in Biological Systems* (pp. 207–241). Springer. (page 67)

Fermigier, M., Limat, L., Wesfreid, J. E., Boudinet, P., & Quilliet, C. (1992). Two-dimensional patterns in rayleigh-taylor instability of a thin layer. *Journal of Fluid Mechanics*, 236, 349–383. (page 134)

Flory, P. J. (1949). The configuration of real polymer chains. *The Journal of Chemical Physics*, 17(3), 303–310. (page 48)

Flory, P. J. (1953). *Principles of polymer chemistry*. Cornell University Press. (page 43, 45)

Giesekus, H. (1982). A simple constitutive equation for polymer fluids based on the concept of deformation-dependent tensorial mobility. *Journal of Non-Newtonian Fluid Mechanics*, 11(1-2), 69–109. (page 42)

Graessley, W. W. (1980). Polymer chain dimensions and the dependence of viscoelastic properties on concentration, molecular weight and solvent power. *Polymer*, 21(3), 258–262. (page 49, 77, 210)

Graham, M. D. (2003). Interfacial hoop stress and instability of viscoelastic free surface flows. *Physics of Fluids*, 15(6), 1702–1710. (page 152)

Groisman, A. & Steinberg, V. (2000). Elastic turbulence in a polymer solution flow. *Nature*, 405(6782), 53. (page 34)

Gugler, G., Beer, R., & Mauron, M. (2010). Coatability of viscoelastic liquid curtain. In *Proceedings of the 15th international coating science and technology symposium, St. Paul , Minnesota*. (page 2)

Haward, S. J., Galindo-Rosales, F. J., Ballesta, P., & Alves, M. A. (2014). Spatiotemporal flow instabilities of wormlike micellar solutions in rectangular microchannels. *Applied Physics Letters*, 104(12), 124101. (page 175)

Herrchen, M. & Öttinger, H. C. (1997). A detailed comparison of various fene dumbbell models. *Journal of Non-Newtonian Fluid Mechanics*, 68(1), 17–42. (page 39)

Huang, D. C. & White, J. L. (1979). Extrudate swell from slit and capillary dies: an experimental and theoretical study. *Polymer Engineering & Science*, 19(9), 609–616. (page 108, 109)

Karim, A. M., Suszynski, W. J., Francis, L. F., & Carvalho, M. S. (2018a). Effect of viscosity on liquid curtain stability. *AIChE Journal*, 64(4), 1448–1457. (page 2, 64)

Karim, A. M., Suszynski, W. J., Griffith, W. B., Pujari, S., Francis, L. F., & Carvalho, M. S. (2018b). Effect of viscoelasticity on stability of liquid curtain. *Journal of Non-Newtonian Fluid Mechanics*, 257, 83–94. (page 2, 19, 20, 60, 81, 96, 131, 136, 215, 220)

Kawale, D., Marques, E., Zitha, P. L., Kreutzer, M. T., Rossen, W. R., & Boukany, P. E. (2017). Elastic instabilities during the flow of hydrolyzed polyacrylamide solution in porous media: Effect of pore-shape and salt. *Soft matter*, 13(4), 765–775. (page 61, 80, 175, 210)

Kays, W. M., Crawford, M. E., & Weigand, B. (2005). *Convective heat and mass transfer*. (page 99)

Keshavarz, B., Sharma, V., Houze, E. C., Koerner, M. R., Moore, J. R., Cotts, P. M., Threlfall-Holmes, P., & McKinley, G. H. (2015). Studying the effects of elongational properties on atomization of weakly viscoelastic solutions using rayleigh ohnesorge jetting extensional rheometry (rojer). *Journal of Non-Newtonian Fluid Mechanics*, 222, 171–189. (page 81)

Kim-e, M. E., Brown, R. A., & Armstrong, R. C. (1983). The roles of inertia and shear-thinning in flow of an inelastic liquid through an axisymmetric sudden contraction. *Journal of non-Newtonian fluid mechanics*, 13(3), 341–363. (page 158)

Kiriakidis, D. G. & Mitsoulis, E. (1993). Viscoelastic simulations of extrudate swell for an hdpe melt through slit and capillary dies. *Advances in Polymer Technology: Journal of the Polymer Processing Institute*, 12(2), 107–117. (page 151)

Kuhn, W. (1934). Über die gestalt fadenförmiger moleküle in lösungen. *Kolloid-Zeitschrift*, 68(1), 2–15. (page 48)

Larson, R. G. (1992). Instabilities in viscoelastic flows. *Rheologica Acta*, 31(3), 213–263. (page 68, 69)

Larson, R. G. (1999). The structure and rheology of complex fluids (topics in chemical engineering). *Oxford University Press, New York• Oxford*, 86, 108. (page 36, 47)

Lindner, A. (2000). *L'instabilité de Saffman-Taylor dans les fluides complexes: relation entre les propriétés rhéologiques et la formation de motifs*. PhD thesis, Université Pierre et Marie Curie-Paris VI. (page 67, 82)

Macosko, C. W. (1994). *Rheology: principles, measurements, and applications*. Wiley-vch. (page 67)

Mathues, W., McIlroy, C., Harlen, O. G., & Clasen, C. (2015). Capillary breakup of suspensions near pinch-off. *Physics of Fluids*, 27(9), 093301. (page 76)

McIlroy, C. & Harlen, O. G. (2014). Modelling capillary break-up of particulate suspensions. *Physics of Fluids*, 26(3), 033101. (page 76)

McKinley, G. H. (2005). Visco-elasto-capillary thinning and break-up of complex fluids. *Annual Rheological Review*, 3, 1–48. (page 36, 41, 71, 73, 75, 82, 210, 211)

McKinley, G. H., Raiford, W. P., Brown, R. A., & Armstrong, R. C. (1991). Nonlinear dynamics of viscoelastic flow in axisymmetric abrupt contractions. *Journal of fluid mechanics*, 223, 411–456. (page 156, 157, 222)

Miller, E., Clasen, C., & Rothstein, J. P. (2009). The effect of step-stretch parameters on capillary breakup extensional rheology (caber) measurements. *Rheologica acta*, 48(6), 625–639. (page 76)

Miyamoto, K. & Katagiri, Y. (1997). Curtain coating. In *Liquid film coating* (pp. 463–494). Springer. (page 2)

Moffatt, H. K. (1964). Viscous and resistive eddies near a sharp corner. *Journal of Fluid Mechanics*, 18(1), 1–18. (page 157)

Morozov, A. N. & van Saarloos, W. (2007). An introductory essay on subcritical instabilities and the transition to turbulence in visco-elastic parallel shear flows. *Physics Reports*, 447(3-6), 112–143. (page 34, 36, 57, 58, 143)

Nigen, S. & Walters, K. (2002). Viscoelastic contraction flows: comparison of axisymmetric and planar configurations. *Journal of non-newtonian fluid mechanics*, 102(2), 343–359. (page 160)

Oldroyd, J. G. (1950). On the formulation of rheological equations of state. *Proc. R. Soc. Lond. A*, 200(1063), 523–541. (page 33)

Oliveira, M. S., Yeh, R., & McKinley, G. H. (2006). Iterated stretching, extensional rheology and formation of beads-on-a-string structures in polymer solutions. *Journal of non-Newtonian fluid mechanics*, 137(1-3), 137–148. (page 68)

Oswald, P. & Saint-Jean, M. (2005). *Rhéophysique: Ou comment coule la matière*. Belin. (page 34, 37, 48, 67)

Papanastasiou, T. C., Macosko, C. W., Scriven, L. E., & Chen, Z. (1987). Fiber spinning of viscoelastic liquid. *AIChE journal*, 33(5), 834–842. (page 18)

Petit, L., Hulin, J.-P., & Guyon, É. (2012). *Hydrodynamique physique 3e édition (2012)*. EDP sciences. (page 29)

Petrie, C. J. (2006). One hundred years of extensional flow. *Journal of non-newtonian fluid mechanics*, 137(1-3), 1–14. (page 36)

Piau, J. M., El Kissi, N., & Tremblay, B. (1990). Influence of upstream instabilities and wall slip on melt fracture and sharkskin phenomena during silicones extrusion through orifice dies. *Journal of non-newtonian fluid mechanics*, 34(2), 145–180. (page 58, 156, 158, 177, 178, 222)

Purnode, B. & Crochet, M. J. (1996). Flows of polymer solutions through contractions part 1: flows of polyacrylamide solutions through planar contractions. *Journal of non-newtonian fluid mechanics*, 65(2-3), 269–289. (page 159)

Raiford, W. P., Quinzani, L. M., Coates, P. J., Armstrong, R. C., & Brown, R. A. (1989). Ldv measurements of viscoelastic flow transitions in abrupt axisymmetric contractions: interaction of inertia and elasticity. *Journal of non-newtonian fluid mechanics*, 32(1), 39–68. (page 158)

Ramos, J. I. (1996). Planar liquid sheets at low reynolds numbers. *International journal for numerical methods in fluids*, 22(10), 961–978. (page 1, 8, 10, 11, 197, 206)

Reiner, M. (1964). The deborah number. *Physics today*, 17(1), 62. (page 22)

Renardy, M. (2000). *Mathematical analysis of viscoelastic flows*, volume 73. Siam. (page 41)

Richardson, S. (1970). The die swell phenomenon. *Rheologica Acta*, 9(2), 193–199. (page 109)

Roche, J. S., Grand, N. L., Brunet, P., Lebon, L., & Limat, L. (2006). Pertubations on a liquid curtain near break-up: Wakes and free edges. *Physics of fluids*, 18(8), 082101. (page 135)

Rodd, L. E., Scott, T. P., Boger, D. V., Cooper-White, J. J., & McKinley, G. H. (2005). The inertio-elastic planar entry flow of low-viscosity elastic fluids in micro-fabricated geometries. *Journal of Non-Newtonian Fluid Mechanics*, 129(1), 1–22. (page 68, 81, 156, 158, 159, 160, 163, 165, 167)

Rodd, L. E., Scott, T. P., Cooper-White, J. J., Boger, D. V., & McKinley, G. H. (2007). Role of the elasticity number in the entry flow of dilute polymer solutions in micro-fabricated contraction geometries. *Journal of Non-Newtonian Fluid Mechanics*, 143(2-3), 170–191. (page 81, 156)

Rodd, L. E., Scott, T. P., Cooper-White, J. J., & McKinley, G. H. (2004). Capillary break-up rheometry of low-viscosity elastic fluids. (page 73, 75, 79, 210)

Rothstein, J. P. & McKinley, G. H. (1999). Extensional flow of a polystyrene boger fluid through a 4: 1: 4 axisymmetric contraction/expansion. *Journal of non-newtonian fluid mechanics*, 86(1), 61–88. (page 65, 156, 157, 158, 222)

Rothstein, J. P. & McKinley, G. H. (2001). The axisymmetric contraction–expansion: the role of extensional rheology on vortex growth dynamics and the enhanced pressure drop. *Journal of non-newtonian fluid mechanics*, 98(1), 33–63. (page 41, 156)

Rouse, P. E. (1953). A theory of the linear viscoelastic properties of dilute solutions of coiling polymers. *The Journal of Chemical Physics*, 21(7), 1272–1280. (page 52)

Rubinstein, M. & Colby, R. H. (2003). *Polymer physics*, volume 23. Oxford University Press New York. (page 79)

Salipante, P., Little, C. A., & Hudson, S. D. (2016). *Jetting Flow of a Shear Banding Fluid*. Technical report. (page 175)

Salipante, P. F., Little, C. A., & Hudson, S. D. (2017). Jetting of a shear banding fluid in rectangular ducts. *Physical review fluids*, 2(3), 033302. (page 175)

Satoh, N., Tomiyama, H., & Kajiwara, T. (2001). Viscoelastic simulation of film casting process for a polymer melt. *Polymer Engineering & Science*, 41(9), 1564–1579. (page 2, 18)

Sattler, R., Gier, S., Eggers, J., & Wagner, C. (2012). The final stages of capillary break-up of polymer solutions. *Physics of Fluids*, 24(2), 023101. (page 74, 211)

Sattler, R., Wagner, C., & Eggers, J. (2008). Blistering pattern and formation of nanofibers in capillary thinning of polymer solutions. *Physical review letters*, 100(16), 164502. (page 74, 211)

Savva, N. & Bush, J. W. M. (2009). Viscous sheet retraction. *Journal of Fluid Mechanics*, 626, 211–240. (page 18)

Sevilla, A. (2011). The effect of viscous relaxation on the spatiotemporal stability of capillary jets. *Journal of Fluid Mechanics*, 684, 204–226. (page 7)

Shaqfeh, E. S. (1996). Purely elastic instabilities in viscometric flows. *Annual Review of Fluid Mechanics*, 28(1), 129–185. (page 36)

Sibley, D. N. (2010). *Viscoelastic Flows of PTT Fluid*. PhD thesis, University of Bath. (page 42)

Stelter, M., Brenn, G., Yarin, A. L., Singh, R. P., & Durst, F. (2002). Investigation of the elongational behavior of polymer solutions by means of an elongational rheometer. *Journal of Rheology*, 46(2), 507–527. (page 82)

Sünderhauf, G., Raszillier, H., & Durst, F. (2002). The retraction of the edge of a planar liquid sheet. *Physics of Fluids*, 14(1), 198–208. (page 2, 18)

T. Min, J. Y. Yoo, H. C. & Joseph, D. D. (2003). Drag reduction by polymer additives in a turbulent channel flow. *Journal of Fluid Mechanics*, 486, 213–238. (page 36)

Tanner, R. I. (1970). A theory of die-swell. *Journal of Polymer Science Part B: Polymer Physics*, 8(12), 2067–2078. (page 108)

Tanner, R. I. (2000). *Engineering rheology*, volume 52. OUP Oxford. (page 112)

Tanner, R. I. (2005). A theory of die-swell revisited. *Journal of non-newtonian fluid mechanics*, 129(2), 85–87. (page 108)

Taylor, G. (1959). The dynamics of thin sheets of fluid. iii. disintegration of fluid sheets. *Proceedings of the Royal Society of London. Series A, Mathematical and Physical Sciences*, (pp. 313–321). (page 16, 218)

Thien, N. P. & Tanner, R. I. (1977). A new constitutive equation derived from network theory. *Journal of Non-Newtonian Fluid Mechanics*, 2(4), 353–365. (page 42)

Tirtaatmadja, V., McKinley, G. H., & Cooper-White, J. J. (2006). Drop formation and breakup of low viscosity elastic fluids: Effects of molecular weight and concentration. *Physics of fluids*, 18(4), 043101. (page 54, 72, 79, 80, 81, 210)

Truesdell, C. & Noll, W. (2004). The non-linear field theories of mechanics. In *The non-linear field theories of mechanics* (pp. 1–579). Springer. (page 33)

Villermaux, E. & Clanet, C. (2002). Life of a flapping liquid sheet. *Journal of fluid mechanics*, 462, 341–363. (page 93)

Virk, P. S. (1975). Drag reduction fundamentals. *AIChE Journal*, 21(4), 625–656. (page 56)

Walters, K. & Rawlinson, D. M. (1982). On some contraction flows for boger fluids. In *Progress and Trends in Rheology* (pp. 193–198). Springer. (page 156, 158, 168)

White, J. L. & Roman, J. F. (1976). Extrudate swell during the melt spinning of fibers—influence of rheological properties and take-up force. *Journal of Applied Polymer Science*, 20(4), 1005–1023. (page 109)

Wu, X. Y., Hunkeler, D., Hamielec, A. E., Pelton, R. H., & Woods, D. R. (1991). Molecular weight characterization of poly (acrylamide-co-sodium acrylate). i. viscometry. *Journal of applied polymer science*, 42(7), 2081–2093. (page 80, 210)

Xue, S.-C., Phan-Thien, N., & Tanner, R. I. (1998). Three dimensional numerical simulations of viscoelastic flows through planar contractions. *Journal of Non-Newtonian Fluid Mechanics*, 74(1-3), 195–245. (page 160)

Zell, A., Gier, S., Rafai, S., & Wagner, C. (2010). Is there a relation between the relaxation time measured in caber experiments and the first normal stress coefficient? *Journal of Non-Newtonian Fluid Mechanics*, 165(19), 1265–1274. (page 35, 79, 80)

Zhang, G., Zhou, J. S., Zhai, Y. A., Liu, F. Q., & Gao, G. (2008). Effect of salt solutions on chain structure of partially hydrolyzed polyacrylamide. *Journal of Central South University of Technology*, 15(1), 80–83. (page 61, 70)

Zimm, B. H. (1956). Dynamics of polymer molecules in dilute solution: viscoelasticity, flow birefringence and dielectric loss. *The journal of chemical physics*, 24(2), 269–278. (page 54)

Appendices

Appendix A

The Taylor equation

In this section, we present a proper derivation of the general force balance equation 1.14 for slender curtains using the local Cauchy equation. This equation was derived by Taylor (Geoffrey Ingram) in the case of Newtonian curtains. Our method is inspired by the methods employed by Ramos (1996) and Aidun (1987) for Newtonian curtains and is based on the Taylor (Brook) expansion of the local vertical velocity fields $u(y,z)$ around the symmetry axis $y=0$.

Cauchy equation and boundary conditions

We consider a liquid curtain extruded from a slot, subjected to gravity g, and made of any continuous material with density ρ, as shown in figure 4.9. We consider a steady and two-dimensional flow in the y-z plane, $z=0$ corresponding to the slot exit and $y=0$ being the symmetry axis. With the notations of §1.1.2, the mass conservation equation 2.10 for an incompressible flow writes

$$\frac{\partial v}{\partial y}+\frac{\partial u}{\partial z}=0 \tag{A.1}$$

and the Cauchy (momentum conservation) equation 2.11 writes

$$\begin{cases} \rho\left(v\dfrac{\partial u}{\partial y}+u\dfrac{\partial u}{\partial z}\right)=\rho g+\dfrac{\partial \pi^*_{yz}}{\partial y}+\dfrac{\partial \pi^*_{zz}}{\partial z} \\ \rho\left(v\dfrac{\partial v}{\partial y}+u\dfrac{\partial v}{\partial z}\right)=\dfrac{\partial \pi^*_{yy}}{\partial y}+\dfrac{\partial \pi^*_{yz}}{\partial z} \end{cases} \tag{A.2}$$

where $v(y,z)$ and $u(y,z)$ are the local velocity components along y and z and where $\boldsymbol{\pi}^*(y,z)$ is the (local) stress tensor. Since the free-surface is situated at $y=h(z)$, the kinematic boundary condition is

$$v=u\,h' \qquad \text{at} \quad y=h \tag{A.3}$$

where $'$ denotes $\mathrm{d}/\mathrm{d}z$, i.e. $h' = \mathrm{d}h/\mathrm{d}z$ is the local curvature. Assuming low surface curvature ($h' \ll 1$), we neglect the Laplace pressure. Besides, we assume that the surrounding gas is dynamically passive with constant atmospheric pressure P_a. Hence, using equation 2.13, the dynamic boundary condition writes

$$\begin{cases} \pi^*_{yy} n_y + \pi^*_{yz} n_z = -P_a n_y \\ \pi^*_{yz} n_y + \pi^*_{zz} n_z = -P_a n_z \end{cases} \quad \text{at} \quad y = h \tag{A.4}$$

where $\boldsymbol{n}$ is the unit vector normal to the free surface, i.e.

$$n_y = \frac{1}{(1+h'^2)^{1/2}} \qquad \text{and} \qquad n_z = -n_y h' = \frac{-h'}{(1+h'^2)^{1/2}} \tag{A.5}$$

Combining equations A.4 and A.5 gives

$$\begin{cases} \pi^*_{yy} - h' \pi^*_{yz} = -P_a \\ \pi^*_{yz} - h' \pi^*_{zz} = h' P_a \end{cases} \quad \text{at} \quad y = h \tag{A.6}$$

Leading order equation

We assume that the flow is symmetric with respect to $y = 0$ which means that v is 0 at the symmetry axis and is an odd function of y. Besides, assuming a Poiseuille-like flow in the slot, we can assume that u is an even function of y and has a maximum value $u_0(z)$ at $y = 0$. In order to derive an equation for u_0, we introduce a small parameter $\epsilon = a/L_c \ll 1$ (curtain aspect ratio) where $2a$ is the slot thickness and L_c is the curtain length which is a characteristic axial length. We can think of this small parameter to be of order $\epsilon = O(h')$ (slenderness ratio). In particular, since y and h are of order a, we can introduce

$$y = \epsilon \bar{y} \qquad \text{and} \qquad h = \epsilon \bar{h} \tag{A.7}$$

where $\bar{y}$ and $\bar{h}$ are of order L_c. We decompose the velocity field in

$$\begin{cases} u = u_0(z) + \epsilon^2 \bar{y}^2 \, u_2(z) + O(\epsilon^4) \\ v = \epsilon \bar{y} \, v_1(z) + O(\epsilon^3) \end{cases} \tag{A.8}$$

Let $u_0 = O(U_s)$ where $U_s = q/2a$ is the mean velocity in the slot. The Taylor expansion of u gives $u_2 = \frac{1}{2}\partial^2 u/\partial y^2 (y = 0, z)$. Assuming a fast convergence towards the plug flow, we assume that $u_2 = O(U_s/L_c^2)$, i.e. $\epsilon^2 \bar{y}^2 \, u_2 = O(\epsilon^2 \, U_s) \ll u_0$.

- Using incompressibility (equation A.1), we obtain at leading order

$$v_1 = -u_0' \tag{A.9}$$

At leading order, the kinematic boundary condition A.3 becomes

$$\bar{h}\, v_1 = \bar{h}' u_0 \tag{A.10}$$

Combining equations A.9 and A.10, we get

$$\bar{h} u_0 = w/\epsilon \qquad \Leftrightarrow \qquad h u_0 = w \tag{A.11}$$

where w is a constant. Using equations A.8 and A.11, the linear flow rate q is

$$\frac{q}{2} \equiv \int_0^h u \,\mathrm{d}y = h u_0 + O(\epsilon^3) = w + O(\epsilon^3) \tag{A.12}$$

• We need a decomposition of the stress components. Since π^*_{yz} must be odd and π^*_{yy} and π^*_{zz} must be even, we write

$$\begin{cases} \pi^*_{zz} = \pi_{zz0}(z) + O(\epsilon^2) \\ \pi^*_{yy} = \pi_{yy0}(z) + O(\epsilon^2) \\ \pi^*_{yz} = \epsilon \bar{y}\, \pi_{yz1}(z) + O(\epsilon^3) \end{cases} \tag{A.13}$$

At leading order, the dynamic boundary conditions A.6 become

$$\begin{cases} \pi_{yy0} = -P_a \\ \bar{h}\, \pi_{yz1} - \bar{h}' \pi_{zz0} = \bar{h}' P_a \end{cases} \tag{A.14}$$

and the z Cauchy equation A.2 becomes

$$\rho u_0 u_0' = \rho g + \pi_{yz1} + \pi'_{zz0} \tag{A.15}$$

• We decompose the stress tensor as

$$\boldsymbol{\pi}^* = -P\boldsymbol{\delta} + \boldsymbol{\sigma} \tag{A.16}$$

and we write

$$\begin{cases} P = P_0(z) + O(\epsilon^2) \\ \sigma^*_{zz} = \sigma_{zz0}(z) + O(\epsilon^2) \\ \sigma^*_{yy} = \sigma_{yy0}(z) + O(\epsilon^2) \\ \sigma^*_{yz} = \epsilon \bar{y}\, \sigma_{yz1}(z) + O(\epsilon^3) \end{cases} \quad \text{with} \quad \begin{cases} \pi_{zz0} = -P_0 + \sigma_{zz0} \\ \pi_{yy0} = -P_0 + \sigma_{yy0} \\ \pi_{yz1} = \sigma_{yz1} \end{cases} \tag{A.17}$$

We also define the local normal stress difference Δ^* as

$$\Delta^* \equiv \sigma^*_{zz} - \sigma^*_{yy} = \Delta_0(z) + O(\epsilon^2) \qquad \text{with} \qquad \Delta_0 = \sigma_{zz0} - \sigma_{yy0} \tag{A.18}$$

The first equation A.14 becomes

$$P_0 = P_a + \sigma_{yy0} \tag{A.19}$$

which gives

$$\pi_{zz0} = -P_a + (\sigma_{zz0} - \sigma_{yy0}) = -P_a + \Delta_0 \tag{A.20}$$

Using this result, P_a disappears from the second equation A.14 which becomes

$$\bar{h}\,\sigma_{yz1} = \bar{h}'\Delta_0 \tag{A.21}$$

• Injecting equations A.20 and A.21 in equation A.15, and replacing $\bar{h}$ by h/ϵ gives

$$\rho u_0 u_0' = \rho g + \frac{h'}{h}\Delta_0 + \Delta_0' = \rho g + \frac{1}{h}\,(h\,\Delta_0)' \tag{A.22}$$

Finally, using the fact that $hu_0 = w$ is constant (equation A.11), we get a force balance equation

$$\boxed{u_0 \frac{\mathrm{d}u_0}{\mathrm{d}z} = g + \frac{u_0}{\rho}\,\frac{\mathrm{d}}{\mathrm{d}z}\left(\frac{\Delta_0}{u_0}\right)} \tag{A.23}$$

for $u_0(z) = u(y = 0, z)$ and $\Delta_0 = \Delta^*(y = 0, z)$ which has the exact same form as the Taylor equation 1.14 which is written for mean values U and Δ. We can easily demonstrate equation 1.14 from equation A.23 by writing the definitions

$$\begin{cases} U = \dfrac{q}{2h} = \dfrac{1}{h}\displaystyle\int_0^h u\,\mathrm{d}y \\ \Delta = \sigma_{zz} - \sigma_{yy} = \dfrac{1}{h}\displaystyle\int_0^h \Delta^*\,\mathrm{d}y \end{cases} \tag{A.24}$$

which, using our decomposition, become

$$\begin{cases} U = \dfrac{1}{h}\left[hu_0 + O(\epsilon^3)\right] = u_0 + O(\epsilon^2) \\ \Delta = \Delta_0 + O(\epsilon^2) \end{cases} \tag{A.25}$$

Therefore, at leading order, the same force balance equation can be written for U and Δ.

Appendix B

Rheology of curtain solutions

[PEO] wt %	t_d min	η_0 Pa.s	η_p Pa.s	n	$1/\dot{\gamma}_c$ s	τ_{fil} s	η_E Pa.s	b	El	U_s m/s	U_1 m/s
0.004	0	0.017	0.0006	1.0	-	0.010	1×10^2	8×10^4	1.1	0.22	0.20
0.004	10	0.017	0.0006	1.0	-	0.0073	7×10^1	5×10^4	0.83	0.29	0.26
0.004	20	0.017	0.0006	1.0	-	0.0050	5×10^1	4×10^4	0.57	0.33	0.29
0.004	40	0.017	0.0006	1.0	-	0.0036	3×10^1	2×10^4	0.41	0.32	0.28
0.004	60	0.017	0.0006	1.0	-	0.0029	3×10^1	2×10^4	0.33	0.32	0.27
0.004	100	0.017	0.0006	1.0	-	0.0024	2×10^1	2×10^4	0.27	0.33	0.28
0.02	0	0.019	0.002	1.0	-	0.060	4×10^2	1×10^5	6.5	0.38	0.27
0.02	10	0.019	0.002	1.0	-	0.030	2×10^2	5×10^4	3.3	0.34	0.27
0.02	20	0.019	0.002	1.0	-	0.018	2×10^2	5×10^4	2.0	0.34	0.26
0.02	40	0.019	0.002	1.0	-	0.015	1×10^2	2×10^4	1.6	0.34	0.27
0.02	60	0.019	0.002	1.0	-	0.010	1×10^2	2×10^4	1.1	0.34	0.27
0.02	100	0.019	0.002	1.0	-	0.008	1×10^2	2×10^4	0.87	0.34	0.28
0.1	0	0.037	0.020	0.96	0.14	0.23	1×10^3	2×10^4	20	0.26	0.14
0.1	10	0.035	0.018	0.95	0.13	0.15	8×10^2	2×10^4	13	0.29	0.17
0.1	20	0.034	0.017	0.95	0.11	0.085	6×10^2	2×10^4	7.6	0.25	0.17
0.1	40	0.030	0.013	0.96	0.050	0.064	6×10^2	2×10^4	6.0	0.25	0.17
0.1	60	0.029	0.012	0.96	0.029	0.041	3×10^2	1×10^4	3.9	0.25	0.18
0.1	100	0.029	0.012	0.95	0.025	0.026	3×10^2	1×10^4	2.5	0.25	0.19
0.2	0	0.12	0.10	0.85	1.3	0.28	2×10^3	1×10^4	17	0.21	0.12
0.2	10	0.084	0.067	0.88	0.50	0.20	1×10^3	1×10^4	13	0.23	0.13
0.2	20	0.075	0.058	0.88	0.33	0.15	1×10^3	1×10^4	10	0.25	0.13
0.2	40	0.063	0.046	0.90	0.25	0.10	1×10^3	1×10^4	7.3	0.27	0.16
0.2	60	0.054	0.037	0.91	0.10	0.06	6×10^2	1×10^4	4.6	0.30	0.18
0.2	100	0.053	0.036	0.91	0.083	0.05	6×10^2	1×10^4	3.9	0.29	0.18
0.4	0	1.2	1.2	0.62	6.7	1.2	6×10^3	3×10^3	33	0.17	0.089
0.4	10	0.68	0.66	0.67	2.5	0.51	3×10^3	2×10^3	17	0.19	0.097
0.4	20	0.48	0.46	0.69	1.4	0.38	2×10^3	2×10^3	14	0.16	0.088
0.4	40	0.33	0.31	0.72	0.71	0.26	2×10^3	3×10^3	11	0.19	0.10
0.4	60	0.25	0.23	0.74	0.40	0.20	2×10^3	4×10^3	9.2	0.18	0.10
0.4	100	0.20	0.18	0.77	0.29	0.12	1×10^3	3×10^3	6.0	0.17	0.10

Table B.1 – Rheological parameters of the PEO solutions with 20 wt% PEG solvent used in curtain experiments, where t_d is the time of degradation. The first columns are similar to table 3.1 and the solvent viscosity is $\eta_s = 0.017$ Pa.s. El is the elasticity number (equation 4.16), $U_s = q/2a$ is the extrusion velocity where q is the linear flow rate, and $U_1 = U(z_1)$ is the liquid velocity measured at $z_1 \approx 2.5$ mm from the slot, i.e. after swelling.

[NaCl] (wt %)	t_d min	η_0 (Pa.s)	η_p (Pa.s)	n	$1/\dot{\gamma}_c$ (s)	τ_{fil} (s)	η_E (Pa.s)	b	El	U_s (m/s)	U_1 (m/s)
0	0	1×10^2	1×10^2	0.20	8×10^2	0.4	2×10^3	1×10^1	2	0.29	0.29
0	10	1×10^2	1×10^2	0.20	8×10^2	0.4	2×10^3	7×10^0	2	0.31	0.30
0	20	1×10^2	1×10^2	0.20	8×10^2	0.3	1×10^3	3×10^0	2	0.31	0.31
0	40	1×10^2	1×10^2	0.20	8×10^2	0.3	1×10^3	3×10^0	2	0.28	0.31
0	60	1×10^2	1×10^2	0.20	8×10^2	0.3	1×10^3	3×10^0	1	0.29	0.31
0	100	1×10^2	1×10^2	0.20	8×10^2	0.2	1×10^3	3×10^0	1	0.31	0.31
0.1	0	0.61	0.61	0.49	2×10^1	0.24	1×10^3	8×10^2	8.2	0.33	0.33
0.1	10	0.61	0.61	0.49	2×10^1	0.19	8×10^2	7×10^2	6.5	0.28	0.30
0.1	20	0.61	0.61	0.49	2×10^1	0.16	8×10^2	7×10^2	5.4	0.29	0.30
0.1	40	0.61	0.61	0.49	2×10^1	0.15	8×10^2	7×10^2	5.1	0.29	0.32
0.1	60	0.61	0.61	0.49	2×10^1	0.14	5×10^2	4×10^2	4.8	0.28	0.30
0.1	100	0.61	0.61	0.49	2×10^1	0.12	5×10^2	4×10^2	4.1	0.27	0.29
0		1×10^2	1×10^2	0.20	8×10^2	0.4	1×10^3	3×10^0	2	0.12	0.12
0.01		8×10^1	8×10^1	0.25	8×10^2	0.4	8×10^2	5×10^0	2	0.13	0.12
0.1		0.70	0.70	0.47	20	0.19	5×10^2	4×10^2	6.2	0.13	0.14
1		0.025	0.024	0.71	0.71	0.077	6×10^2	1×10^4	7.6	0.12	0.12
10		0.0088	0.0078	0.81	0.25	0.050	4×10^2	3×10^4	7.0	0.14	0.13

Table B.2 – Rheological parameters of the salted (NaCl) 0.1 wt% HPAM solutions used in curtain experiments, where t_d is the time of degradation (top) which is unknown for the last liquid (bottom) where salt is added after each PIV measurement. The first columns are similar to table 3.1 and the solvent viscosity is $\eta_s = 0.001$ Pa.s. El is the elasticity number (equation 4.16), $U_s = q/2a$ is the extrusion velocity where q is the linear flow rate, and $U_1 = U(z_1)$ is the liquid velocity measured at $z_1 \approx 2.5$ mm from the slot, i.e. after swelling.

[PEO] (wt %)	η_0 (Pa.s)	η_p (Pa.s)	n	$1/\dot{\gamma}_c$ (s)	α_1	Ψ (Pa.s$^{\alpha_1}$)	τ_{fil} (s)	η_E (Pa.s)	b	El	U_s (m/s)	U_1 (m/s)
0.2	0.70	0.56	0.90	2.0	1.8	0.25	1.1	7×10^3	6×10^3	37	0.040	0.020
0.11	0.35	0.21	0.95	0.56	2	0.040	0.68	4×10^3	1×10^4	28	0.057	0.029
0.048	0.21	0.07	1	-	2	0.014	0.42	2×10^3	2×10^4	21	0.073	0.040
0.024	0.17	0.03	1	-	2	0.005	0.17	9×10^2	2×10^4	9.1	0.098	0.060

Table B.3 – Rheological parameters of the PEO solutions with 40 wt% PEG solvent used in curtain experiments. The first columns are similar to table 3.1 and the solvent viscosity is $\eta_s = 0.14$ Pa.s. El is the elasticity number (equation 4.16), $U_s = q/2a$ is the extrusion velocity where q is the linear flow rate, and $U_1 = U(z_1)$ is the liquid velocity measured at $z_1 \approx 2.5$ mm from the slot, i.e. after swelling.

[PEG] wt %	[PEO] wt %	η_0 Pa.s	η_p Pa.s	n	$1/\dot{\gamma}_c$ s	α_1	Ψ Pa.s$^{\alpha_1}$	τ_{fil} s	η_E Pa.s	b	El
20	0.4	0.21	0.19	0.81	0.4	2	0.0029	0.16	1×10^3	3×10^3	7.8

Table B.4 – Rheological properties of the liquid used as a reference for the investigations on die swell (§4.1.3 and §4.4.1), and on the role of flow rate (§4.2.2) and die geometry (see §4.4.3). All these experiments are performed the same day. This liquid is close to (but not exactly the same as) the degraded ($t_d = 100$ min) 0.4 wt% PEO solution with 20 wt% PEG solvent presented in table B.1. Density is $\rho = 1026$ kg/m^3, surface tension is $\gamma = 62$ mN/m, solvent viscosity is $\eta_s = 0.017$ Pa.s and El is the elasticity number (equation 4.16)

[NaCl] wt %	η_0 Pa.s	η_p Pa.s	n	$1/\dot{\gamma}_c$ s	τ_{fil} s	η_E Pa.s	b	El	U_s m/s	U_1 m/s
0	1×10^2	1×10^2	0.19	6×10^2	0.4	1×10^3	3×10^0	2	0.35	0.33
0.01	3×10^1	3×10^1	0.28	3×10^2	0.3	8×10^2	1×10^1	3	0.36	0.37
0.1	0.52	0.52	0.51	17	0.14	5×10^2	5×10^2	5.0	0.33	0.35
1	0.019	0.018	0.75	0.56	0.064	4×10^2	1×10^4	6.9	0.37	0.36
10	0.0073	0.0063	0.84	0.17	0.057	4×10^2	3×10^4	8.5	0.38	0.34

Table B.5 – Rheological parameters of the salted (NaCl) 0.1 wt% HPAM solutions used in §5.2 for investigations on the extrusion instability. Like in table B.2 (bottom), salt is added after each PIV measurement. The first columns are similar to table 3.1 and the solvent viscosity is $\eta_s = 0.001$ Pa.s. El is the elasticity number (equation 4.16), $U_s = q/2a$ is the extrusion velocity where q is the linear flow rate, and $U_1 = U(z_1)$ is the liquid velocity measured at $z_1 \approx 2.5$ mm from the slot, i.e. after swelling.

Chapter 7

Résumé en français

Dans ce chapitre, nous présentons un résumé des travaux de thèse rédigé en langue française, conformément aux règles de l'EDPIF (École Doctorale 564 Physique en Île-de-France).

Rideau Newtonien

Les rideaux liquides sont de minces lames de liquide s'écoulant à l'air libre à débit constant par gravité. Ils sont souvent extrudées à partir d'une fente et sont notamment utilisée dans l'industrie lors du processus d'enduction au rideau ("curtain coating") qui consiste à faire s'écouler une lame de liquide verticale (peinture, revêtement protecteur, ...) sur un substrat solide en mouvement horizontal à vitesse constante.

La première étude de l'écoulement des rideaux liquides date des années 1960, lorsque Brown (1961) a mesuré le champ de vitesse $U(z)$ d'un liquide Newtonien au sein d'un rideau vertical extrudé depuis une fente, où z est la distance à la sortie de la fente. Il mesure une déviation à la loi classique de la chute libre $U = \sqrt{U_0^2 + 2gz}$ près de la fente, où U_0 est la vitesse en sortie de fente et $g = 9.81$ m/s^2 est la gravité. Physiquement, puisque les particules de fluide sont accélérées par la gravité, le rideau se contracte par conservation du débit, et cette contraction génère des contraintes visqueuses au sein du liquide qui ont un effet sur la vitesse de chute. G. I. Taylor a proposé (dans l'appendice de Brown (1961)) une équation bilan de la forme

$$U\frac{\mathrm{d}U}{\mathrm{d}z} = g + \frac{4\eta U}{\rho}\frac{\mathrm{d}}{\mathrm{d}z}\left(\frac{1}{U}\frac{\mathrm{d}U}{\mathrm{d}z}\right) \tag{7.1}$$

où ρ et η sont la masse volumique et la viscosité dynamique du liquide. Dans cette équation, U est la vitesse moyennée dans l'épaisseur de du rideau. On peut retrouver

cette équation à partir de l'équation de Navier-Stokes pour des rideaux fins, i.e. pour lesquels $\partial h/\partial z \ll 1$ où $2h$ est l'épaisseur locale du rideau (Aidun, 1987; Ramos, 1996). Cette équation montre que, en accord avec l'expérience, l'accélération des particules de fluide est initialement inférieure à g et atteint la valeur asymptotique de chute libre g à une distance de la fente z_v^* qui s'écrit

$$z_v^* = F_v \times z_v \qquad \text{où} \qquad z_v = \left(\frac{(4\eta/\rho)^2}{g}\right)^{1/3} \tag{7.2}$$

et où F_v est une fonction décroissante de la vitesse initiale U_0 et qui est de l'ordre 7 pour $U_0/\sqrt{gz_v} \ll 1$.

Au cours de cette thèse, nous avons été amené à pousser l'analyse de l'équation de Taylor 7.1 plus loin que ce qui avait été initialement fait dans la littérature, notamment pour identifier une courbe maîtresse de l'écoulement. On introduit des variables adimensionnées

$$\begin{cases} \bar{z} = z/z_v \\ \bar{U} = U/U_v \end{cases}, \qquad z_v = \left(\frac{(4\eta/\rho)^2}{g}\right)^{1/3}, \qquad U_v = \sqrt{g\, z_v} = (4\eta g/\rho)^{1/3} \tag{7.3}$$

L'équation de Taylor 7.1 devient

$$\bar{U}\bar{U}' = 1 + \bar{U}'' - \bar{U}'^2/\bar{U} \tag{7.4}$$

La solution générale de cette équation a été trouvée par Clarke (1968, 1966) et s'écrit

$$\bar{U}(\bar{z}) = 2^{-1/3}\left[\left(\frac{\mathrm{Ai}'(Z) + C\,\mathrm{Bi}'(Z)}{\mathrm{Ai}(Z) + C\,\mathrm{Bi}(Z)}\right)^2 - Z\right]^{-1}, \qquad Z = 2^{-1/3}(\bar{z} + k) \tag{7.5}$$

où Ai et Bi sont les fonctions d'Airy et où C et k sont des constante à déterminer grâce aux conditions aux limites en amont et en aval du rideau. La condition en sortie de fente est simplement

$$\bar{U}(\bar{z} = 0) \equiv \bar{U}_0 = \frac{U_0}{U_v} = \frac{\rho U_0 z_v}{4\eta} \tag{7.6}$$

où la vitesse en sortie de fente $U_0 = U(z = 0)$ peut être changée par variation du débit. Il existe trois types de conditions en aval. Si $C > 0$, la solution diverge vers $+\infty$ en temps fini, ce qui correspond à une expérience de "film casting" où la nappe de liquide est étirée par un rouleau tournant à une vitesse arbitrairement grande en aval. Si $C < 0$, la solution passe par $U = 0$ à une distance L_c de la fente. Cela

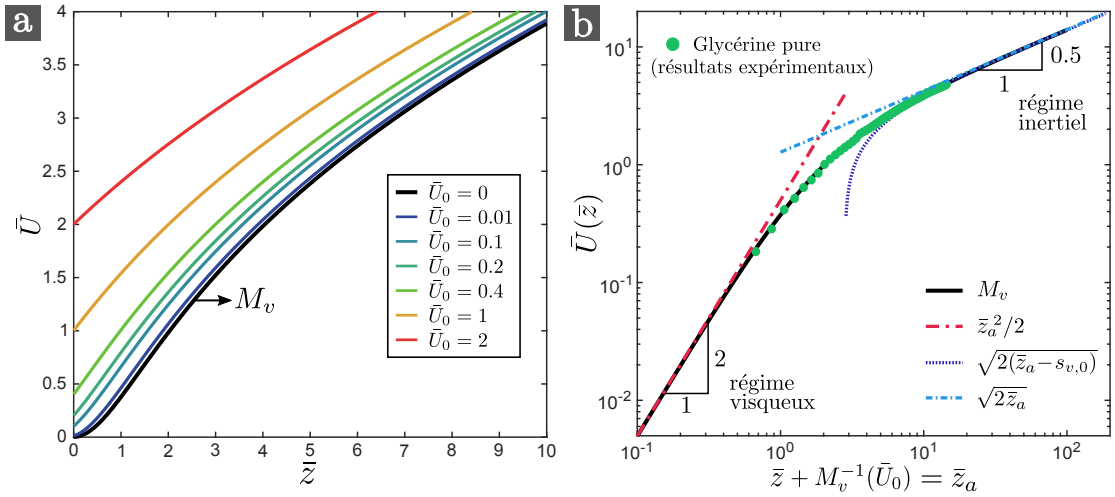

Figure 7.1 – (a) Solution de Clarke (équation 7.5) pour le champ de vitesse d'un rideau Newtonien "infini", i.e. tendant vers une chute libre ($C = 0$), pour différentes vitesses initiales $\bar{U}_0$ comprises entre 0 et 2. (b) Courbe maîtresse M_v et champ de vitesse expérimental pour un rideau de glycérine pure (les points expérimentaux sont translatés le long de l'axe des abscisses selon l'équation 7.7). Les régimes visqueux ($\bar{z} \ll 1$) et inertiels ($\bar{z} \gg 1$) sont décrits par l'équation 7.8

correspond à la transition vers un étalement de la nappe sur une surface horizontale immobile. Enfin, si $C = 0$, la solution tend vers une chute livre à l'infini, c'est à dire que $\bar{U}\bar{U}' \to 1$ pour $\bar{z} \to +\infty$, ce qui correspond à un rideau infiniment long.

La solution de Clarke (équation 7.5) est tracée en figure 7.1.a pour $C = 0$ (rideau "infini" tendant vers une chute libre) et des vitesse initiales $\bar{U}_0$ comprises entre 0 et 2. Toutes les courbes se superposent sur la courbe maîtresse qui correspond à $\bar{U}_0 = 0$ après translation selon l'axe des abscisses. Cette propriété peut s'écrire

$$\boxed{\bar{U}(\bar{z}) = M_v\left(\bar{z} + M_v^{-1}(\bar{U}_0)\right)} \tag{7.7}$$

où M_v est la courbe maîtresse (vitesse initiale nulle, équation 7.5 avec $C = 0$ et $k_0 \approx -2.94583$). Cette propriété se démontre aisément en utilisant le fait que $\bar{z}$ n'apparaît pas explicitement dans l'équation 7.4. Cette courbe est tracée en figure 7.1.b. On observe deux régimes:

$$M_v(\bar{z}) = \begin{cases} \bar{z}^2/2 & \bar{z} \ll 1 : \text{ régime visqueux} \\ \sqrt{2\left(\bar{z} - s_{v,0}\right)} & \bar{z} \gg 1 : \text{ régime inertiel} \end{cases} \tag{7.8}$$

où $s_{v,0} \approx 2.8$. La gravité est initialement équilibrée par la dissipation visqueuse ($\bar{z} \ll 1$) jusqu'à ce que l'inertie finisse par dominer ($\bar{z} \gg 1$). On retrouve une chute libre asymptotique. On peut combiner les équations 7.7 et 7.8 pour obtenir les profils de vitesses $\bar{U}(\bar{z})$ dans ces deux régimes. Notons que le régime visqueux

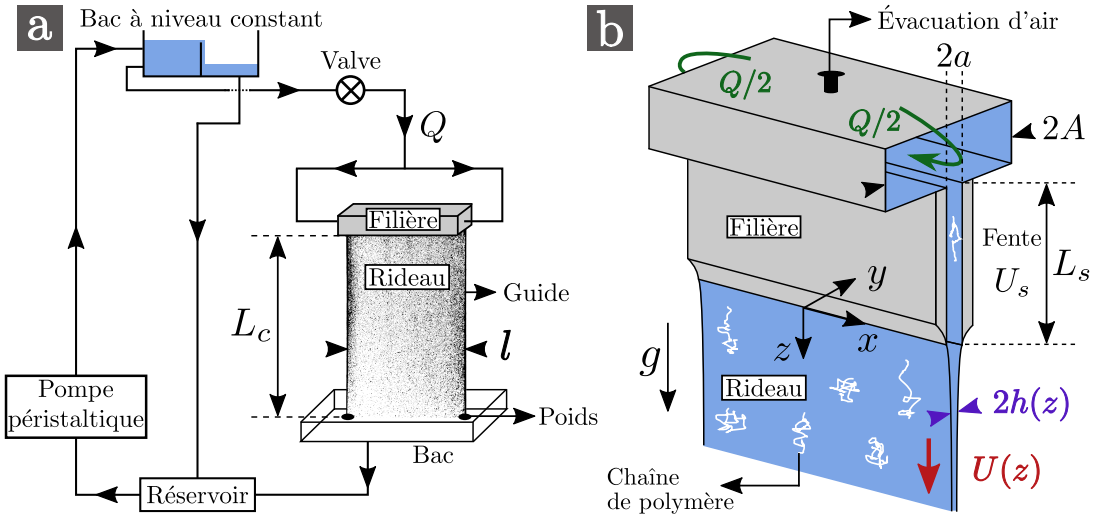

Figure 7.2 – Schéma de la boucle hydraulique (a) et de la filière (b).

n'existe que pour des vitesses initiales $\bar{U}_0 \ll 1$, i.e. $U_0 \ll U_v = \sqrt{gz_v}$, car dans le cas contraire ($\bar{U}_0 \gg 1$), l'inertie domine même près de la fente, auquel cas on a une chute libre $U = \sqrt{U_0^2 + 2gz}$.

Matériel et méthodes

Afin d'étudier l'écoulement et la stabilité des rideaux liquides viscoélastiques, nous formons des rideaux de solutions de polymères. Deux polymères sont utilisés, le poly(oxyde d'éthylène) (PEO) de masse molaire $M = 8 \times 10^6$ g/mol et le polyacrylamide partiellement hydrolysé (HPAM) de masse molaire $M = 15 - 20 \times 10^6$ g/mol. Les chaînes de PEO sont flexibles tandis que le HPAM est un polyélectrolyte dont les chaînes sont semi rigides. La flexibilité des chaînes de HPAM peut être modifiée par ajout de sel à la solution car il agit comme un écran aux charges négatives de la chaîne. Les solutions de PEO sont préparées dans des solvants aqueux, épaissis par ajout de polyéthylène glycol de masse molaire $M = 8000$ g/mol (solvent Newtonien) en concentrations 20 wt% et 40 wt%. La concentration en PEO, notée [PEO], varie entre 0 et 0.4 wt%. On utilise des solutions aqueuses de HPAM à concentration fixée [HPAM] = 0.1 wt% en polymère et avec une concentration en sel variant entre 0 et 10 wt%. Pour un solvant donné, la densité ρ et la tension de surface Γ ne dépendent pas de la concentration en polymère.

Montage expérimental

Afin de former un rideau, nous utilisons le montage présenté en figure 7.2. Les 5 kg de solution s'écoulent au sein d'une boucle grâce à une pompe péristaltique et pas-

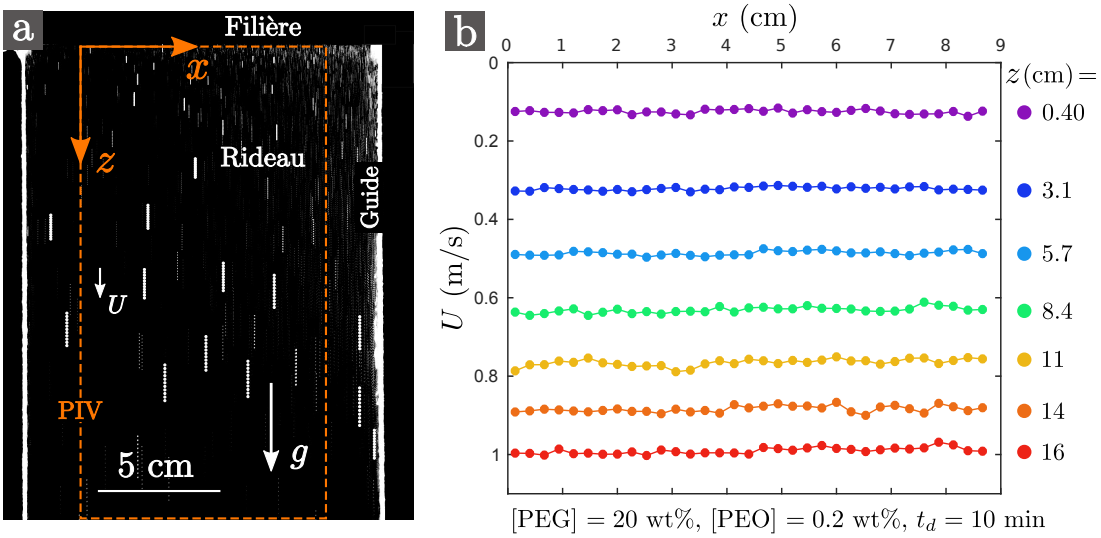

Figure 7.3 – Exemple de mesure de PIV pour une solution de PEO de concentration 0.2 wt% dans un solvant à 20 wt% de PEG. (a): Superposition d'images successives. L'algorithme de corrélation est appliqué à une zone éloignée des guides pour éviter les effets de bords. (b): Composante vertical de la vitesse, i.e. $U(x, z, t)$, en fonction de la coordonnée horizontale x à un temps arbitraire t pour plusieurs distances z à la fente. La longueur du rideau est $L_c = 30$ cm et le débit linéique est $q = 2.3$ cm^2/s.

sent par une filière ("die" en anglais) présentant une fente d'épaisseur $2a = 1$ mm, de longueur $L_s = 10$ cm et de largeur $l = 14.5$ cm. En amont de la fente, l'épaisseur de la filière est $2A = 14$ mm, i.e. $A/a = 14$. Le liquide s'écoule alors librement sous l'effet de la gravité avant d'impacter le fond d'un réservoir immobile à une distance L_c de la sortie de la fente. L_c est la longueur du rideau et varie entre 15 cm et 200 cm. Des guides verticaux sont placés de part et d'autres du rideau afin qu'il ait une forme rectangulaire. Le débit massique Q du rideau est mesuré par pesée. On définit alors le débit linéique q donné par $q = Q/\rho l$ où ρ est la masse volumique du liquide. La vitesse moyenne au sein de la fente est alors $U_s = q/2a$.

Afin de mesurer le champ de vitesse au sein du rideau, on utilise la technique de Vélocimétrie par Images de Particules (PIV). Le liquide est ensemencé de traceurs de taille 50 μm et est éclairé par une puissante lumière blanche et filmé par une caméra rapide. Une séquence d'image est traitée par un algorithme de corrélation d'images de manière à reconstruire le champ de vitesse verticale $U(x, z, t)$ au sein du rideau. Un exemple de superposition d'images et de champ de vitesse est montré en figure 7.3. Dans beaucoup de cas, le champ de vitesse est stationnaire et ne dépend pas de la coordonnée horizontale x. On s'intéresse donc à l'évolution de la vitesse verticale $U(z)$ en fonction de la distance z à la fente.

Caractérisation rhéologique

Afin de caractériser nos solutions de polymère, nous mesurons certaines propriétés de cisaillement à l'aide d'un rhéomètre ARES-G2 équipé d'une géométrie cône-plan de rayon $R_1 = 25$ mm et d'angle $\theta_1 = 0.04$ rad. La viscosité de cisaillement apparente de certaines solutions est présentée en figure 7.4 en fonction du taux de cisaillement $\dot{\gamma}$. Les données sont ajustées par la loi (empirique) de Carreau

$$\eta = \eta_0 \left[1 + \left(\frac{\dot{\gamma}}{\dot{\gamma}_c} \right)^{a_1} \right]^{\frac{n-1}{a_1}} \tag{7.9}$$

où η_0 est la viscosité à zéro cisaillement, n est le degré de rhéofluidification, $\dot{\gamma}_c$ est le taux de cisaillement au delà duquel la viscosité diminue et a_1 code la transition vers le régime rhéofluidifiant. Les solutions de PEO les plus diluées ont une viscosité constante ($n = 1$) tandis que les solutions les plus concentrées sont rhéofluidifiantes. La solution de HPAM non salée est très rhéofluidifiante et l'ajout de sel permet de réduite le degré de rhéofluidification. Á partir des données de viscosité, on peut estimer la concentration critique d'enchevêtrement c^* des solutions de PEO. Elle est liée à la viscosité intrinsèque définie par

$$[\eta] \equiv \lim_{c \to 0} \frac{\eta_0 - \eta_s}{c\, \eta_s} \tag{7.10}$$

où $c = \rho[\text{PEO}]$. On mesure $[\eta] = 0.93$ m^3/kg. En utilisant la relation $c^* = 0.77/[\eta]$ de Graessley (1980), on obtient $c^* = 0.83$ kg/m^3 (ce qui correspond à 0.081 wt%). Nous travaillons donc avec des solutions de PEO diluées et semi diluées. Pour la solution de HPAM non salée, l'équation de Mark-Houwink (Wu et al., 1991; Kawale et al., 2017) donne $[\eta] = 5.0$ m^3/kg et donc $c^* = 0.15$ kg/m^3 (ce qui correspond à 0.015 wt%). La solution de HPAM non salée est donc semi diluée.

Vu que l'écoulement du rideau est extensionnel, nous avons également mesuré la rhéologie extensionnelle de ces solutions à l'aide de la méthode de CaBER (Capillary Breakup Extensional Rheometer). Cette méthode est largement décrite dans la littérature (McKinley, 2005; Rodd et al., 2004; Anna & McKinley, 2001; Tirtaatmadja et al., 2006) et consiste à placer une goutte de liquide entre deux plaques horizontales puis à séparer les plaques jusqu'à ce que la goutte de sépare en deux. En effet, à partir d'une distance critique entre les plaques, une instabilité capillaire engendre un amincissement progressif du pont de liquide reliant les deux "gouttes" situées sur les deux plaques. Pour une goutte de liquide Newtonien, le filament de liquide se rompt rapidement suivant une loi auto-similaire qui n'est pas la même suivant que les forces capillaires sont équilibrées par les forces visqueuses ou iner-

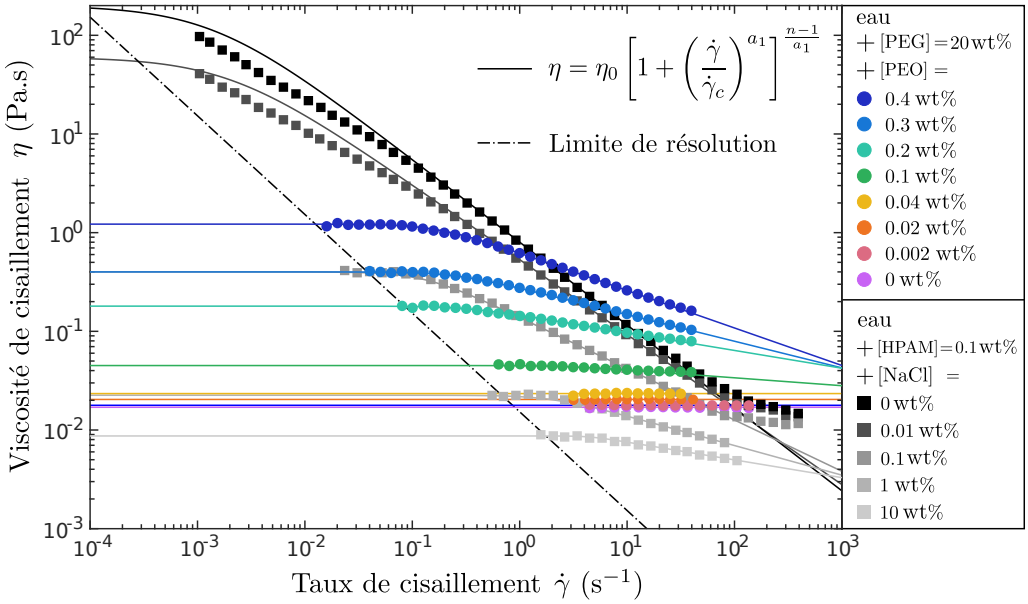

Figure 7.4 – Viscosité de cisaillement $\eta(\dot{\gamma})$ pour des solutions de PEO dans un solvant à 20 wt% de PEG et pour des solutions de HPAM avec différentes concentrations en sel. Les données sont ajustées avec la loi de Carreau 7.9. La limite de résolution de l'appareil (couple minimum mesurable) est montrée.

tielles. En revanche, en présence de polymères, le filament transite vers une forme cylindrique dont le rayon $\mathcal{R}$ décroît en suivant une loi exponentielle

$$\mathcal{R} \propto \exp\left(-t/3\tau_{fil}\right). \tag{7.11}$$

où τ_{fil} est assimilable au temps de relaxation le plus long (ou temps terminal) du spectre de la chaîne de polymère (Entov & Hinch, 1997; McKinley, 2005). Dans ce régime élastique, le taux d'extension $\dot{\epsilon} = -2\,\dot{\mathcal{R}}/\mathcal{R}$ est constant et est tel que $\dot{\epsilon}\tau_{fil} = 2/3$ ce qui est supérieur à la valeur 1/2 au delà de laquelle les chaînes se démêlent ("coil-stretch transition", De Gennes (1974)). Par conséquent, les chaînes finissent par atteindre leur taille maximale et la viscosité extensionelle devient constante. Le filament se déstabilise alors en gouttelettes avant de se rompre (Sattler et al., 2008, 2012; Eggers, 2014).

Le filament est filmé avec une caméra rapide et un objectif permettant une résolution de 1 pixel par micromètre. L'évolution du rayon minimum $\mathcal{R}(t)$ du filament est montré en figure 7.5 avec des images brutes correspondant aux différentes phases décrites plus haut. On mesure des temps de relaxation τ_{fil} compris entre quelques millisecondes et une seconde.

Dans la suite, les valeurs de ces différents paramètres rhéologiques seront utilisés

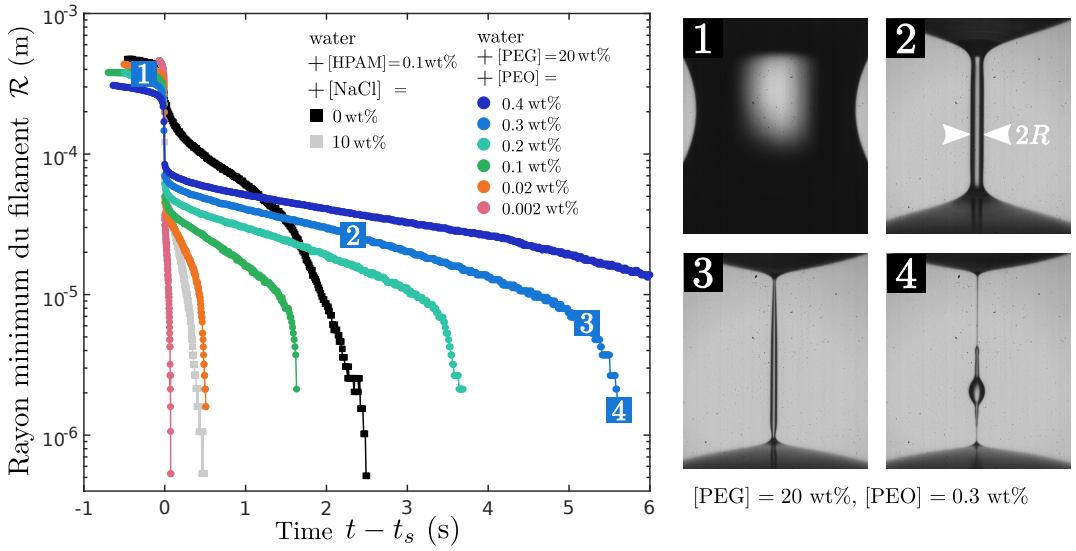

Figure 7.5 – Gauche: Rayon minimum $\mathcal{R}$ du filament en fonction du temps $t - t_s$ où t_s marque la transition vers le régime élasto-capillaire (décroissance exponentielle) pour des solutions de PEO avec un solvant à 20 wt% de PEG et pour des solutions de HPAM. Droite: Quatre images du filament pour une solution de PEO de concentration 0.2 wt% aux quatre temps reportés sur la courbe correspondante à gauche.

pour interpréter les résultats concernant l'écoulement et la stabilité des rideaux liquides viscoélastiques.

Écoulement du rideau

Le montage expérimental présenté en figure 7.2 produit une dégradation progressive des solutions, notamment au niveau de la pompe. Par exemple, le temps de relaxation extensionnel τ_{fil} décroît d'un facteur 10 après une heure de circulation d'une solution (de 5 kg) au sein du montage. Pour résoudre ce problème, deux protocoles ont été mis en oeuvre. Le premier consiste à effectuer plusieurs mesures au cours du temps pour une même solution, et à prélever à chaque fois un échantillon de solution pour les mesures de rhéologie. Ainsi, nous pouvons extraire plus de données avec une seule solution. Le deuxième protocole consiste à ne pas utiliser la pompe et à verser directement la solution dans un réservoir connecté à la filière. On évite ainsi la dégradation.

Écoulement sous gravitaire

Afin d'identifier la particularité des rideaux de liquides viscoélastiques, nous avons réalisé une série de mesures sur trois rideaux: deux Newtoniens (une solution de 20 wt% en PEG, peu visqueux, et de la glycérine, plus visqueuse) et une solution

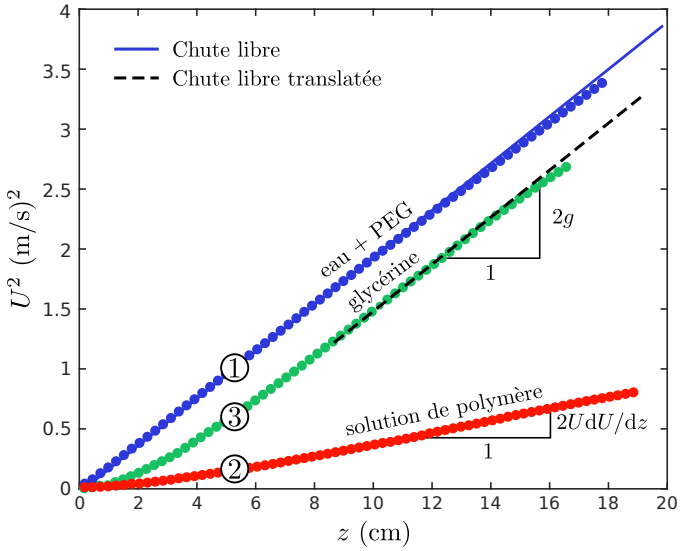

Figure 7.6 – Carré U^2 de la vitesse du liquide en fonction de la distance z à la sortie de la fente pour deux rideaux Newtoniens (1) and (3), respectivement une solution de 20 wt% de PEG (1) et de la glycérine pure (3) de viscosités respectives $\eta = 0.017$ Pa.s and $\eta = 1.5$ Pa.s, et pour une solution de PEO de concentration 0.2 wt% (2) avec un solvant de 20 wt% en PEG de viscosité à cisaillement nul $\eta_0 = 0.12$ Pa.s. La longueur du rideau est $L_c = 30$ cm et la vitesse initiale U_1 à $z_1 \approx 2.5$ mm de la fente est 0.2 m/s, 0.13 m/s and 0.07 m/s pour les liquides (1), (2) and (3) respectivement. L'accélération locale du liquide est $U\mathrm{d}U/\mathrm{d}z$.

de PEO de viscosité de cisaillement intermédiaire. Les résultats sont présentés en figure 7.6 où le carré U^2 de la vitesse verticale est tracé en fonction de la distance z à la sortie de la fente. L'écoulement du rideau Newtonien peu visqueux est une chute libre, i.e. $U^2 = U_0^2 + 2gz$. Le rideau de glycérine présente un régime initial (près de la fente) où l'accélération locale $U\mathrm{d}U/\mathrm{d}z$ est inférieure à g. L'accélération atteint sa valeur asymptotique g à une distance de la fente qui correspond à la valeur z_v^* donnée en équation 7.2. Ce profil de vitesse est très bien décrite par l'équation de Taylor 7.1, comme le montre la figure 7.1.b où les points expérimentaux sont superposée à la courbe maîtresse M_v décrite précédemment. En revanche, le rideau de liquide viscoélastique n'a pas atteint le régime de chute libre après 20 cm de chute alors que sa longueur visqueuse $z_v = ((4\eta_0/\rho)^2/g)^{1/3}$ n'est que de 0.28 cm en se basant sur la viscosité à cisaillement nul. Il existe dont d'autres paramètres rhéologiques qui gouvernent la dynamique de l'écoulement dans le cas des rideaux viscoélastiques.

Influence de la longueur du rideau

Afin d'étudier l'influence de la longueur du rideau sur l'écoulement, nous avons réalisé une série d'expériences avec des solutions de PEO dont le solvant est composé à 40 wt% de PEG. La chute du liquide est stoppée à une distance L_c de la fente par

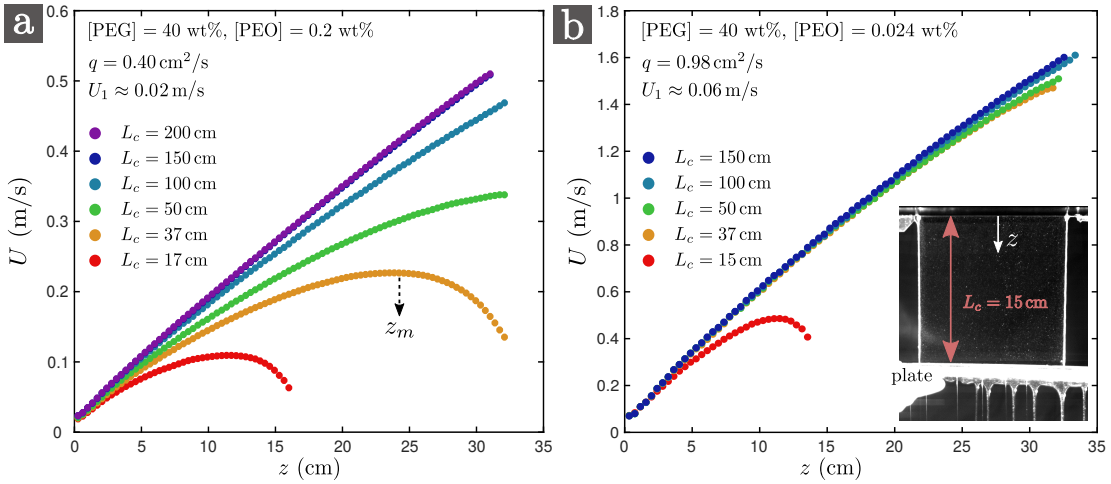

Figure 7.7 – Champ de vitesse $U(z)$ pour $z \leq 32$ cm pour des rideaux de longueur L_c compris entre 15 cm et 200 cm. Le liquide impacte une plaque horizontale fixe placée à une distance L_c de la sortie de la fente (voir l'inset à droite) et atteint une vitesse maximale à une distance z_m de la fente. Les liquides sont des solutions de PEO dans un solvant à 40 wt% de PEG et de concentrations respectives 0.2 wt% et 0.024 wt%. Ils sont extrudés respectivement à des débits $q = 0.40$ cm^2/s and 0.98 cm^2/s.

une plaque horizontale où le liquide s'étale, et L_c est varié entre 15 cm et 200 cm. Les résultats sont présentés en figure 7.7 pour $\tau_{fil} = 1.1$ s (a) et $\tau_{fil} = 0.17$ s (b). La composante verticale de la vitesse doit varier entre $U(z = 0) = U_0$ à la sortie de la fente et $U(z = L_c) = 0$ au moment de la transition vers un écoulement d'étalement. Ainsi, on observe en figure (a) que la vitesse du liquide commence par augmenter du à la gravité et atteint une vitesse maximum à une distance z_m de la fente avant de diminuer à l'approche de la plaque. Á mesure que la longueur du rideau augmente, l'écoulement près de la fente semble converger vers une loi universelle qui ne dépend plus de la valeur de L_c. Cela est confirmé en figure (b) pour le liquide de moindre temps de relaxation pour lequel tous les profils de vitesse, à l'exception de celui associé au rideau le plus court, se superposent sur une seule courbe. Ainsi, comme pour le cas Newtonien, la présence d'une plaque imposant une condition de vitesse nulle en aval du rideau n'impacte de manière significative que la zone de l'écoulement proche de l'impact.

Influence de la vitesse initiale

L'influence du débit a également été étudiée. Une solution de PEO est extrudée à différents débits q compris entre 0.45 cm^2/s et 1.4 cm^2/s et les profils de vitesse au sein du rideau sont présentés en figure 7.8.a pour ces deux débits. On constate que le liquide extrudé à plus haut débit voit sa vitesse augmenter plus vite (les courbes s'éloignent l'une de l'autre). Cela est confirmé en figure 7.8.b où l'accélération à

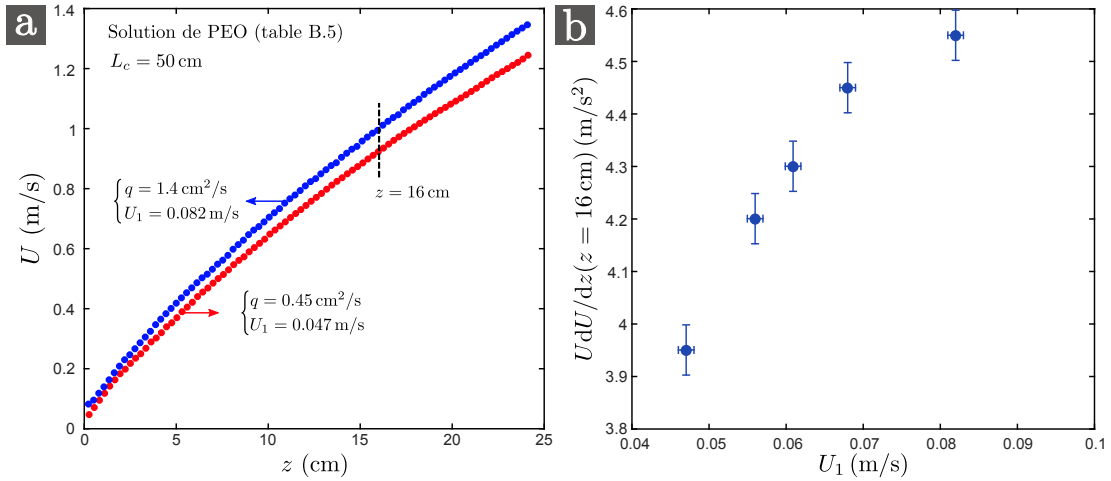

Figure 7.8 – (a): Profil de vitesse $U(z)$ pour une solution de PEO extrudée à des débits $q = 0.45$ cm^2/s et 1.4 cm^2/s. La vitesse U_1 à $z_1 \approx 2.5$ mm de la fente est respectivement 0.047 m/s et 0.082 m/s. (b): Accélération locale $U\mathrm{d}U/\mathrm{d}z$ à $z = 16$ cm de la fente en fonction de U_1. La longueur du rideau est $L_c = 50$ cm.

une distance arbitraire $z = 16$ cm est tracée en fonction de la vitesse initiale U_1 (qui est mesurée à une distance $z_1 = 2.5$ mm de la fente). Cette augmentation de l'accélération est également prédite par l'équation de Taylor 7.1 pour des rideaux Newtoniens.

Influence de la rhéologie

En comparant les profils de vitesse $U(z)$ pour différents rideaux de même longueur et de même débits, on constate que l'écoulement de solutions de mêmes temps de relaxation extensionnel τ_{fil} sont semblables, indépendamment de la valeur des autres parametres rheologiques tels que η_0, $\eta_p = \eta_0 - \eta_s$ (où η_s est la viscosité du solvant) et n ou de la flexibilité des chaînes. Ces résultats sont synthétisés en figure 7.9 où l'accélération du liquide $U\mathrm{d}U/\mathrm{d}z$ (adimensionné par g) mesurée à une distance arbitraire $z = 18$ cm de la fente est tracée en fonction de τ_{fil} pour toutes les solutions utilisées (PEO et HPAM). Notons que les solutions dont le temps de relaxation est très faible, typiquement plus petit que 10 ms, s'écoulent en chute libre, ce qui est en adéquation avec les récentes mesures de Karim et al. (2018b).

Courbe maîtresse

Afin de trouver la longueur caractéristique z_e du régime sous gravitaire dans le cas d'un rideau viscoélastique, on peut écrire l'équation bilan générale de l'écoulement

$$U\frac{\mathrm{d}U}{\mathrm{d}z} = g + \frac{U}{\rho}\frac{\mathrm{d}}{\mathrm{d}z}\left(\frac{\Delta}{U}\right) \tag{7.12}$$

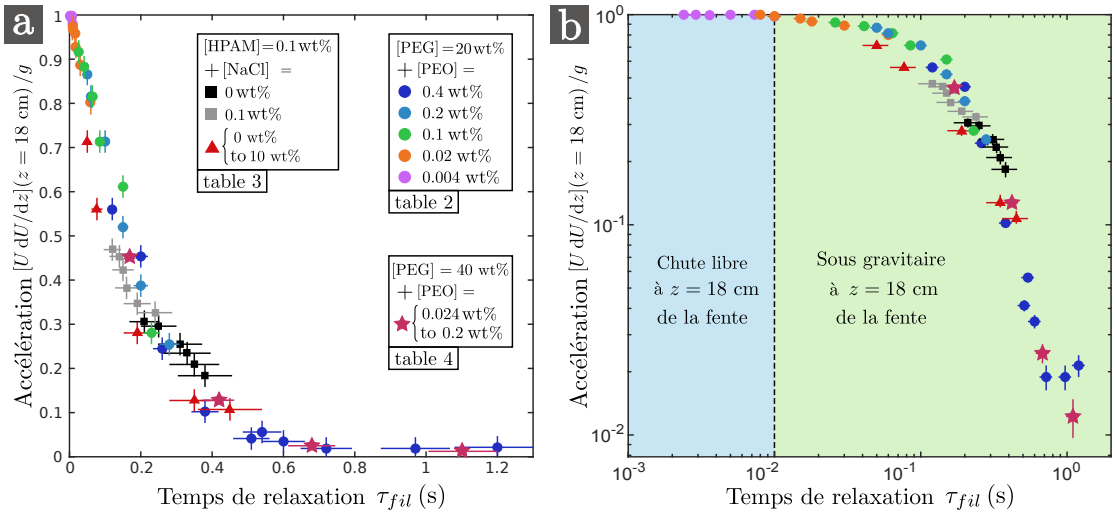

Figure 7.9 – Accélération $U\mathrm{d}U/\mathrm{d}z$ adimensionnée par g, mesurée à $z = 18$ cm de la fente, en fonction du temps de relaxation extensionnel τ_{fil} en échelles linéaires (a) et logarithmique (b) pour toutes les solutions utilisées (PEO et HPAM) et pour des rideaux de longueur $L_c = 30$ cm.

où $\Delta = \sigma_{zz} - \sigma_{yy}$ est la différence de contraintes normales. Notons que U et Δ sont des quantités moyennées dans l'épaisseur du rideau. Dans le cas d'un liquide Newtonien, on trouve $\Delta = 4\eta\mathrm{d}U/\mathrm{d}z$ et l'équation de Taylor 7.4 est retrouvée. Pour un liquide viscoélastique, on a besoin d'une autre équation constitutive, mais nous allons voir comment trouver z_e en se contentant de l'équation bilan. Cette équation peut être écrite en version Lagrangienne où on introduit le temps t tel que $U\mathrm{d}/\mathrm{d}z$ devienne $\mathrm{d}/\mathrm{d}t$. L'équation ainsi obtenue s'intègre en

$$U - U_1 = g(t - t_1) + \frac{1}{\rho}\left(\frac{\Delta}{U} - \frac{\Delta_1}{U_1}\right) \tag{7.13}$$

où l'indice $_1$ fait référence à un altitude arbitraire z_1. Ainsi, puisque le temps de relaxation extensionnel τ_{fil} joue un rôle majeur dans l'écoulement, on peut adimensionner cette équation en faisant apparaître ce paramètre. On obtient alors que les échelles de vitesse et de longueur caractéristiques de l'écoulement sont

$$U_e = g\tau_{fil} \qquad \text{et} \qquad z_e = g\tau_{fil}^2 = U_e^2/g \tag{7.14}$$

Ce résultat peut être retrouvé par un argument simple. Lorsque les particules de fluide tombent en chute libre $U \propto \sqrt{2gz}$, les polymères sont au sein d'un écoulement extensionnel de taux d'extension local décroissant $\dot{\epsilon} = \mathrm{d}U/\mathrm{d}z = g/U$. Si ce taux d'extension devient significativement plus petit que $1/\tau_{fil}$, les contraintes élastiques dues à l'étirement des chaînes deviennent négligeables et on peut attendre un changement de comportement pour l'écoulement. Ainsi, la distance à la fente à laquelle le changement de comportement a lieu est $z_e = g\tau_{fil}^2$ car il correspond à $\dot{\epsilon}\tau_{fil} = O(1)$.

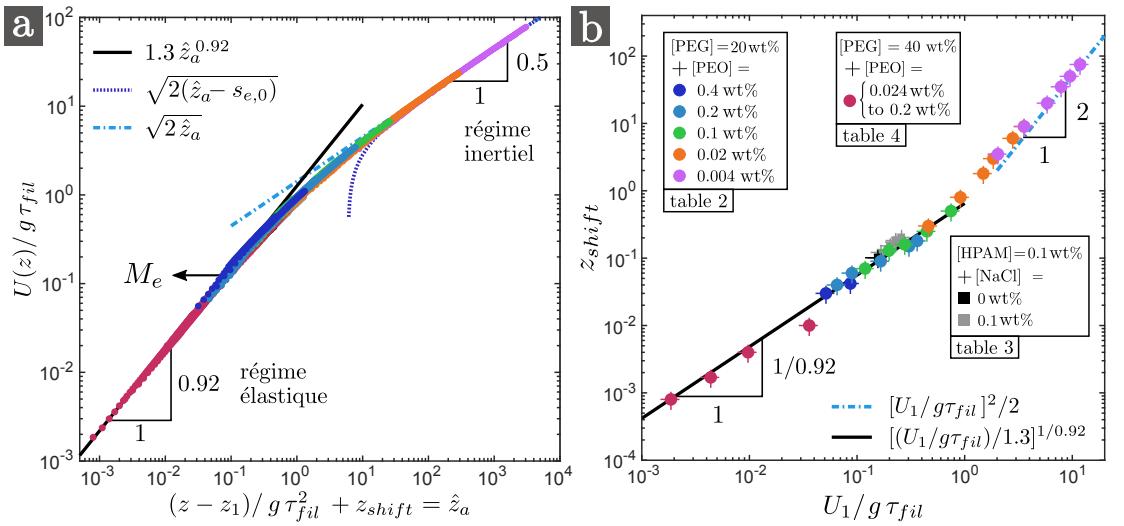

Figure 7.10 – (a): Courbe maîtresse des rideaux liquides viscoélastiques. Profils de vitesse adimensionnés $U(z)/g\tau_{fil}$ en fonction de $(z-z_1)/g\tau_{fil}^2 + z_{shift}$ en échelle logarithmique, où $z_1 \approx 2.5$ mm et où chaque courbe est translatée le long de l'axe des abscisses d'une distance z_{shift} pour regrouper les données sur une même courbe. (b): z_{shift} en fonction de $U_1/g\tau_{fil}$. On constate que $z_{shift} = M_e^{-1}(U_1/g\tau_{fil})$. Dans ces deux courbes, on ne considère que les profils de vitesse qui ne sont probablement pas influencés par la coudition en aval $U(L_c) = 0$.

On peut à présent chercher une courbe maîtresse de l'écoulement par analogie avec les rideaux Newtoniens. Si l'on trace les profils de vitesse adimensionnés U/U_e en fonction de $(z-z_1)/z_e$ (où $z_1 \approx 2.5$ mm) on obtient des courbes de même forme qui, si on les décales d'une distance z_{shift} le long de l'axe des abscisses, se superposent sur une courbe maîtresse M_e, comme présenté en figure 7.10.a. Comme pour les rideaux Newtoniens, l'existence d'une courbe maîtresse suppose que l'on ne prenne en compte que la partie de l'écoulement qui n'est pas influencée par la condition en aval $U(L_c) = 0$. On peut identifier deux régimes: un régime élastique initial (balance gravité-elasticité), qui est l'équivalent du régime visqueux Newtonien (voir figure 7.1.b) et où l'accelération des particules est inférieure à g, suivi d'un régime asymptotique de chute libre, le régime inertiel (balance gravité-inertie). La courbe maîtresse M_e est alors caractérisée par deux comportements différents

$$M_e(\hat{z}) = \begin{cases} K\hat{z}^{\alpha} & \hat{z} \ll 1 : \text{ régime élastique} \\ \sqrt{2\,(\hat{z} - s_{e,0})} & \hat{z} \gg 1 : \text{ régime inertiel} \end{cases} \tag{7.15}$$

où $\hat{z} = z/z_e$. On mesure $K = 1.3 \pm 0.2$ and $\alpha = 0.92 \pm 0.02$. Comme α est proche de 1, le taux d'extension est presque constant dans le régime élastique. Par ailleurs, on mesure $s_{e,0} = 6 \pm 2$. En figure 7.10.b, on trace z_{shift} (paramètre purement expérimental) en fonction de $U_1/g\tau_{fil}$ (où $U_1 = U(z_1)$). On constate que les deux

lois d'échelles sont cohérentes avec $z_{shift} = M_e^{-1}(U_1/g\tau_{fil})$. On peut alors écrire de manière synthétique que le profil de vitesse s'écrit

$$\hat{U}(\hat{z}) = M_e \left(\hat{z} - \hat{z}_1 + M_e^{-1}(\hat{U}_1) \right) \tag{7.16}$$

où $\hat{U} = U/U_e$. La même formule peut également être dérivée de l'équation 7.7 pour les rideaux Newtoniens. Finalement, on déduit que la longueur effective du régime sous gravitaire s'écrit $z_e^* = F_e \times z_e$ où F_e est une fonction décroissante de la vitesse initiale (comme en Newtonien). On mesure $F_e = 12 \pm 5$ lorsque $U_1/g\tau_{fil} \ll 1$.

Influence de la géométrie de la filière

Nous avons réalisé des expériences afin de caractériser l'effet de l'histoire de l'écoulement en amont du rideau. En effet, dans le cas de la filière présentée en figure 7.2.b, les polymères sont soumis à un cisaillement au sein de la fente qui peut engendrer des contraintes élastiques importantes en amont du rideau. Lorsque cette filière est remplacée par un plan incliné sur lequel le liquide s'écoule librement avant de former un rideau (en tombant depuis le bord du plan), on réduit considérablement les contraintes élastiques de cisaillement. Or, on constate que l'écoulement du rideau n'est que peu affecté par ce changement de géométrie. On en déduit que l'histoire de l'écoulement en amont du rideau a un impact très modeste sur l'écoulement de ce dernier.

Stabilité du rideau

La stabilité du rideau a été étudiée sous deux aspects: la dynamique d'ouverture de trous au sein de la nappe et la stabilité de l'écoulement lui même (en l'absence de trou). Ces aspects sont d'un grand intérêt pour l'industrie.

Ouverture de trou

Des trous sont souvent formée au sein du rideau dû à la présence d'impuretés dans le liquide telles que des bulles. Ces trous sont un frein considérable à la technique d'enduction au rideau. Lorsque de tels trous apparaissent, leur taille augmente et le liquide est alors collecté dans le bourrelet qui les entoure ("rim" en anglais). Si les forces visqueuses et élastiques sont négligeables, la dynamique d'ouverture d'un trou résulte d'une balance entre inertie et capillarité. Dans ce cas, dans le référentiel du rideau, la vitesse d'ouverture du bourrelet est donné par la vitesse de Taylor-Culick (Taylor, 1959; Culick, 1960)

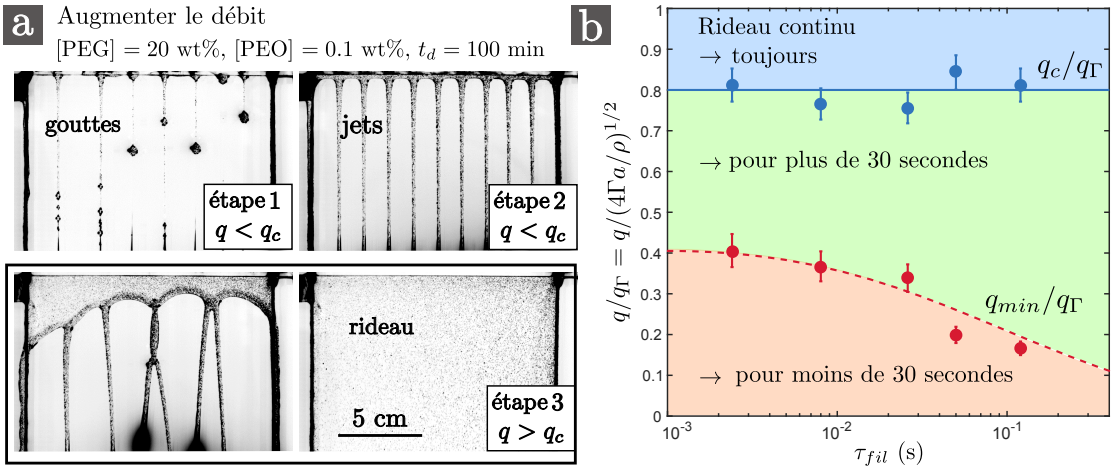

Figure 7.11 – (a): Différents régimes observés lorsque l'on augmente le débit q de 0 à 6 cm^2/s pour une certaine solution de PEO. (b): Débit critique q_c (au delà duquel tout trou est advecté par l'écoulement) et débit minimum q_{min} (en deçà duquel un rideau se brise en moins de 30 secondes), divisés par $q_\Gamma = (4a\Gamma/\rho)^{1/2}$, en fonction du temps de relaxation τ_{fil} pour cinq solutions de PEO solutions. $q_\Gamma = 3.5$ cm^2/s et la longueur du rideau est $L_c = 30$ cm.

$$V = \sqrt{\frac{\Gamma}{\rho h}} \tag{7.17}$$

où $2h = q/U$ est l'épaisseur locale du rideau. Ainsi, dans le référentiel du laboratoire, le bord supérieur du trou se meut à une vitesse $V - U$ qui dépend de z. Il y a donc une compétition entre les forces capillaires tendant à tirer le bord supérieur du bourrelet vers le haut et l'inertie du liquide tendant à refouler le trou vers le bas. Cette compétition peut s'écrire en terme d'un nombre de Weber

$$We = \left(\frac{U}{V}\right)^2 = \frac{\rho h U^2}{\Gamma} = \frac{\rho q U}{2\Gamma} \tag{7.18}$$

qui peut être inférieur à 1 près de la fente et plus grand que 1 en aval. Ainsi, seuls les trous initiés là où $We < 1$ remonterons vers la fente et causeront une brisure irréversible du rideau. Ce scénario devient impossible si $We > 1$ partout, i.e. si la vitesse d'extrusion du liquide est plus grande que la vitesse de Taylor-Culick (calculée en sortie de fente d'épaisseur $2a$). Cela se produit pour un débit supérieur à un débit q_Γ donné par

$$q_\Gamma = \sqrt{\frac{4a\Gamma}{\rho}} \tag{7.19}$$

Lorsque le débit est suffisamment bas, des gouttes ou des jets sont formée en sortie de fente (voir figure 7.11.a). En augmentant le débit, les jets fusionnent

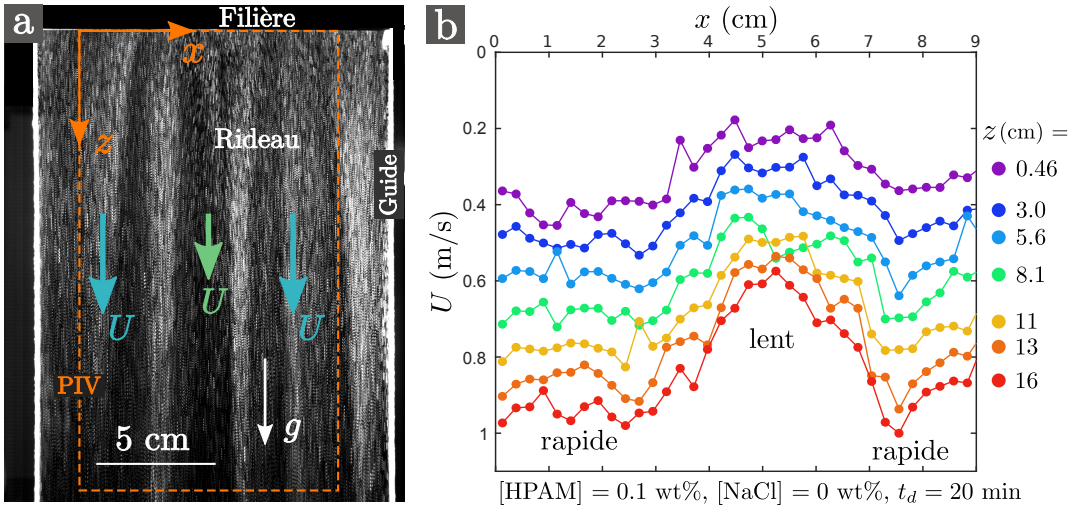

Figure 7.12 – Exemple de mesure de PIV sur une solution de HPAM non salée. (a): Superposition d'images successives. (b): Composante verticale du champ de vitesse, i.e. $U(x, z, t)$, en fonction de la coordonnée horizontale x à différentes distances z de la sortie de la fente à un temps arbitraire t. La longueur du rideau est $L_c = 30$ cm et le débit linéique est $q = 3.1$ cm^2/s.

jusqu'à ce qu'une nappe continue émerge de la fente à un débit critique que l'on note q_c. Ce débit est mesuré pour différentes solution de PEO et les résultats sont donnés en figure 7.11.b en fonction du temps de relaxation τ_{fil}. On trouve que $q_c/q_\Gamma \approx 0.8$ pour toutes ces solutions, ce qui indique que le rideau se forme en effet lorsque la vitesse d'extrusion du liquide devient de l'ordre de la vitesse de Taylor-Culick, avec une correction qui est probablement due au poids du bourrelet.

On observe un scénario différent lorsque le débit est diminué. En particulier, rien de spécial ne se passe lorsque q devient plus petit que q_c. En revanche, un rupture du rideau devient possible si un trou est initié près de la fente. On peut alors définir un débit minimum q_{min} en deçà duquel le rideau de rompt en moins d'une certaine durée, par exemple 30 secondes. Ce débit est mesuré et est tracé en figure 7.11.b en fonction du temps de relaxation τ_{fil}. On constate une diminution de q_{min} avec τ_{fil}, ce qui témoigne d'une plus grande résistance de la nappe. Cet effet a également été reporté par Becerra & Carvalho (2011) et par Karim et al. (2018b).

Modulation du rideau

Pour certaines solutions, l'écoulement du rideau s'est révélé être instationnaire et modulé selon la direction horizontale x, comme le montrent les figures 7.12.a (superposition d'images) et la figure 7.12.b (champ de vitesse) pour une solution de HPAM non salée. Cette instabilité se caractérise par une modulation du champ de vitesse et de l'épaisseur du rideau: des bandes verticales épaisses apparaissent, au

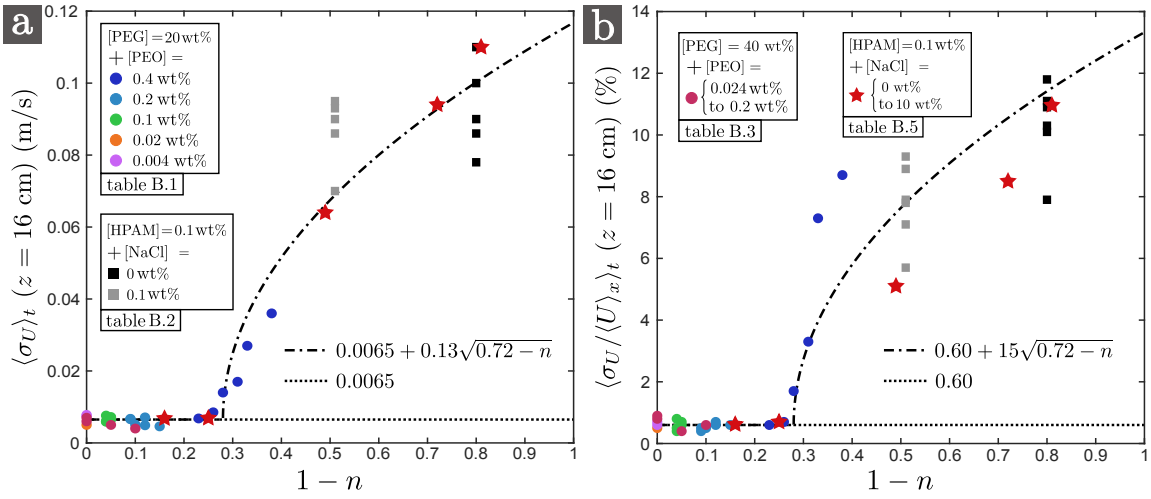

Figure 7.13 – Diagramme de bifurcation. Amplitude absolue $\langle \sigma_U \rangle_t$ (a) et relative $\langle \sigma_U / \langle U \rangle_x \rangle_t$ (b) de la modulation à une distance arbitraire $z = 16$ cm du rideau en fonction de $1 - n$ où n est le degré de rhéofluidification (voir équation 7.9) pour des rideaux de solutions de PEO et de HPAM. σ_U est l'écart type de la distribution de vitesse défini par l'équation 7.20. La modulation commence pour $n < 0.72$ et est de plus en plus marquée à mesure qu'on augmente la rhéofluidification. Les résultats sont comparés à un ajustement de racine carrée.

sein desquelles le liquide est plus rapide que la moyenne. On peut cependant définir un champ de vitesse moyenné selon x et moyenné en temps $\langle \langle U \rangle_x \rangle_t$. Notons que $\langle U \rangle_x$ ne dépend en réalité pas du temps t. Certains champs de vitesses sont présents en figure 7.10, preuve que l'écoulement moyen des rideaux modulés se superpose également la courbe maîtresse M_e identifiée précédemment.

Cette instabilité n'apparaît que pour les solutions les plus rhéofluidifiantes. En particulier, un rideau de HPAM sans sel est modulé et la modulation peut être tuée par simple ajout de sel. Les solutions de PEO les plus rhéofluidifiantes présentent également cette instabilité. Nos résultats sont résumés en figure 7.13 qui est une tentative de diagramme de bifurcation où l'amplitude de l'instabilité est tracée en fonction de $1 - n$, où n est le degré de rhéofluidification (equation 7.9). L'amplitude de la modulation est extraite des résultats de PIV et est définie par rapport à l'écart type σ_U de la distribution de vitesse selon x, i.e.

$$\sigma_U = \sqrt{\left\langle (U - \langle U \rangle_x)^2 \right\rangle_x} \tag{7.20}$$

Les données en figure 7.13 correspondent respectivement à $\langle \sigma_U \rangle_t$ (a: amplitude absolue) et à $\langle \sigma_U / \langle U \rangle_x \rangle_t$ (b: amplitude relative) mesuré à une distance arbitraire $z = 16$ cm de la fente. Bien que les données soient trop dispersées pour conclure sur une loi particulière, la dépendance en n est clairement établie et les rideaux

modulés sont observés pour des degrés de rhéofluidification $n < 0.72$. En particulier, des solutions de grand temps de relaxation et de viscosité constante ($n = 1$) ne présentent pas de modulation.

Origine de l'instabilité

Afin de comprendre d'où vient cette instabilité, nous avons fait une série de mesures avec une filière transparente (une boîte rectangulaire) pour visualiser l'écoulement en amont de la fente. La fente est plus courte ($L_s = 4$ mm au lieu de 10 cm) mais est de même épaisseur $2a = 1$ mm et le rapport d'aspect de la contraction est toujours $A/a = 14$. On s'assure que l'écoulement en amont de la contraction est invariant selon x à l'aide d'un réseau de pailles. L'écoulement est visualisé dans le plan souhaité grâce à une nappe laser.

On constate que la modulation du rideau est liée à une instabilité en amont de la fente. À grand débits, l'écoulement dans la filière près de la contraction devient instationnaire et tridimensionnel, i.e. modulé selon x. Pour des solutions de HPAM pas (ou peu) salées, on observe de longues structures en forme de jets où la vitesse du liquide est bien plus importante qu'ailleurs. Comme le montre la figure 7.14 (solution de HPAM non salée), ces structures sur-alimentent alors la fente en certaines positions où la vitesse est plus grande que la vitesse moyenne attendue pour un écoulement bidimensionnel $U_s = q/2a$. Ces positions correspondent aux positions des bandes épaisses du rideau et il y a donc une continuité entre la structure instable de l'écoulement en amont et en aval de la fente.

Des structures tridimensionnelle de l'écoulement en amont de la fente ont également été observées par Chiba et al. (1990, 1992) pour des solutions rhéofluidifiantes mais les effets étaient beaucoup plus modestes que ceux que nous observons avec le HPAM et l'auteur ne mentionne par de modulation du rideau s'écoulant depuis la fente.

Il est bien connu que les instabilités associées aux écoulements de contraction (axisymétrique ou plane) apparaissent en général au delà d'un nombre de Weissenberg critique pour les liquides viscoélastiaues (Boger & Walters, 2012; Rothstein & McKinley, 1999; McKinley et al., 1991; Cartalos & Piau, 1992; Piau et al., 1990). Nous définissons le nombre de Weissenberg Wi par rapport au temps de relaxation mesuré en CaBER, i.e.

$$Wi = \frac{\tau_{fil}\, U_s}{a} \tag{7.21}$$

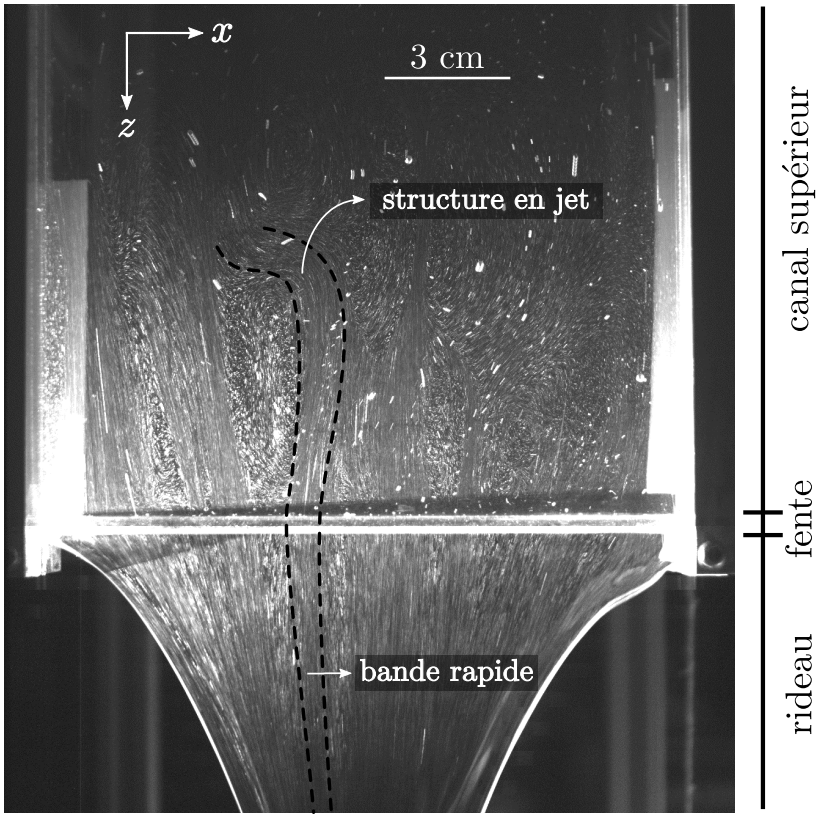

Figure 7.14 – Vue de face de la structure de l'écoulement pour une solution de HPAM non salée. Le rideau sous la fente est modulé et il y a continuité entre la modulation en amont et en aval de la fente: les longues structures en jets dans la filière (où la vitesse du liquide est grande) deviennent les bandes épaisses du rideau. Ici, le rideau n'est pas guidé par des fils afin que la nappe laser éclaire le rideau sans obstacle.

où a/U_s est l'ordre de grandeur du temps passé dans la zone de contraction ou les polymères sont étirés (i.e. où le liquide accélère). On regroupe toutes nos données en figure 7.15 où les rideaux modulés sont positionnés sur une carte $Wi - n$. Les rideaux modulés se trouvent dans la zone de grands Wi et de petits n (solutions rhéofluidifiantes). Cependant, une solution particulière de PEO, préparée dans un solvant de contenant pas de PEG, est dans cette zone alors qu'elle ne présente pas de modulation de rideau. Cela montre que d'autres paramètres rhéologiques doivent être pris en compte pour mieux caractériser l'apparition de l'instabilité. Ce travail constitue une perspective à nos travaux de recherche.

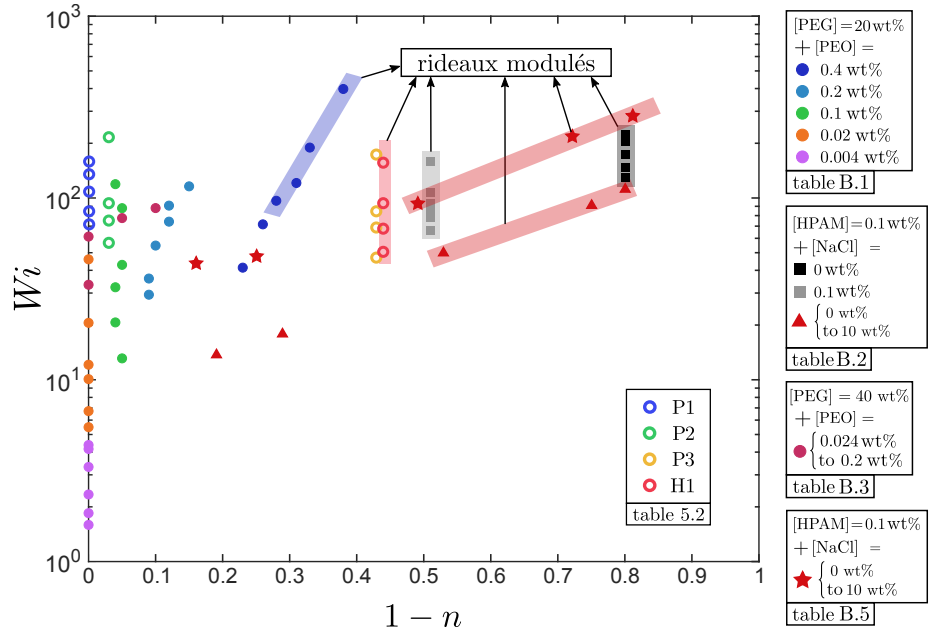

Figure 7.15 – Diagramme de phase des rideaux modulés et non modulés dans le plan $Wi-n$.